

Topological charge pumping in ultracold quantum gases

Dissertation for the award of the degree

"Doctor rerum naturalium" (Dr.rer.nat.)

of the Georg-August-Universität Göttingen

within the doctoral program
of the Georg-August University School of Science (GAUSS)

submitted by
Eric Bertok

from Kassel

Göttingen, September 1, 2023

Thesis Committee:

Prof. Dr. Fabian Heidrich-Meisner
Institut für Theoretische Physik, Georg-August-Universität Göttingen

Prof. Dr. Matthias Krüger
Institut für Theoretische Physik, Georg-August-Universität Göttingen

Prof. Dr. Thomas Weitz
I. Physikalisches Institut, Georg-August-Universität Göttingen

Members of the examination Board:

Reviewer: Prof. Dr. Fabian Heidrich-Meisner
Institut für Theoretische Physik, Georg-August-Universität Göttingen

Second Reviewer: Priv.-Doz. Dr. Salvatore R. Manmana
Institut für Theoretische Physik, Georg-August-Universität Göttingen

Third Reviewer: Prof. Dr. André Eckardt
Institut für Theoretische Physik, TU Berlin (not a member of the examination committee)

Further members of the examination Board:

Prof. Dr. Martin Wenderoth
IV. Physikalisches Institut, Georg-August-Universität Göttingen

Prof. Dr. Matthias Krüger
Institut für Theoretische Physik, Georg-August-Universität Göttingen

Prof. Dr. Thomas Weitz
I. Physikalisches Institut, Georg-August-Universität Göttingen

Prof. Dr. Claus Ropers
IV. Physikalisches Institut, Georg-August-Universität Göttingen and Max Planck
Institute for Multidisciplinary Sciences

Date of the oral examination: 30.08.2023

Contents

1	Introduction	5
1.1	Topology emerges	5
1.2	The central idea of topology	6
1.3	Topology in physics	7
1.4	Ultracold atomic systems and optical lattices	8
1.5	Topological charge pumps	9
1.6	Goals and results of this thesis	10
1.6.1	Disordered Thouless pumps	11
1.6.2	A Thouless pump coupled to a phononic environment	11
1.6.3	Interacting Thouless pumps	12
1.7	Structure of this thesis	13
2	Topology in condensed matter theory	15
2.1	Review of Berry phases and Chern numbers	15
2.1.1	Berry phase	15
2.1.2	Berry Curvature and Chern number	18
2.1.3	Topology of Bloch vectors	20
2.2	Adiabatic theory	21
2.3	Homotopy	22
3	Topological charge pumps	25
3.1	SSH model	25
3.1.1	Bulk-boundary correspondence	26
3.2	Rice-Mele model	27
3.2.1	Bulk Hamiltonian and dispersion relation	27
3.2.2	Current operator and amount of pumped charge	30
3.2.3	Polarization and Wannier functions	31
3.2.4	Current operator for lattice systems and non-adiabatic effects of the pumped charge	32
3.3	Thouless pumps as analogues to Chern insulators	33
3.4	Experimental realizations of Thouless pumps	34
3.4.1	Ultracold atoms	35
3.4.2	Photonic systems	37
4	Numerical methods	39
4.1	Julia	39
4.2	Non-interacting, spin-polarized charge pumps	40

Contents

4.3	Fermionic systems coupled to phonons: Multi-trajectory Ehrenfest	41
4.4	Many-body interacting systems	42
4.4.1	Matrix-product state methods	42
5	Disorder in topological charge pumping	47
5.1	Publication: Effect of disorder on topological charge pumping in the Rice-Mele model	50
6	Topological charge pumps coupled to a phononic bath	65
6.1	Publication: Phonon-induced breakdown of Thouless pumping in the Rice-Mele-Holstein model	68
7	Effects of adding many-body interactions to topological charge pumps	83
7.1	Publication: Splitting of topological charge pumping in an interacting two-component fermionic Rice-Mele Hubbard model	86
7.2	Interaction-induced pumping	97
7.3	Preprint: Interaction-induced charge pumping in a topological many-body system	98
8	Finite temperature pumping in the Rice-Mele Hubbard model	113
9	Conclusion	117
10	Research data	123
11	Acknowledgements	125

1 Introduction

1.1 Topology emerges

In 1985, Klaus von Klitzing was awarded the Nobel price for the discovery of the quantum Hall effect [1, 2]. It was well understood that applying a magnetic field to a flat electric conductor with a flowing electric current causes a perpendicular drift of the electrons, leading to a transverse Hall voltage and a Hall conductance. The reason is the Lorentz force, which forces classical electrons in magnetic fields onto circular paths. Von Klitzing found that the Hall conductance in a 2d electron gas subject to a strong magnetic field and low temperatures is not a continuous function of the magnetic field strength. Instead, he found well-defined plateaus of constant values. Even more surprisingly, these conductivity values came in discrete chunks of an integer number of units. These units were extremely precise, deviating from whole numbers by about $0.000\,000\,1$ [3], much less than could be explained given the amount of control over experimental parameters. The answer to this precision came by Thouless et al. in 1982 in a seminal paper [4] that connected the measured plateaus to a topological invariant, the so called Chern number. Nowadays, topology has emerged as an important concept to classify states of quantum matter in condensed matter theory ¹.

In 1973 Kosterlitz and Thouless pioneered the theory of topological phase transitions in the XY model [9]. Vortices - topological defects in the spin alignment - split up as a function of temperature. This illustrates that the classification scheme of phase transitions is incomplete under Landau theory and that topological invariants can be used to classify these phases [10, 11, 12, 13, 14, 15, 16, 17, 18, 19].

Complementary to condensed matter physics with real materials, quantum simulators [20, 21, 22] permit the experimental realization of generic model Hamiltonians with a high degree of controllability. One of the most promising platforms for this are ultracold quantum gases [23, 24, 25, 26], which have proven to be ideal platforms for studying topological systems [27, 28, 29, 30, 31, 32, 25, 33, 34, 35, 36, 37, 38, 39, 40]. Most of these experiments so far have employed synthetic gauge fields [41] with Floquet engineering [42, 43], a periodic driving of the system, to realize topological band structures, and have focused on non-interacting topological systems. The interplay between interactions and topology can give rise to various exotic phases [17], but challenges remain, for example in the form of heating due to many-body resonances in Floquet engineering

¹Topology is also relevant in classical physics, for example in the phase shift of a Foucault pendulum [5]. Geometric phases, one of the main tools in topology and also central quantities in this thesis, can be used to explain why cats always land on their feet [6, 7] and homotopies can be used to classify skateboard tricks [8].

1 Introduction

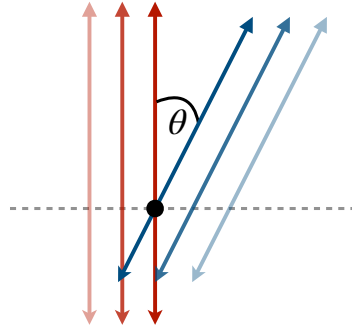


Figure 1.1: Two infinite lines approaching in 3d space will almost always intersect at one point in the generic instance of non-parallel lines. The degenerate case of parallel lines reverts back to generic example when perturbing the system.

[42]. Additionally, interacting systems of two- and higher-dimensions are often difficult to treat numerically and heavily restricted by system size in these studies [29].

A topological charge pump [44, 45] is a one-dimensional, dynamical analogue of a quantum Hall system that is particularly well suited for studying topology, both theoretically [46, 47, 48, 49, 50, 35, 51, 52, 53, 54, 55, 56, 57, 58, 59, 60, 61, 62, 63, 64, 65, 66] and experimentally [33, 34, 67, 38, 68, 69, 70, 71, 72, 73], since no synthetic gauge fields are required and efficient numerical algorithms exist to treat one-dimensional interacting systems in the form of matrix-product state methods [74, 75, 76, 77, 78, 79, 80, 81, 82]. Instead of a robustly quantized Hall conductivity, a topological charge pump pumps a quantized amount of charge in each cycle of a parameter modulation that is given by the same topological invariant as in the quantum Hall effect.

The goal of this thesis is to understand the stability of quantized transport in various contexts, such as disordered systems, quantum systems where energy can be exchanged with a bath and in the presence of genuine many-body interactions.

1.2 The central idea of topology

In mathematics, the field of topology deals with questions about properties of geometric objects that are unchanged during continuous transformations. In other words, topology identifies certain "generic" properties that do not depend on the specifics of a geometric object, like angles, lengths and shape. During continuous transformations, these properties are invariant. In contrast, special cases called "degeneracies" can be lifted to more generic cases [83].

As an example, consider two infinite lines in three dimensional euclidean space that are moving along a common direction towards each other as illustrated in fig. 1.1. For almost all angles θ the lines will eventually touch at a single point. This is the generic case. In the degenerate case of $\theta = 0$, the lines might either pass each other without intersecting or coincide completely, intersecting at all points. A key principle in topology

is the stability of properties under perturbations. In the present example, when starting from the generic case, slightly changing the angle between the lines will almost always keep you in the generic case - the property of intersecting at a single point is stable. On the other hand, when starting from the degenerate case and changing the angle slightly, the generic case is recovered immediately. To each generic case, a topological invariant can be assigned that is dependent on the specific problem in question. Here, it would simply be the number of intersections.

The most famous example², is the fact that a coffee mug and a doughnut are topologically equivalent. Their topological invariant - the number of holes - is unchanged during a continuous transformation from one to the other. Continuous means that there are no "drastic" changes done to the objects.

1.3 Topology in physics

It is natural to ask whether there exist such generic properties in physical systems that are stable to external perturbations and that do not depend on a fine-tuning of parameters. The first of these topological properties was the aforementioned integer quantum Hall (IQH) effect found by von Klitzing [1, 2]: For a two-dimensional electron gas that is pierced with a strong magnetic field, the transverse conductivity is ³ $\sigma_{xy} = \frac{e^2}{2\pi\hbar}\nu$ with ν being exactly integer [84]. The topological invariant ν is the Chern number, which is usually found as a topological invariant in two-dimensional systems. For the IQH effect, ν represents the number of filled Landau levels that form due to the magnetic field. Since then, topology has been found in a multitude of systems, such as one-dimensional spin chains [85, 86, 87], in two-dimensional honeycomb lattices without an external magnetic field but broken time-reversal symmetry [88, 30, 89, 90], in time-reversal invariant systems [91, 92, 93, 94, 95, 96, 97, 98] in the form of Z_2 topological insulators⁴, in twisted bilayer graphene [71, 70, 99, 72], and in superconductors [100, 101, 102, 103]. Topological superconductivity has become a focus point of recent research [102, 104], due to the possibility of Majorana modes [105, 106, 107, 102, 108, 109], which are one approach for a fault-tolerant quantum computer [103].

All of these are examples of "topological states of matter". In Landau theory, phase transitions correspond to a spontaneous change in the local symmetries of the system, for example in the transition from a liquid to a solid, where the continuous translational symmetry is broken down to a discrete translational symmetry. Topological phases of matter go beyond this principle. Two phases can possess the same local symmetries but still belong to distinct topological phases. Their distinction comes from the values of their topological invariants. As long as nothing "drastic" is done to a system - which for physical systems is the closing of an energy gap - it stays in its topological phase. Topological phase transitions occur when closing an energy gap, which corresponds to

²So much so that I intentionally avoid it in talks and as an introduction here.

³Here, e is the electron charge and \hbar is the reduced Planck constant.

⁴These time-reversal invariant Z_2 topological insulators are sometimes referred to as "topological insulators" in the narrow sense.

1 Introduction

the degenerate case from the example above, and the value of the topological invariant can change.

A key concept in topological phases is the bulk-boundary correspondence [110, 111, 112, 113, 114, 115, 116, 116, 117]. Topological invariants are quantities that provide information about the structure of quantum states in the bulk of the system far from the edge. More specifically, they encode global properties of the wavefunctions, such as a winding around the Brillouin zone in the form of a Zak phase [118, 28] or the presence of vortices [9, 105, 102]. One can show that these bulk invariants are linked to the appearance of localized, gapless edge states at the boundary of the system. For the integer quantum Hall effect, the edge states are chiral and given by the orientation and strength of the magnetic field. For each filled Landau level, one of these edge states is filled. The concept of topological protection of bulk invariants extends to the edge states in the sense that their existence and properties are robust against external effects like disorder and weak interactions as long as the bulk gap remains open. Edge states also appear at the interface between two topologically distinct phases, which can be used to investigate topology experimentally [27, 119].

1.4 Ultracold atomic systems and optical lattices

The interplay of topology and many-body interactions is an open question that has recently seen increased interest as state-of-the-art experimental techniques have evolved to allow for the measurement of interacting systems. One of the most promising platforms for this are ultra-cold atomic gases [24, 24, 25, 26], which allow for coherent quantum dynamics in an effectively closed system due to their high degree of controllability. The Feshbach resonance [120] allows for tuning the strength of many-body interactions independently of the tunneling rate⁵ via an external magnetic field, from essentially non-interacting to strongly interacting regimes.

Whereas theoretical physics often deals with models as approximations to a measured effect in a real material, in ultracold atoms, this principle can be flipped on its head: Theoretical models can be designed to have desired features and these models can directly be implemented in the lab, which is why these systems are also called "quantum simulators" [20, 21, 22]. Ultracold atoms are charge neutral, which means that regular magnetic fields are not sufficient to induce the time-reversal symmetry breaking that lies at the heart of Chern insulators and the quantum Hall effect. Instead, synthetic gauge fields have to be created [41]. This can be done, for example, with circular lattice shaking [121, 122, 121, 123, 124, 30, 36] or Raman coupling [31, 125, 126]. A non-zero Chern number leads to an anomalous Hall drift that can be captured with in-situ imaging [33]. Band-mapping techniques [31] can be used to measure the population of topological bands and momentum-distributions. In addition, single atoms and correlated quantum states can be measured via a quantum-gas microscope [127, 128, 129, 130].

⁵The ratio between interaction strength and tunneling can also be tuned via the lattice depth [24].

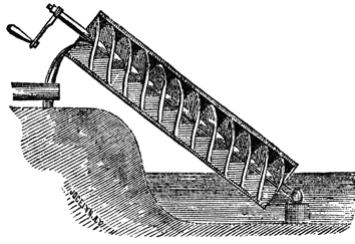


Figure 1.2: A sketch of an Archimedes screw pump [131].

1.5 Topological charge pumps

A central concept in the study of topological systems both theoretically [46, 47, 48, 49, 50, 35, 51, 52, 53, 54, 55, 56, 57, 58, 59, 60, 61, 62, 63, 64, 65, 66] and experimentally [33, 34, 67, 38, 68, 69, 70, 71, 72, 73] is a topological charge pump, also called Thouless pump [44, 45], a one-dimensional dynamical equivalent of a quantum Hall system. The two spatial dimensions of the quantum-Hall effect are replaced by a single spatial dimension and a periodic time-modulation. A Thouless pump can be thought of as a quantum version of an Archimedes pump (fig. 1.2) that transports a well-defined amount of water, each time the pump is rotated once. In a Thouless pump, charge (or spin) is transported through the system during one cycle of the parameter modulation, as long as this modulation is adiabatically slow, meaning the modulation frequency is low compared to the energy gap. The amount of charge pumped is integer-quantized and equal to the same bulk invariant as in the quantum Hall effect, the Chern number. The prototypical model of a Thouless pump is the Rice-Mele model [132], which is a one-dimensional tight-binding lattice model with two dynamically controlled parameters: A staggered, alternating potential offset at each site and a dimerized, alternating hopping. In ultracold-atomic systems, instead of engineering non-trivial topology via synthetic magnetic fields for two-dimensional systems, Thouless pumps permit the study of a corresponding one-dimensional system, in which the role of magnetic field is replaced by a highly tunable external potential that is modulated in time. Thouless pumps are therefore simpler to realize in ultracold atom experiments, especially for interacting systems, where heating during Floquet driving is a challenge.

The Rice-Mele model has recently been experimentally realized in ultracold atoms for both fermions [34, 67, 38] and bosons [33], and in other platforms such as photonic waveguides [68, 69] and optical cavities [73]. This has led to increased theoretical interest in this model, and Thouless pumps in general. It is well established [44] that the transport in Thouless pumps is quantized, as long as the time-modulation is slow. The non-adiabatic effects due to finite pumping speeds are understood to be quadratic in the pumping frequency [56]. For non-interacting charge pumps, the role of disorder has been a focus of recent research [44, 133, 11, 58, 69]. While it is accepted that weak disorder does not break the quantization of pumped charge [44], the breakdown of quantization has been a prevalent subject of current scientific discourse [58, 50]. An open question

1 Introduction

has been the precise mechanism of the breakdown and the connection to an energy-gap closing [34, 58], especially in the context of ultracold-atomic systems, where disorder averages are relevant. A lot of research has been carried out on the topic of Thouless pumps in open systems [134, 10, 61, 135, 136, 137, 138, 139, 140], where it is understood that quantized transport is present even in systems without particle conservation. Prior to this thesis, phonon coupling in a closed Thouless pump has not been studied. In systems with finite temperature [141, 142, 134, 138, 143, 144, 145, 48] it is generally believed that quantized pumping is broken, while the systems themselves stay topological up to a critical temperature [146]. A key remaining question is whether finite temperature can also induce charge pumping. A lot of focus has been set on the study of interacting Thouless pumps, where various exotic adiabatic pumping schemes have been established theoretically, including the pumping of bound pairs [62], pumping in bosonic systems [147, 47, 148, 53, 149], novel kinds of spin pumps [46], pumping in correlated fermion systems [150, 151, 57, 152, 153], nonlinear Thouless pumping [154, 155], pumping in Mott insulators [156], fractional pumping [157, 52, 158] and interaction-induced pumping [159, 160, 161]. Nevertheless, many open questions remain, such as the role of many-body gap closings during the pump cycle, the role of the various kinds of many-body gaps, and the experimental realization of a genuine many-body-interacting topological pump.

1.6 Goals and results of this thesis

In this thesis I will present a series of publications that study the Rice-Mele model in the context of ultracold quantum gases. We will focus on experimentally relevant effects on Thouless pumps, such as disorder, finite temperature, coupling to a bath and strongly-correlated regimes. The theoretical studies are done using numerics that capture many of the features of real experiments, such as finite particle numbers, confining potentials and loss of adiabaticity due to finite pumping speeds.

The primary objective of this thesis is to gain an understanding of the stability of Thouless pumping within ultracold atomic systems, to further understand the mechanisms that govern the breakdown of quantized charge pumping in this context and to explore possibilities of new kinds of many-body Thouless pumps emerging from interactions.

In section 5.1, we show that the disorder-averaged gap, which has been expected to be the relevant quantity for the breakdown of quantized charge transport due to disorder, is not well-suited for predicting the critical disorder strength. Instead, the full energy-gap distributions should be considered, which show a sharp signature at the crossover from quantized to non-quantized pumping. We also employ the Local Chern Marker [162] for the first time for a topological Charge pump, which promises to give positionally resolved information on the topology, even in interacting systems.

Furthermore, we find in section 6.1 that a coupling to a bosonic bath does not preclude quantized charge transport in the Rice-Mele model for sufficiently weak coupling strengths, except for bosons that are resonant with the pumping frequency. For the interacting Rice-Mele model, we present results in sections 7.1 and 7.3 that showcase a splitting of critical points as a function of interaction strength in this system. We find that

crossing a many-body spin-gapless line along the pump cycle does not immediately lead to a breakdown of quantized pumping. We also present an experimental study, where such an interaction-induced pump is measured and verify the results with numerics that incorporate many of the experimental influences on the system. Finally, we show that opening this gap leads to the possibility of robustly quantized interaction-induced charge pumps.

1.6.1 Disordered Thouless pumps

A current focus of research is the interplay between Thouless pumps and disorder, partly because it is present in virtually all experiments. Substrate disorder - as well as many-body interactions - has been introduced in the theory of Thouless pumps as early as the 1984 paper by Niu and Thouless [44]. Generally, it is accepted that weak disorder does not lead to a breakdown of topological robustness or to topological phase transitions as long as the energy gap is preserved [44, 101, 133, 11]. In addition to wanting to understand the breakdown of topology due to disorder, one also finds surprising emergent phenomena due to the interplay of topology and Anderson localization [163]. Due to this disorder-induced localization, single quantum states inside otherwise empty bands without a finite gap to other unoccupied states can be pumped in a quantized fashion, which has been experimentally verified [69]. Anderson localization can also induce topological pumping in an otherwise trivial system [50, 67]. Recently, a quasi-disordered fermionic Rice-Mele model has been realized in an optical superlattice using ultracold atoms [164]. The authors measure a breakdown of topological charge pumping due to strong disorder strength, as well as disorder-induced pumping. A recent theoretical work [58] has studied the breakdown for random disorder using a Floquet approach and found an intriguing link between a localization-delocalization transition of Floquet states and the onset of non-quantized pumping.

In the first publication of this thesis (section 5.1), we study the Rice-Mele model in the presence of random on-site disorder. Whereas [58] presented an approximate link between the closing of the single-particle gap and the breakdown of quantized charge transport, we make this connection more precise by considering the full energy gap distributions as a function of disorder strength. Instead of the disorder averaged gap, the closing of the most likely energy gap predicts the breakdown of quantized pumping. The gap distributions transition from a Gaussian to an exponential distribution at the critical disorder strength. We also employ several techniques that have not yet been utilized for disordered charge pumps, such as the local Chern marker [162, 165, 166, 167, 168, 167, 169] and its local deviation from unity. We find a strong relationship between the breakdown of quantized pumping and these measures. The methods can be utilized in many-body interacting systems, in which Floquet techniques are not expected to work well, due to heating.

1.6.2 A Thouless pump coupled to a phononic environment

The second publication of this thesis deals with Thouless pumps coupled to an environment. Topological systems with finite temperature [141, 142, 134, 138, 143, 144, 145, 48],

1 Introduction

as well as open systems [136, 138, 140, 134, 139, 135, 61, 61, 10, 137] - either in thermal equilibrium or in non-equilibrium settings - have seen a lot of theoretical and experimental progress recently. The geometric phase employed to define topological phases in equilibrium and zero-temperature situations can be generalized to finite temperature via the ensemble geometric phase [141, 146] and to open systems via the Uhlmann phase [145, 138]. Generally, it is expected that finite temperature breaks the topologically quantized charge transport in Thouless pumps [48, 56]. This is due to the fact that the observable of pumped charge is no longer equal to the topological invariant, even though the system remains topological below a critical temperature [141, 146]. In chapter 8, I will present preliminary results for a finite-temperature interacting Rice-Mele model.

One can also consider open topological charge pumps that can exchange particles or energy with an environment. Here, it has been demonstrated that dissipation can be used to induce topology [136]. Dissipation has also been shown to assist topological pumping [61]. A related area of research is topology in non-hermitian systems [63, 170, 171, 172, 173, 174]. Open quantum systems can be experimentally realized in optical cavities [175, 176]. A self-driving Thouless pump has recently been reported in such a system [73].

In our paper presented in section 6.1, we couple a fermionic Rice-Mele model to a bath of phonons via a Holstein coupling [177]. While the whole system is closed, energy can be transferred between the electronic and phononic sector. We employ the semiclassical multitrajjectory Ehrenfest method [178, 179, 180] to treat the phonon sector classically. We demonstrate a breakdown of quantization at an arbitrarily small finite electron-phonon coupling when the driving frequency equals the phonon frequency. Interestingly, in the non-quantized regime, the charge pumping direction reverses, leading to negative charge pumping, which can be explained via effective Rice-Mele parameters arising from the phonon coupling terms. Outside this resonant pumping, there exists a critical electron-phonon-coupling strength, below which the quantization of pumped charge holds.

1.6.3 Interacting Thouless pumps

Although topology is still an active area of research even in non-interacting quantum systems, where a complete classification of the types of topological systems is known [11, 13, 14, 17], the role of many-body interactions promises a myriad of exotic and surprising effects due to the inherent complexity of phase transitions, in these systems. Due to this complexity, there does not currently exist a classification of all interacting topological phases of matter, although a subset of phases have been classified [12, 15, 16, 17, 19]. While topology is generally preserved when turning on weak interactions, due to an adiabatic connection to the non-interacting system, many-body interactions can induce topological phase transitions [181, 182, 183, 184, 185]. Prime examples of interacting topological states are the fractional quantum Hall states [186, 187], which are expected to be realizable in optical lattices [29, 188].

Thouless pumps are an ideal platform to study interaction effects in topology, since their 1d nature makes them both easier to realize and control experimentally with ultracold atoms [33, 34, 67, 38] as well as more easily treatable numerically with matrix-

product-state methods [74, 75, 76, 77, 78, 79, 80, 81, 82]. Interacting charge pumps have therefore been a focus of theoretical efforts [147, 46, 47, 154, 157, 148, 156, 51, 52, 158, 53, 150, 151, 57, 149, 62, 159, 160, 161, 153, 155]. Our paper presented in section 7.1 studies an interacting Rice-Mele model with two-component fermions subject to an on-site repulsive Hubbard interaction. The same model has been studied before in [150], where the authors claim a breakdown of topological charge pumping in the strongly interacting limit. This loss of quantization has also been experimentally reported in an optical lattice system [38]. In our work, we characterize this loss of quantization as a topological phase transition, which occurs due to critical points moving out of the pump cycle as a function of increasing interaction strength. We study two toy models, where the gap is open everywhere except at these critical points. Without the gap-opening terms, the model reduces to the Rice-Mele Hubbard model of [150, 38], and the critical interaction strength for the onset of non-quantized charge pumping aligns with the crossing of the critical points from the pump cycle. The loss of quantization can be explained with a crossing of a spin-gapless line, which is a feature of the Mott insulator phase of the ionic Hubbard model [189, 190, 191, 192, 193, 194, 195, 196], which is realized in between the critical points.

In a second work, and in collaboration with experimentalists from [38], we also study the possibility of interaction-induced pumping in this model in section 7.3. Shifting the pump cycle, such that a single critical point is encircled only for finite interaction and varying the strength of the latter, we observe interaction-induced pumping. The amount of charge pumped is approximately quantized for the first pump period when starting in the Mott phase and first traversing the band-insulator before crossing the spin-gapless line, and ending back in the Mott phase, although the system is technically non-adiabatic after crossing the gapless line. Beyond the first pump cycle, the pumped charge quantization breaks down. We explain this breakdown in detail by numerically calculating the correlations in the charge and spin sector. We find that crossing the spin-gapless line immediately excites the spin-sector without exciting the charge sector, thus initially protecting the quantized pumping of charge despite a gap closing. These spin-excitations are later converted to charge excitations when reaching the band-insulating regime afterwards. This work constitutes one of the first experimental observations of pumping in a topological system which is genuinely due to many-body interactions.

1.7 Structure of this thesis

This thesis is organized as follows. In chapter 2 I will summarize and review the basics of geometric phases, also called Berry phases, which are the foundation of topology in Condensed matter theory. Using Berry phases, the topological invariant of Thouless pumps, the Chern number, can be defined. I will also address the adiabatic perturbation theory which is needed to understand non-adiabatic effects of Thouless pumps and introduce the topic of adiabatic deformations, called homotopies.

Chapter 3 starts with the definition of the SSH model as the basic model for a symmetry protected topological phase, with which the bulk-boundary correspondence can

1 Introduction

be explained. Using this, I will introduce the Rice-Mele model which is the focus of all publications in this thesis. I discuss its dispersion relation, connect the pumped charge to the shifting of Wannier centers and introduce the current operator. The Chern number is demonstrated to be equal to the pumped charge. I also introduce the many-body polarization as a many-body equivalent to the Berry phase and describe the equivalence between the quantum Hall effect and Thouless pumping. The chapter finishes with a discussion of experimental realizations of Thouless pumps. In chapter 4, I briefly summarize the numerical techniques used here; exact diagonalization, multi-trajectory Ehrenfest, Lanczos and matrix-product state (MPS) methods.

Chapter 5 shows results for the disordered Rice-Mele model. I present results for the phonon-bath-coupled Rice-Mele model in chapter 6. Finally, chapter 7 shows results for the interacting Rice-Mele Hubbard model and its extensions. I give an account of preliminary results for a finite-temperature interacting Rice-Mele model in chapter 8 before concluding in chapter 9 with a short discussion and outlook.

2 Topology in condensed matter theory

2.1 Review of Berry phases and Chern numbers

Central to the theory of topological insulators and topological charge pumps are the concepts of geometric phases, also called Berry phases. This concept was first introduced by Sir Michael Berry in 1984 as part of his seminal paper [197]. A Berry phase is a phase angle of a complex vector that is obtained during the evolution of this vector along a parameter path. The idea was later formalized in the context of representation theory of fiber bundles, see for example [198]. Here, I will take a mostly heuristic approach and briefly review the key concepts of geometric phases and corresponding topological invariants like Chern numbers directly in the context of quantum mechanical systems. The Berry phase constitutes the foundation of the topology of quantum states while the Chern number is the central topological invariant that will dictate the amount of pumped charge in topological charge pumps. To connect the Chern number to the pumped charge in Thouless pumps, I will summarize the key results of the adiabatic perturbation theory [199, 200, 201] and the modern theory of polarization [202]. I will follow [110] and [203] closely in this chapter.

2.1.1 Berry phase

Topology in condensed matter theory is the study of global, generic properties of systems that are unchanged by local transformations. Berry phases are geometric phases that combine local properties coming from local gauge transformations into a global phase that is unchanged during these gauge transformations. A local gauge transformation in quantum mechanics assigns a phase $\beta(R)$ to a state vector $|u(R)\rangle$ via

$$|u(R)\rangle \mapsto |\tilde{u}(R)\rangle = e^{-i\beta(R)} |u(R)\rangle, \quad (2.1)$$

where R is a parameter of the physical system, which can be, for example, external potentials, magnetic fields, time or real-space position. The state vectors $|u(R)\rangle$ are taken to be the instantaneous eigenstates of a parameter-dependent Hamiltonian $H(R)$. We first consider a discrete set of parameters R_1, R_2, \dots , with corresponding states $|u_j\rangle = |u(R_j)\rangle$. The Berry phase is then defined as

$$\phi = -\text{Im} \ln [\langle u_0 | u_1 \rangle \langle u_1 | u_2 \rangle \dots \langle u_{N-1} | u_0 \rangle]. \quad (2.2)$$

ϕ is the sum of relative phases of a closed ring of states. Whereas a relative phase between two states $\phi_{1,2} = -\text{Im} \ln [\langle u_1 | u_2 \rangle]$ changes under a local gauge transformation eq. (2.1)

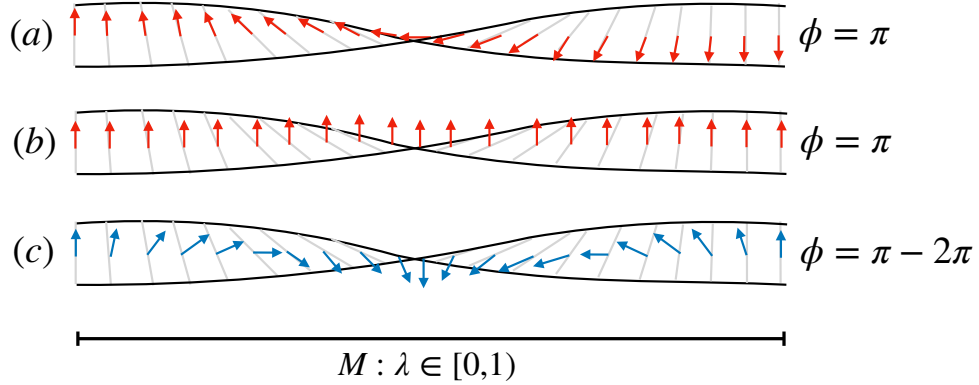


Figure 2.1: Schematic representation of three different local gauges of quantum states in a Möbius band geometry. (a) Parallel transport gauge: $A(\lambda) = 0$ and $-\text{Im} \ln \langle \bar{u}_{\lambda=1} | \bar{u}_{\lambda=0} \rangle = \pi$. (b) Twisted parallel transport gauge: $A(\lambda) = \pi$ and $-\text{Im} \ln \langle \bar{u}_{\lambda=1} | \bar{u}_{\lambda=0} \rangle = 0$. (c) Twisted parallel transport gauge with an additional twist of -2π . $A(\lambda) = -\pi$ and $-\text{Im} \ln \langle \bar{u}_{\lambda=1} | \bar{u}_{\lambda=0} \rangle = 0$. For all three gauges, the Berry phase is $\pi \text{ mod. } 2\pi$, which reflects the half rotation of the Möbius band.

as

$$\phi_{1,2} \mapsto \tilde{\phi}_{1,2} = \phi_{1,2} e^{-i(\beta_2 - \beta_1)}, \quad (2.3)$$

the Berry phase is invariant under all local gauge transformations, since all states in eq. (2.2) come in pairs of a bra and a ket. However, ϕ is only invariant when seen as a phase angle, meaning that there is a branch ambiguity when taking the logarithm. To see this, consider a local gauge transformation for L states on a ring of the form

$$\beta_j = 2\pi j/L. \quad (2.4)$$

which makes the Berry phase pick up an additional phase of 2π .

Consider now a continuous parameter set, such that the paths in this set are parametrized with the real parameter $\lambda \in M = [0, 1]$ and $|u(\lambda = 0)\rangle = |u(\lambda = 1)\rangle$. The continuum limit of eq. (2.2) is

$$\phi = -\text{Im} \oint \langle u_\lambda | \partial_\lambda u_\lambda \rangle d\lambda, \quad (2.5)$$

where the Berry connection or Berry potential $A(\lambda) = -\text{Im} \langle u_\lambda | \partial_\lambda u_\lambda \rangle = \langle u_\lambda | i\partial_\lambda u_\lambda \rangle$ is the relative phase between neighboring states to first order in the parameter λ . Equivalently to eq. (2.3), the Berry connection is not gauge invariant and transforms according to

$$\tilde{A}(\lambda) = A(\lambda) + \frac{d\beta(\lambda)}{d\lambda}. \quad (2.6)$$

2.1 Review of Berry phases and Chern numbers

The Berry phase eq. (2.5) is well-defined as a phase angle.

To assign an interpretation to the Berry phase, we consider three local gauges for states on a closed path on a parameter manifold that twists like a Möbius band, shown in fig. 2.1.

The first gauge we consider is the parallel transport gauge, which is defined via a vanishing Berry connection, which is depicted in fig. 2.1 (a):

$$\bar{A}(\lambda) = \langle \bar{u}_\lambda | i\partial_\lambda \bar{u}_\lambda \rangle = 0. \quad (2.7)$$

Parallel transport is a term from differential geometry and essentially means that tangent vectors on a manifold twist in accordance to the underlying manifold so that they are "as parallel as possible" given the curvature of the manifold itself. Here, the Möbius band twists by an angle π during the circular path from $\lambda = 0$ to $\lambda = 1$. In a parallel transport gauge the Berry curvature, measuring the phase difference of neighboring states, is zero during a transversal of this path. Notice that the state vectors in fig. 2.1 (a) turn exactly in accordance to the underlying manifold, denoted by the grey lines. Comparing the phase angles between the states $|\bar{u}(0)\rangle$ and $|\bar{u}(2\pi)\rangle$, they point in opposite directions and therefore we have

$$\bar{\phi} = -\text{Im} \ln \langle \bar{u}_{\lambda=1} | \bar{u}_{\lambda=0} \rangle = \pi. \quad (2.8)$$

Therefore, the Berry phase is the phase that is remaining after parallel transporting vectors along the periodic path and is exactly the twist that is inherent in the manifold of eigenstates due to the Möbius band geometry. We will use the parallel transport gauge for connecting the Berry phase to physical observables in the context of adiabatic perturbation theory in section 2.2.

A second gauge, named the "twisted parallel transport gauge" is shown in fig. 2.1 (b). Here, the phase twist of π is distributed across each state via a local gauge transformation $\beta(\lambda) = \pi\lambda$, such that the Berry connection is constant:

$$\tilde{A}(\lambda) = \langle \tilde{u}_\lambda | i\partial_\lambda \tilde{u}_\lambda \rangle = \pi \quad (2.9)$$

but the gauge is cyclic as a result since $|\tilde{u}(0)\rangle = |\tilde{u}(1)\rangle$.

As a third example showcasing the gauge independence modulo 2π of the Berry phase, consider starting from the twisted parallel transport gauge but applying an additional phase $\beta(\lambda) = -2\pi\lambda$:

$$\tilde{\tilde{A}}(\lambda) = \langle \tilde{\tilde{u}}_\lambda | i\partial_\lambda \tilde{\tilde{u}}_\lambda \rangle = \pi - 2\pi. \quad (2.10)$$

$|\tilde{\tilde{u}}(0)\rangle = |\tilde{\tilde{u}}(1)\rangle$ still holds, as is evident in fig. 2.1 (c), but the Berry phase is now

$$\tilde{\tilde{\phi}} = \bar{\phi} - 2\pi, \quad (2.11)$$

where $\bar{\phi} = \pi$ is the Berry phase in the parallel transport gauge eq. (2.8).

Note that the Berry phase itself is not quantized and can take any value depending on the physical system and the resulting ground-state manifold. However, all possible local

2 Topology in condensed matter theory

gauge transformations can be characterized by an integer winding number m , such that [203]

$$\tilde{\phi} = \phi + 2\pi m, \quad (2.12)$$

where the tilde denotes an arbitrary local gauge transformation. This is because a gauge transformation necessarily needs to assign a well-defined phase angle $\beta(\boldsymbol{\lambda})$ to a state $|u(\boldsymbol{\lambda})\rangle$. One can use this fact to prove that the Chern number is an integer, which I will demonstrate in the next section.

2.1.2 Berry Curvature and Chern number

For an N -dimensional parameter space, the Berry connection is

$$A_\mu = \langle u_\lambda | i\partial_\mu u_\lambda \rangle \quad (2.13)$$

where $\mu \in \{1, \dots, N\}$. If we consider a closed path P , the Berry phase along that path becomes

$$\phi = \oint_P \mathbf{A} \cdot d\boldsymbol{\lambda}, \quad (2.14)$$

which is the line integral of A along P . Using Stokes' theorem for the two-dimensional submanifold S that is bounded by P , the Berry phase can be calculated via a surface integral of the Berry curvature Ω , defined as the curl of the Berry connection:

$$\Omega_{\mu,\nu} = \partial_\mu A_\nu - \partial_\nu A_\mu = -2 \text{Im} \langle \partial_\mu u | \partial_\nu u \rangle, \quad (2.15)$$

$$\phi = \oint_P \mathbf{A} \cdot d\boldsymbol{\lambda} = \int_S \Omega_{\mu\nu} ds_\mu \wedge ds_\nu. \quad (2.16)$$

Here, \wedge is the usual exterior product of differential forms, indicating that the Berry curvature is a two-form, or a pseudovector in the language of vector analysis, making it equivalent to the magnetic field in electrodynamics. The Berry phase ϕ is therefore also called "Berry flux" through the surface S . Both ϕ and Ω are gauge invariant while the Berry potential A is not, mirroring the situation in classical electrodynamics, where the magnetic flux and magnetic field are gauge invariant, but the gauge potential is not.

What happens if a closed surface is considered, like a torus? In that case we cannot globally use Stokes' theorem as in general we cannot find a smooth gauge for the entire surface. A torus parameter manifold is the situation we will encounter in this thesis for either two-dimensional crystals or one-dimensional systems with a periodic time-dependence. In that case, the parameters will either be $\boldsymbol{\lambda} = (k_x, k_y)$ or $\boldsymbol{\lambda} = (k_x, t)$, respectively, where k_μ is the quasimomentum, which is periodic in the Brillouin zone (see section 2.1.3). The parameter manifold \mathcal{T} is then the Brillouin zone (BZ) or the mixed space of a one-dimensional Brillouin zone and time.

For such a torus \mathcal{T} , we use Stokes' theorem on two subsurfaces S and \bar{S} such that $\mathcal{T} = S \cup \bar{S}$ and $S \cap \bar{S} = P$ is a common closed loop, as shown in fig. 2.2. The Berry phase

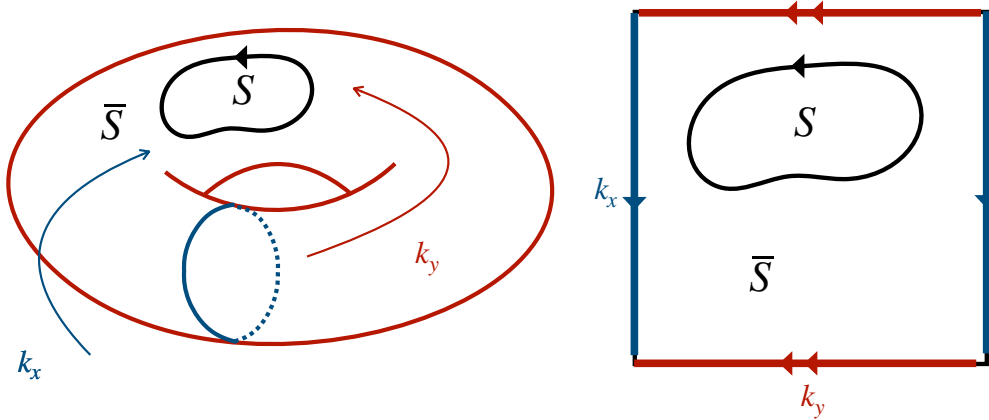


Figure 2.2: The Brillouin zone of a two-dimensional material is a closed surface in the form of a torus spanned by the crystal momenta k_x and k_y . The Berry phase around a close loop on the torus is calculated as the Berry flux through two subsurfaces S and \bar{S} .

around P is equal for both subsurfaces:

$$\begin{aligned}\phi &= \oint_{\partial S} \mathbf{A}_S(\boldsymbol{\lambda}) \cdot d\boldsymbol{\lambda} = \int_S \boldsymbol{\Omega}(\boldsymbol{\lambda}) dS \\ &= \oint_{\partial \bar{S}} \mathbf{A}_{\bar{S}}(\boldsymbol{\lambda}) \cdot d\boldsymbol{\lambda} = - \int_{\bar{S}} \boldsymbol{\Omega}(\boldsymbol{\lambda}) dS.\end{aligned}\quad (2.17)$$

The Berry connections for each subsurface are connected via a gauge transformation:

$$\mathbf{A}_{\bar{S}}(\boldsymbol{\lambda}) = \mathbf{A}_S(\boldsymbol{\lambda}) - \nabla\beta(\boldsymbol{\lambda}).\quad (2.18)$$

From eq. (2.17) and eq. (2.11) it follows that

$$\int_{BZ=S+\bar{S}} \boldsymbol{\Omega}(\boldsymbol{\lambda}) dS = \oint_{\partial S} \nabla\beta(\boldsymbol{\lambda}) \cdot d\boldsymbol{\lambda} = 2\pi C.\quad (2.19)$$

Because the gauge $\beta(\boldsymbol{\lambda})$ is smooth along P and has to be well-defined after going around the closed loop, eq. (2.19) calculates the winding of the phase angle β around the loop, which therefore must be an integer multiple of 2π . C is the Chern number, which is the relevant topological invariant for 2d systems and topological charge pumps.

I conclude this brief review of Chern numbers with a particularly useful form of the Chern number, which is commonly used in the context of charge pumps. For a parameter manifold of a periodic time parameter $t \in [0, 1]$ and the quasi momentum $k \in [0, 2\pi]$, the Chern number can be expressed as the winding of the Berry phase with respect to k

2 Topology in condensed matter theory

around a pump cycle parametrized by t :

$$\begin{aligned}
\int_T \boldsymbol{\Omega}(\boldsymbol{\lambda}) dS &= \int_0^1 dt \int_0^{2\pi} dk (\partial_t A_k - \partial_k A_t) \\
&= \int_0^1 dt \int_0^{2\pi} dk \partial_t A_k \\
&= \int_0^1 dt \partial_t \int_0^{2\pi} dk A_k \\
&= \int_0^1 dt \partial_t \phi,
\end{aligned} \tag{2.20}$$

where in the second line, the twisted parallel transport gauge eq. (2.9) was used.

2.1.3 Topology of Bloch vectors

The formalism of Chern numbers and Berry phases can directly be applied to crystalline materials. From Bloch's theorem, we know that the eigenstates of a periodic lattice Hamiltonian are

$$|\Psi_{n,\mathbf{k}}\rangle(\mathbf{r}) = e^{i\mathbf{k}\cdot\mathbf{r}} |u_{n,\mathbf{k}}(\mathbf{r})\rangle, \tag{2.21}$$

where $|u_{n,\mathbf{k}}\rangle$ are the cell-periodic Bloch functions and n denotes the band index. The Brillouin zone in d dimensions, consisting of all \mathbf{k} vectors in the first reciprocal unit cell, can be regarded as a closed parameter manifold, more specifically a d -torus, as \mathbf{k} and $\mathbf{k} + \mathbf{G}$ correspond to the same physical state. Thus, the \mathbf{k} -vectors take the role of the parameter in earlier sections. Taking a closed path in the Brillouin zone, one has for the Berry phase and Berry connection of the n 'th band:

$$\phi_n = \oint \mathbf{A}_n(\mathbf{k}) \cdot d\mathbf{k}, \tag{2.22}$$

$$A_{n\mu}(\mathbf{k}) = \langle u_{n\mathbf{k}} | i\partial_\mu u_{n\mathbf{k}} \rangle. \tag{2.23}$$

For two-dimensional systems, the Brillouin zone is a 2-torus and the Chern number can be calculated as the integral over the entire Brillouin zone:

$$C_n = \frac{1}{2\pi} \int_{\text{BZ}} \Omega_{n,xy} d^2k, \tag{2.24}$$

$$\Omega_{n,\mu\nu}(\mathbf{k}) = \partial_\mu A_{n\nu}(\mathbf{k}) - \partial_\nu A_{n\mu}(\mathbf{k}) = -2 \text{Im} \langle \partial_\mu u_{n\mathbf{k}} | \partial_\nu u_{n\mathbf{k}} \rangle. \tag{2.25}$$

Two-dimensional systems with a non-zero Chern number are called Chern insulators or quantum anomalous Hall insulators, the most famous of which is the Haldane model [88]. It can be shown that time-reversal symmetry needs to be broken in order for non-trivial Chern numbers to occur. Usually this is done via an external magnetic field. The Haldane model does the same via a complex next-nearest-neighbor hopping and does not need an external magnetic field.

In one-dimensional systems, the entirety of the 1d Brillouin zone is a closed path. The Berry phase over the entire Brillouin zone

$$\phi_n = \oint_{\text{BZ}} A_n(k) dk = \oint_{\text{BZ}} \langle u_{nk} | i\partial_k u_{nk} \rangle \quad (2.26)$$

is called the Zak phase [118]. In general, it is not quantized and like any Berry phase can take any phase value. This situation changes in systems with additional symmetries, where the Zak phase can become quantized like the Chern number, making it a topological invariant in these systems. One example of this is the Su-Schrieffer-Heeger (SSH) model [204], where the quantized Zak phase leads to the definition of a quantized winding number.

2.2 Adiabatic theory

The Chern number introduced in the last section is an instantaneous measure of parameter dependent Hamiltonians. In any time-dependent experiment, we have to consider the time-variable not only in a parametric sense but as a fundamental variable of the time-dependent Schrödinger equation

$$i\hbar\partial_t |\Psi\rangle = \hat{H} |\Psi\rangle. \quad (2.27)$$

For an arbitrary time-evolution, this equation needs to be solved as arbitrary non-adiabatic effects can occur. If the time-dependence is sufficiently slow, the non-adiabatic effects can be ignored except for the lowest orders in perturbation theory, which is dubbed the adiabatic theorem [205]. Explicitly we consider the parameter $\lambda(t)$ to depend slowly on time t and define the instantaneous eigenstates as

$$H(\lambda)|n(\lambda)\rangle = E_n(\lambda)|n(\lambda)\rangle. \quad (2.28)$$

The energy levels E_n are assumed to be non-degenerate. Anticipating the dynamical phase evolution for the n 'th eigenstate $\gamma(t) = \frac{1}{\hbar} \int_0^t E_n(t') dt'$, consider the ansatz

$$|\psi(t)\rangle = c(t)e^{-i\gamma(t)}|n(t)\rangle, \quad (2.29)$$

meaning that we allow for an additional phase during time-evolution. The solution for $c(t)$ is [203, 110]

$$c(t) = e^{i\phi(t)}, \quad (2.30)$$

$$\phi(t) = \int_0^t A_n(t') dt' = \int_{\lambda(0)}^{\lambda(t)} A_n(\lambda) d\lambda, \quad (2.31)$$

where ϕ is the Berry phase on the path from $\lambda(0)$ to $\lambda(t)$. The Berry phase does not depend on the time taken but only on the path itself - hence the name "geometric phase". If the states are considered to be in a parallel transport gauge eq. (2.7), the Berry phase

2 Topology in condensed matter theory

vanishes during the time-evolution and only the dynamical phase remains. Therefore, in an adiabatic time-evolution, the quantum states follow the parallel transport gauge [206].

To describe charge transport, one has to go beyond first order, as the current operator in quantum mechanics vanishes for real states or states with a global phase evolution. The second order solution reads [203]:

$$|\psi(t)\rangle = e^{i\phi(\lambda(t))} e^{-i\gamma(t)} |n(\lambda(t))\rangle + \dot{\lambda} |\delta n(t)\rangle, \quad (2.32)$$

with

$$|\delta n\rangle = -i\hbar \sum_{m \neq n} \frac{\langle m | \partial_\lambda n \rangle}{E_n - E_m} |m\rangle = -i\hbar \sum_{m \neq n} \frac{\langle m | (\partial_\lambda H) | n \rangle}{(E_n - E_m)^2} |m\rangle. \quad (2.33)$$

As in the first order solution, there is no explicit time-evolution present, meaning the admixture of the instantaneous state $|n\rangle$ with the other states $|m \neq n\rangle$ are only depending on the path taken, as long as the time-evolution is slow enough. An adiabatic parameter can be defined as [203]

$$\alpha = \hbar \dot{\lambda} \frac{\langle m | \partial_\lambda n \rangle}{E_n - E_m}. \quad (2.34)$$

The time-evolution is called quasi-adiabatic, if $\alpha \ll 1$, meaning that the variation of the state $|n\rangle$ is small compared to the energy gap $\Delta E = E_m - E_n$ of the system. The quasi-adiabatic time-evolution is at the center of quantized charge transport in topological charge pumps. Essentially, during a quasiadiabatic evolution, the evolved states are equal to the instantaneous eigenstates of the system in the parallel transport gauge with an additional stationary admixture of higher energy levels that can lead to topological charge transport.

From eq. (2.33), it becomes clear that the present adiabatic theorem only holds for non-degenerate systems. The theory can be extended to degenerate systems, where the geometric phase has to be replaced by a more general $U(n)$ generator that acts in the degenerate subspace [207]. In this thesis, only the non-degenerate case is considered.

2.3 Homotopy

A key concept of topology is the robustness of topological invariants with respect to continuous transformations. As a geometric example, consider the number of holes of a closed manifold as a topological invariant. Smooth deformations of the manifold, like stretching cannot change the topological invariant. This is due to the fact that topological invariants are quantized (either to integer or an integer multiple of a constant) and thus cannot change continuously from one value to another. The only way to change the number of holes in the above example is to cut open the manifold or glue it together at some other point. Such a transformation is no longer continuous and can lead to jumps in the topological invariant.

To apply this concept to physical systems, one needs the formalism of homotopy [198]. Homotopies essentially interpolate between two continuous functions f and g in a smooth and continuous fashion. In quantum physics, these functions are the Hamiltonians $\hat{H}_1(\lambda)$ and $\hat{H}_2(\lambda)$ and a homotopy is a series of Hamiltonians $\hat{H}_\alpha(\lambda)$ with $\alpha \in [1, 2]$ that interpolate between them in such a way that all \hat{H}_α stay non-degenerate (or retain the same degenerate subspaces for degenerate systems). This usually means that the energy gap has to remain open for topological robustness to hold. If along the path from $\alpha = 1$ to $\alpha = 2$ the energy gap closes, a topological phase transition can occur, which changes the topological invariant of the system. When exploring the different channels of breakdown of topological charge pumping later in this thesis (section 7.3), it will therefore be a central question, whether the perturbations, like disorder, electron-phonon-coupling or many-body interactions leave the energy gap open. Closing the gap, one expects a topological phase transition to be able to occur, potentially leading to a breakdown of topological pumping. Two Hamiltonians that are connected via a homotopy, are called adiabatically connected. Topological invariants for adiabatically connected Hamiltonians with the same symmetries cannot change. On the other hand, two systems with differing topological invariant cannot be adiabatically connected. Notice that a gap closing can also occur in a Hamiltonian $\hat{H}(\lambda)$ as a function of the parameter λ , for example if the system becomes degenerate at a particular point in time. However, we will see later in section 7.1, that such a gap-closing is not necessarily a sufficient criterion for the breakdown of quantized charge pumping, at least for the first pump cycle.

3 Topological charge pumps

A topological charge pump or Thouless pump [45, 44] is a physical system that transports an integer-quantized amount of charge without an external bias voltage. The system is modulated in time adiabatically slowly so that the time-evolved states are to a good approximation the instantaneous eigenstates of the system. We will focus on one-dimensional charge pumps, although higher-dimensional pumps exist [55, 117]. It can be shown via adiabatic perturbation theory [199, 200, 201] and the modern theory of polarization [202, 208], that the amount of charge pumped is equal to the Chern number, which can be calculated as the winding of the Berry phase along the pump cycle. In this chapter I will briefly introduce the SSH model [204], which is the prototypical model for symmetry-protected topological phases before introducing in detail the main model of this thesis, the Rice-Mele model [132], which smoothly interpolates between trivial and non-trivial phases of the SSH model. I will then describe the quantum-mechanical current operator and will outline how topological charge pumping occurs in the Rice-Mele model. I will also summarize recent experimental developments in the Rice-Mele model and charge pumping in general.

3.1 SSH model

The SSH model [204] is a one-dimensional tight-binding chain with a dimerized hopping controlled by the dimerization δ :

$$\hat{H}(\delta) = -J \sum_{j=1}^L (1 + \delta(-1)^j) \left(\hat{c}_j^\dagger \hat{c}_{j+1} + h.c. \right), \quad (3.1)$$

where \hat{c}_j^\dagger creates a fermion on site j . For two-band models, the bulk Hamiltonian $\hat{H}(k) = e^{ikj} \hat{H} e^{-ikj}$ can be expanded in Pauli matrices $\boldsymbol{\sigma} = (\sigma_x, \sigma_y, \sigma_z)^T$:

$$\hat{H}(k) = J \mathbf{d}(k) \cdot \boldsymbol{\sigma}, \quad (3.2)$$

where the hopping constant J can be set to 1. From $\hat{H}(k)^2 = |\mathbf{d}|^2 \mathbb{1}$, we obtain $E_{\pm} = \pm |\mathbf{d}|$. From homotopy arguments, we know that any topological invariant cannot change unless the Hamiltonian becomes degenerate. Here, the gap closing happens at $\mathbf{d} = \mathbf{0}$, which corresponds to $\delta = 0$. Thus, for the non-degenerate system, only the direction of the \mathbf{d} vector is of importance. For the SSH model, the explicit values are

$$d_x = 1 + \delta + (1 - \delta) \cos(k); \quad d_y = (1 - \delta) \sin(k); \quad d_z(k) = 0. \quad (3.3)$$

3 Topological charge pumps

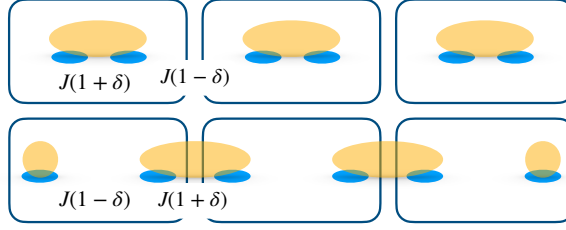


Figure 3.1: The two topological phases of the SSH model: Top: Strong intracell hopping and weak intercell hopping with no edge states present. Bottom: Weak intracell hopping and strong intercell hopping leads to two weakly coupled sites on either edge that host zero energy edge states.

The system's chiral symmetry [209, 206, 11] $\sigma_z \hat{H}(k) \sigma_z = -H(k)$ leads to the eigenstates on the Bloch sphere, parametrized by \mathbf{d} , to lie in the x-y plane. Therefore, one can define a winding number around the degeneracy at the origin: The Zak phase ϕ becomes either 0 or π , which corresponds to the number of times the d-vector wraps around the origin when sweeping through the entire Brillouin zone. Without the chiral symmetry, the d-vector would carve out a closed loop in all $\mathbb{R}^3/\mathbf{0}$ and any such closed loop could be continuously transformed to a point, making a winding number ill-defined. Therefore, the SSH model gives an example of a symmetry protected topological phase.

3.1.1 Bulk-boundary correspondence

Topological invariants like the Chern number or the Zak phase are bulk properties that are inherent in the periodic system without the presence of boundaries. However, also systems with open boundary conditions possess topological invariants, which are tied to the bulk properties. As an example, consider an open SSH model with two edges on either side. Depending on the dimerization, one can have either strong bonds inside each unit cell or between unit cells with two dangling weakly coupled sites at the edges, see fig. 3.1. One can now define the topological invariant of the number of these zero energy-edge states on the left on sublattice A N_A minus the number of edge states on sublattice B N_B : $\nu = N_A - N_B$. One can show [110] that adiabatic deformations do not change this number of edge states on one side of the system and that it is equal to the bulk winding number. The connection of bulk properties and edge states is called "bulk-boundary correspondence" and is a general statement about topological phases. Although it is well-established for common topological systems in a variety of different settings, the full general proof is an active area of research [114, 112, 117]. For Chern insulators, 2d materials with non-zero Chern number, usually achieved via an external magnetic field, the in-gap edge states manifest as chiral edge states that propagate along the boundary of the system with a group velocity in only one direction along the edge. The Thouless charge pumps that are considered in this thesis are dynamical versions of these Chern insulators, which I will demonstrate in section 3.3. Experimentally, topological

edge states have recently become measurable, in the context of ultracold atomic gases [119, 27, 40] or with photonic systems [210, 211].

3.2 Rice-Mele model

The Rice-Mele model is the prototypical model for a topological charge pump. It was first introduced to study linearly conjugated diatomic polymers [132]. The model describes a one-dimensional lattice with dimerized hopping, like in the SSH model, and an additional staggered on-site potential:

$$\begin{aligned} \hat{H}(\delta, \Delta) = & -J \sum_{j=1}^L (1 + \delta(-1)^j) \left(\hat{c}_j^\dagger \hat{c}_{j+1} + \text{H.c.} \right) \\ & + \Delta \sum_{j=1}^L (-1)^j \hat{c}_j^\dagger \hat{c}_j, \end{aligned} \quad (3.4)$$

where δ controls the hopping dimerization and Δ is the alternating onsite energy offset. For convenience the lattice spacing is set to 1. For $\Delta = 0$, the SSH model is recovered. Δ breaks the chiral symmetry of the SSH model, making the Zak phase non-quantized. The Rice-Mele model is a topologically protected charge pump in the following sense: For a general pair of (δ, Δ) , the instantaneous system is not topological, except for $\delta = 0$. However, modulating the system in time by letting δ and Δ change as a function of t along a periodic pump cycle, and doing so sufficiently slowly as shown in the adiabatic theorem, one has an effective parameter torus in the mixed space of time and crystal momentum. This closed two-dimensional parameter space leads to the Chern number as the natural topological invariant for a charge pump. In the thermodynamic limit and for periodic boundary conditions, the Chern number is exactly the amount of charge that is pumped during one pump cycle.

In the remainder of this section I will demonstrate the emergence of quantized charge transport: First the Rice-Mele model is solved in momentum space, leading to a two-dimensional effective Brillouin zone in time and crystal momentum. Next, the Wannier basis is introduced in the context of the modern theory of polarization [202] which creates a link between the charge polarization and the Berry connection. Then, using the adiabatic perturbation theory introduced in section 2.2, together with the quantum mechanical current operator, one can write the amount of charge pumped through the system as the Chern number.

3.2.1 Bulk Hamiltonian and dispersion relation

In the thermodynamic limit and for periodic boundary conditions, the momentum space bulk-Hamiltonian of eq. (3.4) is

$$\hat{H}(k, t) = J \begin{pmatrix} -\Delta(t)/J & -1 + \delta(t) - (1 + \delta(t)) \exp(-ik) \\ -1 + \delta(t) - (1 + \delta(t)) \exp(ik) & \Delta(t)/J \end{pmatrix}, \quad (3.5)$$

3 Topological charge pumps

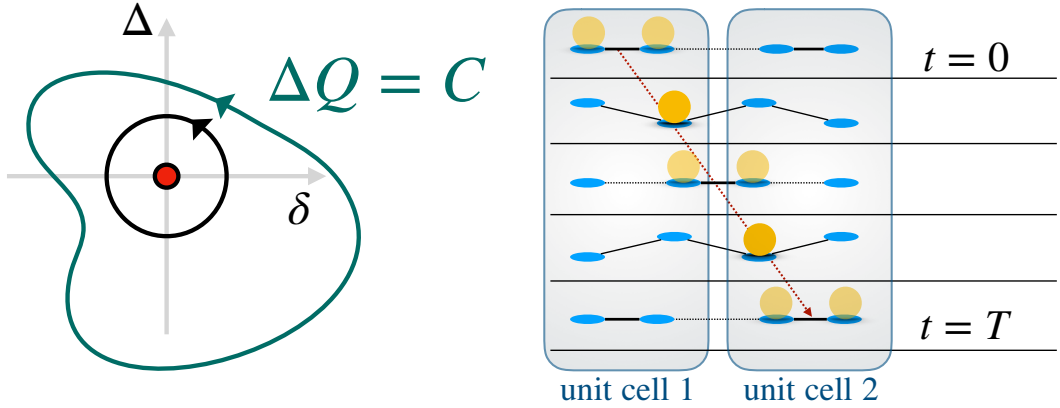


Figure 3.2: Left: Two topologically equivalent pump cycles in the δ - Δ -plane. The amount of pumped charge per cycle is equal to the winding around the origin and does not depend on the specific path taken. Right: Sketch of the Wannier states along the pump cycle. During half a pump cycle, the trivial and non-trivial phases of the SSH model are smoothly connected and the particles shift by half a unit cell.

where both δ and Δ depend on time t . In the language for two-band models, it becomes $\hat{H}(k, t) = J\mathbf{d}(k, t) \cdot \boldsymbol{\sigma}$ with

$$d_x = -1 + \delta - (1 + \delta) \cos(k); \quad d_y = -(1 + \delta) \sin(k); \quad d_z(k) = -\Delta/J, \quad (3.6)$$

which is equivalent to the SSH model eq. (3.3) with an additional z-component controlled by the chiral symmetry breaking term Δ . The dispersion relation $\epsilon(k, t)$ is

$$\epsilon(k, t) = \sqrt{\mathbf{d}(t) \cdot \mathbf{d}(t)} \quad (3.7)$$

and the gap closes at $\mathbf{d} = \mathbf{0}$. Consider a pump cycle

$$\begin{aligned} \delta(t) &= \delta_0 \cos(t/T) \\ \Delta(t) &= \Delta_0 \sin(t/T) \end{aligned} \quad (3.8)$$

and let t go from 0 to the pump period T . In the $\delta - \Delta$ plane, the pump cycle surrounds the gap closing at the origin. At each time, the Zak phase can be calculated with eq. (2.26). The Chern number is then the winding of the Zak phase when going around the pump cycle (see eq. (2.20)):

$$C = \int_0^T dt \partial_t \phi. \quad (3.9)$$

Therefore, the Chern number for the Rice-Mele model is equal to the number of times, the pump cycle encircles the origin. Intuitively, the resulting pumping can be understood

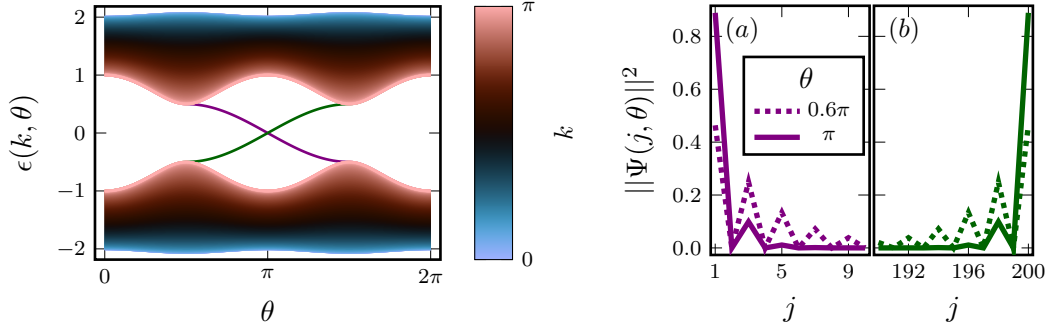


Figure 3.3: Left: Band structure of the Rice-Mele model as a function of crystal momentum k and pump parameter θ . The green (purple) lines indicate the energy levels of the edge states that are localized at the right (left) edge for an OBC system.

Right: Local density of the edge states on the left (a) and right (b) sides of the system. The dashed lines correspond to a pump parameter close to the emergence of the edge states from the bands. The solid lines are at the edge-state degeneracy at $\theta = \pi$.

from fig. 3.2 and from the Wannier states (see section 3.2.3). At $t = 0$, the system is in the trivial phase of the SSH model with a Zak phase of 0. The instantaneous eigenstates are dimerized inside each unit cell. After a quarter of the pump cycle at $t/T = 0.25$, the dimerization is turned off and the local potential becomes minimal in the second site of the unit cell. The instantaneous eigenstates are localized on these sites. At $t/T = 0.5$, the potential staggering is vanishing again and the dimerization results in the non-trivial SSH phase, with strong bonds across unit cells. The Zak phase at this point is π and the Wannier centers have shifted by half a unit cell to the right. For the remainder of the pump cycle this process repeats, going from the non-trivial SSH phase to the trivial one. The Zak phase increases to 2π which is equivalent to 0 and the instantaneous states return to the starting configuration, with all Wannier states having shifted by one unit cell.

In the left subplot of fig. 3.3 the dispersion relation for a Rice-Mele model with periodic boundary conditions is plotted as a function of the crystal momentum k , represented by the color and a pump angle $\theta(t) = 2\pi t/T$. Additionally, the energy spectrum is calculated for a system with open boundary conditions. The in-gap edge states are plotted with the dispersion relation in a mixed open- and periodic-boundary plot. Note that these edge states are a superposition of different k -eigenstates and have no well-defined crystal momentum. The edge states emerge after a quarter of the pump cycle out of the $k = \pi$ gap and become zero-energy states at $\theta = \pi$. These zero energy states are the edge states of the SSH model on the left and right edge respectively. The in-gap levels can be colored depending on which edge the states occupy. The green [purple] lines correspond to the right [left] edge. On the right side of fig. 3.3, the local density of the edge states on the

3 Topological charge pumps

left and right edge are plotted for $\theta = 0.6\pi$ and $\theta = \pi$. The edge states emerge from the bulk states and become maximally localized at the SSH point $\theta = \pi$.

The pumping can be understood from the evolution of the edge states: An edge state on the right side emerges from the valence band of the bulk, evolves into a zero energy edge state at $\theta = \pi$ and then transitions into the conduction band. At the same time, an edge state on the left edge transitions from the conduction band down into the valence band. The charge pump therefore works like a conveyor belt, pushing charge in the valence [conduction] band to the right [left] [110]. This is another instance of the bulk-boundary correspondence. The Chern number C_n of a bulk band n can be calculated via the net number of edge states N crossing the band gap on both edges ¹. Defining N_r [N_l] as the number of edge states leaving [entering] the filled band on the right [left] edge, one has

$$C_n = (N_r + N_l)/2. \quad (3.10)$$

For instantaneous numerical calculations, this is a useful tool to calculate the Chern number.

3.2.2 Current operator and amount of pumped charge

To calculate the pumped charge in a quasiadiabatic pump cycle, we need the quantum mechanical current operator. The current operator in quantum mechanics can be defined via the velocity operator, which formally derives from the Heisenberg time-derivative of the position operator [203]:

$$\hat{\mathbf{v}} = \frac{-i}{\hbar} [\hat{\mathbf{r}}, \hat{H}]. \quad (3.11)$$

For a periodic system, the bulk group velocity and current operator become

$$\hat{\mathbf{v}}_{\mathbf{k}} = \frac{1}{\hbar} \nabla_{\mathbf{k}} \hat{H}(\mathbf{k}), \quad (3.12)$$

$$\hat{j}_{\mathbf{k}} = -e/m \hat{\mathbf{v}}_{\mathbf{k}}. \quad (3.13)$$

We will set both the electric charge e and the mass m to 1 in the remainder of this thesis. Consider a completely filled band n that is gapped from all other bands. The amount of pumped charge \mathcal{Q} is the time-integral of the expectation value of the current operator in the k-space representation with N unit cells [110]:

$$\mathcal{Q}_n = \frac{1}{N} \int_0^T dt \sum_{\mathbf{k} \in \text{BZ}} \langle \tilde{u}_n(\mathbf{k}, t) | \partial_{\mathbf{k}} \hat{H}(\mathbf{k}, t) | \tilde{u}_n(\mathbf{k}, t) \rangle, \quad (3.14)$$

where the tilde on the u-functions of the Bloch waves denotes the time-evolved states. For sufficiently slow pumping, the solution for the evolved states is given by the adiabatic

¹This situation changes for Floquet systems, in which anomalous Floquet topological insulators can have edge states in conjunction with a trivial bulk invariant [42, 212, 119].

theorem in eq. (2.33):

$$|\tilde{u}_n(t)\rangle = e^{i\phi(t)} e^{-i\gamma(t)} |u_n(t)\rangle - i\hbar \sum_{m \neq n} \frac{\langle u_m | \partial_t u_n \rangle}{\epsilon_n - \epsilon_m} |u_m\rangle. \quad (3.15)$$

Inserting this into eq. (3.14), carrying out a continuum limit for the k-space and eliminating diagonal terms, as their k-space integral vanishes, one obtains [45, 110, 203]

$$\Delta Q_n = -\frac{1}{\pi} \text{Im} \int_0^T dt \int_{\text{BZ}} dk \sum_{m \neq n} \frac{\langle u_n | \partial_k \hat{H}(k, t) | u_m \rangle \langle u_m | \partial_t u_n \rangle}{\epsilon_m - \epsilon_n} \quad (3.16)$$

$$= -\frac{1}{\pi} \text{Im} \int_0^T dt \int_{\text{BZ}} dk \sum_{m \neq n} \langle \partial_k u_n | u_m \rangle \langle u_m | \partial_t u_n \rangle \quad (3.17)$$

$$= -\frac{1}{\pi} \text{Im} \int_0^T dt \int_{\text{BZ}} dk \langle \partial_k u_n | \partial_t u_n \rangle \quad (3.18)$$

$$= \frac{1}{2\pi} \int_0^T dt \int_{\text{BZ}} dk \Omega_{n,kt} = C_n. \quad (3.19)$$

In the second line, the parallel transport gauge eq. (2.7) was used. Eq. (3.19) is the central result of the theory of topological charge pumps, directly equating the pumped charge in a quasi-adiabatic pump to the Chern number of the filled band. It was first proven by Thouless [45].

If one is only interested in the quasi-adiabatic contribution, it therefore suffices to calculate the Chern number in an instantaneous basis. In experimental realizations of Thouless pumps, the effective pumping period can be much larger than what the quasi-adiabatic formula necessitates. For finite pumping frequencies, non-adiabatic contributions emerge, which go beyond the second order in adiabatic perturbation theory, and in general can excite the system irreversibly. In this context, a good definition of quasi-adiabaticity is the occupancy of excited bands as the pumping is smoothly turned off. If this excitation occupancy vanishes after the pumping has stopped, the quasi-adiabatic approximation holds. Recently there have been conceptual developments, for example in the definition of a non-adiabatic Zak-phase analogue [213].

3.2.3 Polarization and Wannier functions

For spatially localized systems, like an atom, the electrical polarization P can easily be defined via the displacement of the electrons relative to the nucleus. For the bulk of crystalline systems, this approach fails due to the fact that the electronic wavefunctions are delocalized across the entire bulk, making their center of charge undefined [214, 110]. The ill-defined position expectation values of the Bloch waves can be defined via the Wannier functions, as the inverse Fourier transforms of the Bloch functions [215]:

$$|w_{j,n}\rangle = \frac{V}{(2\pi)^3} \int_{\text{BZ}} dk e^{-ik \cdot j} |\psi_{nk}\rangle, \quad (3.20)$$

3 Topological charge pumps

where V is the unit cell volume. $|w_{j,n}\rangle$ is localized at lattice site j , decays exponentially if a smooth gauge is chosen for the Bloch functions and all Wannier states for $j \in 1, \dots, L$ span the full band n , just as the Bloch waves do, as the transformation in eq. (3.20) is unitary. It can be shown [110] that the expectation of the position operator \hat{x} is

$$\langle w_{j,n} | \hat{x} | w_{j,n} \rangle = \frac{i}{2\pi} \int_{-\pi}^{\pi} dk \langle u_n(k) | \partial_k u_n(k) \rangle + j = \phi + j. \quad (3.21)$$

Thus, the Wannier states have a weight on site j that is dependent on the Zak phase ϕ . The modern theory of polarization [202, 214] identifies this Zak phase as the electric bulk polarization:

$$P = \phi = \frac{i}{2\pi} \int_{-\pi}^{\pi} dk \langle u(k) | \partial_k u(k) \rangle \quad (3.22)$$

From the continuity equation, we know that current is the time-derivative of polarization [203]:

$$J = \frac{dP}{dt}. \quad (3.23)$$

From Thouless' formula above, we also know that the current in an adiabatically modulated system is nothing but the Berry curvature integrated over the filled band:

$$J = \frac{i}{2\pi} \int_{BZ} dk \langle \partial_k u_n | \partial_t u_n \rangle, \quad (3.24)$$

which together with eq. (3.23) leads to eq. (3.22). The adiabatic pumping of charge can now be interpreted as a shifting of all Wannier states to the next unit cells during one pump cycle, since

$$\Delta P = \phi_k(T) - \phi_k(0) = C. \quad (3.25)$$

To calculate the polarization, and by that, the Berry phase numerically, we use the exponential position operator [208]:

$$\hat{X}^e = e^{i\frac{2\pi}{L}\hat{x}}, \quad (3.26)$$

where L is the number of sites. This operator can also be used to calculate the spin-Berry phase for a two-component system. For the charge and spin operators one has [190]

$$\hat{X}_{C,S}^e = \exp [i(2\pi/L)\Sigma_j j (\hat{n}_{j\uparrow} \pm \hat{n}_{j\downarrow})]. \quad (3.27)$$

3.2.4 Current operator for lattice systems and non-adiabatic effects of the pumped charge

For the numerical studies showcased in this thesis, we will only consider tight-binding lattice models. While the current operator eq. (3.13) can be applied to a finite periodic

3.3 Thouless pumps as analogues to Chern insulators

lattice model, we are specifically interested in effects that can break the periodicity of the lattice, such as disorder or electron-phonon coupling, or in interacting models, where the k -states are no longer well-defined. Thus, the current operator in real space is needed, which takes the form [110]

$$\hat{J}(t) = i \sum_{j=1}^L \left(t_j(t) \hat{c}_j^\dagger \hat{c}_{j+1} - \text{H.c.} \right), \quad (3.28)$$

with the time-dependence originating from the hopping constants $t_j(t)$. We will use the expectation value of eq. (3.28) to calculate the pumped charge as a function of time in real-time evolution numerics. The expectation value vanishes for instantaneous eigenstates $|\Psi(t)\rangle$, because the admixture from the adiabatic theorem is missing in that case. Instead, using the time-evolved states $\hat{U}(t)|\Psi(0)\rangle$, all non-adiabatic effects to every order are included. The time-evolution operator $\hat{U}(t) = \mathcal{T}e^{-i\hbar \int_0^t dt' \hat{H}(t')}$ with the time-ordering operator \mathcal{T} has to be approximated numerically using finite time-differences, see chapter 4. The time-dependence of the Hamiltonian $\hat{H}(t)$ is entirely contained in the pump cycle $(\delta(t), \Delta(t))$ in eq. (3.8). The amount of adiabaticity is controlled by the pump period T . For large T , the pumped charge is nearly equal to the Chern number. Fast pumping (small T), leads to irreversible excitations during each pump cycle, which can lead to pumped charges lower or higher than the quantized amount. Recently, the non-adiabatic effects have been characterized using Floquet theory [56]. It is shown that the dependence of the deviation from quantized charge values can become non-analytic and proportional to the square of the driving frequency ω^2 when the driving is switched on rapidly, due to an imperfect occupation of Floquet states at $t = 0$. This is usually apparent from oscillations in the pumped charge $Q(t)$. To remedy this, we will switch on the pumping smoothly (chapter 4).

3.3 Thouless pumps as analogues to Chern insulators

From eq. (3.19), one can see that the pumped charge per cycle in a quasi-adiabatic evolution is only dependent on the instantaneous quantity of the Berry curvature of the mixed time-quasi-momentum Brillouin zone $(k_x, t) \in \text{BZ}$. This makes it natural to make the substitution $k_y \leftrightarrow t$ in this limit and to directly consider two-dimensional materials with a non-zero Chern number, called Chern insulators. If one considers such a material on a cylinder, meaning that one dimension is cyclic (like the time t in Thouless pumps), analogues of the pumped charge and the emerging edge states as a function of t can be made. In particular, the dispersion relation $\epsilon(k_x, k_y)$ will look identical to fig. 3.3, with t being replaced by k_y . The edge states are now stationary along the two edges of the cylinder and still exponentially localized into the bulk but completely delocalized along the edge: The edge states are a superposition of many k_x states, which leads to the localization perpendicular to the edge. On the other hand the edge states have well-defined k_y values. The linear dispersion of the edge states are now to be understood as having a constant group-velocity $v_{k_y} = \partial_{k_y} \epsilon$. From fig. 3.3, one can see that the group

3 Topological charge pumps

velocity is positive [negative] on the right [left] edge. For this reason, Chern insulators are said to have chiral edge states. The overlap between forward- and backward moving edge states on opposite edges is exponentially suppressed with the distance between the edges. For macroscopic material samples one can therefore ignore the scattering of forward- and backward-movers, leading to dissipation-less edge-currents on the boundary of Chern insulators.

The analogy between Chern insulators and topological charge pumps makes the latter an invaluable tool in both the theory of topological materials and in experimental realizations of topological systems. From a theoretical point of view, one-dimensional systems are easier to study than two-dimensional systems. This is especially relevant for many-body interacting systems, which are often efficiently numerically solvable in 1d for hundreds of sites, using state-of-the-art techniques like matrix-product-state methods (chapter 4) but can lack efficient methods for 2d, for example in cases where quantum monte-carlo [216, 217, 218, 219] suffers from the sign problem. Even though one cannot directly treat all relevant many-body interaction types for 2d in such a manner using charge pumps, as, e.g. nearest-neighbor interactions in 1d differ from the 2d case, charge pumps are prime candidates to explore the rich physics of the interplay of topology and many-body interactions. The interplay of disorder and topology is also simplified in the 1d case, as Anderson localization [163] has no critical disorder strength in 1d. In summary, topological charge pumps are natural "simplest case" systems to study topology in condensed matter.

On the other hand, the analogy between Thouless pumps and Chern insulators can be used to study systems beyond 3d [55, 101]. This is done by experimentally realizing and studying a two-dimensional adiabatic charge pump with two time-directions t_1 and t_2 . With the $t - k$ analogy, a 4d quantum Hall system is realized and the bands of such a system are then topologically characterized by the second Chern number [220].

On the experimental side, one-dimensional Thouless pumps are often easier to prepare and control than two-dimensional Chern insulators. In ultra-cold atomic experiments using optical lattices, Chern insulators are realized by generating a synthetic gauge field [41]. As the atoms are charge-neutral, magnetic fields that are needed for Chern insulators have to be generated using techniques such as laser-induced tunneling or lattice shaking [25]. Thouless pumps do not need a synthetic magnetic field, as the electric dipole forces by the laser fields that create the lattice and the time-dependent control thereof is sufficient to create the dynamical analogue of a Chern insulator [33].

3.4 Experimental realizations of Thouless pumps

Pumps where exactly one electron is pumped have first been realized in metallic tunneling junctions [221, 222]. Although the quantization of pumped charge is achieved, these pumps resemble classical pumping as the dynamics are not coherent and utilize the coulomb blockade for pumping single charges. Coherent Thouless charge pumps have since been realized in ultra-cold atomic systems, using optical lattices for bosons [33] and fermions [34, 67, 38], in photonic waveguide systems [68, 69], in superconducting circuits

[223], in twisted bilayer graphene [70, 71, 72] and in optical cavities [73].

3.4.1 Ultracold atoms

Ultracold atoms in optical superlattices [23] have emerged as an ideal setup to experimentally study Thouless pumps [33, 34, 67, 38] and topology in general [25]. This comes down to the high degree of controllability and their flexibility to engineer systems that go beyond standard material conditions. Ultracold atomic systems consist of a dilute gas of neutral atoms that are confined via light-matter interactions. The potential energy landscape that the atoms feel gets generated by an optical dipole potential from laser fields, using the AC-Stark effect [224], that has the form [25]

$$V(\mathbf{x}) = \alpha |\mathbf{E}(\mathbf{x})|^2, \quad (3.29)$$

with the electric field E and the polarizability of the atoms α , which can depend on the laser frequency. This light-field can be used to trap a cloud of neutral atoms in all three dimensions by using a harmonic confining potential [23]. On top of that, standing laser waves can create a periodic lattice, which defines sites of high intensity, where atoms sit. Depending on the phases, wavelengths and amplitude of the lasers, periodic lattices, quasi-periodic lattices or quasi-disordered lattices can be realized. By tuning the lasers in a time-dependent manner, these lattices can be made dynamic. Lattices can be twisted, shifted, shaken and rotated both slowly and quickly [25]. Since the atoms are neutral, regular magnetic fields cannot be used to break time-reversal symmetry and induce topology. Instead, in cold gas experiments, synthetic gauge fields are created, using a variety of methods like laser assisted Raman-tunneling or lattice shaking [42, 25]. In addition to the harmonic trapping potential, it is also possible to engineer edges [27, 119, 40], although edge states are more naturally studied in photonic systems, by propagating light near the edge of the photonic crystal [225, 68, 211].

Atoms are cooled to near absolute zero via various techniques, such as laser cooling [226] and evaporative cooling [227]. The loading schemes vary depending on the specific experiment. These loading schemes are not perfect and defects, for example in the form of thermal holes, can form. For a charge pump this can lead to an overall lower pumped charge than the quantized value [48]. Despite the name, ultracold atomic systems are considerably hot - when compared to the Fermi energy [228]. One therefore always expects a certain fraction of atoms in the excited state [33].

Another key feature of ultracold atomic gases is the tunability of the strength of many-body interactions. This is done via the Feshbach resonance² [120]: The system is pumped with optical or magnetic fields, which correspond to the binding energy of two atoms. As a results, one can either resonantly enhance the formation of the bound state, increasing the many-body interaction or detune it to effectively realize non-interacting systems. The Feshbach resonance has made ultracold atomic gases an ideal setting in the cutting-edge area of study of interacting topological quantum systems and has lead

²Or via the lattice depth.

3 Topological charge pumps

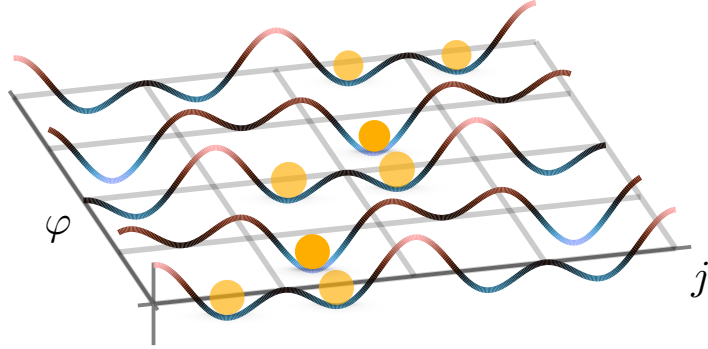


Figure 3.4: Superlattice generated by overlapping a short and a long lattice and tuning the phase φ of the short lattice. j denotes the position of the effective lattice points, where atoms sit in the tight-binding lattice due to the dipole interaction. For a quasi-adiabatic modulation, a state initially in a symmetric superposition shifts one unit cell to the right as φ is rotated once.

to increased theoretical interest in this direction [147, 46, 47, 154, 157, 148, 156, 51, 52, 158, 53, 150, 151, 57, 149, 62, 159, 160, 161, 153, 155].

The dynamical control of the dipole potential makes it very practical to engineer a Thouless pump in ultracold atomic systems. A common realization is given by overlapping two lasers, one with a short periodicity d_s and one with a long periodicity $d_l > d_s$. The potential this generates is given by [33, 66]

$$V_s \sin^2(\pi x/d_s + \pi/2) + V_l \sin^2(\pi x/d_l - \varphi/2), \quad (3.30)$$

where $V_{l,(s)}$ is the lattice depth of the long (short) lattice. The phase φ is dynamically modulated, sliding the long lattice across the short one, which generates the potentials that are sketched in fig. 3.4. Depending on $V_{l,(s)}$ depth, either Landau levels of a free particle in a magnetic field or a tight-binding lattice model can be realized [33]. In the tight-binding limit with $V_s \gg V_l$, the Rice-Mele model eq. (3.4) is realized. From fig. 3.4, we see that the states are pumped exactly as described before: The instantaneous states shift one unit cell when the phase φ is rotated once. In this continuum picture it is also apparent that the potential minima stay stationary at all times. This is what necessitates a quantum description of the Thouless pump, as particles have to tunnel to the site of lowest potential energy through a finite barrier. In contrast, a classical particle would be stuck at each local minimum and would not get pumped.

To measure the topological drift, one can employ in-situ imaging [33, 34, 67, 38], where the particle cloud is observed directly inside the lattice as it is pumped. The edge-state energy levels and dispersion relation can be measured via band-mapping, for example via time-of-flight measurements [31], where the lattice is switched off and the gas is allowed to expand freely under the effect of gravity. In the far field limit, one then measures the velocity of the particles, which gives information about the energy versus the quasi-momentum.

3.4 Experimental realizations of Thouless pumps

Apart from 1d topological pumps, ultracold quantum gases are capable of realizing a plethora of topological phases of matter. This can be done via Floquet engineering [43], where the optical lattice is modulated quickly instead of slowly to engineer effective Hamiltonians that can be topological in nature [43, 119]. This gives ultracold quantum gases yet another distinct feature, in the possibility to engineer anomalous Floquet topological systems [42, 119], in which the bulk invariants are no longer necessarily tied to edge states, due to the periodicity of quasi-energy spectrum. Here, the heating of the atoms gives a limit on how long the dynamics can be investigated.

Another avenue are synthetic dimensions [229], where internal degrees of freedom, such as internal atomic energy levels are used as lattice "sites", so that higher-dimensional lattice systems and pumps are possible [158].

Disorder, which will be the main topic of section 5.1, can be realized in ultra-cold atomic systems, either as quasi-disorder by superimposing an incommensurate potential [230, 67], or as true random disorder potentials using a speckle pattern [231] or digital micromirror device [232, 233, 234].

3.4.2 Photonic systems

Photonic systems, more specifically evanescently coupled optical waveguides can be used to realize a multitude of discrete quantum mechanical systems [235]. The refractive index of a three-dimensional block of material is changed locally via femtosecond laser writing. Light is then propagated through the waveguides along the z -axis, such that the $x - y$ plane can be used as a two-dimensional lattice system. This works because the paraxial Helmholtz equation for the electric field is formally equivalent to a time-dependent Schrödinger equation. The z spatial dimension takes the role of time t , which makes the method especially suited to resolve time-evolution of quantum systems, as no fine time-resolution is needed for the experiment. Changing the local refractive index as a function of z , one can then also engineer time-dependent discrete systems, such as topological charge pumps or Chern insulators usually realized via circular shaking [225].

Recently this method has been used to realize a disordered Rice-Mele model [69]. While usually optical wave guides are especially practical for detecting topological edge states, it has also become possible to measure bulk drift in these systems. Especially disordered pumps with highly localized initial states [236] - which in the language of optical waveguides simply means shining a narrow localized laser beam on the sample - can be realized in photonic systems, as no state-preparation is needed and the engineering of arbitrary refractive index profiles can engineer various types of disorder. As a drawback, full many-body-interacting systems, especially fermionic systems with many-body interaction are not realizable in photonic systems, due to the bosonic nature of light. However, the platform permits the study of non-linear quantum systems, and therefore interactions in the mean-field limit, where the strong electric fields can lead to soliton formation, which can have topological character [155, 237].

4 Numerical methods

In this chapter I will briefly review the numerical methods that were used for the simulations of topological charge pumps in the manuscripts from the following chapters. The main problem is to numerically solve the time-dependent Schrödinger equation

$$i\hbar\partial_t |\Psi(t)\rangle = \hat{H}(t) |\Psi(t)\rangle. \quad (4.1)$$

The initial state $|\Psi(0)\rangle$ has to be calculated via ground-state algorithms before carrying out the time-evolution. For topological charge pumps, which are usually realized experimentally in a deep lattice limit, we focus on one-dimensional tight-binding models of the general form

$$\hat{H}(t) = - \sum_{j,\sigma} J_j(t) \left(\hat{c}_{j\sigma}^\dagger \hat{c}_{j+1\sigma} + \text{h.c.} \right) \quad (4.2)$$

$$+ \sum_{j,\sigma} V_j(t) \hat{c}_{j\sigma}^\dagger \hat{c}_{j\sigma} + U \sum_j \hat{n}_{j\uparrow} \hat{n}_{j\downarrow}, \quad (4.3)$$

with the hopping $J_j(t)$, the local potential $V_j(t)$ and a many-body Hubbard interaction strength U . The sum σ runs over both spins \uparrow, \downarrow . $\hat{n}_{j,\sigma} = \hat{c}_{j\sigma}^\dagger \hat{c}_{j\sigma}$ is the number operator on site j .

For spin-polarized systems, the sum over σ is dropped and $U = 0$. We are also interested in phonon-induced breakdown of Thouless pumping, which will be the topic of section 6.1. For this, the non-interacting Hamiltonian will be coupled to phonons via $\hat{H}_{\text{ph}} + \hat{H}_{e\text{-ph}}$ with

$$\hat{H}_{\text{ph}} = \hbar\omega \sum_{i=1}^L \hat{b}_i^\dagger \hat{b}_i, \quad (4.4)$$

$$\hat{H}_{e\text{-ph}} = -\gamma \sum_{i=1}^L \left(\hat{b}_i^\dagger + \hat{b}_i \right) \hat{n}_i, \quad (4.5)$$

with bosonic creation operators \hat{b}_j^\dagger on site j .

Finally, we are also interested in finite-temperature effects for interacting charge pumps (chapter 8), which necessitates the time-evolution of all eigenstates.

4.1 Julia

Julia [238] is a new all-purpose language that is built from the ground up for high-performance computing. It combines a convenient and easy to learn syntax which is

similar to python or Matlab with speeds that rival or even surpass C. It is used for all projects highlighted in this thesis¹, for both the numerical simulations as well as the data-analysis and plotting. I will briefly list a few advantages of the language that make it an ideal language for the study of quantum systems and numerical studies in general:

- Julia is just-in-time compiled, meaning that it can be used for both interactive computations in notebooks as well as highly performing scripts that can be run on a cluster. The first time a function is encountered during a session it is compiled automatically. Each subsequent call is then highly optimized to the specific argument types provided to the function.
- Julia is built with modularity in mind, meaning that functions can be written very generically and reused often. All built-in functions as well as user functions automatically distinguish between the types of multiple arguments provided to the function, which is called multiple-dispatch. In practice this can be used, for example, to define different models as their own type. Calling a Hamiltonian function then automatically constructs the correct model-specific Hamiltonian depending on the model type, without needing different names for each Hamiltonian function. With this, simulation routines can be written generically for all possible models.
- Unicode characters can be used as part of the syntax which unclutters code and makes variable names more meaningful (e.g. Ψ for wavefunctions).
- Many standard routines for matrix diagonalization, inversion and linear solvers are included in Julia and use highly optimized routines that automatically use parallel computing capabilities.
- Julia is fully open-source, which together with its modularity means it is easy to adapt specific packages to your specific problem.
- Julia is fast without needing complicated syntax. Simple loops perform as well as C code. Algorithms do not need to be vectorized to perform well.
- Many relevant packages, such as the iTensor package [239] for matrix-product state methods, which is used in this thesis, are developed in Julia.

4.2 Non-interacting, spin-polarized charge pumps

First, we consider non-interacting, spin-polarized charge pumps. Such models are the focus of the next two chapters, where disordered, non-interacting charge pumps (section 5.1) and non-interacting charge pumps coupled to classical phonons (section 6.1) are studied. For both cases, we employ periodic boundary conditions, as disordered systems can make the distinction between Anderson-localized states and topological edge states hard to

¹With the exception of the project in section 6.1, where Python was used.

4.3 Fermionic systems coupled to phonons: Multi-trajectory Ehrenfest

resolve. In such non-interacting models, it is convenient to directly work in the local site basis, in which the Hamiltonian becomes

$$(H_{ij})_{\text{pbc}} = \begin{pmatrix} V_1(t) & J_1^*(t) & 0 & \cdots & 0 & J_L(t) \\ J_1(t) & V_2(t) & J_2^*(t) & \ddots & & 0 \\ 0 & J_2(t) & \ddots & & \ddots & \vdots \\ \vdots & \ddots & & \ddots & J_{L-2}^*(t) & 0 \\ 0 & & \ddots & J_{L-2}(t) & V_{L-1}(t) & J_{L-1}^*(t) \\ J_L^*(t) & 0 & \cdots & 0 & J_{L-1}(t) & V_L(t) \end{pmatrix}, \quad (4.6)$$

which is a simple $L \times L$ matrix that can directly be diagonalized using standard methods [240]. The ground state is given as a Slater determinant consisting of all eigenstates below the Fermi-energy ϵ_F , which is chosen to lie inside the band gap, such that the lowest band is completely filled. In practice it is most convenient and efficient to calculate the time-evolution for all single particle eigenstates $|\lambda_{\epsilon_\alpha}\rangle$ with $\epsilon_\alpha < \epsilon_F$ in parallel by propagating the matrix

$$(\boldsymbol{\lambda}_{\epsilon_1} \quad \boldsymbol{\lambda}_{\epsilon_2} \quad \cdots \quad \boldsymbol{\lambda}_{\epsilon_N}) \quad (4.7)$$

with $(\boldsymbol{\lambda}_{\epsilon_\alpha})_j = \langle j | \lambda_{\epsilon_\alpha} \rangle$.

For the time-evolution, the Crank-Nicholson method is used [241, 242], which is unitary and numerically stable:

$$\hat{U}(t+dt, t) = \left(1 - i \frac{H(t + \frac{dt}{2})}{2} dt\right) \left(1 + i \frac{H(t + \frac{dt}{2})}{2} dt\right)^{-1} + \mathcal{O}(dt^3). \quad (4.8)$$

4.3 Fermionic systems coupled to phonons: Multi-trajectory Ehrenfest

In order to simulate the time-evolution of non-interacting electronic systems that are coupled to phonons, we employ the multi-trajectory Ehrenfest method [243], which is an approximate semi-classical method that treats the phonons classically. This method is efficient and reliable in the regime of small phonon frequencies. The bosonic operators are written as $\hat{b}_i^\dagger = \sqrt{\frac{m\omega}{2\hbar}} \left(\hat{x}_i + \frac{\hat{p}_i}{m\omega}\right)$, which after rescaling leads to the phononic and electron-phonon coupling Hamiltonians respectively:

$$\hat{H}_{\text{ph}} = \frac{\omega}{2} \sum_{i=1}^L (\hat{x}_i^2 + \hat{p}_i^2) \quad (4.9)$$

$$\hat{H}_{e\text{-ph}} = -\sqrt{2}\gamma \sum_{i=1}^L \hat{x}_i \hat{n}_i. \quad (4.10)$$

4 Numerical methods

In the multitrajectory Ehrenfest method, the classical phonon position and momenta are sampled from the Wigner function

$$W_0 = \frac{1}{\pi} e^{-(x-(x))-(p-(p))^2}. \quad (4.11)$$

The electronic wave function can then be quantum-mechanically evolved with the Hamiltonian

$$\hat{H}_{\text{el}} = \hat{H}_{\text{RM}}(t) - \sqrt{2}\gamma \sum_{i=1}^L x_i(t) \hat{n}_i, \quad (4.12)$$

where the phonon coordinates x_i act as a local potential, whereas the phononic degrees of freedom are evolved classically with the Hamiltonian formalism with

$$H_{\text{cl}} = \frac{\omega}{2} \sum_{i=1}^L (x_i^2 + p_i^2) - \sqrt{2}\gamma \sum_{i=1}^L x_i \langle \Psi_e(t) | \hat{n}_i | \Psi_e(t) \rangle. \quad (4.13)$$

More details can be found in the Manuscript highlighted in section 6.1 or in [243].

4.4 Many-body interacting systems

For many-body interacting quantum systems, several methods come to mind that can treat the full time-evolution of fermionic ground states: Lanczos methods [244, 242] are used for periodic or open boundary conditions and where the dynamics of the ground state and a few excited states are sufficient, as is the case for zero-temperature calculations. For finite temperature numerics, all eigenstates have to be time-evolved, which necessitates full exact diagonalization [245]. These methods are heavily restricted by system size due to the exponential growth of the many-body basis size. Quantum Monte-Carlo methods [246, 216, 217, 218, 247, 219] are preferable but usually suffer from the sign problem for fermionic systems. Dynamical mean-field theory (DMFT) [248] is an alternative method that maps the many-body problem onto a local impurity problem and generally works best for higher dimensional systems (it becomes exact for an infinite coordination number).

For one-dimensional systems with open boundary conditions, the cutting edge methods are matrix-product state methods [76, 249, 250, 82], which can treat systems with hundreds of sites but are restricted by the amount of non-adiabatic excitation and the resulting entanglement growth during the real-time simulation, which effectively limits the propagation time.

4.4.1 Matrix-product state methods

For good reviews on matrix-product state methods see [251, 250]. I will briefly recap the basics of matrix-product state methods and outline new developments and algorithms that have been used in the manuscripts that are part of this thesis.

Two seminal papers by Steven White [74, 75] introduced density matrix renormalization group (DMRG) methods for efficiently finding ground states of one-dimensional many-body systems. Since then various methods have been developed to treat quantum mechanical time-evolution as well [76, 77, 78, 79, 80, 81, 82]. Matrix-product states have formalized these methods into a language that can efficiently describe ground states of one-dimensional many-body systems which are compressed while keeping all relevant correlations. Mathematically, the compression is based on the compression of a matrix M according to the Frobenius norm $\|M\|^2 = \sum_{i,j} |M_{i,j}|^2$, which is most efficiently done via a singular value decomposition (SVD) $M = USV^\dagger$, where S is a diagonal matrix containing the (sorted in descending order) singular values s_i . If the s_i decrease sufficiently quickly with i , it suffices to keep only a few singular values and to truncate the size of the matrices accordingly. This is used, for example, in image compression.

DMRG and MPS methods reveal a practical link between this matrix compression and the physically relevant quantity of entanglement. We start from an arbitrary state written in the many-body basis:

$$|\Psi\rangle = \sum_{\sigma_1, \dots, \sigma_L} c_{\sigma_1, \dots, \sigma_L} |\sigma_1, \dots, \sigma_L\rangle, \quad (4.14)$$

where $\vec{\sigma} = |\sigma_1, \sigma_2, \dots, \sigma_L\rangle$ denotes the local degrees of freedom on sites $1 \dots L$. For a bipartitioning of a state $|\psi\rangle$ into two subsystems A and B

$$|\psi\rangle = \sum_{\vec{\sigma}_i, \vec{\sigma}_j} \psi_{\vec{\sigma}_i \vec{\sigma}_j} |\vec{\sigma}_i\rangle_A |\vec{\sigma}_j\rangle_B, \quad (4.15)$$

the coefficients can be written as a matrix $\psi_{\vec{\sigma}_i \vec{\sigma}_j}$. Carrying out a singular value decomposition, we arrive at the Schmidt decomposition of the quantum state [250]:

$$|\psi\rangle = \sum_{a=1}^r s_a |a\rangle_A |a\rangle_B, \quad (4.16)$$

with $|a\rangle_A = \sum_{\vec{\sigma}_i} U_{a\vec{\sigma}_i} |\vec{\sigma}_i\rangle_A$, $|a\rangle_B = \sum_{\vec{\sigma}_j} V_{a\vec{\sigma}_j}^\dagger |\vec{\sigma}_j\rangle_B$. Tracing out one of the subsystems, the reduced density matrix is

$$\hat{\rho}_A = \sum_{a=1}^r s_a^2 |a\rangle_{AA} \langle a|, \quad (4.17)$$

and the von Neumann entanglement entropy is

$$S_{A|B}(|\psi\rangle) = -\text{Tr} \hat{\rho}_A \ln \hat{\rho}_A = -\sum_{a=1}^r s_a^2 \ln s_a^2. \quad (4.18)$$

The size of the singular matrix r can now be truncated depending on the distribution of the s_i , which means that states with low entanglement can be efficiently written in the Schmidt decomposition. The matrix-product state is defined by starting from the

4 Numerical methods

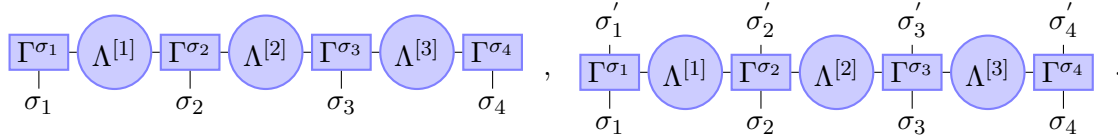
left end of the system, considering the subsystems of the first site $|\sigma_1\rangle$ and the rest $|\sigma_2 \dots \sigma_L\rangle$ and carrying out an SVD on that link. One can then truncate the singular matrix and reshape all matrices of the SVD according to the truncation, depending on the entanglement on that link. One then sweeps through the system from left to right, carrying out successive SVDs on all links until one arrives at

$$|\psi\rangle = \sum_{\sigma_1, \dots, \sigma_L} A^{\sigma_1} A^{\sigma_2} \dots A^{\sigma_{L-1}} A^{\sigma_L} |\sigma_1, \dots, \sigma_L\rangle, \quad (4.19)$$

where the A^{σ_j} are matrices of different sizes, such that their product reproduces the many-body coefficients $c_{\sigma_1, \dots, \sigma_L} = \sum_{a_1, \dots, a_{L-1}} A_{a_1}^{\sigma_1} A_{a_1, a_2}^{\sigma_2} \dots A_{a_{L-2}, a_{L-1}}^{\sigma_{L-1}} A_{a_{L-1}}^{\sigma_L}$. The diagonal singular matrices are most readily read off from a different but equivalent grouping of matrices [250]:

$$|\psi\rangle = \sum_{\sigma_1, \dots, \sigma_L} \Gamma^{\sigma_1} \Lambda^{[1]} \Gamma^{\sigma_2} \Lambda^{[2]} \Gamma^{\sigma_3} \Lambda^{[3]} \dots \Gamma^{\sigma_{L-1}} \Lambda^{[L-1]} \Gamma^{\sigma_L} |\sigma_1, \dots, \sigma_L\rangle, \quad (4.20)$$

where the $\Lambda^{[j]}$ are diagonal matrices sitting on the link (bond) between two physical sites and containing the singular values. This size of these matrix gives the "bond-dimension", which is a measure of the degree of entanglement on that bond. Γ^{σ_j} encode the physical degrees of freedom. More details can be found in [250, 251]. The strength of MPS methods for 1d systems is due to the fact that the entanglement for gapped 1d systems follows an area law [252, 253], which means that the entanglement is constant with respect to system size. MPS methods are also convenient due to the diagrammatic representation of both states and operators. The state eq. (4.20) and a many-body operator $\hat{O} = \sum_{\sigma_1, \dots, \sigma_L, \sigma'_1, \dots, \sigma'_L} c_{(\sigma_1, \dots, \sigma_L)(\sigma'_1, \dots, \sigma'_L)} |\sigma_1, \dots, \sigma_L\rangle \langle \sigma'_1, \dots, \sigma'_L|$ for $L = 4$ are represented as



Connected lines imply a summation over the index (either a physical index σ_j or the index corresponding to the bond ($j \leftrightarrow j + 1$)).

Ground-state search can then be carried out via DMRG by finding the Lagrange multiplier λ that extremizes [250]

$$\langle \psi | \hat{H} | \psi \rangle - \lambda \langle \psi | \psi \rangle, \quad (4.21)$$

which is done iteratively by varying only the components of a single tensor at a time and sweeping through the entire chain in this way left and right until convergence is achieved.

Various methods exist for carrying out time-evolutions in the MPS language, such as time-dependent DRMG (tDMRG) [77, 78], time-evolving block decimation (TEBD) [76] and time-dependent variational principle (TDVP) [79, 80, 82]. I have used mainly the TEBD method, which can be easily implemented in a few lines of code, given a tensor package, such as iTensor [239]. TEBD is based on a Trotter decomposition, where

the Hamiltonian is split between even and odd bonds and each time step propagator is decomposed as [250]

$$e^{-i\hat{H}dt} = e^{-i\hat{H}_{\text{odd}} dt/2} e^{-i\hat{H}_{\text{even}} dt} e^{-i\hat{H}_{\text{odd}} dt/2} + O(dt^3). \quad (4.22)$$

The exponentials of the Hamiltonian are operators acting on two sites and can be applied to the MPS directly. The same method can also be applied to infinite matrix-product states, which consist of a single matrix that represents the bulk of the system. This infinite time-evolving block decimation (iTEBD) has been used in section 7.1. During the time-evolution, entanglement is generally built up in the form of increasing bond dimensions. This means that there is a limit on how far the system can be propagated in time accurately, although various methods exist to extend this time-limit [250]. For the simulation of Thouless charge pumps, the condition that the pumping should be done adiabatically slowly seems to be detrimental in this respect. However, during quasi-adiabatic dynamics, the states mostly resemble instantaneous ground states and therefore the entanglement is usually small during the time-evolution. This advantage is relativized by the fact that MPS methods work most efficiently in systems with open boundary conditions. For systems with an additional harmonic trapping potential, for example, the propagated states do not resemble the instantaneous states after the first pump cycle, due to the fact that the edge states of topologically systems are always obeying a sudden approximation [54], where states do not jump across the entire system when hitting an edge but rather pumping further up the trap, or accumulating at the edge for a flat system.

A new development in MPS methods is the usage of tangent-space methods in uniform, infinite matrix-product states. For an exhaustive introduction, see [82]. In tangent-space methods, the states that can be written as infinite MPS with a given bond-dimension are interpreted as a manifold. Summing two MPS does not yield another MPS, which makes the space of all MPS non-linear. However, the MPS states can be differentiated and a tangent space can be defined, indicating the gradients in which the MPS can change while keeping their bond-dimension fixed. the "variational uniform matrix product state" algorithm (VUMPS) can now be seen as finding the MPS inside the manifold of fixed bond-dimension that best approximates the true many-body ground state, which is done via a projection onto the tangent space. The VUMPS algorithm, which is implemented in a subpackage for iTensor [254], is used in section 7.1 for finding the ground state for infinite systems.

5 Disorder in topological charge pumping

A hallmark of topological systems is the robustness of topological invariants to perturbations in the system. These perturbations come about in many different manifestations and essentially boil down to the question, whether the energy gap between the topological, filled band and the surrounding bands is closed. Most naturally, this scenario is given by considering the ground state of a non-interacting system as the filled valence band and making sure that the gap to the conduction band remains open. For interacting systems, one has to consider the many-body gap.

A type of perturbation of particular interest is disorder, since it is a naturally occurring phenomenon in virtually all experiments. The generalization of Thouless pumping in the presence of disorder and many-body interactions was first introduced by Niu and Thouless in their 1984 paper [44], in which they employed twisted boundary conditions and Greens functions to study quantized particle pumping. They come to the conclusion that disorder does not break topological pumping, as long as the energy gap remains open.

Recently, the interplay between disordered systems and topology has attracted increased interest, both for understanding relevant experiments that necessarily contain disorder and also for non-trivial connections between localization and topology. In disordered single-particle systems, Anderson localization [163] leads to exponentially localized eigenstates, which has been experimentally confirmed, for example in [255, 256]. For 1d systems, this localization happens at any finite disorder strength. The crossover of topology from 1d localization to 2d localization has been subject to recent research [257]. Disordered topological systems also become relevant in twisted bilayer graphene, where the twist between two sheets of graphene leads to a Chern mosaic [99].

I discussed before in section 3.2.3 that the shifting of localized Wannier functions are at the heart of topological charge pumping in 1d systems. Nevertheless, it is interesting to ask how exactly localization and topological charge pumping affect each other.

In translationally invariant systems topological invariants are defined via Brillouin zone integrals, which usually implies that a completely filled and energetically isolated band is necessary for a topological protection to hold. However, the momentum-distribution function of a single exponentially localized particle is flat, meaning that the Brillouin zone, although not filled, is homogeneously occupied by such a state. As a result, Wannier-Stark localization [258] - the single-particle localization due to a linear tilt of the lattice - can be used to pump localized single-particle states in a quantized fashion [259, 260]. Anderson localization due to disorder leads to a uniform sampling of the Brillouin zone in a similar way [261]. This has recently been used to pump a localized bulk state in a disordered photonic system [69] in a nearly quantized fashion.

Another development that combines disorder and topology in an unexpected way was

the discovery of the topological Anderson insulator [262]. In these systems, quantized conductance plateaus are realized for a disordered system which is metallic without disorder, which shows that topological effects can not only be robust to disorder but also be induced by it. Here, the appearance of a mobility gap becomes important. Even for gapless systems, disorder induces a finite mobility gap, which can induce topology. Such a phase has been experimentally realized in a photonic system [210]. In more general topological systems it has been established that localization can also protect topological order, for example in Majorana edge states [263]. Analogous to topological Anderson insulators, disorder can also induce topologically quantized pumping where none would exist without disorder [50, 164].

In a recent paper, a direct connection between localization of Floquet states and breakdown of quantized charge transport in a Thouless pump was demonstrated [58]. The distinction between Floquet states, which are the stationary states that include the virtual admixture of excited bands due to the periodic driving, is important, as Hamiltonian eigenstates do not possess a localization-delocalization transition in 1d. On the other hand, the precise connection between the closing of the minimum energy gap along the pump cycle and the critical disorder strength for the breakdown of quantized pumping has not been clearly established.

In quantum gas experiments, disorder can be achieved via quasi-disorder, via an incommensurate additional potential overlaid with the optical lattice [264, 265, 67]. Truly random disorder potentials have recently become available as well via speckle potentials [231] or digital micromirror devices [232, 233, 234]. There exist subtle differences between quasi-adiabatic disorder and uncorrelated disorder. For a quasi-periodic disorder, there exists a critical disorder strength for the localization of eigenstates in 1d, for example. In these experiments [35, 33, 34, 67, 39], the in-situ images of the shifting particle clouds usually measure many independent realizations of one-dimensional tubes that are separated by strong laser fields, in which the charge pumps are realized. The disorder in each of these tubes can be considered uncorrelated. Therefore, measuring the particle cloud with in-situ methods effectively averages over many disorder realizations.

For this reason, we would like to understand the effect of random disorder potentials on Thouless pumps in detail and to quantify the dependence between the energy gap and topological transport in a disorder-averaged system. In this chapter I will present a publication, in which we characterize the breakdown of adiabatic topological pumping for free fermions due to random disorder. We employ a multitude of instantaneous measures, as well as finite pumping speed simulations of the pumped charge.

For a disordered system, as well as in many-body interacting systems, the Chern number in the language of the periodic part of Bloch functions, as introduced in section 2.1.3 cannot be used and a representation in the position basis is needed. One commonly used method for disordered and interacting systems are twisted boundary conditions [44]. Here instead, we employ the so called local Chern marker (LCM) [162, 167, 168], which is a position-resolved local quantity that recovers the topology of the entire system when averaged over a large bulk region. Before our publication, the local Chern marker has been used in two-dimensional finite Chern insulators without disorder [162, 165, 166].

The local Chern marker recovers the Chern number when integrated over a large bulk region far away from the boundaries. Integrating over the entire sample, including the edges, the Chern number is zero because globally an open boundary condition system is necessarily topologically trivial¹.

In our publication, we generalize and extend the definition of the local Chern marker to a periodic one-dimensional system with periodic driving and also utilize it for the first time in disordered systems. For this, care has to be taken, since there exists no "time operator" in quantum mechanics. Therefore, our formulation is a time- and position-local operator that gives a site-resolved local measure of topological charge transport while recovering the quantized, nontrivial value when integrating over the entire periodic system. We find that the disorder-induced breakdown of quantized pumping is visible in the distributions of the local Chern marker fluctuations.

Additionally, we employ the entanglement spectrum [267], which encodes topological information in the lowest eigenvalues of a non-interacting effective entanglement Hamiltonian. This has recently been used in an interacting bosonic pump [53], where spectral winding was found. In disordered systems, the level statistics of the entanglement spectrum have been used to distinguish topological and trivial phases [268].

The minimum energy gap distributions for each disorder realization along the pump cycle are shown to undergo a transition from a Gaussian to an exponential distribution at the critical disorder strength, which can be seen from the most likely energy gap, rather than the disorder averaged gap.

Finally, the Chern number can readily be calculated as the winding of the many-body polarization P , calculated via the exponentiated position operator eq. (3.26). For disordered systems, the polarization is not well-behaved in usual disorder-averages, as the time along the pump cycle, where P jumps from $-\pi$ to π is different for each disorder realization. Disorder averages therefore average values slightly above $-\pi$ and slightly below π to a value close to zero, which is incorrect. We introduce the method of circular averages of the polarization for this reason, which maps P onto a circle before averaging, which eliminates this problem.

We compare all instantaneous measures as well as finite time calculations and observe a good agreement for the critical disorder strength for all measures. We show that the disorder-averaged gap is not well suited to pinpoint the topological breakdown due to disorder. Instead, one should look at the gap distributions and the most likely gap. As an outlook, the most interesting direction is the combination of disorder and many-body interactions, due to the highly debated topic of many-body localization [269, 270]. It is unclear how Floquet approaches in the low-frequency limit [58] can be extended to interacting systems, while the local Chern marker has recently been extended to interacting systems [271]. Both the many-body polarization and the entanglement spectrum are naturally computed in the many-body picture.

¹Due to the edge states, the entire system is necessarily gapless. While the bulk region can be topologically nontrivial, these edge states render the whole system trivial. For example, in an OBC Rice-Mele model, the edge state on the right edge jumps instantaneously to the left edge in an adiabatic pump cycle, canceling the bulk drift of charge [266].

5.1 **Publication: Effect of disorder on topological charge pumping in the Rice-Mele model**

Article reprinted with permissions from Andrew L. C. Hayward, Eric Bertok , Ulrich Schneider and Fabian Heidrich-Meisner.

Phys. Rev. A 103, 043310 (2021)

<https://doi.org/10.1103/PhysRevA.103.043310>

Copyright (2021) by the American Physical Society.

Author contributions: E.B. reworked the manuscript from an earlier draft made by A.L.C.H.. A.L.C.H and F.H.M. conceived the idea for this project. Local Chern marker expressions were derived by A.L.C.H. E.B. implemented all algorithms from scratch, reproduced the data, recalculated all previous results, remade all figures and carried out new calculations for additional plots (Figs. 2,4,5,8,9,10,11,13,15,16). E.B. had the idea to employ a circular mean to average the many-body polarizations and the use the mode of the gap-distributions as an indicator of the breakdown of topological charge pumping. All authors contributed to the interpretation of results and discussion of the data. F.H.M rewrote the introduction.

Effect of disorder on topological charge pumping in the Rice-Mele modelA. L. C. Hayward,^{1,2} E. Bertok¹, U. Schneider,³ and F. Heidrich-Meisner^{1,*}¹*Institute for Theoretical Physics, Georg-August-Universität Göttingen, Friedrich-Hund-Platz 1, 37077 Göttingen, Germany*²*Arnold Sommerfeld Center for Theoretical Physics, Ludwig-Maximilians-Universität München, 80333 München, Germany*³*Cavendish Laboratory, University of Cambridge, J.J. Thomson Avenue, Cambridge CB3 0HE, United Kingdom*

(Received 30 October 2020; revised 27 February 2021; accepted 8 March 2021; published 7 April 2021)

Recent experiments with ultracold quantum gases have successfully realized integer-quantized topological charge pumping in optical lattices. Motivated by this progress, we study the effects of static disorder on topological Thouless charge pumping. We focus on the half-filled Rice-Mele model of free spinless fermions and consider random diagonal disorder. We use both static and time-dependent simulations to characterize the charge pump. The set of measures that we compute in the instantaneous basis include the polarization, the entanglement spectrum, and the space-integrated local Chern marker. As a first main result, we conclude that the space-integrated local Chern marker is best suited for a quantitative determination of topological transitions in a disordered system. In the time-dependent simulations we use the time-integrated current to obtain the pumped charge in slowly periodically driven systems. As a second main result, we observe and characterize a disorder-driven breakdown of the quantized charge pump. There is an excellent agreement between the static and the time-dependent ways of computing the pumped charge. The topological transition occurs well in the regime where all states are localized on the given system sizes. This observation is consistent with previous studies and the topological transition is therefore not tied to a delocalization-localization transition of Hamiltonian eigenstates. For individual disorder realizations, the breakdown of the quantized pumping occurs for parameters where the spectral bulk gap inherited from the band gap of the clean system closes, leading to a globally gapless spectrum. As a third main result and with respect to the analysis of finite-size systems, we show that the disorder average of the bulk gap severely overestimates the stability of quantized pumping. A much better estimate is the typical value of the distribution of energy gaps, also called mode of the distribution. We discuss our results in the context of recent quantum-gas experiments that realized charge pumps.

DOI: [10.1103/PhysRevA.103.043310](https://doi.org/10.1103/PhysRevA.103.043310)**I. INTRODUCTION**

The physics of topological charge pumps [1,2] has attracted intensified interest due to recent quantum-gas experiments realizing charge pumps with fermions [3] or strongly interacting bosons [4], and a spin pump [5]. These experiments observe quantized pumping over a number of cycles despite the fact that finite particle numbers and inhomogeneous systems were considered. Current theoretical efforts investigate the stability of charge pumps in optical lattices in genuine many-body systems [6–18], in noninteracting systems with disorder [19–24], with dissipation [25], or as a proximity effect [26]. Moreover, there are recent conceptual developments as well, for instance, concerning the introduction of the boundary charge [17,27–29].

A common notion is that topological properties remain protected against small amounts of disorder [2,30–33]. Considering a topological insulator, one expects the integer quantization of a topological invariant to remain robust as long as the bulk gap stays intact. Therefore, a disorder drawn from a bounded disorder distribution (e.g., a box distribution), whose width is significantly smaller than the many-body gap, does

not lead to a breakdown of topological quantization (see, e.g., Ref. [30]). Remarkably, disorder can also induce topological properties into a system, leading to the so-called topological Anderson insulator [34], which has been investigated experimentally [35,36]. Different from the scenario studied here, Titum *et al.* [37] introduced the case of an anomalous Floquet-Anderson insulator that is characterized by a winding number rather than a Chern number and possess fully localized Floquet eigenstates.

Another interesting direction concerns topology in quasicrystals [38]. Two recent experiments (using ultracold atoms [36] and a photonic system [39]) have investigated the stability of a topological charge pump with noninteracting particles against disorder. The fermionic quantum-gas experiment [36] has realized a quasiperiodic disorder potential that is akin to the Aubry-André model [40]. Both disorder-induced quantized pumping as well as the breakdown of topology in a sufficiently strong disorder potential has been observed.

Note that Aubry-André-like systems have been realized in several quantum-gas experiments [41–44], while more general forms of quasicrystals are at the heart of recent experimental efforts [45–48]. A number of theoretical studies has addressed the stability of topological properties against this type of quasidisorder, including, e.g., the SSH model [49]. The effect of disorder on an SSH model has also been investigated in a recent quantum-gas experiment [35].

*Corresponding author: fabian.heidrich-meisner@uni-goettingen.de

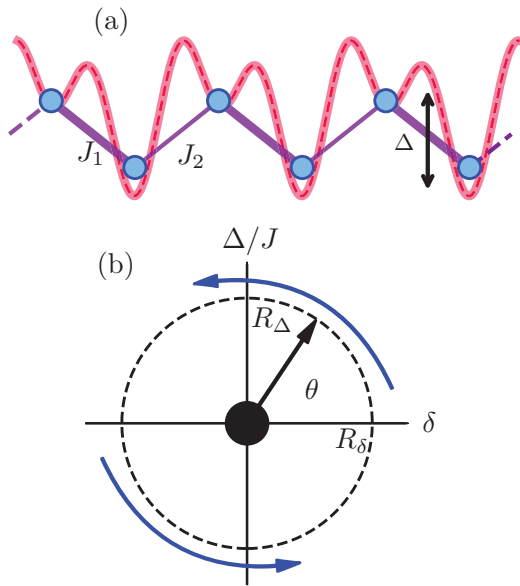


FIG. 1. Rice-Mele model. (a) A bichromatic potential with a ratio of two between the two optical wavelengths can, in the deep-lattice limit, be described by a lattice model with alternating tunneling strength $J_{1,2}$ and a staggered potential Δ . (b) We consider a charge pump that traces a path through this parameter space which encircles the central degeneracy. The cycle is parametrized by the angle θ , R_δ , and R_Δ .

Motivated by these experimental developments, we theoretically investigate the stability of topological properties of charge pumps against disorder in systems of noninteracting fermions. We concentrate on the half-filled Rice-Mele model with periodic boundary conditions (see the sketch in Fig. 1) and introduce random disorder in the on-site potentials. The problem of charge pumping in the presence of disorder has previously been addressed in a number of related studies [19,36,50]. In Ref. [19] a different model has been investigated using open boundary conditions, with an emphasis on the pumping of charge between edge states. As a result, they report the existence of a disorder-driven topological transition into a trivial state. A very appealing perspective on a disordered charge pump, modeled by the Rice-Mele model, has been put forward in Ref. [50]: While the Hamiltonian eigenstates are fully localized in one dimension with random on-site disorder for any disorder strength [51], there is a delocalization-localization transition in the Floquet eigenstates at the point where quantized pumping breaks down. Our work extends the analysis and theoretical understanding in several ways. First and complementary to the approach of [19], we use periodic boundary conditions that circumvent the complication of identifying edge states. Their unambiguous identification is complicated in the presence of randomness due to possible Anderson-localization of all single-particle states. Instead, we characterize the charge pump by four bulk quantities: The polarization, the entanglement spectrum, the local Chern marker and its integral as a measure for the bulk Chern number, and, finally, the integrated time-dependent current. The first three quantities are studied in the instantaneous eigenbasis, and the integrated current is

extracted from time-dependent simulations with finite-period pump cycles.

We give a brief account of our main results. The polarization is the most established object for the description of adiabatic transport [52]. We argue that the representation of the polarization as an angular variable simplifies its analysis. The entanglement spectrum contains information about quantized charge pumping via the spectral flow as has been discussed in [11]. Here we show that the quantized winding is preserved in the presence of weak disorder, while symmetries protecting the topology of the Su-Schrieffer-Heeger (SSH) model [53] that is visited twice in a clean system are broken.

Generally, in an inhomogeneous system, one cannot rely on the classification and expressions for topological invariants of lattice-translational invariant systems and hence a need for real-space version arises, as was emphasized in [54]. The usual path is to work with many-body wave functions and twisted boundary conditions, just as in the description of the integer quantum Hall effect. The local Chern marker provides an alternative tool for the calculation of an invariant in inhomogeneous systems. The local Chern marker has originally been introduced to capture aspects of topology in spatially inhomogeneous and/or finite systems [55] such as they arise in the presence of a trapping potential or interfaces (see, e.g., [56]). Here we use the local Chern marker to obtain the global Chern number of our disordered systems by integration over the spatial coordinate. For this purpose we generalize the expression for the local Chern marker to a time-periodic situation in the adiabatic limit. For the critical disorder strength we observe an excellent agreement between the integrated local Chern marker and the pumped charge obtained from sufficiently slow time-dependent simulations. We stress that our work focuses on finite systems as they are realized in ultracold quantum gases. Recently, another form of the local Chern marker has been studied for odd dimensions by using an effective adiabatic propagator [57].

The analysis of the spatial dependence of the local Chern marker and its fluctuations around the bulk Chern number provides a useful quantitative measure for the topological transition. We argue that the integrated local Chern marker and the integrated current are the best suited to identify the transition point at which quantized charge pumping breaks down. In particular, the pumped charge, which is equivalent to the time-integrated current, can readily be accessed in cold-atom experiments [3,4,36].

Since most quantum-gas experiments measure an average over many one-dimensional realizations with varying disorder potentials, it is important to carefully analyze the full distribution of the relevant measures. We show that the disorder-average of the bulk gap overestimates the critical disorder strength, while the mode, the most likely value, agrees very well with the point at which the disorder-averaged measures for topological charge pumping start to deviate from integer values. This insight may be relevant for the analysis of experimental data [36] as well as of numerical studies of finite systems [50].

The plan of this exposition is the following. In Sec. II we introduce the Rice-Mele model and the types of disorder studied in this work. Section III discusses the set of measures used to characterize the quantized charge pumping. Our results are

presented in Sec. IV, where we discuss static measures and the results of time-dependent simulations. We conclude with a summary and a discussion in Sec. V. In the Appendix, we discuss results from an additional parameter set.

II. MODEL

The Rice-Mele model [58] describes a one-dimensional lattice system of spinless fermions with alternating hopping-matrix elements and a staggered on-site potential, illustrated schematically in Fig. 1(a). It can be written as

$$H = \sum_{j=0}^{L-1} [-J_j \hat{c}_j^\dagger \hat{c}_{j+1} + \text{H.c.} + V_j \hat{n}_j]. \quad (1)$$

Here j is the site index, $J_j = J[1 + (-1)^j \delta]$ is an alternating tunneling rate [with $J_j = J_1$ (J_2) for j even (odd)], and $V_j = (\frac{-1)^j \Delta}{2}$ is the on-site staggered potential. For simplicity we parametrize the alternating tunneling with the dimensionless dimerization parameter $\delta \in [-1, 1]$ and with $J = (J_1 + J_2)/2$ setting the energy scale. The strength of the staggered potential is given by Δ . The operator \hat{c}_j^\dagger creates a fermion on site j and $\hat{n}_j = \hat{c}_j^\dagger \hat{c}_j$. We use a smooth pumping scheme of the form

$$(\Delta/J, \delta) = (R_\Delta \sin \theta, R_\delta \cos \theta). \quad (2)$$

Note that at $\theta = 0(\pi)$ the SSH model is realized in its topological (trivial) phase.

We consider uniform, bounded diagonal disorder. An instance of random diagonal disorder results from a modification of the on-site potential:

$$V_j \rightarrow V_j + \epsilon_j. \quad (3)$$

Here ϵ_j is an energy drawn from the uniform distribution $\epsilon_j \in \frac{w}{2}[-1, 1]$, where w is the disorder strength.

III. METHODS AND OBSERVABLES

A. Polarization

To characterize the topological properties of a charge pump, one can consider the evolution of the many-body polarization $P(t)$ over the course of the adiabatic driving of a time-dependent Hamiltonian [52]. The integral over the time derivative of P yields the pumped charge:

$$\Delta Q = \int_0^{\Delta t} dt \partial_t P(t). \quad (4)$$

For a system with translational invariance, the polarization is usually formulated in terms of the cell-periodic part of the momentum eigenstates in the unit cell, here denoted by $|u(k)\rangle$, leading to

$$P = \frac{i}{2\pi} \int dk \langle u(k) | \partial_k u(k) \rangle. \quad (5)$$

In the case of a disordered system, the quasimomentum k is no longer a good quantum number and the topological invariants must be constructed in the position basis.

For a finite system with periodic boundary conditions, we use the exponentiated position operator, which is, following

Resta [59], given by $\hat{X}^e = \exp(i\frac{2\pi}{L}\hat{X})$. $\hat{X} = \sum_{j=1}^L j \hat{c}_j^\dagger \hat{c}_j$ is the total position operator. Then we obtain

$$P(t) = \frac{Qa}{2\pi} \text{Im} \ln \langle \Psi(t) | \hat{X}^e | \Psi(t) \rangle \pmod{Qa}, \quad (6)$$

where $|\Psi(t)\rangle$ is a many-body wave function. Importantly, P is only defined modulo Qa , which has units of a dipole moment, while a is the lattice spacing set to unity and Q symbolizes the charge. This expression for the many-body polarization reduces to the usual form for noninteracting fermions for a filled band [52,60–62].

For a many-body state, which is a Slater determinant composed of single-particle states ψ_i , the polarization can be written as

$$P(t) = \frac{Qa}{2\pi} \text{Im} \ln \det \Psi^\dagger e^{-i\frac{2\pi}{L}\hat{X}} \Psi. \quad (7)$$

Here $\Psi_{ij} = \psi_i(j)$ is different from the many-body wave function in Eq. (6), and $|\psi_i\rangle$ are the occupied single-particle states. The total transported charge ΔQ is related to the polarization via Eq. (4).

For a charge pump we see that the quantization of transported charge corresponds to the winding of the polarization. This winding is necessarily quantized, which seems like a contradiction, i.e., it seems to preclude nonquantized pumping. This can be reconciled by realizing that, for gapless states, the polarization becomes nonanalytic [20].

B. Local Chern marker

The local Chern marker [55] (LCM) is a local observable that can capture some aspects of topology from “local” (real-space) properties of a system. In the present work it is mainly used as a tool for computing the Chern number of inhomogeneous systems with periodic boundary conditions. Moreover, we will analyze the information contained in the spatial fluctuations of the local Chern marker $C(j)$. An alternative to the local Chern marker for the description of spatially inhomogeneous systems has recently been used in [36] using twisted boundary conditions.

We start from the expression for the Chern number of a spatially two-dimensional translational invariant system with a quasimomentum (k_x, k_y) ,

$$C = -\frac{1}{\pi} \text{Im} \int dk_x \int dk_y \sum_{p \in \mathcal{B}} \sum_{q \notin \mathcal{B}} \langle p, k_x, k_y | \partial_{k_x} | q, k_x, k_y \rangle \langle q, k_x, k_y | \partial_{k_y} | p, k_x, k_y \rangle, \quad (8)$$

where \mathcal{B} is a filled band, or set of occupied states. To arrive at a real-space representation, we need to identify the projection operators onto the occupied and unoccupied single-particle subspaces. Inserting a resolution of the identity by summing over an additional set of occupied single-particle states $|n, k_x, k_y\rangle$ yields (omitting k_x and k_y quantum numbers in the states $|n\rangle$ to avoid cluttering the formula)

$$C = -\frac{1}{\pi} \text{Im} \int dk_x \int dk_y \sum_{n \in \mathcal{B}} \sum_{p \in \mathcal{B}} \sum_{q \notin \mathcal{B}} \langle p | n \rangle \langle n | \partial_{k_x} | q \rangle \langle q | \partial_{k_y} | p \rangle. \quad (9)$$

By replacing the k_x integral with a sum over states, one can rewrite this as

$$C = -\frac{2}{L} \text{Im} \sum_{k_x} \int dk_y \sum_n \sum_{p \in \mathcal{B}} \sum_{p \notin \mathcal{B}} \langle p|n \rangle \langle n|\partial_{k_x}|q \rangle \langle q|\partial_{k_y}|p \rangle \quad (10)$$

$$= -\frac{2}{L} \int dk_y \text{Im Tr} [\hat{P} \partial_{k_x} \hat{Q} \partial_{k_y} \hat{P}], \quad (11)$$

where we use the cyclic property of the trace, and the trace is here expressed via

$$\text{Tr} \cdot = \sum_n \sum_{k_x} \langle n, k_x, k_y | \cdot | n, k_x, k_y \rangle \quad (12)$$

and

$$\begin{aligned} \partial_{k_y} \hat{P} &= \sum_{p \in \mathcal{B}} (\partial_{k_y} |p, k_x, k_y \rangle) \langle p, k_x, k_y | \\ &+ |p, k_x, k_y \rangle (\partial_{k_y} \langle p, k_x, k_y |). \end{aligned} \quad (13)$$

Here \hat{P} and $\hat{Q} = \mathbb{1} - \hat{P}$ are projection operators onto the occupied and unoccupied states, respectively. The local Chern marker $C(\mathbf{r})$ is found by inserting a complete set of basis states $|\mathbf{r}\rangle$ in the position basis:

$$C_{\text{LCM}} = -\frac{2}{L} \text{Im} \sum_{\mathbf{r}} C(\mathbf{r}) = \frac{2}{L} \text{Im} \sum_{\mathbf{r}} \langle \mathbf{r} | \hat{P} \partial_{k_x} \hat{Q} \partial_{k_y} \hat{P} | \mathbf{r} \rangle. \quad (14)$$

The result is the bulk Chern number C_{LCM} , where the subindex LCM indicates that it is computed from the local Chern marker. Equation (14) is the usual expression for the local Chern marker (by omitting the sum over \mathbf{r}) for a spatially inhomogeneous system in two spatial dimensions.

Using the correspondence for an adiabatic periodic system with pumping frequency Ω and a synthetic dimension, under which $\Omega t = \theta \leftrightarrow k_y$, we can find an analogous expression for a one-dimensional charge pump, starting from Eq. (11). However, as there is no analogous real-space operator for the time dimension, the derivative and integral with respect to time has to be computed explicitly while the trace over the site index j is omitted in Eq. (11):

$$C(j) = -\frac{2}{L} \text{Im} \int_0^{2\pi} d\theta \langle j | \hat{P} \partial_k \hat{Q} \partial_\theta \hat{P} | j \rangle. \quad (15)$$

For the k derivative we obtain, using the product rule,

$$\hat{P} (\partial_k \hat{Q}) = \partial_k (\hat{P} \hat{Q}) - (\partial_k \hat{P}) \hat{Q} = -(\partial_k \hat{P}) \hat{Q}, \quad (16)$$

since $\hat{P} \hat{Q} = 0$. For a finite system, the minimum quasimomentum difference is $dk = 2\pi/L$. Hence, we may replace the k derivative in Eq. (16) by the finite-difference form

$$\begin{aligned} (\partial_k \hat{P}) \hat{Q} &= \frac{\hat{P}(k+dk) - \hat{P}(k)}{dk} \hat{Q}(k) \\ &= \frac{\hat{P}(k+dk)}{dk} \hat{Q}(k) \\ &= \frac{L}{2\pi} \hat{X}^{e^\dagger} \hat{P}(k) \hat{X}^e \hat{Q}(k), \end{aligned} \quad (17)$$

where in the first line, $\hat{P} \hat{Q} = 0$ was used. In the second line, the exponential position operator $\hat{X}^e = \exp(i\frac{2\pi}{L} \hat{X})$ acts as the

generator of momentum translations of $dk = 2\pi/L$, which is applied from both sides to the operator $\hat{P}(k)$. Inserting Eqs. (16) and (17) into Eq. (15), we thus arrive at the LCM for a charge pump with periodic boundary conditions:

$$C(j) = \text{Im} \frac{1}{\pi} \int_0^{2\pi} d\theta \langle j | \hat{X}^{e^\dagger} \hat{P}(\theta) \hat{X}^e \hat{Q}(\theta) [\partial_\theta \hat{P}(\theta)] | j \rangle. \quad (18)$$

Translation-invariant systems (with periodic boundary conditions) will have a constant LCM. The introduction of disorder breaks the translational symmetry, leading to a fluctuating, position-dependent LCM. However, so long as the system has a band gap, the sum $C_{\text{LCM}} = \sum_j C(j)$ of the LCM is expected to be quantized.

In the case of a gapless system, the kernel of Eq. (18) is discontinuous. This leads to nonquantized values for C_{LCM} when the system is gapless, indicating a breakdown of quantized pumping.

To compute the local Chern marker, we use a discretized form with periodic boundary conditions. Using that $\hat{Q} \partial_\theta \hat{P} = \hat{Q} (\partial_\theta \hat{P}) \hat{P} = \lim_{d\theta \rightarrow 0} \hat{Q}(\theta) \hat{P}(\theta + d\theta) \hat{P}(\theta) / d\theta$, we arrive at

$$C(j) = \frac{1}{\pi} \sum_{n=0}^{N_\theta-1} \text{Im} \langle j | \hat{X}^{e^\dagger} \hat{P}(\theta_n) \hat{X}^e \hat{Q}(\theta_n) \hat{P}(\theta_{n+1}) \hat{P}(\theta_n) | j \rangle. \quad (19)$$

Here $\theta_n = 2\pi n/N_\theta$, and N_θ is the number of points in the discretization of θ with a step size $d\theta = \theta_{n+1} - \theta_n$.

Our numerical analysis shows that in the topological phase, this converges to a fixed value for $C(j)$ as $d\theta$ is decreased. The projector $\hat{P}(\theta)$ is not necessarily continuous. However, the integral over this function is well defined and converges with decreasing $d\theta$. The sum $C_{\text{LCM}} := \sum_j C(j)$ yields the Chern number for a translationally invariant system as our discussion shows.

In the simulations we use $d\theta/2\pi = 10^{-3}$ which gives a Chern number which is quantized with an accuracy of $1 - C_{\text{LCM}} = \pm 10^{-4}$ at $w = 0$ and for individual realizations for $w/J \lesssim 2$, which is shown in Fig. 2. In the trivial phase at $w/J > 3$, a sizable dependence on $d\theta$ of the LCM can persist even up to $d\theta/2\pi = 10^{-5}$ for individual realizations (data not shown). This can lead to a smaller accuracy of 10^{-1} . Therefore, the quantitative results for the LCM in the trivial phase are less reliable for single disorder realizations. However, due to the disorder average, the mean of the integrated LCM $\overline{C_{\text{LCM}}}$ is two orders of magnitude more reliable when compared to single realizations.

We will apply this approach to inhomogeneous systems in this work and the results and comparison with other measures will lead to consistent results for integer quantization of C_{LCM} in the topological phase.

C. Entanglement spectrum

The entanglement spectrum is given by the eigenvalues of the entanglement Hamiltonian \hat{H}_E and can be defined with the reduced density matrix $\hat{\rho}_A$ of a spatial bipartition of the system into two halves (A and B) [63]:

$$\frac{1}{Z} \hat{\rho}_A = e^{-\hat{H}_E}. \quad (20)$$

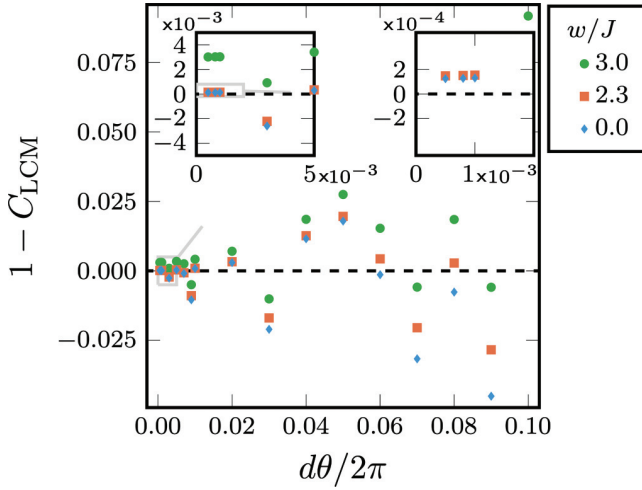


FIG. 2. Convergence of the integrated local Chern marker. Main panel: LCM calculated for a single disorder realization as a function of discretization $d\theta/2\pi$ in the sum in Eq. (19) for $L = 400$ and for $w/J = 0, 2.3, 3$ (colors). The dashed line indicates a perfect quantization of the Chern number of 1. Insets: Left: Zoom into the main panel for small discretizations. Right: Further zoom, showing the region of convergence beyond $d\theta/2\pi = 1 \times 10^{-3}$.

\hat{H}_E is a dimensionless free-fermion operator that is strictly positive due to the normalization requirement of the reduced density matrix $\hat{\rho}_A$. The entanglement eigenvalues (EEVs) are the eigenvalues of \hat{H}_E . The EEVs $-\ln\Lambda_\mu^2$ are related to the Schmidt values Λ_μ that are found in a Schmidt decomposition of the two halves of the system. We can compute these values of the free-fermion Hamiltonian directly from the reduced density matrix, which can be obtained from the single-particle correlation matrix $C_{ij} = \langle \hat{c}_i^\dagger \hat{c}_j \rangle$ computed in the many-body ground state, as described by Peschel [64]. Writing \hat{H}_E in its single-particle eigenbasis, $\hat{H}_E = \sum_{\alpha=1}^L \epsilon_\alpha \hat{d}_\alpha^\dagger \hat{d}_\alpha$, the partition function is $Z = \prod_{\alpha=1}^L \frac{1}{1+e^{-\epsilon_\alpha}}$. The eigenvalues Λ_μ^2 in the full many-body space of the reduced density matrix $\hat{\rho}_A$ result from fixing a set of occupations $\mathbf{n} = \{n_\alpha\}$. Every choice for these occupations corresponds to a many-body state $|\mu\rangle$ indexed by μ . They are given by

$$-\ln(\Lambda_\mu^2) = \sum_{\alpha=1}^L [-\ln(v_\alpha)n_\alpha - \ln(1-v_\alpha)(1-n_\alpha)], \quad (21)$$

where v_α are the eigenvalues of the single-particle correlation matrix $\langle \hat{c}_i^\dagger \hat{c}_j \rangle$ when i, j are restricted to one half of the system. As the states are all localized for finite disorder, the entanglement across one cut in the system is independent of the boundary conditions for a sufficiently large system. The same is true for zero disorder due to translational invariance.

The eigenvalues v_α are symmetrically spread around 0.5 and the low-lying eigenstates of the entanglement Hamiltonian are strongly localized at the chosen cut, see [64]. We assign a particle-number imbalance ΔN_μ to a state defined by \mathbf{n} as follows: Focusing on the states of the correlation matrix (when restricted to a subsystem) localized on the left side of the subsystem, eigenvalues $v_\alpha < 0.5$ (> 0.5) correspond to states on the left (right) side of the cut and are assigned a label

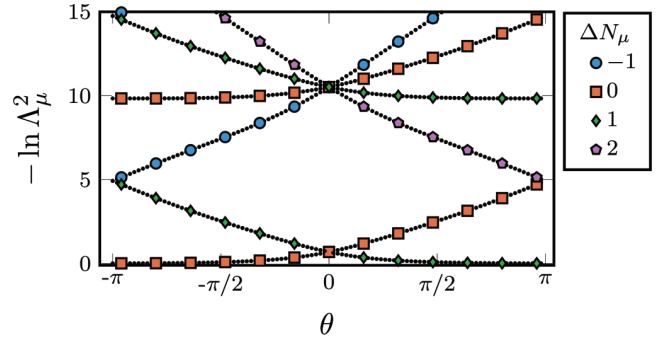


FIG. 3. Entanglement spectrum of the Rice-Mele model. We plot the entanglement eigenvalues $-\ln\Lambda_\mu^2$, where Λ_μ are the corresponding Schmidt values, versus the pump parameter θ . Results for the pump cycle with $R_\delta = 0.5$, $R_\Delta = 2.3$, and no disorder, calculated from the free-fermion solution for $L = 400$ (see also [11]). The spectra are in general unbounded, but here we only show the lowest few eigenvalues, which, in general, contain the important topological information [63]. The labels ΔN_μ (indicated by markers on every eighth data point) correspond to the particle imbalance for each entanglement eigenvalue. Notice that entanglement eigenvalues in the spectrum wind either up or down or have no winding if $\Delta N_\mu = \Delta N_0$, where ΔN_0 is the lowest eigenvalue per cycle. After one cycle, the spectrum has the same values, but with all labels increased by 1 (which occurs at $\theta = 0$), indicating the pumping of a single charge.

$N_\alpha = -1$ ($+1$). In order to calculate particle imbalances of the full many-body spectrum of $\hat{\rho}_A$, states on the left (right) side of the cut are counted as unoccupied (occupied) in Eq. (21), which is then evaluated for all possible occupations \mathbf{n} . The total particle imbalance of the many-body state $|\mu\rangle$ is

$$\Delta N_\mu = \sum_{\alpha=1}^L N_\alpha n_\alpha. \quad (22)$$

The imbalance $\Delta N_0 = 0$ is assigned to the unique lowest EEV ($\mu = 0$) for $\theta \in (-2\pi, 0)$.

Figure 3 shows the entanglement spectrum of the clean system ($w/J = 0$) over the course of one pump cycle ($R_\delta = 0.5$, $R_\Delta = 2.3$) [11]. Under an adiabatic modulation of the pumping parameters, the entanglement spectrum shows a continuous flow as long as the system is gapped. As was discussed in [11], the spectral flow and its nontrivial winding structure is a hallmark of the topological nature of the charge pump. After one pump cycle, the spectrum returns to itself but the particle imbalances ΔN_μ increase by 1, indicating the pumping of one charge across the system. For instance, the state $|\mu = 0\rangle$ with the largest eigenvalue increases its particle imbalance by one (see Fig. 3 at $\theta = 0$). The multifold degeneracy of the entanglement spectrum at $\theta = 0$ is a result of the chiral symmetry protecting the topological phase of the SSH model.

D. Time-integrated current

A time dependence is introduced in Eq. (2) by parametrizing the pump parameter $\theta = \theta(t) = 2\pi t/T$ with time. We drive periodically with a period T by propagating all single-particle states of the lower half of the spectrum via the Crank-Nicholson method (see Sec. III E).

For the Rice-Mele model, the total current operator is given by

$$\hat{J} = i \sum_{j=1}^L (J_j \hat{c}_j^\dagger \hat{c}_{j+1} - \text{H.c.}), \quad (23)$$

identifying the $(L + 1)$ th with the first site, realizing periodic boundary conditions. In praxis, we compute $\langle \hat{J} \rangle / L$, which should yield $\Delta Q = 1$ when integrated over one pump cycle. This is a physical quantity that allows us to connect to experiments. The expectation value of the ground-state current is identically zero. The quantized pumping arises from the virtual admixtures into the higher bands, which are proportional to $O(1/T)$, where T is the pump period. In this way the integrated current over one pump cycle converges to a constant in the $T \gg J$ limit.

The effect of nonadiabatic pumping has been studied in several works, see, e.g., [65,66]. For sufficiently slow pumps, it has been shown that the corrections to the exact quantization scale according to $O(1/T^2)$ [65].

E. Numerical methods

For the static calculations we directly diagonalize the single-particle Hamiltonian at each θ . For the discretization of the LCM we take $d_\theta / 2\pi = 10^{-4}$. For the real-time simulations we propagate all single-particle eigenstates of $\hat{H}(t = 0)$ that are populated at half-filling. The propagator is approximated for each time t via the Crank-Nicholson method (see, e.g., [67] and references therein)

$$\hat{U}(t, dt) = (1 + i\hat{H}(t)dt/2)^{-1} (1 - i\hat{H}(t)dt/2) + \mathcal{O}(dt^3), \quad (24)$$

with a time step of $dtJ = 0.05$. The full propagator then reads $\hat{U}(T) = \prod_{t_s} \hat{U}(t_s, dt)$ with $t_s = dt s$, $s \in 0, 1, \dots, T/dt$.

IV. RESULTS

In the main text all calculations are carried out using the parameters $(R_\delta = 0.5, R_\Delta = 2.3)$. In the Appendix a subset of the calculations have been carried out using the parameters from [50]. A comparison between both parameter sets yields no discernible change in the critical disorder strength.

A. Energy spectra

We will compare our measures for the topological properties to the spectral properties of the static Hamiltonians of the charge pump. The common notion is that the topological invariant cannot change while the spectral bulk gap persists as w increases. The single-particle spectrum for $(R_\delta = 0.5, R_\Delta = 2.3)$ is shown in Fig. 4 for various points along the pump cycle for a single disorder realization. For this realization we see a gap closing at $w/J \approx 3.14$ and $\theta = 0$. The color indicates the Chern number C_{LCM} of each band calculated via the integrated local Chern marker at half-filling (see Secs. III B and IV E). As long as the bands are clearly separated, C_{LCM} is quantized.

The gap closing can occur at any point in the pump cycle. Relevant information about a topological breakdown is

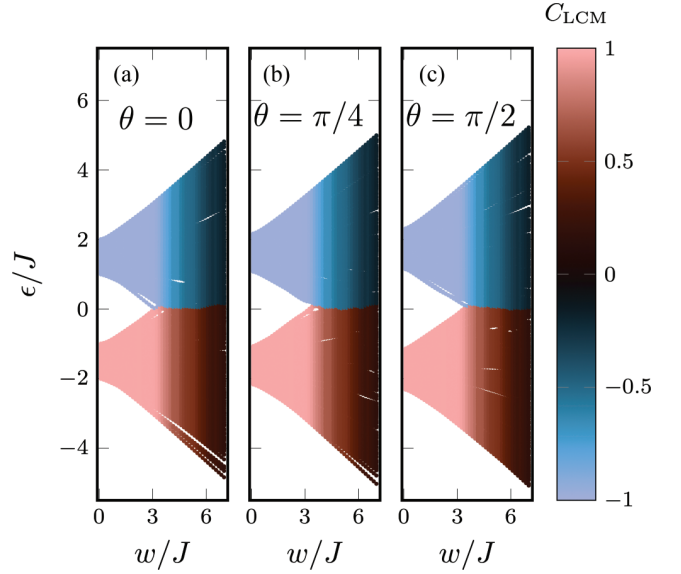


FIG. 4. Spectrum of the disordered Rice-Mele model for periodic boundary conditions as a function of increasing disorder strength. We plot the spectrum for a single disorder realization for $L = 400$ and for three values of the pump angle θ . The bands are colored based on C_{LCM} at half-filling. Edge states do not appear, due to the use of periodic boundary conditions.

therefore encoded in the minimum gap over the entire pump cycle:

$$\Delta \epsilon_{\min} := \min_{\theta} \Delta \epsilon(\theta) / J. \quad (25)$$

Figure 5 shows the distribution of the minimum gap over $n = 500$ disorder realizations for $w/J = 2, 2.75, 2.95, 3.3, 4.45$. For $w/J = 2, 2.75$, the distributions are symmetric and their mean is a meaningful quantity. For $w/J = 2.95$, most realizations have a minimum gap of zero, which leads to a transition to exponential distributions from this point onward. These distributions have a maximally likely value, the mode, of the minimum gap of zero. The transition to an exponential distribution is exemplified by the insets in Fig. 5(a). Notice that in the insets, different bin sizes are used. In Fig. 5(b) we show the minimum gap as a function of disorder strength w/J . Black dots indicate single realizations. The red circles and blue ribbon denote the mean and standard deviation over all realizations, respectively. The orange diamonds show the mode of the minimum gap distributions. For every w we use a different disorder seed to generate the on-site potentials to preempt a dependence on single realizations. While the mean gap closes gradually at around $w/J \approx 3.25$, the mode of the gap shows a very sharp transition to zero at $w/J = 2.95$. We argue that the mode and not the mean gap is a meaningful quantity to predict the topological transition of the local Chern marker and the pumped charge, which will be substantiated in Sec. IV G.

Since the single-particle gap of the clean system at $\theta = \pi/2$ is Δ , there is, in principle, a disorder realization for which the gap closes at that point for $w \geq \Delta$, where the disorder realization is exactly the (oppositely) staggered potential with strength $-\Delta$. A single, individual realization, however, has measure zero and hence is expected to become irrelevant in

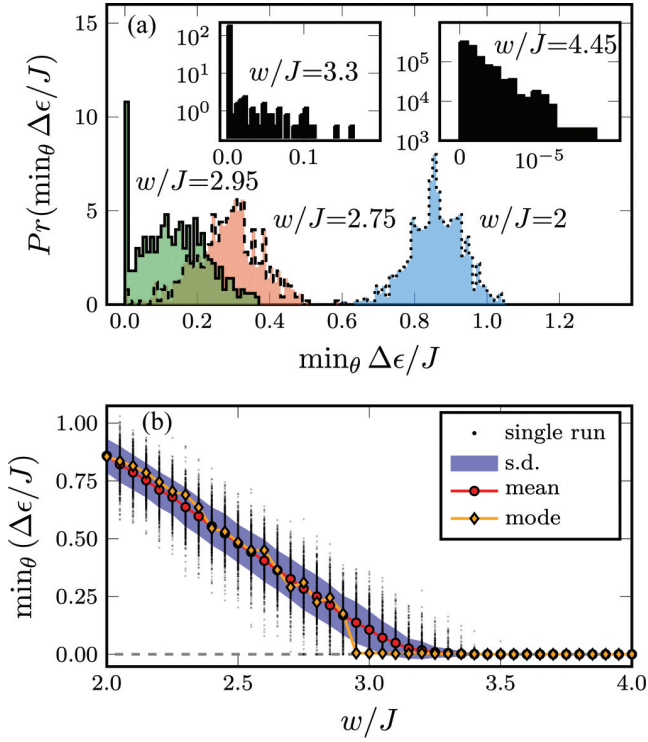


FIG. 5. Energy gap for diagonal disorder. (a) Main panel: Distribution of the minimum energy gap along the pump cycle $\min_\theta \Delta\epsilon/J$, for $w/J = 2, 2.75, 2.95$ over $n = 500$ disorder samples. The most likely value, the mode, for the minimum gap becomes zero at around $w/J \approx 2.95$. Insets: Minimum gap distributions for $w/J = 3.3, 4.45$, and smaller bin sizes. (b) We show the magnitude of the bulk gap as a function of w/J . We plot the minimum value found along the whole pump cycle. The red circles and shaded region correspond to the mean and the standard deviation, respectively, computed for $L = 400$. The orange diamonds indicate the mode, which vanishes at $w/J \approx 2.95$. We use a linear θ grid of $d\theta/2\pi = 0.0001$ that determines the accuracy of finding the minimum gap in a given realization. The dashed line corresponds to a vanishing gap.

the thermodynamic limit and for the disorder average over finite systems.

The minimum band gap in the absence of disorder is $\Delta\epsilon = 2J$ at $\theta = 0$ for the chosen cycle and parameters used in this paper, whereas the critical disorder strength needed to close the mode is $w/J = 2.95$. This illustrates that the disorder strength can in fact exceed the gap width of the single-particle spectrum without spoiling the quantized pumping behavior.

B. Localization of single-particle states

To demonstrate that our numerically simulated system sizes are sufficient to capture the localized nature of the single-particle states, we compute the inverse participation ratio. Full localization at any $w > 0$ is the expected behavior in one dimension for random diagonal disorder [68].

The inverse participation ratio I is a means of quantifying the degree of localization for a state:

$$I(|\psi\rangle) = \frac{\sum_i |\langle\psi|i\rangle|^4}{\langle\psi|\psi\rangle}. \quad (26)$$

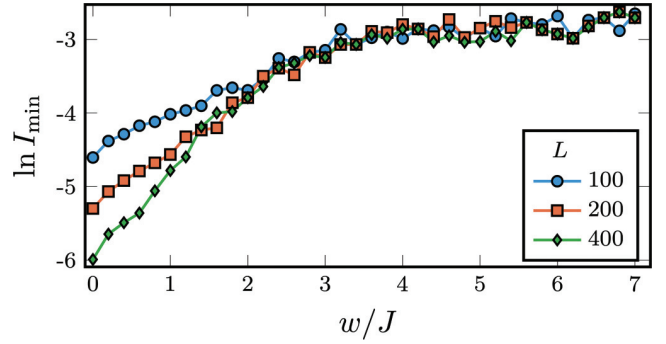


FIG. 6. Minimum inverse participation ratio I_{\min} for diagonal disorder. We take the minimum IPR over θ and over 40 disorder realizations as a function of w , for various system sizes. At $w/J \approx 1.5$, I_{\min} becomes independent of system size for systems $L \geq 400$, indicating that all single-particle states are localized with a localization length much smaller than system size.

Here I is calculated in the real-space basis, where $|\psi\rangle$ is a single-particle eigenstate and $\langle\psi|i\rangle$ is the amplitude on a site i . For a completely localized state that has weight on only one site $I = 1$, whereas for a totally delocalized one $I = 1/L$, where L is the system size.

Figure 6 shows the minimum value $I_{\min} := \min_{\theta,s} I$ of the entire spectrum over one pump cycle and over all given disorder realizations indexed by s , corresponding to the most delocalized state. The observed behavior is compatible with the expectation of all states being localized for any finite disorder strength. At low disorder there are states which appear delocalized across the entire system because of the localization length exceeding the system size, indicated by the L dependence of I_{\min} . At higher disorder strengths, the maximally delocalized state is quite short ranged, with a length scale that is much shorter than the system length.

For all finite w , I_{\min} is much larger than $1/L$, which is the typical value for a fully delocalized state. For $w/J > 1.5$, I_{\min} is no longer dependent on system size for $L = 400$, indicating a localization length much shorter than system size. Crucially, even in this region, quantized pumping is still possible on finite systems and for the disorder average, which will be shown below. This agrees with the analysis of [50], where the breakdown of quantized pumping has been linked to a delocalization-localization transition of Floquet eigenstates, which occurs deep in the regime of localized single-particle Hamiltonian eigenstates.

C. Entanglement spectrum

Disorder in the on-site potentials breaks the chiral symmetry at $\theta = 0, \pi$ which lead to the topological and the trivial phase of the SSH model, respectively. We see in Figs. 7(a) and 7(b) that, for small disorder, the entanglement spectrum is perturbed as w becomes finite, but the topological winding structure of the states is preserved. The degeneracies in the entanglement spectrum persist at weak disorder yet, since chiral symmetry is broken, they are shifted to arbitrary positions along the pump cycle, depending on the specific disorder realization. At large disorder strength, there are discontinuities in the entanglement spectrum as exemplified by the data in

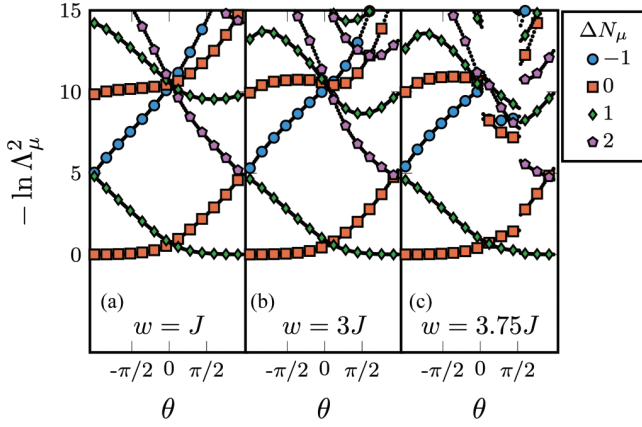


FIG. 7. Entanglement spectrum for diagonal disorder for several disorder strengths versus pump parameter θ . (a) $w = J$, (b) $w = 3J$, (c) $w = 3.75J$, computed for $L = 400$ sites. We show data for one fixed disorder configuration and vary w . ΔN_μ (markers drawn on every eighth data point) are the particle imbalances for each entanglement eigenvalue $-\ln \Lambda_\mu^2$. Λ_μ is the corresponding Schmidt value.

Fig. 7(c). These signal the breakdown of quantized charge pumping. The position and number of these discontinuities is highly dependent on the particular disorder realization chosen. Therefore, from the entanglement spectrum, it is more cumbersome to extract the exact transition at the breakdown of the quantized pumping than for other measures discussed here.

D. Polarization

Figures 8 and 9 show data for the polarization P , calculated via Eq. (7) for $n = 40$ disorder realizations as a function of the pump parameter $\theta \in [0, 2\pi)$ for various disorder strengths. Due to P being defined modulo 2π , it is convenient to use a polar plot with P being the angular variable and θ being the radial one. In fact, this is a natural representation, as the P values lie on a circle.

In earlier works, the polarization has been utilized with open boundary conditions and directly linked with bulk-boundary correspondence [20]. Here we employ periodic boundaries. First, we discuss the conventional way of plotting P as a function of θ , which is seen in Fig. 8. Complications arise due to the disorder when performing naive disorder averages: For $w/J = 2.8$, the polarization for each sample shows a 2π discontinuity that stems from the definition of the polarization. These 2π discontinuities lie near $\theta = \pi/2$, the exact position of which is slightly shifted due to disorder. This leads to a mean polarization that is close to zero [see Fig. 8(a) around $\theta = \pi/2$]. Physically relevant discontinuities due to gap closings appear around $\theta = 0$, or wherever the first gap closing occurs along the pump cycle. Ideally, in the disorder average, the 2π discontinuities should not lead to a discontinuity in the mean (red dots), which, however, is the case here. For $w/J = 3.2, 3.4$, this issue is amplified, as additional 2π discontinuities appear for various θ . Due to these 2π discontinuities, the naive disorder averaged polarization appears more continuous than it should [see Fig. 8(c) between $\theta = 3\pi/2$ and $\theta = 2\pi$].

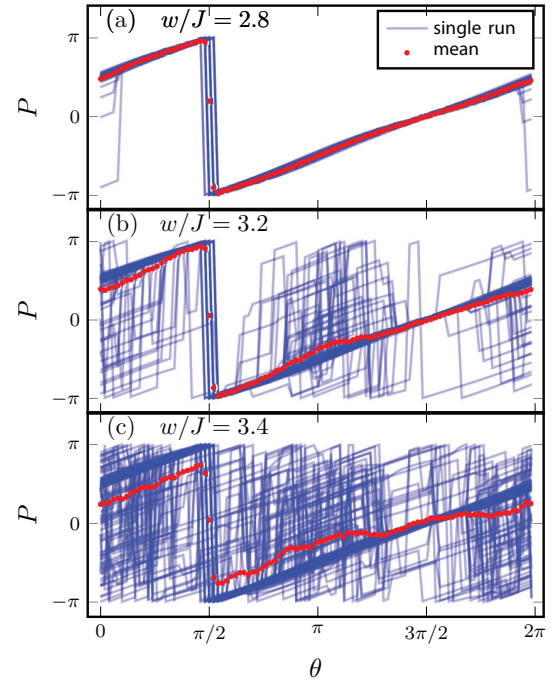


FIG. 8. Polarization P versus pump parameter for diagonal disorder. For each value of the disorder strength w , we show the polarization for 40 disorder realizations as a function of the pump parameter θ for $L = 400$. 2π discontinuities appear near $\theta = \pi/2$ for $w/J = 2.8$ which lead to discontinuities in the mean. For $w/J = 3.2$ and $w/J = 3.4$, the 2π discontinuities appear at various points along the pump cycle, which leads to an apparent but misleading continuous mean polarization.

Plotting P as an angular variable instead, as in Fig. 9, circumvents this problem, as points near π and $-\pi$ are close to each other. The colored dots show the circular mean

$$\bar{P}(\theta) = \text{atan2} \left(\frac{1}{n} \sum_{j=1}^n \sin P(\theta)_j, \frac{1}{n} \sum_{j=1}^n \cos P(\theta)_j \right), \quad (27)$$

which is the natural averaging procedure for points on a circle, for each pumping time θ , where atan2 is the two-argument arctangent. Single realizations are shown as blue lines. For low disorder strengths, all realizations lie on top of each other and the circular mean exhibits a smooth dependence on θ with winding 1. From $w/J = 2.8$ onward, some realizations display discontinuities as indicated by the jumps in the blue lines. At $w/J = 2.8$, only a few realizations have such jumps, whereas for $w/J = 3.4$, almost all polarizations are discontinuous, with individual realizations showing multiple discontinuities of arbitrary size. The circular mean becomes visually discontinuous around $w/J \approx 3$, indicating that the quantization breaks down in a large number of realizations. Comparing the regular mean to the circular mean in Figs. 8(c) and 8(e) show that the former exhibits no such discontinuities except the trivial one at $\theta = \pi/2$. We associate these discontinuities in the circular mean with the breakdown of quantized charge pumping. In this case, the winding number of the polarization is ill-defined: It is impossible to know whether the jump in the polarization is clockwise or counterclockwise for

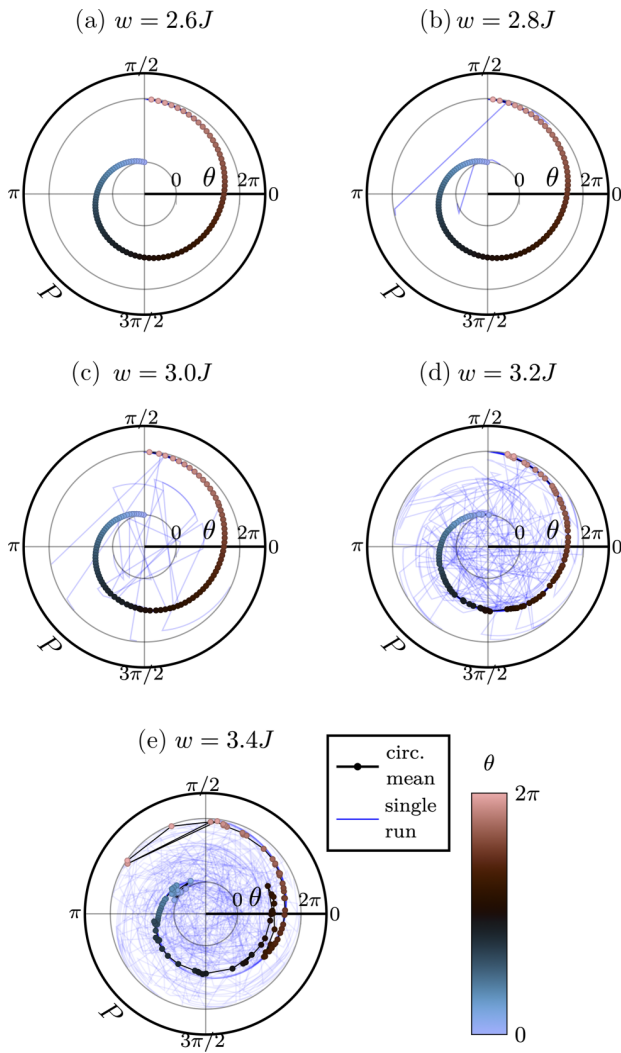


FIG. 9. Polarization P versus pump parameter for diagonal disorder. For each value of the disorder strength w , we show the polarization as an angular variable for 40 disorder realizations against the pump parameter θ for $L = 400$.

single realizations. Despite this fact, the circular mean retains a sense of direction in its winding and winds around exactly once, meaning that on average, charge is transported across the system in a well-defined direction. For a topologically trivial pump cycle, the circular mean shows no winding, as expected (data not shown). This suggests that the circular mean of the polarization still preserves information on the quantized pumping inherited from the neighboring topological phase even beyond the critical disorder strength.

E. Chern number from integrated local Chern marker

Local Chern marker and its fluctuations. The local Chern marker $C(j)$ is shown for $w/J = 2, 3, 3.6$ in Figs. 10(a)–10(c) for a single disorder realization. For zero disorder (data not shown here), the local Chern marker is $C(j) = 1/L$ (within our numerical accuracy) as expected. As w increases, fluctuations around this value emerge and increase as w grows. For $w/J = 3.6$, integer quantization clearly no longer holds.

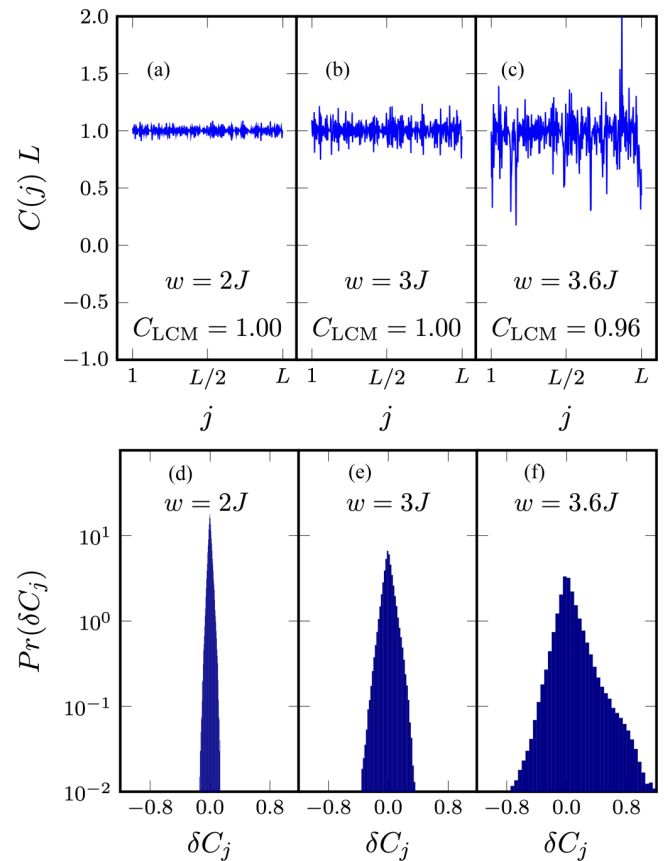


FIG. 10. Local Chern marker. (a)–(c) $C(j)L$ versus position j for a single realization of diagonal disorder and for disorder strengths (a) $w = 2J$, $C_{\text{LCM}} = 1.00$, (b) $w = 3J$, $C_{\text{LCM}} = 1.00$, and (c) $w = 3.6J$, $C_{\text{LCM}} = 0.97$, computed for $L = 400$. (d)–(f) Normalized distribution of local Chern-marker fluctuations $\delta C(j) = 1 - C(j)L$ for (d) $w = 2J$, (e) $w = 3J$, and (f) $w = 3.6J$ from 500 disorder realizations for $L = 400$. Note that the distribution in (f) is slightly skewed towards positive values, see Fig. 11.

We next demonstrate that the spatial fluctuations of the local Chern marker defined via

$$\delta C(j) = 1 - C(j)L \quad (28)$$

contain relevant information and can be used to pinpoint the transition. A local Chern marker $LC(j) > 1$ [$\delta LC(j) < 0$] implies that an excess amount of charge crosses site j per pump cycle, while for $LC(j) < 1$ [$\delta LC(j) > 0$] a lesser amount moves through. In order for the system to possess an integer-quantized Chern number, these fluctuations have to cancel out after summing over the whole sample. Our analysis shows that this happens for individual realizations in the topological regime.

The respective distributions of $\delta C(j)$ obtained from $n = 500$ disorder configurations are plotted in Figs. 10(d) and 10(f). In the topological regime [see Fig. 10(d)], $\text{Pr}[\delta C(j)]$ is symmetric and sharply peaked around zero, while the variance gradually increases as the transition point is approached. For $w = 3.6J$, the distribution becomes skewed towards $\delta C(j) > 0$. In order to determine the breakdown of the quantized pumping, we compute the skewness γ of the

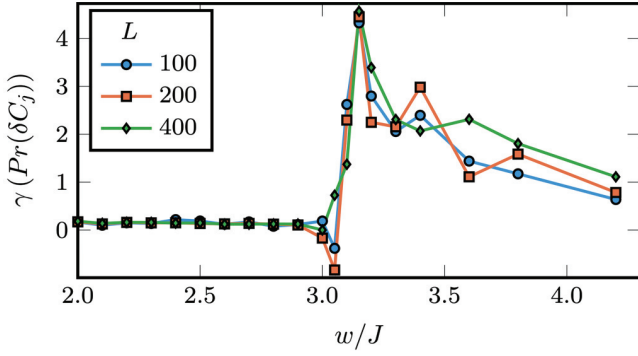


FIG. 11. Transition from distributions of local Chern marker fluctuations. Skewness γ of the distribution of local Chern number fluctuations $\text{Pr}[\delta C(j)]$ versus disorder strength for $L = 100, 200, 400$. Computed from 500 disorder realizations for $w/J \geq 3$ and from 100 realizations for $w/J < 3$.

distributions from

$$\gamma = \frac{\frac{1}{nL} \sum_{i=1}^{nL} (x_i - \bar{x})^3}{[\frac{1}{nL} \sum_{i=1}^{nL} (x_i - \bar{x})^2]^{3/2}}, \quad (29)$$

with x_i being $C(j)$ computed for a given disorder realization. The dependence of γ on the disorder strength is shown in Fig. 11 for $L = 100, 200, 400$. Remarkably, the skewness exhibits a strong signature at the transition: on small systems it first decreases but then sharply increases. The best estimate from our available data for the transition point is $w/J = 3.0$. There is no detectable L dependence for the transition point for the system sizes considered here within the used grid of $\Delta w = 0.1J$ around the transition region. The nonzero skewness can be understood as follows. As the gap closes, states from the original bands will mix with those of the lower bands, mixing in a tendency of an opposite charge transport. Since the states are localized due to disorder, this occurs locally, and results in a deficit of $C(j)$ and hence locally larger values of $\delta C(j)$, without changing the mode of the $\delta C(j)$ distributions. We conclude that the analysis of the full distribution of local Chern marker fluctuations and of its moments is very useful to obtain a quantitative picture of the breakdown, as will be substantiated by the following comparison with the pumped charge from the time-integrated current.

Integrated local Chern marker and breakdown of quantized pumping. Figure 12 shows the breakdown of the quantized integrated local Chern marker as a function of w for different system sizes L . Black dots indicate single realizations. The red line and the blue shaded region are the disorder averages and standard deviation, respectively.

The sum

$$C_{\text{LCM}} = \sum_j C(j) \quad (30)$$

and thus the total Chern number remains quantized up to $w \approx 2.3J$ within our numerical accuracy, while for larger values $2.3J < w \lesssim 3J$, C_{LCM} starts to slowly decrease, due to rare realizations without exact quantization. An interesting question concerns the system-size scaling of the mean Chern number in the transition region (see the discussion and further references in [54]). Since our work is concerned with the properties of ensembles of finite-size systems as realized

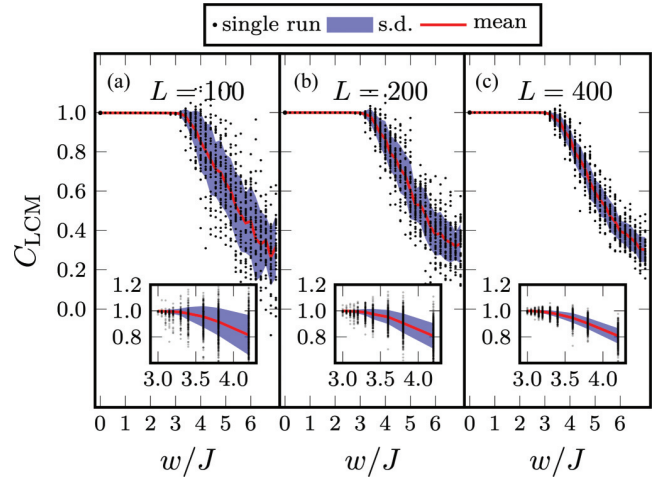


FIG. 12. Sum C_{LCM} of the local Chern marker C_{LCM} for diagonal disorder as a function of w . (a) $L = 100$, (b) $L = 200$, (c) $L = 400$. Main panel: 40 samples at each disorder strength. Insets: Zoom into the transition region with 500 samples. The red line indicates the mean value for each disorder strength and the standard deviation is represented by the shaded region.

in quantum-gas experiments, we do not further pursue this direction and leave this for future research. We further note that finite-size corrections for the pumped charge were studied in [69].

At strong disorder $w/J \gtrsim 3$, the system becomes gapless and hence the Chern number is ill-defined. We therefore expect a breakdown of the quantized charge pumping supported by the data. Nevertheless, C_{LCM} still spreads around a central mean value over all realizations. This mean value, however, starts to deviate from $C_{\text{LCM}} = 1$ and indicates the breakdown of the quantization of the charge pump. The fluctuations around this mean value decrease as L increases. Note that the standard deviation around the disorder-averaged Chern number \bar{C}_{LCM} increases just at the point where C_{LCM} ceases to be quantized.

For single realizations, the notion that a topological quantity cannot change without a gap closing is confirmed, which is shown in Fig. 13. We plot the integrated local Chern marker C_{LCM} versus the minimum gap $\min_{\theta} \Delta \epsilon$ for each realization and different disorder strengths. Points on the left with $\min_{\theta} \Delta \epsilon / J \lesssim 10^{-5}$ indicate realizations that close the energy gap, with a minimum gap size that scales with the θ -grid size used for calculating the energy. The C_{LCM} for these realizations exhibits noninteger values with a spread that increases for larger w/J . The points on the right side of the figure correspond to realizations that do not close the gap and have an integer-quantized C_{LCM} . Their minimum gap is invariant under the θ -grid size used for the energy search. For large w/J , the ratio of gap-closing realizations increases sharply. We thus conclude that the breakdown of topological charge pumping on *finite* systems occurs due to sufficiently many individual realizations acquiring close-to-zero gaps well before the mean (disorder-averaged) minimum gap closes. This scenario applies to the finite-size quantum-gas experiments where typically $L \sim 100$ and averages over many one-dimensional systems are measured.

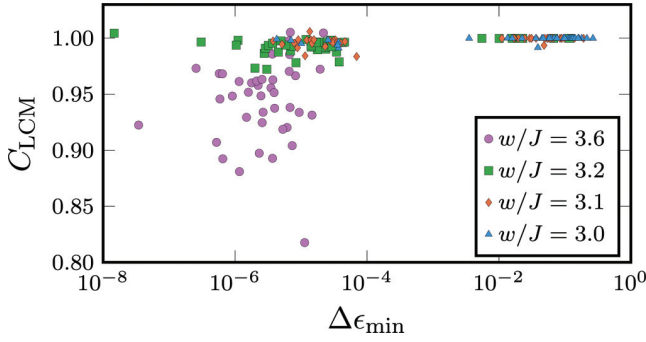


FIG. 13. Correlation between C_{LCM} and energy gap. We compare C_{LCM} to the minimum global energy gap for 40 disorder realizations for each value of w . We see that realizations with nonquantized C_{LCM} lie in the vicinity of vanishing energy gaps that are of the order of 10^{-6} in the chosen θ grid for the energy calculation. These points shift to the left when refining the θ grid, whereas points on the right remain unchanged (not shown). The spread of C_{LCM} increases for increasing w . The two outliers on the right side are atypical realizations with poor convergence for the LCM. All data computed for $L = 400$.

F. Time-dependent case and integrated current

In this section we study the dependence of the time-integrated current Eq. (23) on the finite period of the pump cycle.

In the adiabatic limit, any finite system will ultimately have an exactly quantized integrated current, as the system is gapped. However, the gaps in some systems may become exponentially small in the system size. On the other hand, a finite period T can lead to nonquantized behavior due to Landau-Zener tunneling [65], even in the presence of a band gap.

We first discuss the evolution of the time-dependent current as a function of time, for various periods T (data not shown here). For $T/J = 10$, the pumped charge per period is never quantized, due to nonadiabatic excitations to the second band. The quantization of the pumped charge sets in at $T/J = 100$ for large values of w in the vicinity of $w = 3J$. For such a slow driving, pumping below the critical disorder strength $w/J \approx 3$ leads to quantized particle pumping. Beyond that disorder strength, the pumped charge ceases to be quantized.

In Fig. 14 we show the distribution of the pumped charge, calculated from the time-integrated current over 500 disorder realizations and for various pumping periods T . For $T = 10J$, the pumped charge is not quantized, presumably due to Landau-Zener tunneling into the second band. For $T = 100J$ and $T = 1000J$, the average pumped charge is similar to what has been found for the Chern number computed via the LCM. Quantization breaks down at the critical disorder strength $w/J \approx 3$.

G. Comparison between instantaneous and time-dependent measures

Figure 15 shows a comparison between the disorder average of the minimum energy gap, the deviation of C_{LCM} from $C = 1$, the skewness of local Chern marker distribu-

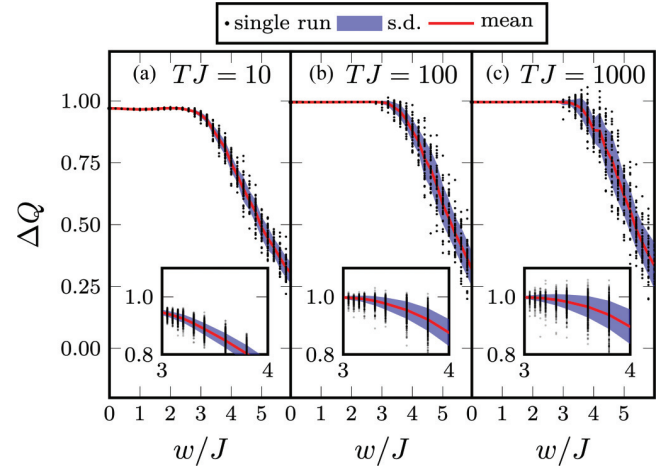


FIG. 14. Distribution of pumped charge computed from the time-integrated current as a function of disorder strength. Computed for a number of period lengths T . Main plots: $n = 40$ samples for each disorder point and time-step $dtJ = 0.1$. Insets: Transition region computed for $n = 500$ realizations and $dtJ = 0.05$ ($L = 400$).

tions, and the time-integrated local current as a function of w/J . We have also studied the parameters from [50] using the integrated local Chern marker and consistently observe a breakdown at $w/J \approx 3$, in agreement with [50].

Interestingly, the pumped charge ΔQ obtained from the time-dependent simulations and C_{LCM} are very similar to each other even in the trivial regime. This should be taken with some caution, due to the aforementioned numerical difficulty of obtaining converged results from the local Chern marker in the trivial regime for individual realizations (see Sec. III B).

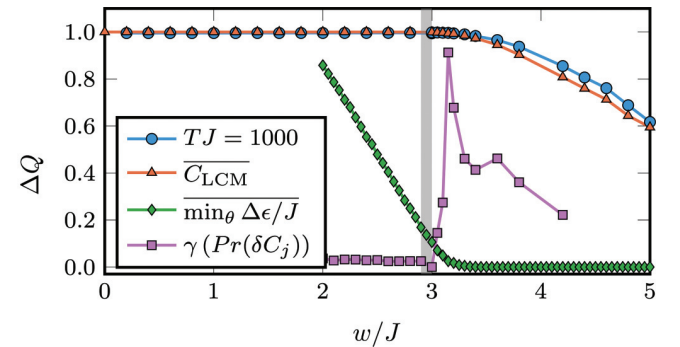


FIG. 15. Comparison of different measures for the pumped charge. We compare C_{LCM} , the average pumped charge computed from the time-integrated current as a function of disorder strength, the mean minimum gap found along the pump cycle, and the skewness of LCM distributions. The skewness has been scaled down for better visibility. The shaded region indicates the point where the mode of the minimum gap along the pump cycle closes at $w/J \approx 2.95 \pm 0.05$. Similar results were obtained in [50] from Floquet states for different parameters. At larger values of $w \gg 8J$, one finds $C = 0$ [50]. Computed for a pump period of $T = 1000J$. $n = 500$ ($n = 40$) samples were included in the average for each value of w/J for $3 < w/J < 4.2$ ($w/J \leq 3$, $w/J \geq 4.2$), $L = 400$.

We stress that the breakdown of the Chern number quantization occurs at $w/J \approx 3$, whereas the mean minimum gap closes at $w/J \approx 3.3$, while the observed breakdown of integer quantization of C_{LCM} and the pumped charge ΔQ agrees well with the closing of the typical value of the gap, the mode (vertical shaded region). This value also agrees well with the onset of a significant skewness γ in the distribution of local Chern markers. These observations further support our assertion that the most likely gap, rather than the disorder-averaged gap, should be considered when quantifying the transition point.

In conclusion, all three quantities computed in the instantaneous basis and the integrated current suggest the stability of quantized charge pumping at weak disorder. A breakdown is observed for $w/J \gtrsim 3$ and can best be read-off from the skewness of the distributions of local Chern-marker fluctuations, consistent with the closing of the most likely energy gap. The pumped charge is directly accessible in experiments [3,4,36] and should therefore agree with the theoretical predictions for adiabatically slow pumping on finite systems.

V. SUMMARY AND DISCUSSION

In this work we studied the Rice-Mele model of spinless fermions in the presence of random diagonal disorder. We used exact diagonalization to compute a set of static measures to characterize the properties of a charge pump, including the polarization, the entanglement spectrum, and the integrated local Chern marker. These quantities were computed in the instantaneous eigenbasis. We demonstrated that all these measures indicate a breakdown of the quantized charge pumping at sufficiently strong disorder. The breakdown of quantized pumping manifests itself as a breakdown of winding in the spectral flow of the entanglement spectrum. Plotting the polarization as an angular variable makes the breakdown particularly transparent in this quantity. The integrated local Chern marker appears to be the best suited for determining the transition point quantitatively.

In particular, the fluctuations of the local Chern marker around the bulk Chern number provide relevant information about the breakdown. It would be very desirable to develop a qualitative interpretation of these fluctuations. For instance, it remains open whether nonlocal adiabatic processes play a role in topological charge pumping. These effects were described by Khemani *et al.* [70] as a consequence of adiabatic variations of a single on-site potential in an Anderson insulator. The situation in a charge pump is not entirely different although there, the variation of on-site potentials happens in a correlated fashion.

The critical disorder strength obtained from the integrated local Chern marker agrees well with the point at which the bulk gap closes, while for finite systems we emphasized the importance of sample-to-sample fluctuations. In particular, we demonstrated that the typical value of the minimum bulk gap along the gap cycle is much better suited to describe the distribution obtained from finite systems, rather than the disorder-averaged gap. This may not be surprising, given the known existence of Lifshitz tails at the edges of spectra of

disordered systems (see, e.g., [71]). The topological transition occurs in an Anderson insulator, showing that topological charge pumping is robust against localization, consistent with the results of [36].

We complemented the analysis with time-dependent simulations of the time-periodic pump process and observe deviations from integer-quantized pumping due to a breakdown of adiabaticity for fast pumping. For sufficiently slow pumping we find agreement with the critical disorder strength obtained from the bulk Chern number computed in the instantaneous basis.

In this work we presented a comprehensive comparison of several measures from the instantaneous basis and direct time-dependent simulations. Matching the physical picture for local transport processes to the Floquet-localization picture of Ref. [50] would be an interesting next direction. In this regard, the limit of frequency going to zero in the Floquet picture might be subtle on finite systems, as one should recover the behavior of the instantaneous-basis behavior (see [50]).

Several studies have already theoretically addressed the question of charge pumping in an interacting system [6–17], which should be realizable in state-of-the-art quantum-gas experiments [3–5,36]. Conceptually and from a methodological point of view, the question arises which approaches are

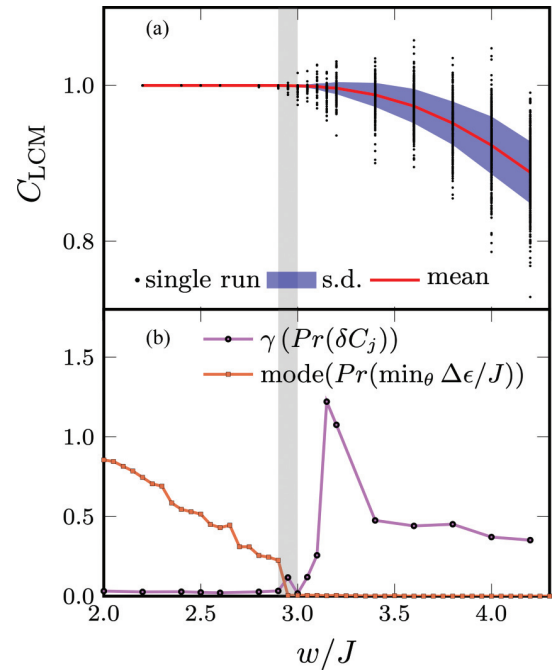


FIG. 16. Comparison of different measures for the pumped charge for an alternative parameter set. For $(R_\Delta = 3, R_\delta = 0.5)$, which is equivalent to parameters used in [50], we compare (a) C_{LCM} as a function of disorder strength, and (b) the skewness of LCM distributions and the mode of the minimum gap along the pump cycle. The shaded region indicates the point where the mode of the minimum gap along the pump cycle closes at $w/J \approx 2.95 \pm 0.05$. Compared to the results of the main text, the mean of the LCM decreases slower past the transition point at $w/J \approx 2.95 \pm 0.05$ but the transition point is unchanged. Computed for $n = 500$ samples in the average for each value of w/J , $L = 400$.

best suited to compute the Chern number for a charge pump in a many-body system. The direct calculation of the current in time-dependent simulations will always work, yet requires making the pump period large. The Floquet approach of Ref. [50] cannot easily be extended to the many-body case, where most Floquet approaches are based on the high-frequency limit [72], opposite to the regime of low frequencies relevant for charge pumps. An extension of the local Chern marker to interacting systems would be desirable (see [73] for recent work in this direction), while polarization and entanglement spectrum can be computed in the many-body case as well (see, e.g., [11]).

Another, related future direction would be to combine the effects of disorder and interactions and to investigate the possibility of topological charge pumping in both a disordered ergodic and in the many-body localized phase [74,75] (see also the discussion in [36,50]). Finally, the stability of topological pumping in quasiperiodic potentials other than Aubry-André type might be interesting as well.

ACKNOWLEDGMENTS

We acknowledge helpful discussions with M. Aidelsburger, J. Bardarson, F. Pollmann, and H. Schomerus. We thank M.

Aidelsburger for pointing out Ref. [70] to us, J. Bardarson for bringing Refs. [37,54] to our attention, and H. Schomerus for directing us to literature on Lifschitz tails [71]. This research was funded by the Deutsche Forschungsgemeinschaft (DFG, German Research Foundation) via Research Unit FOR 2414 under Project No. 277974659. U.S. acknowledges funding from EPSRC via grant (No. EP/R044627/1) and Programme Grant DesOEQ (No. EP/P009565/1).

APPENDIX: ADDITIONAL RESULTS

Figure 16 shows the LCM, the skewness of the local Chern marker distributions γ , and the mode of the distribution of the minimum energy gap along the pump cycle for the parameters ($R_\Delta = 3, R_\delta = 0.5$), which corresponds to the parameters used in [50]. All three quantities predict a breakdown of quantized charge pumping at $w/J = 2.95 \pm 0.05$, similar to the parameters in the main text. A possible reason for this is that $R_\delta = 0.5 < R_\Delta/J$ for both parameter sets. The minimum gap during a pump cycle is therefore only controlled by R_δ . Compared to the results presented in the main text, the mean of the LCM shows a shallower decrease beyond the critical disorder strength.

-
- [1] D. J. Thouless, *Phys. Rev. B* **27**, 6083 (1983).
 [2] Q. Niu and D. Thouless, *J. Phys. A: Math. Gen.* **17**, 2453 (1984).
 [3] S. Nakajima, T. Tomita, S. Taie, T. Ichinose, H. Ozawa, L. Wang, M. Troyer, and Y. Takahashi, *Nat. Phys.* **12**, 296 (2016).
 [4] M. Lohse, C. Schweizer, O. Zilberberg, M. Aidelsburger, and I. Bloch, *Nat. Phys.* **12**, 350 (2016).
 [5] C. Schweizer, M. Lohse, R. Citro, and I. Bloch, *Phys. Rev. Lett.* **117**, 170405 (2016).
 [6] E. Berg, M. Levin, and E. Altman, *Phys. Rev. Lett.* **106**, 110405 (2011).
 [7] D. Rossini, M. Gibertini, V. Giovannetti, and R. Fazio, *Phys. Rev. B* **87**, 085131 (2013).
 [8] Y. Ke, X. Qin, Y. S. Kivshar, and C. Lee, *Phys. Rev. A* **95**, 063630 (2017).
 [9] Y. Kuno, K. Shimizu, and I. Ichinose, *New J. Phys.* **19**, 123025 (2017).
 [10] M. Nakagawa, T. Yoshida, R. Peters, and N. Kawakami, *Phys. Rev. B* **98**, 115147 (2018).
 [11] A. Hayward, C. Schweizer, M. Lohse, M. Aidelsburger, and F. Heidrich-Meisner, *Phys. Rev. B* **98**, 245148 (2018).
 [12] T. Qin, A. Schnell, K. Sengstock, C. Weitenberg, A. Eckardt, and W. Hofstetter, *Phys. Rev. A* **98**, 033601 (2018).
 [13] F. Mei, G. Chen, N. Goldman, L. Xiao, and S. Jia, *New J. Phys.* **21**, 095002 (2019).
 [14] L. Stenzel, A. L. C. Hayward, C. Hubig, U. Schollwöck, and F. Heidrich-Meisner, *Phys. Rev. A* **99**, 053614 (2019).
 [15] L. Lin, Y. Ke, and C. Lee, *Phys. Rev. A* **101**, 023620 (2020).
 [16] S. Greschner, S. Mondal, and T. Mishra, *Phys. Rev. A* **101**, 053630 (2020).
 [17] Y.-T. Lin, D. M. Kennes, M. Pletyukhov, C. S. Weber, H. Schoeller, and V. Meden, *Phys. Rev. B* **102**, 085122 (2020).
 [18] J. A. Marks, M. Schüler, J. C. Budich, and T. P. Devereaux, *Phys. Rev. B* **103**, 035112 (2021).
 [19] J. Qin and H. Guo, *Phys. Lett. A* **380**, 2317 (2016).
 [20] K.-I. Imura, Y. Yoshimura, T. Fukui, and Y. Hatsugai, *J. Phys.: Conf. Ser.* **969**, 012133 (2018).
 [21] R. Wang and Z. Song, *Phys. Rev. B* **100**, 184304 (2019).
 [22] M. Ippoliti and R. N. Bhatt, *Phys. Rev. Lett.* **124**, 086602 (2020).
 [23] S. Hu, Y. Ke, and C. Lee, *Phys. Rev. A* **101**, 052323 (2020).
 [24] P. Marra and M. Nitta, *Phys. Rev. Research* **2**, 042035 (2020).
 [25] L. Arceci, L. Kohn, A. Russomanno, and G. E. Santoro, *J. Stat. Mech.* (2020) 043101.
 [26] L. Wawer, R. Li, and M. Fleischhauer, [arXiv:2009.04149](https://arxiv.org/abs/2009.04149).
 [27] M. Pletyukhov, D. M. Kennes, J. Klinovaja, D. Loss, and H. Schoeller, *Phys. Rev. B* **101**, 161106(R) (2020).
 [28] M. Pletyukhov, D. M. Kennes, J. Klinovaja, D. Loss, and H. Schoeller, *Phys. Rev. B* **101**, 165304 (2020).
 [29] C. S. Weber, K. Piasotski, M. Pletyukhov, J. Klinovaja, D. Loss, H. Schoeller, and D. M. Kennes, *Phys. Rev. Lett.* **126**, 016803 (2021).
 [30] X.-L. Qi and S.-C. Zhang, *Rev. Mod. Phys.* **83**, 1057 (2011).
 [31] M. Z. Hasan and C. L. Kane, *Rev. Mod. Phys.* **82**, 3045 (2010).
 [32] C.-K. Chiu, J. C. Y. Teo, A. P. Schnyder, and S. Ryu, *Rev. Mod. Phys.* **88**, 035005 (2016).
 [33] N. R. Cooper, J. Dalibard, and I. B. Spielman, *Rev. Mod. Phys.* **91**, 015005 (2019).
 [34] J. Li, R.-L. Chu, J. K. Jain, and S.-Q. Shen, *Phys. Rev. Lett.* **102**, 136806 (2009).
 [35] E. J. Meier, F. A. An, A. Dauphin, M. Maffei, P. Massignan, T. L. Hughes, and B. Gadway, *Science* **362**, 929 (2018).
 [36] S. Nakajima, N. Takei, K. Sakuma, Y. Kuno, P. Marra, and Y. Takahashi, [arXiv:2007.06817](https://arxiv.org/abs/2007.06817).

- [37] P. Titum, E. Berg, M. S. Rudner, G. Refael, and N. H. Lindner, *Phys. Rev. X* **6**, 021013 (2016).
- [38] Y. E. Kraus, Y. Lahini, Z. Ringel, M. Verbin, and O. Zilberberg, *Phys. Rev. Lett.* **109**, 106402 (2012).
- [39] A. Cerjan, M. Wang, S. Huang, K. P. Chen, and M. C. Rechtsman, *Light Sci. Appl.* **9**, 178 (2020).
- [40] S. Aubry and G. André, *Ann. Israel Phys. Soc.* **3**, 18 (1980).
- [41] M. Schreiber, S. S. Hodgman, P. Bordia, H. P. Lüschen, M. H. Fischer, R. Vosk, E. Altman, U. Schneider, and I. Bloch, *Science* **349**, 842 (2015).
- [42] M. Rispoli, A. Lukin, R. Schittko, S. Kim, M. E. Tai, J. Léonard, and M. Greiner, *Nature (London)* **573**, 385 (2019).
- [43] P. Bordia, H. Lüschen, S. Scherg, S. Gopalakrishnan, M. Knap, U. Schneider, and I. Bloch, *Phys. Rev. X* **7**, 041047 (2017).
- [44] G. Roati, C. D’Errico, L. Fallani, M. Fattori, C. Fort, M. Zaccanti, G. Modugno, M. Modugno, and M. Inguscio, *Nature (London)* **453**, 895 (2008).
- [45] A. Dareau, E. Levy, M. B. Aguilera, R. Bouganne, E. Akkermans, F. Gerbier, and J. Beugnon, *Phys. Rev. Lett.* **119**, 215304 (2017).
- [46] K. Viebahn, M. Sbroscia, E. Carter, J.-C. Yu, and U. Schneider, *Phys. Rev. Lett.* **122**, 110404 (2019).
- [47] S. V. Rajagopal, T. Shimasaki, P. Dotti, M. Račiūnas, R. Senaratne, E. Anisimovas, A. Eckardt, and D. M. Weld, *Phys. Rev. Lett.* **123**, 223201 (2019).
- [48] T. Xiao, D. Xie, Z. Dong, T. Chen, W. Yi, and B. Yan, *arXiv:2011.03666*.
- [49] T. Liu and H. Guo, *Phys. Lett. A* **382**, 3287 (2018).
- [50] M. M. Wauters, A. Russomanno, R. Citro, G. E. Santoro, and L. Privitera, *Phys. Rev. Lett.* **123**, 266601 (2019).
- [51] E. Abrahams, P. W. Anderson, D. C. Licciardello, and T. V. Ramakrishnan, *Phys. Rev. Lett.* **42**, 673 (1979).
- [52] R. Resta, *Rev. Mod. Phys.* **66**, 899 (1994).
- [53] W. P. Su, J. R. Schrieffer, and A. J. Heeger, *Phys. Rev. Lett.* **42**, 1698 (1979).
- [54] A. Altland, D. Bagrets, and A. Kamenev, *Phys. Rev. B* **91**, 085429 (2015).
- [55] R. Bianco and R. Resta, *Phys. Rev. B* **84**, 241106(R) (2011).
- [56] B. Irsigler, J.-H. Zheng, and W. Hofstetter, *Phys. Rev. Lett.* **122**, 010406 (2019).
- [57] J. Sykes and R. Barnett, *arXiv:2011.04771*.
- [58] M. J. Rice and E. J. Mele, *Phys. Rev. Lett.* **49**, 1455 (1982).
- [59] R. Resta, *Phys. Rev. Lett.* **80**, 1800 (1998).
- [60] R. Resta, *Ferroelectrics* **136**, 51 (1992).
- [61] R. D. King-Smith and D. Vanderbilt, *Phys. Rev. B* **47**, 1651 (1993).
- [62] H. Watanabe and M. Oshikawa, *Phys. Rev. X* **8**, 021065 (2018).
- [63] H. Li and F. D. M. Haldane, *Phys. Rev. Lett.* **101**, 010504 (2008).
- [64] I. Peschel and V. Eisler, *J. Phys. A: Math. Theor.* **42**, 504003 (2009).
- [65] L. Privitera, A. Russomanno, R. Citro, and G. E. Santoro, *Phys. Rev. Lett.* **120**, 106601 (2018).
- [66] Y. Kuno, *Eur. Phys. J. B* **92**, 195 (2019).
- [67] S. R. Manmana, A. Muramatsu, and R. M. Noack, in *Lectures on the Physics of Highly Correlated Electron Systems IX: Ninth Training Course in the Physics of Correlated Electron Systems and High-Tc Superconductors*, edited by A. Avella and F. Mancini, AIP Conf. Proc. No. 789 (AIP, New York, 2005), p. 269.
- [68] P. W. Anderson, *Phys. Rev.* **109**, 1492 (1958).
- [69] R. Li and M. Fleischhauer, *Phys. Rev. B* **96**, 085444 (2017).
- [70] V. Khemani, R. Nandkishore, and S. Sondhi, *Nat. Phys.* **11**, 560 (2015).
- [71] G. Mezincescu, *Commun. Math. Phys.* **158**, 315 (1993).
- [72] A. Eckardt, *Rev. Mod. Phys.* **89**, 011004 (2017).
- [73] M. Anton and A. Rubtsov, *arXiv:2009.01801*.
- [74] D. A. Abanin, E. Altman, I. Bloch, and M. Serbyn, *Rev. Mod. Phys.* **91**, 021001 (2019).
- [75] R. Nandkishore and D. Huse, *Annu. Rev. Condens. Matter Phys.* **6**, 15 (2015).

6 Topological charge pumps coupled to a phononic bath

In the last chapter, I presented results for the breakdown of topological charge pumping due to disorder. Here, we will continue with the topic of quantization breakdown but will instead focus on the effects of pumping in an open system with a bath. Open quantum systems can be realized in different conceptual varieties. Here, we will treat the electronic system as a subsystem that is coupled to harmonic oscillators at each lattice site. We consider a bath of quantum mechanical phonons, which realizes the Holstein-Model [177] with an additional periodic Rice-Mele modulation in the electronic sector. Note that we do not aim at describing ultracold quantum gases in this project, since phonons cannot be realized in these systems.

Even though ultracold atoms can be regarded as nearly closed, finite temperature and effects of open quantum systems, where particle numbers need not be conserved, are inevitable in experiments. Therefore, the interplay between topology and open systems has been a focus of recent research [136, 138, 140, 134, 139, 135, 61, 61, 10, 137]. Here, the Lindblad formalism is often used to treat open systems quantum-mechanically. It has been shown that dynamics under adiabatic modulations are susceptible to dephasing in open systems, even in the presence of a finite energy gap [272].

For systems at finite temperature, generalizations to Berry phases for mixed states have been developed, for example in [145, 273, 138, 141], which show a topological character below a critical temperature. One can also gain topological information via the entanglement spectrum [273] and local unitary (LU) classifications [134]. The bath has also been shown the capability to induce topology in the open system [140]. We will come back to the question of finite temperature charge pumps in chapter 8. There has also been recent progress in the classification of open systems via symmetry classes [10].

Recent works have studied the robustness of topological edge states when coupling to a thermal bath of bosons is present, via a master equation approach [274] and via Liouvillian dynamics [275, 276]. In this context it was found that topological order decreases as the temperature of the bath is increased.

Our system, the Rice-Mele Holstein model is a closed system at zero temperature. Nevertheless, the electronic subsystem can be considered open, in the sense that energy can be transferred into the phononic subsystem. Phonons can have a profound impact on the physics of an electronic sector. Polarons [277], composite particles made up of electrons and phonons, can form, which lead to relaxation dynamics of excited charge carriers [278, 279], melting of charge-density waves [280, 281] and thermalization [282].

Here, we will mainly use the phonon bath as the easiest possible bath that can be coupled to electrons and that can in principle be treated quantum mechanically exactly

6 Topological charge pumps coupled to a phononic bath

in DMRG calculations [74, 75, 76, 77, 78, 79, 80, 81, 82, 283]. Phonons are known for destabilizing topological edge states, for example in Majorana systems, due to coupling of edge states to the bulk [135]. On the other hand dissipation can also stabilize topological pumps [61].

Another well-established numerical approach for electron-phonon systems is the semiclassical treatment of the phononic sector via the multitrajjectory Ehrenfest method [178, 179, 180]. In particular, it was found that for small phonon frequencies, this method is both efficient and reliable in simulating electron-phonon coupled systems [243]. Since we are interested in this phonon frequency regime, we employ this method, in which phonon trajectories are simulated classically and a trajectory average is performed which gives the first order contribution in a $\hbar > 0$ approximation of the phonons [243].

The initially randomly chosen phonon coordinates connect this project to the disordered system of the last chapter. Whereas there we dealt with a static disorder, here the physics can be effectively described via time-dependent random potentials for each trajectory. As a main contribution to the present manuscript, I suggested the analysis of an effective pump cycle due to the random potentials. The random potentials enter the electronic Hamiltonian in the form of the random phonon coordinates x_i as

$$\hat{H}_{\text{el}} = \hat{H}_{\text{RM}}(t) - \sqrt{2}\gamma \sum_{i=1}^L x_i(t) \hat{n}_i, \quad (6.1)$$

where \hat{H}_{RM} is the Rice-Mele hamiltonian and γ is the electron-phonon coupling strength. The key insight is the fact that the dimerization of the Rice-Mele model δ does not change due to the presence of the semiclassical phonons, and that only the local potentials are changed via the term $x_i(t) \hat{n}_i$. One can therefore define an effective pumping path in the plane of δ and

$$\bar{\Delta}(t) = \Delta(t) - \frac{2\sqrt{2}\gamma}{LN_{\text{traj}}} \sum_{i=1}^{N_{\text{traj}}} \left(\sum_{j \in \text{even}}^L x_{i,j}(t) - \sum_{j \in \text{odd}}^L x_{i,j}(t) \right), \quad (6.2)$$

which averages the potential offset between A and B sites of a unit cell due to the phonon trajectories into an effective staggering parameter. The effective pumping path mirrors all properties of the usual pumping path for the Rice-Mele model, as shown in fig. 3.2 in section 3.2.1: A gap closing occurs at the origin of the $\delta - \bar{\Delta}$ plane and the winding of the pumping path around the origin predicts the quantized pumping and change in pumping direction of charge. We employ this visualization to distinguish the quantized charge pumping in the presence of phonons for various pump frequencies.

For pump frequencies that equal the phonon frequency, we discover a resonance, where the phonon number and the energy in the phonon sector grow in each cycle, until the quantized transport breaks down. This happens for arbitrarily small electron-phonon coupling. In the effective pumping path picture, we see that the path winds around circularly (as δ and $\bar{\Delta}$ are out of phase with a phase $\pi/2$) at first but gains ellipticity with each pump cycle until δ and $\bar{\Delta}$ are in phase and the path is a line that crosses

the gap closing. At the gap closing, the electronic system is excited to the higher band which makes pumping non-quantized. Afterwards, the effective pump cycle reverses and a non-quantized pump is observed that pumps in the opposite direction, although the modulation stays in the same orientation. Beyond the resonance frequency, there exists a finite electron-phonon coupling until which quantized transport is stable.

Intriguingly, the stability diagram that plots the critical pump frequency over the phonon coupling has a strong resemblance to a regular classical resonance curve: For frequencies higher than resonance, the transmissibility is lower than for frequencies below resonance. This mirrors the observed critical coupling strengths, as a low (high) transmission from the classical driving frequency (the external pumping) and the harmonic oscillators (phonons) are expected to lead to a weaker (stronger) critical electron phonon coupling. We were not able, however, to prove a direct link between these two measures, so it remains an intriguing thought for now. As a next step, it would be interesting to couple semiclassical phonons to an interacting charge pump, due to the thermalization effects that happen due to polaron formation.

Please note that the manuscript presented here has an erratum that has been appended here as well. Due to a sign mistake in the classical propagator, the results change quantitatively. However, all qualitative results from the main manuscript stay unchanged.

6.1 Publication: Phonon-induced breakdown of Thouless pumping in the Rice-Mele-Holstein model

Article reprinted with permissions from Suman Mondal, Eric Bertok and Fabian Heidrich-Meisner.

Phys. Rev. B 106, 235118 (2022)

<https://doi.org/10.1103/PhysRevB.106.235118>

Erratum:

Phys. Rev. B 107, 239903 (2023)

<https://doi.org/10.1103/PhysRevB.107.239903>

Copyright (2023) by the American Physical Society.

Author contributions: S.M. wrote the manuscript, carried out the numerical calculations and analyzed the data and prepared the figures. E.B. and F.H.M conceived the original idea for this project. F.H.M suggested the study of the breakdown of topological pumping due to phonons with the multitrajectory Ehrenfest method. E.B. suggested the interpretation of the effective pumping paths due to the phonons and the resulting gap closings resulting in the change from positive to negative pumping. All authors contributed to the interpretation of results and discussion of the data and contributed to revisions of the text.

Phonon-induced breakdown of Thouless pumping in the Rice-Mele-Holstein modelSuman Mondal , Eric Bertok , and Fabian Heidrich-Meisner *Institut für Theoretische Physik, Georg-August-Universität Göttingen, D-37077 Göttingen, Germany*

(Received 16 September 2022; revised 14 November 2022; accepted 22 November 2022; published 12 December 2022)

Adiabatic and periodic variation of the lattice parameters can make it possible to transport charge through a system even without net external electric or magnetic fields, known as Thouless charge pumping. The amount of charge pumped in a cycle is quantized and entirely determined by the system's topology, which is robust against perturbations such as disorder and interactions. However, coupling to the environment may play a vital role in topological transport in many-body systems. We study the topological Thouless pumping, where the charge carriers interact with local optical phonons. The semiclassical multitrajectory Ehrenfest method is employed to treat the phonon trajectories classically and charge carriers quantum mechanically. We find a breakdown of the quantized charge transport in the presence of phonons. It happens for any finite electron-phonon coupling strength at the resonance condition when the pumping frequency matches the phonon frequency, and it takes finite phonon coupling strength away from the resonance. Moreover, there exist parameter regimes with non-quantized negative and positive charge transport. The modified effective pumping path due to electron-phonon coupling accurately explains the underlying physics. In the large coupling regime where the pumping disappears, the phonons are found to eliminate the staggering of the on-site potentials, which is necessary for the pumping protocol. Finally, we present a stability diagram of quantized pumping as a function of the time period of pumping and phonon coupling strength.

DOI: [10.1103/PhysRevB.106.235118](https://doi.org/10.1103/PhysRevB.106.235118)**I. INTRODUCTION**

A Thouless charge pump, on a fundamental level, is a one-dimensional dynamic equivalent to the quantum Hall effect. The robust transport of quantized charge in an adiabatic pump cycle, defined by periodic variation of lattice parameters, was first introduced almost four decades ago by Thouless [1]. Recently, this fundamental physical phenomenon has been experimentally demonstrated in a variety of quantum systems, such as ultracold atoms in optical lattices and photonic lattices [2–8]. The robustness of quantization is attributed to the underlying topological protection, which is not altered under small perturbations such as disorder and interaction. In recent years, studying the effect of disorder, different kinds of interaction and nonlinearity have been a topic of immense interest [9–26]. On the experimental front, topological Thouless pumping has been studied in the presence of disorder [27] and strongly correlated regimes [28]. In the attempt to extend the concept of topology to finite temperature and open quantum systems [29–39], Thouless charge pumping has also been studied in these contexts [35,37,38].

The robustness of the topological properties of a system against an open environment is important to study since quantum systems, in general, always interact with the environment. There are several studies that deal with open topological systems that investigate the density matrix by solving the master equation [40–42]. We study a closed system where the topological system is a subsystem, and the rest of the system acts as an environment. The dynamics, in this case, is unitary. In our case, we consider an ensemble of uncoupled classical

harmonic oscillators as the environment. In the solid-state context, this realizes Einstein phonons. Our primary goal is to study the breakdown of topology in the presence of the coupling to the environment. Note that the interplay between the topology and the phonon has been studied before for different systems such as quantum Hall and systems with Majorana fermions [43–46].

One of the very crucial aspects of many-body physics is the interaction with the lattice degree of freedom. Phonons arise naturally as the lattice vibrations at any finite temperature in a real material. The electron-phonon (*e-ph*) coupling can cause instabilities in the metallic state, leading to a plethora of important phenomena, e.g., polaron formation [47], superconductivity, and charge density waves [48–53]. The phononic degrees of freedom show a drastic effect on the dynamical properties as a result of the exchange of energies between the electronic and phononic sectors [54–61]. A great deal of research has been done to analyze the effect of phonons on the dynamics of the charge density wave and Mott phases [54,55,57,59,60], Bloch oscillations [58,61], the equilibration of excited charge carriers [56], and thermalization [62]. The formation of and evolution of polarons have also been extensively studied [63–68]. One theoretical model that represents such strongly correlated *e-ph* systems where the electrons are coupled to the local phonons is the Holstein model [69].

In this work, we analyze the stability of the topology where the system is coupled to a phononic environment. The transport of charge in Thouless charge pumping is studied using the Rice-Mele model [70] subjected to optical phonons, which we dub the Rice-Mele-Holstein model. We use the semiclassical

method known as multitrajectory Ehrenfest (MTE) [71–74] and time evolve the initial state with the phonons in the ground state. The trajectory-based mixed quantum-classical dynamics was traditionally introduced to study electron-nuclear systems, which works best in the adiabatic limit of phonons with oscillator frequencies smaller than the electronic bandwidth [71–74].

In our analysis with the MTE method, we see a breakdown of topological charge pumping (TCP) in the presence of phonons. At resonance, when the phonon frequency and pumping frequency are equal, the TCP breaks for any finite value of e -ph coupling. In the minimal e -ph coupling limit, the TCP eventually disappears at the higher pump cycles. It takes a finite e -ph interaction before the TCP breaks down away from the resonance. In other words, the TCP is stable at sufficiently finite e -ph coupling in this case. The breakdown of TCP is complimented with a gap closing in the spectrum of the instantaneous effective Hamiltonian during the evolution.

Apart from quantized pumping, parameter regimes where nonquantized positive and negative pumping happen exist. The analysis of an effective pumping path very efficiently explains different aspects, such as the direction of pumping and breakdown of pumping. Here, the effective pumping path is the modified Rice-Mele path due to the coupling between the phonon position, which changes dynamically, and on-site electron density. The direction of winding around the origin and the origin crossing by the effective pumping path determine the direction and breakdown of pumping, respectively. We present a stability diagram for the quantized pumping as a function of e -ph coupling strength and pumping period. For a fixed e -ph coupling (small), the diagram displays a signature of reentrant TCP as a function of time period of pumping; that is, the quantization of the pumped charge reappears after losing quantization near the resonance.

In summary, the main findings of this paper are as follows:

- (i) We see a robust quantized pumping with finite electron-phonon coupling for a wide range of parameters which eventually disappears at large electron-phonon coupling.
- (ii) A resonance effect exists where the quantized pumping breaks down for any finite electron-phonon coupling.
- (iii) The system exhibits a phenomenon of negative pumping, where the charge flows opposite to the driving, in some parameter regime, but this occurs outside the quantized regime.

The rest of this paper is organized as follows. In Sec. II, we review the model and the methods used in this work. There we introduce the Rice-Mele model that defines the Thouless pumping protocol and extend it with a Holstein-like coupling to local phonons. Next, we briefly explain the trajectory-based semiclassical MTE method, which is employed to perform the time evolution, and describe the observables used to analyze the physics. The concept of an effective pumping path is introduced at the end of that section. The discussion of results starts in Sec. III. In that section, we explain the breakdown of TCP and nonquantized pumping in terms of the pumped charge, effective pumping paths, and instantaneous eigenvalue spectra at resonance. In Sec. IV, we do an analysis similar to that in Sec. III when the system is out of resonance. Then, we describe the stability diagram obtained as a function of the time period of pumping and e -ph coupling strength in Sec. V. Finally, we draw conclusions in Sec. VI.

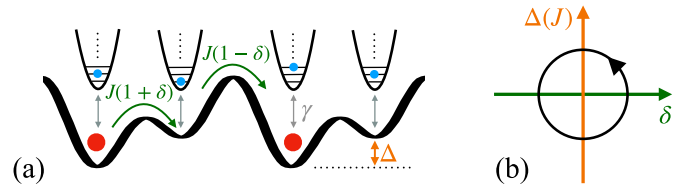


FIG. 1. A pictorial representation of system parameters is shown. (a) Potential landscape at a specific point in time during a pump cycle that determines the hopping dimerization δ and staggered potential Δ . The phonon bath at every site is represented by the harmonic oscillator potential, coupled to the site with strength γ . (b) The pumping protocol. If the system parameter winds around the origin adiabatically, quantized pumping is expected for $\gamma = 0$.

II. MODEL AND METHOD

A. The Rice-Mele model

The Thouless pumping protocol can be defined by the Rice-Mele model [70], a time-dependent Hamiltonian with a time t varying superlattice potential, given by

$$\hat{H}_{\text{RM}}(t) = \sum_{i=1}^L -J(1 + (-1)^i \delta(t)) (\hat{c}_i^\dagger \hat{c}_{i+1} + \text{H.c.}) + \sum_{i=1}^L (-1)^i \frac{\Delta(t)}{2} \hat{n}_i, \quad (1)$$

that changes the hopping amplitude and on-site potential with time. Here, \hat{c}_i (\hat{c}_i^\dagger) and \hat{n}_i are the fermionic (say, electrons) annihilation (creation) and on-site number operators, respectively, at site i in a system consisting of L sites. $\delta(t)$ and $\Delta(t)$ are the hopping dimerization and on-site staggered potential, respectively, that vary with t ,

$$\delta(t) = A_\delta \sin\left(\frac{2\pi t}{T} + \phi\right), \quad (2)$$

$$\Delta(t) = A_\Delta \cos\left(\frac{2\pi t}{T} + \phi\right),$$

where T is the pumping period and $\tau = t/T$ can be considered the pumping parameter. ϕ is an offset of the pumping protocol which is considered to be $\phi = \pi/2$ in this work, realizing $\Delta(t) = 0$ and $\delta(t) > 0$ at $t = 0$, known as the Su-Schrieffer-Heeger [75] limit. An example of the potential landscape is shown in Fig. 1(a) for some t which demonstrates the hopping dimerization and staggered potential. The unit cell of the lattice consists of two sublattices A and B , implying the existence of two bands. For finite A_δ and A_Δ , the band gap is always finite for all t at half filling, and t defines a pumping trajectory that winds around the gap-closing point at $\Delta = \delta = 0$, as shown in Fig. 1(b). For an adiabatic change of τ (large enough T), the topological nature ensures the pumping of a quantized amount of charge Q in a pump cycle. We can quantify the total number of charges pumped during the time evolution by integrating the current at a particular bond between two sites (the first odd bond is considered in our results) as

$$Q(t) = \int_0^t I_{i,i+1}(t) dt, \quad (3)$$

where

$$I_{i,i+1}(t) = -2\text{Im}J_{i,i+1}(t)\langle\Psi(t)|\hat{c}_{i+1}^\dagger\hat{c}_i|\Psi(t)\rangle \quad (4)$$

is the current at time t at the bond between sites i and $i+1$, which has a time-dependent hopping amplitude $J_{i,i+1} = J[1 + (-1)^i\delta(t)]$.

B. The Rice-Mele-Holstein model

The coupling between charge carriers (electrons) and optical phonons extends the Rice-Mele model [Eq. (15)] to the Rice-Mele-Holstein model. The Holstein-like coupling is defined by the dispersionless phonons, also known as Einstein phonons, coupled to the local electronic state, given by

$$\hat{H}(t) = \hat{H}_{\text{RM}}(t) + \hat{H}_{\text{ph}} + \hat{H}_{e\text{-ph}}. \quad (5)$$

Here, \hat{H}_{ph} and $\hat{H}_{e\text{-ph}}$ are the phonon and e -ph coupling parts of the Hamiltonian, which are given by

$$\hat{H}_{\text{ph}} = \hbar\omega \sum_{i=1}^L \hat{b}_i^\dagger \hat{b}_i \quad (6)$$

and

$$\hat{H}_{e\text{-ph}} = -\gamma \sum_{i=1}^L (\hat{b}_i^\dagger + \hat{b}_i) \hat{n}_i. \quad (7)$$

\hat{b}_i (\hat{b}_i^\dagger) are the bosonic annihilation (creation) operators of the phonons at site i . ω and γ are the phonon frequency and e -ph coupling strength, respectively. The e -ph coupling is shown in Fig. 1(a), which illustrates how the phonon bath is coupled to a site.

The Thouless pump in this scenario can be studied with the real-time evolution of an initial state $|\Psi(0)\rangle$ under the influence of a time-dependent Hamiltonian $\hat{H}(t)$. In our calculation we consider $|\Psi(0)\rangle$ to be

$$|\Psi(0)\rangle = |\Psi_e(0)\rangle |\Psi_{\text{ph}}(0)\rangle, \quad (8)$$

where $|\Psi_e(0)\rangle$ is the ground state of $\hat{H}_{\text{RM}}(0)$ at half filling and $|\Psi_{\text{ph}}(0)\rangle = \prod_{i=1}^L |\psi_{\text{ph}}^i(0)\rangle$ represents the ground state of \hat{H}_{ph} where at each site i , phonons are in the ground state $|\psi_{\text{ph}}^i(0)\rangle$ of each individual oscillator.

C. Multitrajectory Ehrenfest method

In principle, the problem can be simulated using numerical methods such as exact diagonalization, Lanczos time evolution, and the time-dependent density matrix renormalization group (tDMRG) methods to capture the exact dynamics for relatively smaller systems [59,76–79], although not straightforwardly in the adiabatic regime. In this work, we employ a semiclassical approximate approach called the multitrajectory Ehrenfest method, which treats phonons classically and averages over independent trajectories. Since we are primarily interested in the regime of small phonon frequencies where we expect the most immediate effect on the pump, we choose MTE, which is efficient and reliable in this regime [74]. This method simplifies our problem to such an extent that it can be solved using the single-particle eigenstates of the Hamiltonian. The classical trajectory-based MTE method is described extensively in Ref. [74], and in the following, we describe

it briefly. To apply the MTE method the phononic operators are represented in real space via $\hat{b}_i^\dagger = \sqrt{\frac{m\omega}{2\hbar}}(\hat{x}_i + \frac{\hat{p}_i}{m\omega})$, and by using the natural length scale for the harmonic oscillators $l_0 = \sqrt{\frac{\hbar}{m\omega}} = 1$ and $\hbar = 1$, we get

$$\hat{H}_{\text{ph}} = \frac{\omega}{2} \sum_{i=1}^L (\hat{x}_i^2 + \hat{p}_i^2), \quad (9)$$

ignoring the constant term $-\omega L/2$, and

$$\hat{H}_{e\text{-ph}} = -\sqrt{2}\gamma \sum_{i=1}^L \hat{x}_i \hat{n}_i. \quad (10)$$

Under the MTE approximation, $|\Psi(0)\rangle$ can now be evolved by initializing the different sets of phonon coordinates $\{x_i(0), p_i(0)\}$, which define different independent trajectories. Here, $\{x_i(0), p_i(0)\}$ are randomly drawn from the distribution given by the Wigner function W_0 centered around $\langle x \rangle = 0$ and $\langle p \rangle = 0$. W_0 is the phase space representation of the harmonic oscillator ground state $|\psi_{\text{ph}}(0)\rangle$,

$$W_0 = \frac{1}{\pi} e^{-\frac{1}{2}(x-p)^2 - \frac{1}{2}(x+p)^2}. \quad (11)$$

The electronic wave function $|\Psi_e(0)\rangle$ evolves under the Hamiltonian

$$\hat{H}_{\text{el}} = \hat{H}_{\text{RM}}(t) - \sqrt{2}\gamma \sum_{i=1}^L x_i(t) \hat{n}_i, \quad (12)$$

which depends on only the dynamical position $x_i(t)$ of the phonons, $i \frac{\partial}{\partial t} |\Psi_e\rangle = \hat{H}_{\text{el}} |\Psi_e\rangle$. The phonon coordinates simultaneously propagate in phase space via the Newtonian mechanics under the influence of the classical Hamiltonian,

$$H_{\text{cl}} = \frac{\omega}{2} \sum_{i=1}^L (x_i^2 + p_i^2) - \sqrt{2}\gamma \sum_{i=1}^L x_i \langle \Psi_e(t) | \hat{n}_i | \Psi_e(t) \rangle, \quad (13)$$

as $\dot{x}_i = \frac{\partial H_{\text{cl}}}{\partial p_i}$, $\dot{p}_i = -\frac{\partial H_{\text{cl}}}{\partial x_i}$.

The expectation value of any observable \hat{O} can be calculated by averaging over all the trajectories as

$$\langle \hat{O}(t) \rangle = \frac{1}{N_{\text{traj}}} \sum_{i=1}^{N_{\text{traj}}} \langle \Psi_i(t) | \hat{O} | \Psi_i(t) \rangle, \quad (14)$$

where N_{traj} is the number of trajectories and $|\Psi_i(t)\rangle$ is the time-evolved initial electronic wave function $|\Psi_e(0)\rangle$ at time t for the i th trajectory. In the following section, we present the results where we always consider $J = 1$, making all the parameters unitless, and express everything in units of J and $A_\Delta = 4A_\delta = 3$, defining a closed path around the gap-closing point at the origin in Fig. 1(b). Considering the limitations of the multitrajectory Ehrenfest method as mentioned above, we take $\omega = 0.1J$, which is small compared to J . In our numerical simulation, we always start the pumping protocol from a short negative time ($-\frac{T}{16J}$) without any phonon coupling and drive it slowly (compared to the actual pumping speed) to $t = 0$, where we quench γ . The slow drive before $t = 0$ leads to a smoother pumping during the execution of the pump cycles [13].

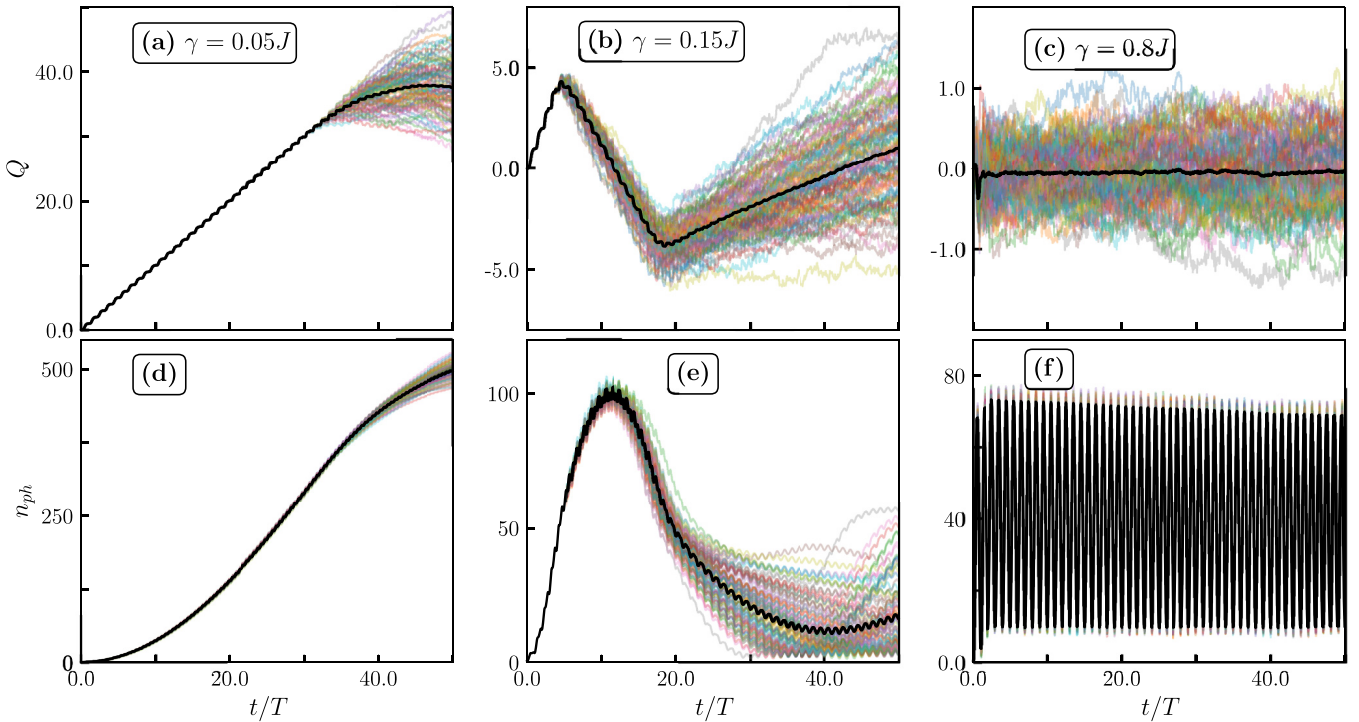


FIG. 2. Observables obtained in the time evolution in 50 pump cycles at resonance for $N_{\text{traj}} = 100$ and $\omega = 0.1J$ with $T = 2\pi/\omega$. $Q(t)$ for all the trajectories (lines with transparent colors) and the trajectory average $Q(t)$ (black line) are shown in (a)–(c) for $\gamma = 0.05J$, $0.15J$, and $0.8J$, respectively. Similar to what we did in (a)–(c), we plot the phonon density n_{ph} in (d)–(f), respectively.

D. Effective pumping path

As mentioned above, the electronic dynamics is determined by \hat{H}_{el} given in Eq. (12), which has two parts. The first part contains the control parameters $[\delta(t)$ and $\Delta(t)]$, which defines a pumping path, as shown in Fig. 1(b). We expect the pumping to be positively or negatively quantized depending on the direction of the winding around the origin. The second part of \hat{H}_{el} gives rise to another source of the on-site potential on top of the staggered $\Delta(t)$ by coupling $x_i(t)$ with the on-site \hat{n}_i . This additional source of the on-site potential may alter the effective staggered potential between the sublattices, leading to a deviation in the pumping path from the original one defined by \hat{H}_{RM} . We can quantify the effective pumping path in the $(\delta, \bar{\Delta})$ plane, where $\bar{\delta}(t) = 2\delta(t)$ is the hopping dimerization, which is unchanged, and $\bar{\Delta}(t)$ is the trajectory and unit-cell-averaged potential difference between two sublattices, given by

$$\bar{\Delta}(t) = \Delta(t) - \frac{2\sqrt{2}\gamma}{LN_{\text{traj}}} \sum_{i=1}^{N_{\text{traj}}} \left(\sum_{j \in \text{even}}^L x_{i,j}(t) - \sum_{j \in \text{odd}}^L x_{i,j}(t) \right). \quad (15)$$

The following sections explain different phenomena, such as the breakdown of pumping and negative charge pumping using the effective pumping path. See Ref. [80].

III. RESONANCE CONDITION

While the Rice-Mele (RM) model shows robust TCP, the nonzero coupling ($\gamma > 0$) with the phonons gives rise to very

rich physics. We begin the analysis with the condition when the phonon frequency matches the pumping frequency ($\omega = 2\pi/T$). ω is considered to be $0.1J$, which fixes the pumping period as $T = 2\pi/\omega$. In this scenario, the dynamics are adiabatic enough in the RM limit ($\gamma = 0$) with robust quantized pumping. The question is whether this TCP survives at finite γ . To answer this, we calculate different quantities during 50 pump cycles with different e -ph coupling strengths γ . In Figs. 2(a)–2(c) we plot $Q(t)$ for $\gamma = 0.05J$, $0.15J$, and $0.8J$, respectively, for 100 trajectories (transparent lines) where the average $Q(t)$ over the trajectories is represented by the opaque black line. We can see that even for a very small value of $\gamma = 0.05J$, the TCP breaks down in the later pump cycles. For $\gamma = 0.15J$, we see a complex behavior in pumping; it changes the direction of pumping after a few cycles. For a large value of $\gamma = 0.8J$, the pumping ceases to occur. We notice that when the quantization of pumping breaks down, $Q(t)$ becomes trajectory dependent and fluctuates around the average value. This behavior is similar to pumping in a disorder potential [21], which is not surprising since each trajectory is initialized with random initial values of $\{x_i(0), p_i(0)\}$.

Interestingly, the phonon excitation is very distinct in different parameter regimes of γ . Figures 2(d)–2(f) show the behaviors of the phonon density given by

$$n_{\text{ph}} = \frac{1}{L} \sum_{i=1}^L \left(\frac{x_i^2}{2} + \frac{p_i^2}{2} \right) \quad (16)$$

for the same parameters considered in Figs. 2(a)–2(c), respectively. Even though $Q(t)$ is quantized in the first few pump cycles for smaller γ [Figs. 2(a) and 2(b)], n_{ph} continuously in-

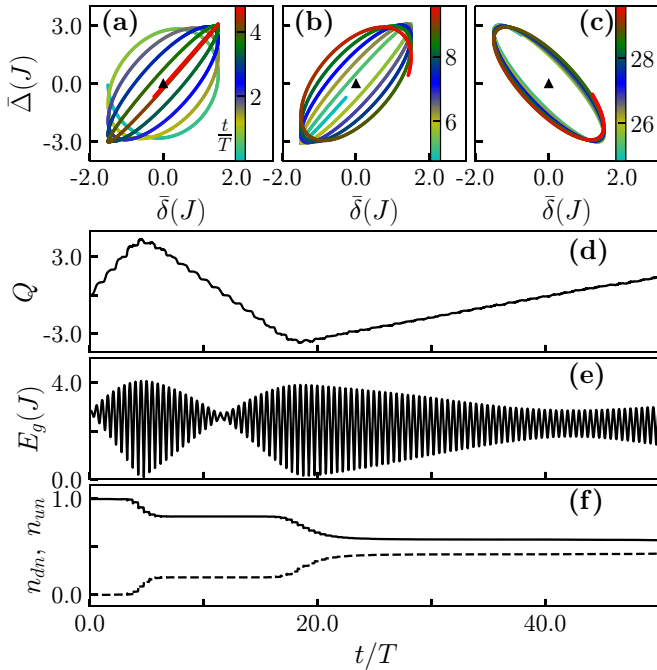


FIG. 3. Trajectory-averaged quantities are displayed here at resonance for $\gamma = 0.15J$, $\omega = 0.1J$, and $T = 2\pi/\omega$ with $N_{\text{traj}} = 100$. The trajectory-averaged effective pumping path is shown for three different time windows in (a)–(c), corresponding to Fig. 2(b), which is also shown in (d) for reference. The black triangles mark the origins where the gap should vanish. The direction of winding around the origin signifies the direction of pumping. $E_g(t)$ is shown in (e), and $n_{\text{dn}}(t)$ (solid line) and $n_{\text{up}}(t)$ (dashed line) are plotted in (f).

creases, and eventually, the quantization of $Q(t)$ breaks down. When the pumping is completely suppressed [Fig. 2(c)], n_{ph} oscillates around a finite number with the frequency ω .

A. Negative charge pumping

The intricate evolution of $Q(t)$ seen in Fig. 2(b) is observed in a finite range of γ . To explain the multiple changes in pump direction, we analyze the effective pumping path. As discussed in Sec. II D, the instantaneous value of $x_i(t)$ can modify the effective pumping path. The pumping path defined by $(\bar{\delta}(t), \bar{\Delta}(t))$ is plotted for different time segments of the plot shown in Fig. 2(b), where the pumped charge is first positive (quantized) and then negative (nonquantized) and becomes positive (nonquantized) again with time, in Figs. 3(a)–3(c), respectively. The color bar represents the number of pump cycles t/T . We can see from Figs. 3(a)–3(c) that the path winds the origin (solid black triangle) first counterclockwise, then clockwise, and then in a counterclockwise direction again, respectively, which explains the direction of pumping. To check further why the quantization breaks down, we look into the trajectory-averaged gap in the spectrum of instantaneous $\hat{H}_{\text{el}}(t)$ given by

$$E_g(t) = E_{L/2+1}^{\text{el}}(t) - E_{L/2}^{\text{el}}(t), \quad (17)$$

where $\{E_{\alpha}^{\text{el}}(t)\}$ is the time-dependent energy spectrum of $\hat{H}_{\text{el}}(t)$ along with the occupancy of its lower (n_{dn}) and upper (n_{up}) bands with time. We can already see from Fig. 3(a) that, at the end of the first few cycles, the effective pumping path

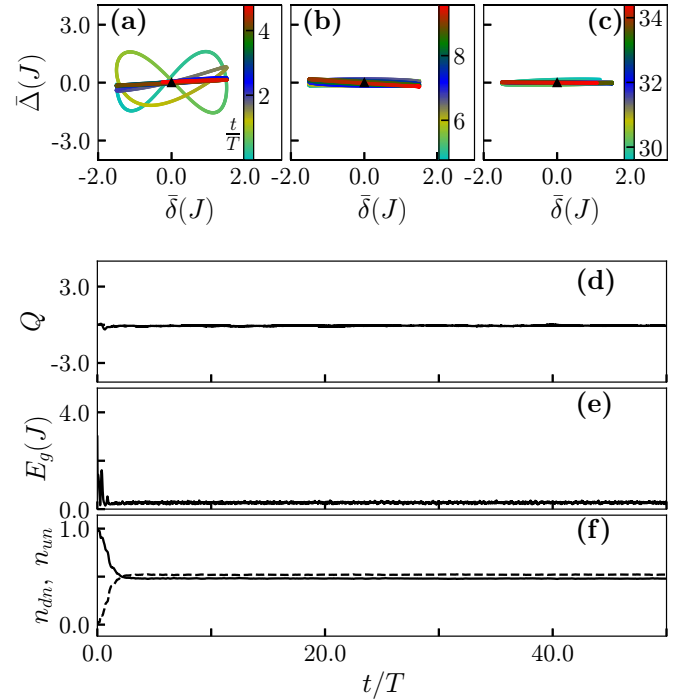


FIG. 4. Explanation of the breakdown of pumping at resonance for $\gamma = 0.8J$, $\omega = 0.1J$, and $T = 2\pi/\omega$. Different quantities are plotted after averaging over 100 trajectories. The effective pumping path is shown for three different time windows in (a)–(c), corresponding to Fig. 2(c), which is also shown in (d) for reference. The black triangles mark the origins where the gap should vanish. The frequent crossing of the origin by the effective pumping path signifies the breakdown of TCP. $E_g(t)$ is shown in (e), and $n_{\text{dn}}(t)$ (solid line) and $n_{\text{up}}(t)$ (dashed line) are plotted in (f).

crosses the origin, where the gap in the spectrum of $\hat{H}_{\text{el}}(t)$ should close. $E_g(t)$ plotted in Fig. 3(d) exactly captures this gap closing. Until this point, n_{dn} (solid line) and n_{up} (dashed line) show that particles in $|\Psi(t)\rangle$ completely occupy the lower band, giving rise to the quantized pumping in this time segment. However, at $E_g = 0$, partial excitation to the upper band happens nonadiabatically, which can be inferred from the finite n_{up} . After this first gap-closing point, $E_g(t)$ becomes finite again, and since the effective pumping path winds in the opposite direction in this segment [Fig. 3(b)], it results in the negative charge pumping. The partial occupancy of the lower band breaks the quantization. A similar gap closing is detected again during the evolution, which populates the upper band further. The counterclockwise winding of the effective pumping path [Fig. 3(c)] suggests a positive pumping (nonquantized) since $E_g(t)$ is finite at later times.

B. Breakdown of pumping

To compare the previous situation with the case shown in Fig. 2(c) where the pumping is entirely absent, we carry out a similar analysis in Fig. 4. Here, the phonon coupling drastically perturbs the staggering nature of the potential, and the effective pumping path becomes flat along the $\bar{\delta}$ axis, which crosses the origin in every pump cycle [Figs. 4(a)–4(c)]. As a result, $Q(t)$ does not change with time. The vanishing $E_g(t)$, shown in Fig. 4(e), signifies nonadiabatic dynamics

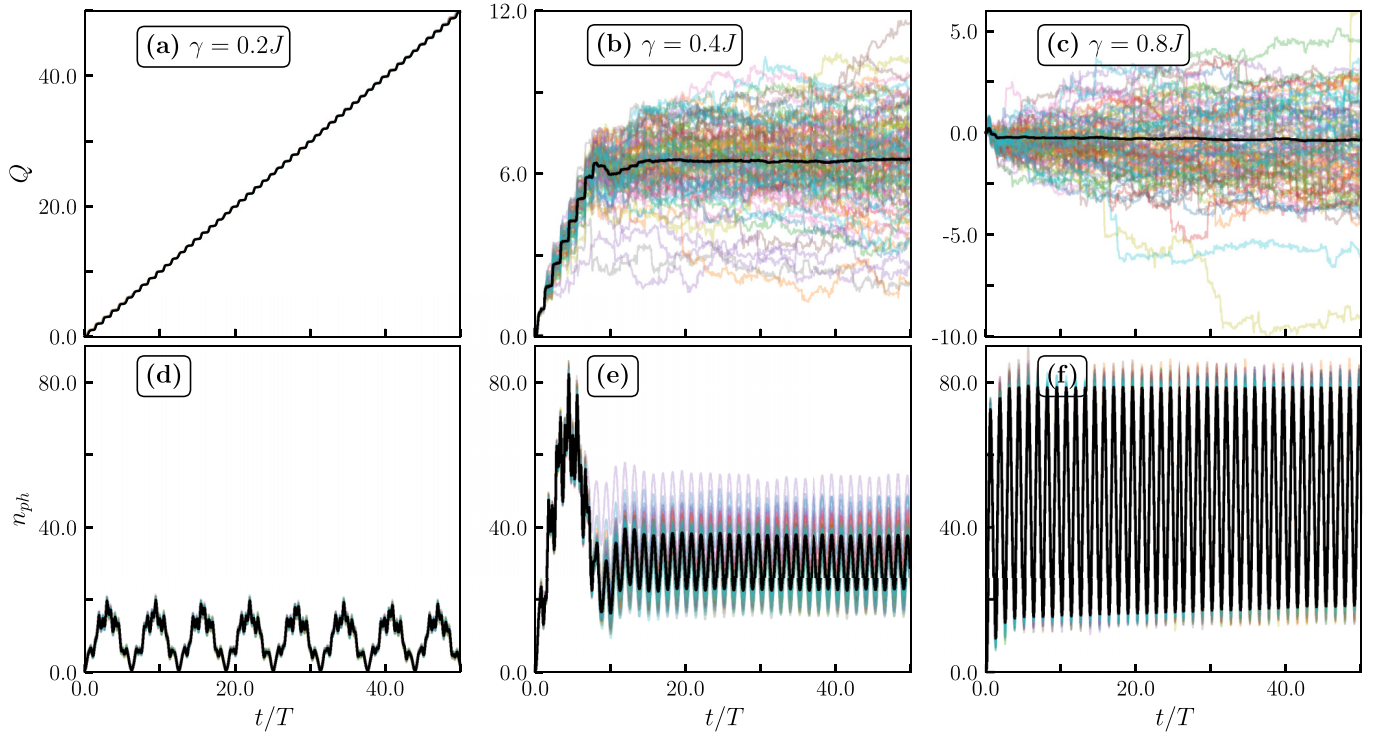


FIG. 5. Observables obtained in the time evolution in 50 pump cycles away from resonance for $N_{\text{traj}} = 100$ and $\omega = 0.1J$ with $T = 50/J$. $Q(t)$ for all the trajectories (lines with transparent colors) and the trajectory average $Q(t)$ (black line) are shown in (a)–(c) for $\gamma = 0.2J$, $0.4J$, and $0.8J$, respectively. Similar to what we did in (a)–(c), we plot the phonon density n_{ph} in (d)–(f), respectively.

under $\hat{H}_{\text{el}}(t)$, leading to a breakdown of pumping. In this region, $E_g(t)$ is not exactly zero, which is a finite-size effect, and is expected to be zero in the thermodynamic limit. $n_{\text{dn}} \sim n_{\text{up}}$ shown in Fig. 4(f) also suggests no change in $Q(t)$ as $|\Psi(t)\rangle$ is equally mixed in both bands.

IV. OUT OF RESONANCE CONDITION

Moving away from resonance, we encounter different physical properties. In this regime, the pumping is found to be quantized at a sufficiently finite value of γ . Ultimately, with increasing γ , the TCP breaks down. We analyze the same quantities studied in the previous section to capture the physics. In Figs. 5(a)–5(c), we plot $Q(t)$ for $\gamma = 0.2J$, $0.4J$, and $0.8J$, respectively, for 100 trajectories (transparent lines) where the average $Q(t)$ over the trajectories is represented by the opaque black line. Even though the initial $\{q_i, p_i\}$ are different for different trajectories, for finite $\gamma = 0.2J$, we see quantized $Q(t)$ all the way to the 50th pump cycle, and $Q(t)$ for all the trajectories merge together, which implies a robust TCP at finite phonon coupling γ .

We observe different effects in the dynamics by increasing γ to $0.4J$. In this case, the charge pumping breaks down after a few pump cycles, and $Q(t)$ is not quantized anymore in the few initial pumping cycles that still exhibit finite pumping. For different trajectories, $Q(t)$ shows a substantial fluctuation from the average value as a result of topologically unprotected dynamics, which stems from the breakdown of TCP and largely depends on the initial conditions. Further increasing $\gamma = 0.8J$, the pumping breaks down from the beginning, and $Q(t)$ for all the trajectories shows a large fluctuation similar to the $\gamma = 0.4J$ case.

A. Quantized pumping with phonons

Unlike the resonance case where the TCP breaks down for small γ [Fig. 5(a)] at later pump cycles, in this case, TCP may remain stable at small γ . We confirm the stability by analyzing the behavior of $n_{\text{ph}}(t)$. Figures 5(d)–5(f) show $n_{\text{ph}}(t)$ for the same parameters considered in Figs. 5(a)–5(c), respectively. We see that $n_{\text{ph}}(t)$ periodically reaches zero after every few pump cycles [Fig. 5(e)] for the $\gamma = 0.2J$ case. Also, the extreme value of $n_{\text{ph}}(t)$ is comparatively smaller [compare with Fig. 2(d)]. This behavior is completely different from the resonance case where n_{ph} keeps increasing in the initial pump cycles where pumping is quantized [compare with Figs. 2(d) and 2(e)]. This regular oscillatory behavior of n_{ph} guarantees the same dynamics for further pump cycles beyond the 50th cycle, and TCP survives. In Fig. 5(f), for the first few cycles where pumping is nonzero, the trend of $n_{\text{ph}}(t)$ looks similar to the $\gamma = 0.2J$ case. However, the features look comparable to the resonance case when the pumping is absent [compare Figs. 5(f) and 2(f)].

The effective pumping path for $\gamma = 0.2J$ also suggests a robust winding, which is shown in Figs. 6(a)–6(c). We can see that the pumping path evolves similarly for different time windows and does not have any trend to collapse towards the origin, indicating robust TCP. $Q(t)$, $E_g(t)$, n_{dn} , and n_{up} are plotted in Figs. 6(d)–6(f), respectively, for this case. The finite $E_g(t)$ and $n_{\text{dn}} = 1$ ($n_{\text{up}} = 0$) at all times illustrate the adiabatic dynamics under $\hat{H}_{\text{el}}(t)$, securing the quantization of pumping.

To summarize, we observe a significant difference at small γ when comparing pumping at resonance and away from resonance. The behavior of $n_{\text{ph}}(t)$ and the effective pumping

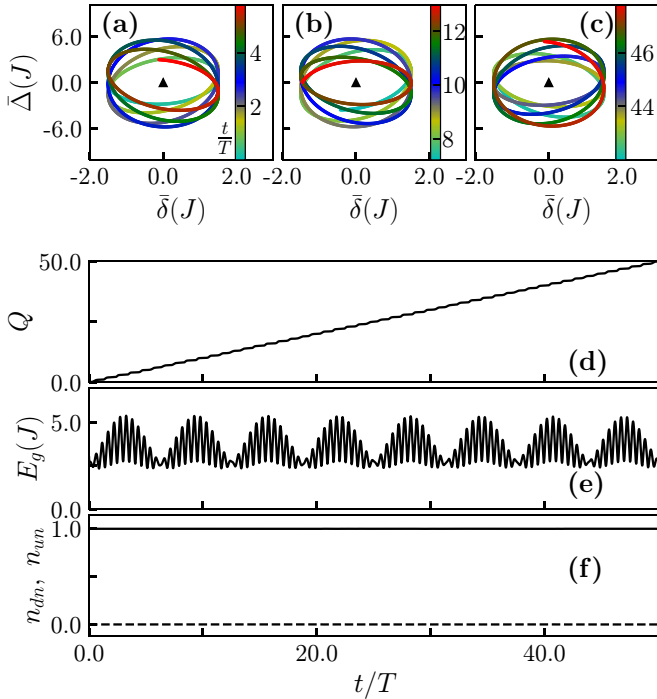


FIG. 6. Different quantities are displayed here after averaging over trajectories with $N_{\text{traj}} = 100$ to analyze the quantized pumping at finite $\gamma = 0.2J$ away from resonance where $\omega = 0.1J$ and $T = 50/J$. The effective pumping path is shown for three different time windows in (a)–(c), corresponding to Fig. 5(a), which is also shown in (d) for reference. The black triangles mark the origins where E_g should vanish. $E_g(t)$ is shown in (e), and $n_{\text{dn}}(t)$ (solid line) and $n_{\text{up}}(t)$ (dashed line) are plotted in (f).

path suggests stable pumping over the simulated time window for the out of resonance case. We stress that this does not rule out a change in behavior at very long times beyond the reach of simulations.

B. Breakdown of pumping

As mentioned above, for larger γ the TCP breaks down. To analyze the breakdown of pumping with increasing γ , we again pay attention to $E_g(t)$. We show the trajectory-averaged $Q(t)$ and $E_g(t)$ in Figs. 7(a) and 7(b), respectively, for the first four pump cycles with $T = 50/J$. Here, we consider $N_{\text{traj}} = 200$ to calculate the average. Comparing the two plots, we can see that $E_g(t)$ starts to vanish at certain times near the critical region ($\gamma \approx 0.4J$) and finally vanishes during the entire pump cycle for larger γ . The vanishing of E_g with time makes the dynamics under \hat{H}_{el} nonadiabatic, and as a result, the TCP breaks down. Note that the negative charge pumping is also present in the off-resonant case [see the deep blue region of Fig. 7(a)].

V. STABILITY DIAGRAM

Until now, we have considered only two time periods of pumping ($T = \frac{2\pi}{0.1J}$ and $50/J$) in our analysis to detect the breakdown of TCP. Now we uncover this phenomenon by varying T . To this end, we perform the calculation for different γ and T for the first 50 pump cycles with $N_{\text{traj}} = 100$

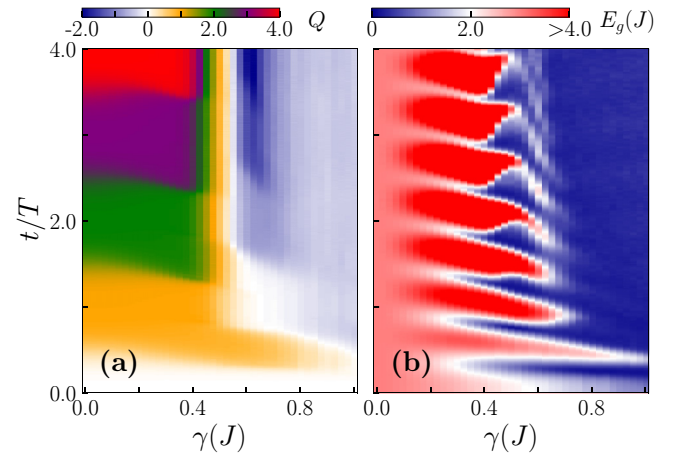


FIG. 7. (a) The trajectory-averaged $Q(t)$ and (b) $E_{\text{gap}}(t)$ are shown away from resonance with $T = 50/J$, $\omega = 0.1J$, and $N_{\text{traj}} = 200$. The breakdown of quantized pumping near $\gamma \sim 0.4J$ is portrayed.

and calculate the trajectory-averaged Q in a pump cycle by averaging the pumped charge in all the cycles. We portray the result in Fig. 8(a) as a function of γ and T , where the color bar represents the average Q in a cycle. The properties of the stability diagram are discussed below.

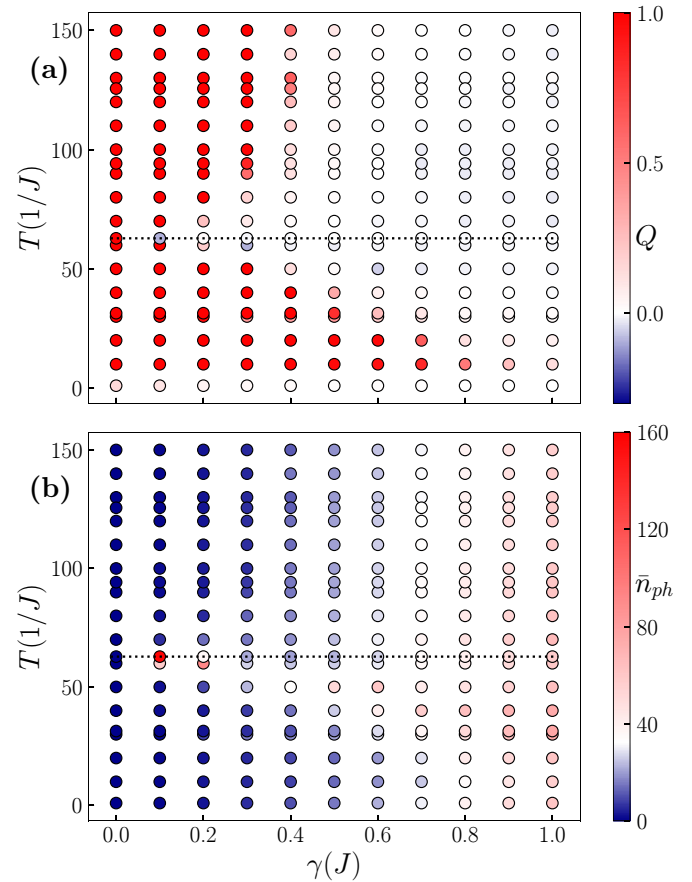


FIG. 8. Stability diagram in the T vs γ plane depending on the trajectory-averaged (a) Q in a cycle and (b) \bar{n}_{ph} . Here, we consider $N_{\text{traj}} = 100$ and average Q and \bar{n}_{ph} over 50 pump cycles. The dashed lines represent the time period of phonons ($\frac{2\pi}{\omega}$).

In the limit of very small $T \sim 1/J$, the TCP is always absent due to a very fast pumping speed which leads to a nonadiabatic evolution. For higher values of T , the TCP breaks down after a critical γ except at resonance (marked by the dashed line), where it breaks down immediately for $\gamma > 0$. An important feature of the stability diagram is the reentrance of quantized pumping as a function of T in a certain parameter regime. For example, with $\gamma = 0.2J$, the quantization of pumping occurs in the order of a nonquantized-quantized-nonquantized-quantized manner as T increases. The reentrance of TCP with increasing T is clearly a consequence of the resonance at $T = 2\pi/\omega$. Simulations with other values of small ω exhibit qualitatively similar physical phenomena at the resonance and away from the resonance (not shown).

We also calculate the time-averaged phonon density, given by

$$\bar{n}_{\text{ph}} = \frac{1}{t} \int_0^t n_{\text{ph}} dt \quad (18)$$

and shown in Fig. 8(b) as a function of γ and T . Like in the previous calculation, \bar{n}_{ph} is averaged over $N_{\text{traj}} = 100$ trajectories and 50 pump cycles. The result complements the stability diagram of Q [Fig. 8(a)] very well. We notice that the phonon excitation in the TCP region is small compared to the TCP-broken region. Around the resonance ($T = 2\pi/\omega$), marked by the dashed line, \bar{n}_{ph} grows faster for smaller γ , which is responsible for the early breakdown in this region.

VI. CONCLUSIONS

In conclusion, we have studied the Thouless charge pumping in the presence of optical phonons. The Rice-Mele pumping protocol extended with Holstein-like coupling to the local dispersionless phonons was used. We considered the initial conditions where the subsystems are decoupled and the phonons are in their ground state. We utilized a semiclassical approach known as the multitrajectory Ehrenfest method to analyze the system's dynamics where the electrons are treated quantum mechanically and phonon trajectories are evolved classically.

The analysis revealed a breakdown of quantized pumping induced by the phonons for any finite value of the e -ph coupling when the phonon frequency and pumping frequency match. Moreover, in this case, for smaller e -ph coupling, nonquantized positive and negative pumping is observed. The direction of pumping is accurately explained using the effective pumping path, which is the modified Rice-Mele path due to the coupling of phonon position with the electronic density. The effective pumping path was found to be winding around the origin in counterclockwise and clockwise directions for

the time windows with positive and negative pumping, respectively. The nonadiabatic nature of the dynamics affects the quantization of pumping in this regime. The nonadiabaticity is visible from the gap in the energy spectrum of the instantaneous Hamiltonian. When the pumping vanishes at higher values of e -ph coupling, the effective pumping path is seen to cross the origin in every cycle during the evolution, which explains the breakdown.

When the pumping period is out of resonance, the phonon-induced breakdown of the quantized pumping still exists. Yet a parameter regime of robust quantized pumping exists before it breaks down at the larger e -ph coupling. The periodically oscillating phonon number evolution and nonshrinking stable effective pumping path signal the robustness of quantization in this case. The adiabatic nature of the pumping does not hold after the breakdown of pumping for larger e -ph coupling, which is visible from the energy spectrum of the instantaneous Hamiltonian.

We obtained a stability diagram as a function of e -ph coupling and the time period of pumping. A wide region of quantized pumping was observed in the parameter space of finite e -ph coupling. As a result of resonance, a reentrant behavior of the quantized pumping was observed where, at a fixed e -ph coupling, the quantization reappears after a breakdown near the resonance as a function of the time period of pumping.

These results lead to an avenue of further analysis worth studying. One could do a similar analysis for quantum phonons. The system could be simulated using the tDMRG method with the local basis optimization technique [59,76]. Starting the pump from different initial states may lead to interesting outcomes. One should further consider scenarios of stable quantized pumping even in the presence of phonons. A half-filled Holstein model, for instance, could host a charge density wave state [48–50], depending on parameters, with a many-body gap. One could also extend the model for the phonons with dispersion. The addition of dispersion allows the phonons to transport energy to other sites, whereas local oscillators can do that only via electrons. The sign of the dispersion may also matter as the minimum changes its position in k space from $k = 0$ to $k = \pi$ with the sign.

The numerical data plotted in the figures are partially available [80].

ACKNOWLEDGMENTS

We thank M. ten Brink for helpful discussions. This research was funded by the Deutsche Forschungsgemeinschaft (DFG, German Research Foundation) via Research Unit FOR 2414 under Project No. 277974659.

- [1] D. J. Thouless, *Phys. Rev. B* **27**, 6083 (1983).
- [2] M. Lohse, C. Schweizer, O. Zilberberg, M. Aidelsburger, and I. Bloch, *Nat. Phys.* **12**, 350 (2016).
- [3] C. Schweizer, M. Lohse, R. Citro, and I. Bloch, *Phys. Rev. Lett.* **117**, 170405 (2016).

- [4] S. Nakajima, T. Tomita, S. Taie, T. Ichinose, H. Ozawa, L. Wang, M. Troyer, and Y. Takahashi, *Nat. Phys.* **12**, 296 (2016).
- [5] Y. E. Kraus, Y. Lahini, Z. Ringel, M. Verbin, and O. Zilberberg, *Phys. Rev. Lett.* **109**, 106402 (2012).

- [6] Y. Ke, X. Qin, F. Mei, H. Zhong, Y. S. Kivshar, and C. Lee, *Laser Photonics Rev.* **10**, 995 (2016).
- [7] A. Cerjan, M. Wang, S. Huang, K. P. Chen, and M. C. Rechtsman, *Light: Sci. Appl.* **9**, 178 (2020).
- [8] Z. Fedorova, H. Qiu, S. Linden, and J. Kroha, *Nat. Commun.* **11**, 3758 (2020).
- [9] P. Titum, E. Berg, M. S. Rudner, G. Refael, and N. H. Lindner, *Phys. Rev. X* **6**, 021013 (2016).
- [10] Y. Ke, X. Qin, Y. S. Kivshar, and C. Lee, *Phys. Rev. A* **95**, 063630 (2017).
- [11] A. Hayward, C. Schweizer, M. Lohse, M. Aidelsburger, and F. Heidrich-Meisner, *Phys. Rev. B* **98**, 245148 (2018).
- [12] M. Nakagawa, T. Yoshida, R. Peters, and N. Kawakami, *Phys. Rev. B* **98**, 115147 (2018).
- [13] L. Privitera, A. Russomanno, R. Citro, and G. E. Santoro, *Phys. Rev. Lett.* **120**, 106601 (2018).
- [14] M. M. Wauters, A. Russomanno, R. Citro, G. E. Santoro, and L. Privitera, *Phys. Rev. Lett.* **123**, 266601 (2019).
- [15] B. A. van Voorden and K. Schoutens, *New J. Phys.* **21**, 013026 (2019).
- [16] R. Wang and Z. Song, *Phys. Rev. B* **100**, 184304 (2019).
- [17] Y. Kuno and Y. Hatsugai, *Phys. Rev. Res.* **2**, 042024(R) (2020).
- [18] L. Lin, Y. Ke, and C. Lee, *Phys. Rev. A* **101**, 023620 (2020).
- [19] P. Marra and M. Nitta, *Phys. Rev. Res.* **2**, 042035(R) (2020).
- [20] S. Greschner, S. Mondal, and T. Mishra, *Phys. Rev. A* **101**, 053630 (2020).
- [21] A. L. C. Hayward, E. Bertok, U. Schneider, and F. Heidrich-Meisner, *Phys. Rev. A* **103**, 043310 (2021).
- [22] S. Mondal, S. Greschner, L. Santos, and T. Mishra, *Phys. Rev. A* **104**, 013315 (2021).
- [23] Y. Kuno and Y. Hatsugai, *Phys. Rev. B* **104**, 045113 (2021).
- [24] E. Bertok, F. Heidrich-Meisner, and A. A. Aligia, *Phys. Rev. B* **106**, 045141 (2022).
- [25] Q. Fu, P. Wang, Y. V. Kartashov, V. V. Konotop, and F. Ye, *Phys. Rev. Lett.* **128**, 154101 (2022).
- [26] T. Tuloup, R. W. Bomantara, and J. Gong, *arXiv:2205.10978*.
- [27] S. Nakajima, N. Takei, K. Sakuma, Y. Kuno, P. Marra, and Y. Takahashi, *Nat. Phys.* **17**, 844 (2021).
- [28] A.-S. Walter, Z. Zhu, M. Gächter, J. Minguzzi, S. Roschinski, K. Sandholzer, K. Viebahn, and T. Esslinger, *arXiv:2204.06561*.
- [29] J. E. Avron, M. Fraas, G. M. Graf, and O. Kenneth, *New J. Phys.* **13**, 053042 (2011).
- [30] C.-E. Bardyn, M. A. Baranov, C. V. Kraus, E. Rico, A. İmamoğlu, P. Zoller, and S. Diehl, *New J. Phys.* **15**, 085001 (2013).
- [31] O. Viyuela, A. Rivas, and M. A. Martin-Delgado, *Phys. Rev. Lett.* **112**, 130401 (2014).
- [32] Z. Huang and D. P. Arovas, *Phys. Rev. Lett.* **113**, 076407 (2014).
- [33] O. Viyuela, A. Rivas, and M. A. Martin-Delgado, *Phys. Rev. Lett.* **113**, 076408 (2014).
- [34] E. P. L. van Nieuwenburg and S. D. Huber, *Phys. Rev. B* **90**, 075141 (2014).
- [35] D. Linzner, L. Wawer, F. Grusdt, and M. Fleischhauer, *Phys. Rev. B* **94**, 201105(R) (2016).
- [36] F. Grusdt, *Phys. Rev. B* **95**, 075106 (2017).
- [37] C.-E. Bardyn, L. Wawer, A. Altland, M. Fleischhauer, and S. Diehl, *Phys. Rev. X* **8**, 011035 (2018).
- [38] R. Unanyan, M. Kiefer-Emmanouilidis, and M. Fleischhauer, *Phys. Rev. Lett.* **125**, 215701 (2020).
- [39] A. Altland, M. Fleischhauer, and S. Diehl, *Phys. Rev. X* **11**, 021037 (2021).
- [40] O. Viyuela, A. Rivas, and M. A. Martin-Delgado, *Phys. Rev. B* **86**, 155140 (2012).
- [41] A. Rivas, O. Viyuela, and M. A. Martin-Delgado, *Phys. Rev. B* **88**, 155141 (2013).
- [42] Y. He and C.-C. Chien, *Phys. Rev. B* **106**, 024310 (2022).
- [43] Y. Vinkler-Aviv and A. Rosch, *Phys. Rev. X* **8**, 031032 (2018).
- [44] G. Goldstein and C. Chamon, *Phys. Rev. B* **84**, 205109 (2011).
- [45] C. Knapp, T. Karzig, R. M. Lutchyn, and C. Nayak, *Phys. Rev. B* **97**, 125404 (2018).
- [46] P. P. Aseev, P. Marra, P. Stano, J. Klinovaja, and D. Loss, *Phys. Rev. B* **99**, 205435 (2019).
- [47] H. Fröhlich, *Adv. Phys.* **3**, 325 (1954).
- [48] J. E. Hirsch and E. Fradkin, *Phys. Rev. B* **27**, 4302 (1983).
- [49] R. H. McKenzie, C. J. Hamer, and D. W. Murray, *Phys. Rev. B* **53**, 9676 (1996).
- [50] R. J. Bursill, R. H. McKenzie, and C. J. Hamer, *Phys. Rev. Lett.* **80**, 5607 (1998).
- [51] A. Altland and B. D. Simons, *Condensed Matter Field Theory* (Cambridge University Press, Cambridge, 2010).
- [52] D. Emin, in *Polarons* (Cambridge University Press, Cambridge, 2012), pp. 86–94.
- [53] F. Hébert, B. Xiao, V. G. Rousseau, R. T. Scalettar, and G. G. Batrouni, *Phys. Rev. B* **99**, 075108 (2019).
- [54] H. Matsueda, S. Sota, T. Tohyama, and S. Maekawa, *J. Phys. Soc. Jpn.* **81**, 013701 (2012).
- [55] G. De Filippis, V. Cataudella, E. A. Nowadnick, T. P. Devereaux, A. S. Mishchenko, and N. Nagaosa, *Phys. Rev. Lett.* **109**, 176402 (2012).
- [56] F. Dorfner, L. Vidmar, C. Brockt, E. Jeckelmann, and F. Heidrich-Meisner, *Phys. Rev. B* **91**, 104302 (2015).
- [57] H. Hashimoto and S. Ishihara, *Phys. Rev. B* **96**, 035154 (2017).
- [58] Z. Huang, M. Hoshina, H. Ishihara, and Y. Zhao, *Ann. Phys. (Berlin, Ger.)* **531**, 1800303 (2019).
- [59] J. Stolpp, J. Herbrych, F. Dorfner, E. Dagotto, and F. Heidrich-Meisner, *Phys. Rev. B* **101**, 035134 (2020).
- [60] D. Jansen, C. Jooss, and F. Heidrich-Meisner, *Phys. Rev. B* **104**, 195116 (2021).
- [61] Z. Huang, A. D. Somoza, C. Peng, J. Huang, M. Bo, C. Yao, J. Li, and G. Long, *New J. Phys.* **23**, 123020 (2021).
- [62] J. Kogoj, L. Vidmar, M. Mierzejewski, S. A. Trugman, and J. Bonča, *Phys. Rev. B* **94**, 014304 (2016).
- [63] L. Vidmar, J. Bonča, M. Mierzejewski, P. Prelovšek, and S. A. Trugman, *Phys. Rev. B* **83**, 134301 (2011).
- [64] G. Li, B. Movaghar, A. Nitzan, and M. A. Ratner, *J. Chem. Phys.* **138**, 044112 (2013).
- [65] P. Werner and M. Eckstein, *Europhys. Lett.* **109**, 37002 (2015).
- [66] Z. Huang, L. Chen, N. Zhou, and Y. Zhao, *Ann. Phys. (Berlin, Ger.)* **529**, 1600367 (2017).
- [67] L.-C. Ku and S. A. Trugman, *Phys. Rev. B* **75**, 014307 (2007).
- [68] D. Golež, J. Bonča, L. Vidmar, and S. A. Trugman, *Phys. Rev. Lett.* **109**, 236402 (2012).
- [69] T. Holstein, *Ann. Phys. (NY)* **8**, 325 (1959).

- [70] M. J. Rice and E. J. Mele, *Phys. Rev. Lett.* **49**, 1455 (1982).
- [71] P. Ehrenfest, *Z. Phys.* **45**, 455 (1927).
- [72] J. C. Tully, *Faraday Discuss.* **110**, 407 (1998).
- [73] A. Kirrander and M. Vacher, in *Quantum Chemistry and Dynamics of Excited States* (Wiley, Hoboken, NJ, 2020), Chap. 15, pp. 469–497.
- [74] M. ten Brink, S. Gräber, M. Hopjan, D. Jansen, J. Stolpp, F. Heidrich-Meisner, and P. E. Blöchl, *J. Chem. Phys.* **156**, 234109 (2022).
- [75] W. P. Su, J. R. Schrieffer, and A. J. Heeger, *Phys. Rev. Lett.* **42**, 1698 (1979).
- [76] C. Brockt, F. Dorfner, L. Vidmar, F. Heidrich-Meisner, and E. Jeckelmann, *Phys. Rev. B* **92**, 241106(R) (2015).
- [77] S. R. Manmana, A. Muramatsu, and R. M. Noack, in *Lectures on the Physics of Highly Correlated Electron Systems IX: Ninth Training Course in the Physics of Correlated Electron Systems and High- T_c Superconductors*, AIP Conf. Proc. No. 789 (Melville, NY, 2005), pp. 269.
- [78] G. Vidal, *Phys. Rev. Lett.* **93**, 040502 (2004).
- [79] U. Schollwöck, *Ann. Phys. (NY)* **326**, 96 (2011).
- [80] S. Mondal, E. Bertok, and F. Heidrich-Meisner, [arXiv:2209.06124](https://arxiv.org/abs/2209.06124).

Erratum: Phonon-induced breakdown of Thouless pumping in the Rice-Mele-Holstein model [Phys. Rev. B 106, 235118 (2022)]

Suman Mondal, Eric Bertok and Fabian Heidrich-Meisner

Institut für Theoretische Physik, Georg-August-Universität Göttingen, D-37077 Göttingen, Germany

(Dated: June 8, 2023)

Here we rectify a mistake in the implementation of the semi-classical approach of our article. The correction leads to a quantitative change in the results. However, qualitatively the physics extracted from the numerical data remains valid. The interpretation, discussion and conclusions of the article are not affected by the error. In the following, we clarify the mistake in detail. Then we update the results with rectified numerical data and mention the changes that should be done to the manuscript.

In order to evolve the phonon coordinates $\{x_i(t), p_i(t)\}$ simultaneously with the evolution of the quantum mechanical electronic part, we can use the exact solution of the equations of motion

$$\dot{x}_i = \frac{\partial H_{cl}}{\partial p_i}, \quad \dot{p}_i = -\frac{\partial H_{cl}}{\partial x_i} \quad (1)$$

as,

$$x_i(t + \delta t) = x_i(t)\cos(\omega\delta t) + p_i(t)\sin(\omega\delta t) + \frac{\sqrt{2}\gamma n_i}{\omega}(1 - \cos(\omega\delta t)) \quad (2)$$

and

$$p_i(t + \delta t) = -x_i(t)\sin(\omega\delta t) + p_i(t)\cos(\omega\delta t) + \frac{\sqrt{2}\gamma n_i}{\omega}\sin(\omega\delta t). \quad (3)$$

In our article, we implemented the above equations incorrectly; we used the wrong signs for the second and first terms of the equations for $x_i(t + \delta t)$ and $p_i(t + \delta t)$, respectively, on the right-hand side.

Figure 1 of this Erratum should replace Fig. 2 of the paper. The upper panel of Fig. 1 shows the pumped charge during 50 pump cycles at resonance for the same parameters considered in our article. In Fig. 1(a), the quantized pumping breaks down earlier in comparison to our article. In Fig. 1(b), the direction of pumping changes thrice in the same time limit in contrast to the published result, where it happens twice. This is, however, parameter dependent. Other choices of parameters lead to two changes in the direction of pumping. There is no critical change in Fig. 1(c). Analyzing the current result, we arrive at the same conclusions as before about the negative charge pumping and the breakdown of pumping at resonance. The lower panel of Fig. 1, which shows the number of phonons $n_{ph}(t)$, modifies accordingly.

Figures 2 and 3 should replace Figs. 3 and 4 of the paper, respectively. Figure 2 (Fig. 3) explains the underlying physics of the negative charge pumping (breakdown of pumping) in terms of the effective pumping path

[Fig. 2 (a-c) (Fig. 3 (a-c))], the energy gap at the center of the instantaneous spectrum [Fig. 2(e) (Fig. 3(e))], and the occupancy of the lower and upper half of the instantaneous spectrum [Fig. 2(f) (Fig. 3(f))]. Even though the figure changes quantitatively, the qualitative physics remains the same, and we can explain the physics the same way as in the article.

In the corrected results, for Fig. 3 of the Erratum, the pumping path crosses the origin late compared to Fig. 4 of our paper, where it crosses the origin within the first two cycles. This leads to differences in E_g , n_{up} and n_{down} also. In conclusion, similar to the discussion in our paper, the non-adiabatic dynamics cause the breakdown of the topological charge pumping.

Fig. 4 of the Erratum, which should replace Fig. 5 of the paper, shows the same quantities where the pumping period is away from resonance. Here also, the approximate features remain the same as in the published results. The existence of a quantized pump at finite electron-phonon coupling [finite γ , Fig. 4(a)] and breakdown at higher γ [Fig. 4(c)] can be seen in the upper panel. The behavior of n_{ph} [Fig. 4(d-f)] is also similar to the previous result. Here we have considered the time period of pumping as $T = 90/J$ instead of $T = 50/J$, which yields qualitatively the same behavior as in the original data. Also, we consider $\gamma = 0.2J$, $0.5J$, and $1.0J$, respectively for Figs. 4(a-c), which differs from the parameters of Fig. 5 of our paper. However, at this new value of $T = 90/J$, the updated values of $\gamma = 0.2J$, $0.5J$, and $1.0J$ target the same parameter regimes of quantized pumping, the intermediate region, and breakdown of pumping, respectively, as in the paper.

The quantized pumping at finite γ away from the resonance is explained with the help of an effective pumping path in Fig. 5, along with other quantities. Figure 5 replaces Fig. 6 of the paper. The findings are the same as before; the stable trajectory of the effective pumping path around the origin protects the quantization. The actual path is different from the previous result, which is not important for topological protection.

Figure 6, which should replace Fig. 7 of the paper, signifies the same physics as before. The gap closing of the instantaneous spectrum complements the breakdown of quantized pumping. The only difference is that we do not see clear negative charge pumping in this parameter regime ($T = 90/J$), which is parameter-dependent.

The stability diagram, shown in Fig. 7, also looks similar and shows all the features as before (replacing Fig. 8 of the paper); the parameter regime of quantized pumping, resonance, and reentrant quantization of pumping.

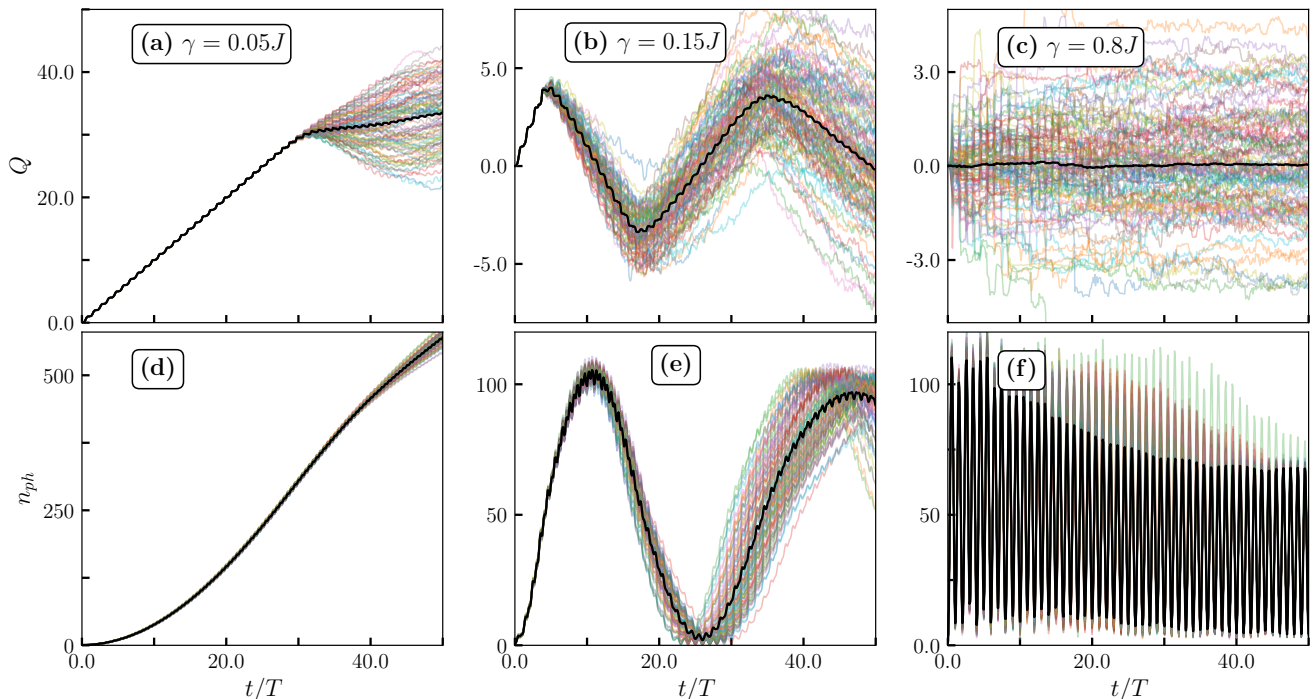


FIG. 1: Observables obtained in the time evolution in 50 pump cycles at resonance for $N_{traj} = 100$ and $\omega = 0.1J$ with $T = 2\pi/\omega$. The $Q(t)$ for all the trajectories (lines with transparent colours) and trajectory average $Q(t)$ (black line) is shown in (a-c) for $\gamma = 0.05J$, $0.15J$, and $0.8J$, respectively. Similar to (a-c), we plot the phonon density n_{ph} in (d-f), respectively.

There are two minor differences. The total pumped charge goes to zero more gradually after the breakdown of quantization which can be observed from the gradual change in the shade of red in Fig. 7(a) (away from resonance). Moreover, the breakdown regime of quantization moves slightly.

According to the discussion above, the article needs to be changed in the following places:

The last line of Sec. IIIA should be modified from "The counterclockwise winding ... is finite at later times." to "The anti-clockwise winding ... $E_g(t)$ is finite in this time window."

The second line in Sec. IIIB needs to be modified from "Here, the phonon coupling drastically perturbs the staggering nature of the potential, and the effective pumping path becomes flat along the $\bar{\delta}$ axis, which crosses the origin in every pump cycle [Figs.4(a) - 4(c)]." to "Here, the phonon coupling drastically perturbs the staggered nature of the potential, and the effective pumping path eventually becomes flat along the $\bar{\delta}$ axis which crosses the origin in every pump cycle [Fig. 4(c)]."

The fourth line in Sec. IIIB needs to be modified from "The vanishing $E_g(t)$, shown in Fig. 4(e), signifies a nonadiabatic dynamics under $\hat{H}_{el}(t)$ leading to a breakdown of pumping." to "The vanishing $E_g(t)$ in later

pump cycles, shown in Fig. 4(e), signifies a nonadiabatic dynamics under $\hat{H}_{el}(t)$ leading to the breakdown of pumping."

At the end of Sec. IIIB, the line "The $n_{dn} \sim n_{up}$ shown in ... equally mixed in both the bands" should be replaced by "The n_{dn} and n_{up} shown in Fig. 4(f) also suggests the excitation of the upper band as a result of non-adiabatic dynamics."

Since we are showing the out-of-resonance case for a different parameter set in the new results, the parameter values must be changed in some places. In the fifth line of the first paragraph of Sec. IV, the parameters should be updated to " $\gamma = 0.2J$, $0.5J$, and $1.0J$ ". In the first line of the next paragraph, the " γ to $0.4J$ " should be replaced by " γ to $0.5J$ ". Also, the last line of the same paragraph should be replaced with "Further increasing $\gamma = 1.0J$... $\gamma = 0.5J$ case". In the third line of Sec. IVB, the parameter should be updated with $T = 90/J$. Also, in the fifth line, there is a change of parameter from ($\gamma \approx 0.4J$) to ($\gamma \approx 0.5J$). The last line of Sec. IVB should be removed since, at this parameter set, we do not see negative charge pumping, which is a parameter dependent phenomenon.

In the first line of Sec. V, the parameter should be updated to ($T = \frac{2\pi}{0.1J}$ and $90/J$).

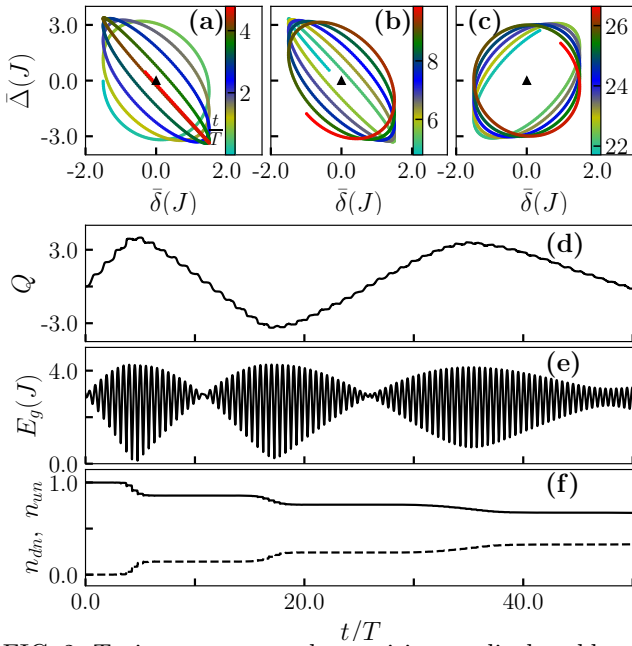


FIG. 2: Trajectory averaged quantities are displayed here at resonance for $\gamma = 0.15J$, $\omega = 0.1J$ and $T = 2\pi/\omega$ with $N_{traj} = 100$. The trajectory averaged effective pumping path is shown for three different time windows in (a), (b), and (c) corresponding to Fig. 1(b), which is also shown in (d) for reference. The black triangles mark the origins where the gap should vanish. The direction of winding around the origin signifies the direction of pumping. The $E_g(t)$ is shown in (e) and $n_{dn}(t)$ (solid line) and $n_{up}(t)$ (dashed line) are plotted in (f).

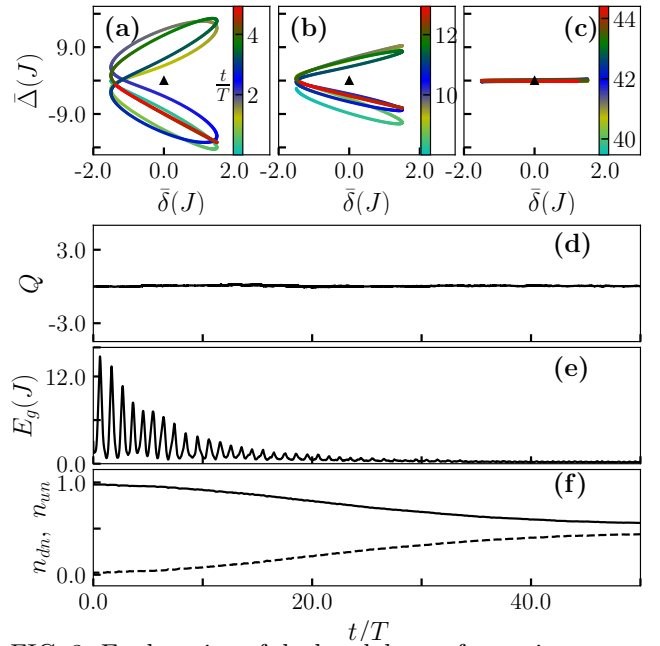


FIG. 3: Explanation of the breakdown of pumping at resonance for $\gamma = 0.8J$, $\omega = 0.1J$ and $T = 2\pi/\omega$. Different quantities are plotted after averaging over 100 trajectories. The effective pumping path is shown for three different time windows in (a), (b), and (c) corresponding to Fig. 1(c), which is also shown in (d) for reference. The black triangles mark the origins where the gap should vanish. The frequent crossing of origin by the effective pumping path in later pump cycles signifies the breakdown of TCP. The $E_g(t)$ is shown in (e) and $n_{dn}(t)$ (solid line) and $n_{up}(t)$ (dashed line) are plotted in (f).

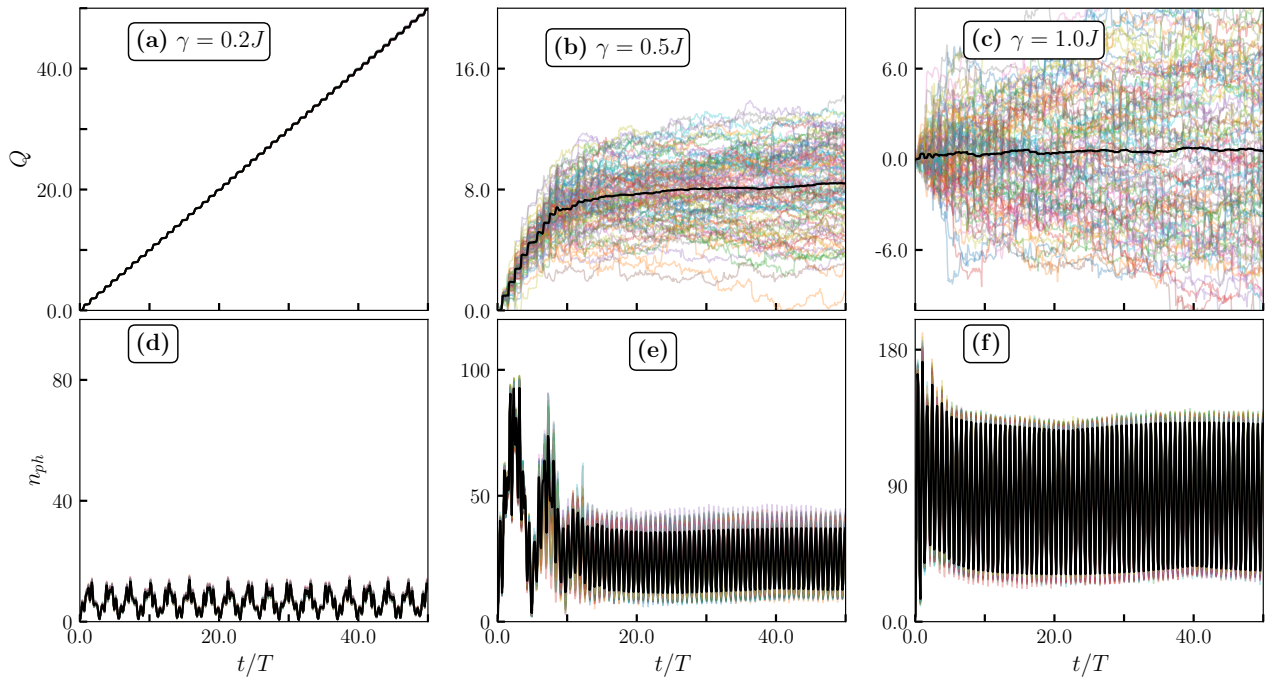


FIG. 4: Observables obtained in the time evolution in 50 pump cycles away from resonance for $N_{traj} = 100$ and $\omega = 0.1J$ with $T = 90/J$. The $Q(t)$ for all the trajectories (lines with transparent colours) and trajectory average $Q(t)$ (black line) is shown in (a-c) for $\gamma = 0.2J$, $0.5J$, and $1.0J$, respectively. Similar to (a-c), we plot the phonon density n_{ph} in (d-f), respectively.

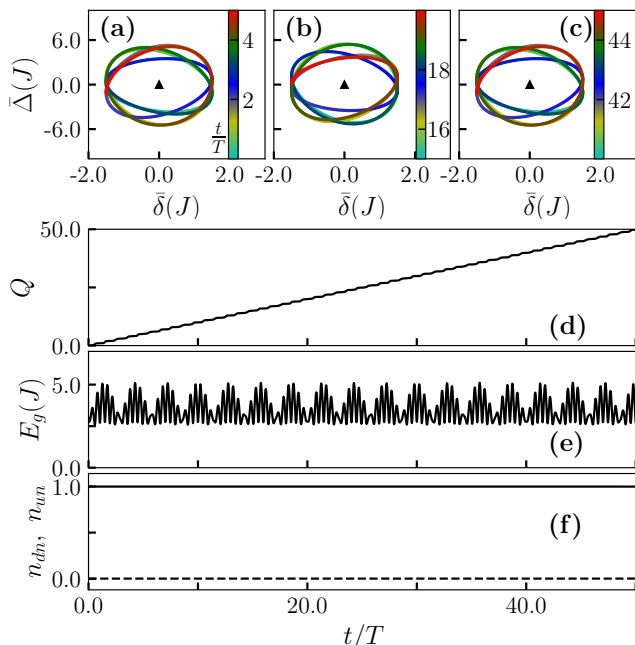


FIG. 5: Different quantities are displayed here after averaging over trajectories with $N_{traj} = 100$ to analyze the quantized pumping at finite $\gamma = 0.2J$ away from resonance where $\omega = 0.1J$ and $T = 90/J$. The effective pumping path is shown for three different time windows in (a), (b), and (c), corresponding to Fig. 4(a), which is also shown in (d) for reference. The black triangles mark the origins where the E_g should vanish. The $E_g(t)$ is shown in (e) and $n_{dn}(t)$ (solid line) and $n_{up}(t)$ (dashed line) are plotted in (f).

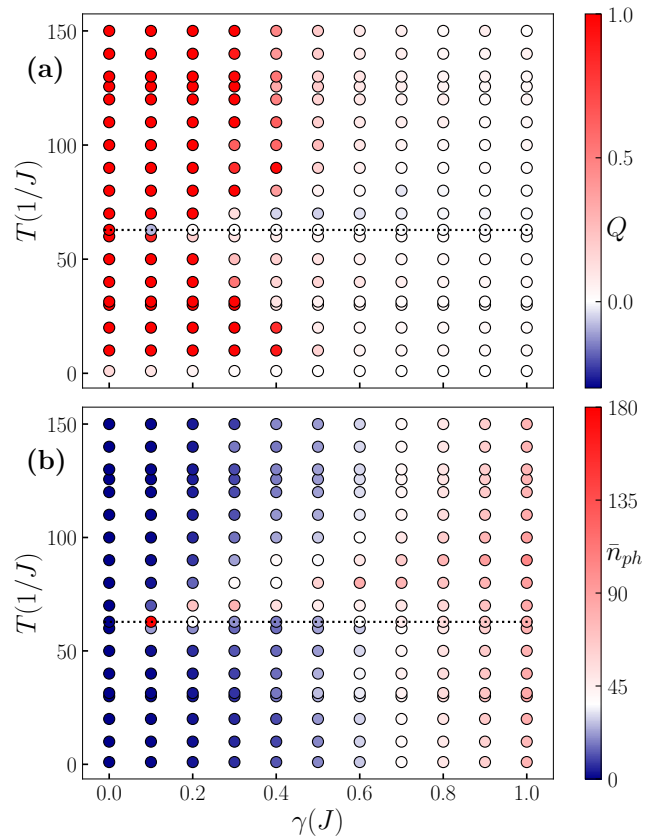


FIG. 7: The figure represent a stability diagram in T vs γ plane depending on the trajectory averaged (a) Q in a cycle and (b) \bar{n}_{ph} . Here we consider $N_{traj} = 100$ and average the Q and \bar{n}_{ph} over fifty pump cycles. The dashed lines represent the time period of phonons ($\frac{2\pi}{\omega}$).

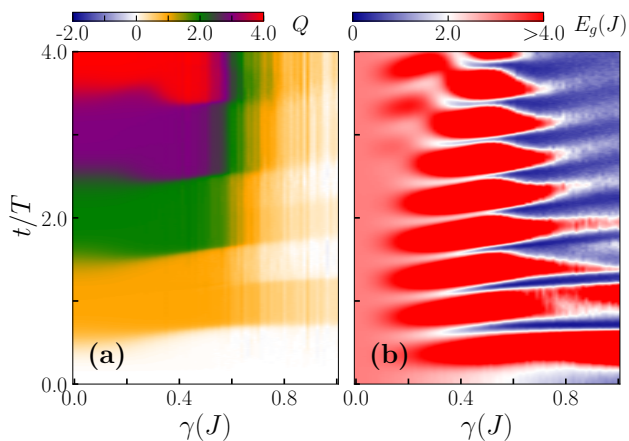


FIG. 6: (a) The trajectory averaged $Q(t)$ and (b) $E_{gap}(t)$ are shown away from resonance with $T = 90/J$, $\omega = 0.1J$ and $N_{traj} = 200$. The breakdown of quantized pumping near $\gamma \sim 0.5J$ is portrayed

7 Effects of adding many-body interactions to topological charge pumps

In this chapter I will introduce results on Thouless pumps in interacting systems. For closed, non-interacting systems, there exists a complete classification of all topological phases of matter, as a function of dimension and symmetry, which is coined the "periodic table of topology" [13, 14]. This classification has been extended to e.g. systems with additional symmetries [11], Floquet systems [18] and open systems [10].

One of the holy grails of topological systems research is a classification of topological states of matter for interacting systems. It has been shown that interaction effects change the number of possible distinct topological phases. For instance, strong many-body correlation effects can adiabatically connect two distinct non-interacting phases without closing a gap [12]. Interactions can also induce topology in an otherwise trivial system [284]. Progress has been made for a subset of models, such as fermionic models in 3 dimensions [19], one-dimensional Floquet systems [16] or interacting spin pumps [46], however, a full classification is out of reach. This is due to the plethora of exotic phases that exist in interacting systems; Mott insulators [285, 286, 287, 184, 156, 17, 288], spin liquids [289, 290], charge density waves [291, 292] and more [293].

In general, for moderate to low interaction strengths, it is expected that the non-interacting topology remains intact upon turning on interactions. One can understand this in a similar way to Fermi-liquid theory: Turning on interactions that do not necessarily lead to a topological phase transition adiabatically connects the non-interacting system to the phase of the interacting model which has mostly the same properties as its non-interacting counterpart [294].

For strong and more general many-body interactions, one has to deal with phase transitions that break this adiabatic connection to the free system, which can lead to surprising consequences, such as the breakdown of topological pumping [150, 38] but also induce new topological phases that have no counterpart in the non-interacting theory [159, 160, 39, 295]. One of the first examples of an interacting topological phase was the fractional quantum Hall effect [186, 187], which is an active area of research to this day [296, 297]. Here, the usually integer quantized Hall response is fractionalized. This can be explained via quasi-particles with fractional charge and statistics, so called anyons. Fractional quantum Hall states [298, 29, 188] and fractional charge pumps [157, 52, 299] have been proposed to be realizable in optical lattices.

Depending on the type of interaction, one also has to address charge and spin pumping

in a unified framework: A Hubbard interaction of the form

$$\hat{H}_{\text{int}} = U \sum_j \hat{n}_{j,\uparrow} \hat{n}_{j,\downarrow} \quad (7.1)$$

in a two-component fermionic system with spins \uparrow, \downarrow can couple the spin and charge sector. Spin-excitations can move with a different velocity to charge excitations and the effective quasi-particles can acquire fractional charge.

Due to this complexity, Thouless pumps are an ideal setting for researching interaction effects in topological systems, since their one-dimensional nature allows for both a simpler experimental realization in ultra-cold atomic systems and for an efficient numerical treatment using matrix-product state methods. Interacting topological pumping has been studied theoretically in bosonic [47, 157, 53, 149] and fermionic [158, 150, 151, 152, 159, 160, 153] systems. So far, most experiments on charge pumps have been done in the non-interacting setting. Recently, interactions in Thouless pumps have been experimentally studied in the mean-field setting [155, 300] and in a fermionic system [38].

In [152], an interacting topological pump in a Fermi-Hubbard-Harper model has been studied via instantaneous measures like the Berry phase and the many-body gaps. A phase diagram of critical points with singular Berry phase was presented that included regions with vanishing gap but well-defined Berry phase jumps by 2π . A so far open question has therefore been how these gapless regions manifest in real-time simulations of the pumped charge. This question is addressed in our following manuscript in this chapter.

The motivation of the present paper has initially come from the ionic Hubbard model [189], which has been the focus of many theoretical investigations [190, 191, 192, 193, 194, 195, 196]. The ionic Hubbard model is a one-dimensional fermionic model with repulsive Hubbard interaction of the form in eq. (7.1) with an additional staggered potential. When considering a spinful Rice-Mele model with an additional Hubbard interaction term, it is automatically realized for points along the pump cycle with vanishing hopping dimerization. It is known that the ionic Hubbard model hosts three different phases that are controlled by the staggered potential strength (or alternatively the interaction strength): A band-insulator with double-occupancies for strong staggering, a Mott-insulator with single-occupancies for low staggering, and an intermediate phase between band-insulator and Mott-insulator known as the "spontaneously dimerized insulator" or "bond-order wave", where the system spontaneously forms dimerized states. These phases differ by their many-body gaps in the charge and spin-sector. Crucially, these three phases can also be characterized by Berry phases and the analogous spin-Berry phases, which are both quantized to either 0 or π in the different phases [190].

We know that (spin-) Berry phases correspond to the position of the Wannier states and that their winding predicts the quantized pumped charge (spin) in an adiabatically modulated system. Therefore, we proposed to connect the different phases of the ionic Hubbard model adiabatically via a dimerized hopping, such that the quantized values of 0 or π are continuously transformed into each other. One then expects that surrounding critical points at the phase boundaries with an adiabatic cycle leads to the realization of

an adiabatic charge pump. Note that the concept of adiabatically connecting different symmetry-protected phases of an interacting system via an additional parameter has also been proposed in [159]. Initially, the idea was to connect the SDI phase with the BI due to the fact that the SDI phase has a finite spin- and excitation gap [192]. However, it has been challenging to pump this close to the critical points due to the fact that finite-size effects are dominant in their vicinity [51]. Instead, we focus on pumping through the Mott insulator.

We employ both time-dependent Lanczos calculations [242] for a periodic system and infinite time-evolving block decimation for calculating the pumped charge. We observe that upon adding a Hubbard interaction, the critical point of the spinful Rice-Mele model at the origin splits into two critical points where the Berry phase jumps. These critical points are the BI - SDI phase transition points and can be identified by a jump in the Berry phase. Connecting the BI and MI phases now amounts to pumping around a single critical point, which is achieved via a pump cycle that is shifted in the staggering-direction when compared to a usual Rice-Mele pump. Along the pump cycle, a dimerized Mott phase is traversed. In the limit of no potential offsets, this is a correlated SSH model, which has recently been shown to possess non-trivial spin-edge states and an adiabatic connection to the free SSH model [183]. Between the critical points in the Mott phase, the spin-gap vanishes. This gapless line seems to preclude quantized pumping through the Mott phase. Nevertheless, we observe nearly quantized charge pumping along the shifted pump cycle across the gapless line for the *first* pump cycle. I will come back to the breakdown of adiabaticity in section 7.3, where we study the time-dependence of charge- and spin-correlation and the breakdown of adiabaticity due to the gapless line in detail. In order to make the pumping through the gapless Mott phase topologically protected for many pump cycles, we also introduce two additional terms to the Hamiltonian that open the gap in the Mott phase. For these extended models, the pumping becomes robust and quantized over many pump cycles.

Our work sheds light on a recent experiment that has studied exactly our setup of a fermionic Rice-Mele pump with an additional Hubbard interaction [38]. There, the authors claim to observe a breakdown of quantized charge pumping for large interaction strengths. Instead, our work shows that what is measured is the change from a topologically non-trivial pump cycle, where critical points are encircled to a trivial pump cycle where the critical points have moved out of the pump cycle due to the Hubbard interaction. We argue that non-adiabatic effects play only a secondary role in the first pump cycle and that it is essentially impossible to detect them when not pumping for many pump periods. This is relevant since the experiment [38] does not go beyond the first cycle. The critical interaction-strength where this happens aligns with the experimentally observed onset of lowered pumped charge. Having shown that it is possible to split the critical points via a Hubbard interaction, we also introduce the possibility of interaction-induced pumping, which is the focus of section 7.3. After the publication of our paper in question, a similar split of critical points has been found in a non-interacting system of coupled Rice-Mele chains [65].

7.1 Publication: Splitting of topological charge pumping in an interacting two-component fermionic Rice-Mele Hubbard model

Article reprinted with permissions from Eric Bertok, Fabian Heidrich-Meisner and Armando A. Aligia.




Phys. Rev. B 106, 045141 (2022)

<https://doi.org/10.1103/PhysRevB.106.045141>

Copyright (2021) by the American Physical Society.

Author contributions: E.B. wrote the manuscript, carried out the numerical calculations, analyzed the data and prepared the figures. A.A.A. had the idea to study pumping in the ionic Hubbard model, suggested the toy models for the opening of the many-body gap and wrote the appendix. F.H.M. suggested to focus on the splitting of singularities and their effect on pumping. E.B. suggested the concept of interaction-induced pumping. All authors contributed to the interpretation of results, discussion of the data and revisions of the manuscript.

Splitting of topological charge pumping in an interacting two-component fermionic Rice-Mele Hubbard model

E. Bertok ¹, F. Heidrich-Meisner ^{1,*}, and A. A. Aligia ^{1,2}

¹*Institute for Theoretical Physics, Georg-August-Universität Göttingen, Friedrich-Hund-Platz 1, 37077 Göttingen, Germany*

²*Instituto de Nanociencia y Nanotecnología CNEA-CONICET, Centro Atómico Bariloche and Instituto Balseiro, 8400 Bariloche, Argentina*



(Received 12 May 2022; accepted 6 July 2022; published 27 July 2022; corrected 13 February 2023)

A Thouless pump transports an integer amount of charge when pumping adiabatically around a singularity. We study the splitting of such a critical point into two separate critical points by adding a Hubbard interaction. Furthermore, we consider extensions to a spinful Rice-Mele model, namely, a staggered magnetic field or an Ising-type spin coupling, further reducing the spin symmetry. The resulting models additionally allow for the transport of a single charge in a two-component system of spinful fermions, whereas in the absence of interactions, zero or two charges are pumped. In the SU(2)-symmetric case, the ionic Hubbard model is visited once along pump cycles that enclose a single singularity. Adding a staggered magnetic field additionally transports an integer amount of spin while the Ising term realizes a pure charge pump. We employ real-time simulations in finite and infinite systems to calculate the adiabatic charge and spin transport, complemented by the analysis of gaps and the many-body polarization to confirm the adiabatic nature of the pump. The resulting charge pumps are expected to be measurable in finite-pumping speed experiments in ultracold atomic gases for which the SU(2) invariant version is the most promising path. We discuss the implications of our results for a related quantum-gas experiment by Walter *et al.* [[arXiv:2204.06561](https://arxiv.org/abs/2204.06561)].

DOI: [10.1103/PhysRevB.106.045141](https://doi.org/10.1103/PhysRevB.106.045141)

I. INTRODUCTION

The advent of ultracold quantum-gas experiments [1–3] has opened the possibility of directly probing quantum many-body systems on lattice models to a high precision. Strongly interacting systems can give rise to many exotic phases that often arise due to the competition between different energy scales [4]. An open question in condensed matter theory is the precise interplay between many-body physics and topology. Thouless charge pumps [5–7] provide a practical framework to study interacting topological systems in a reduced spatial dimension due to their highly controllable experimental realizations. Experimentally, Thouless pumps have been realized in ultracold atoms for both bosons [8] and fermions [9–11], as well as in photonic systems [12].

In a Thouless pump, an integer amount of charge is pumped per pump cycle when adiabatically changing parameters such that a degeneracy (or critical point) is enclosed without closing a gap. The prototypical model for a noninteracting charge pump, the Rice-Mele model [13], has a single degeneracy at the origin as seen in Fig. 1(a). Δ is the strength of a staggered potential and δ is the strength of the hopping dimerization. For a noninteracting two-component fermionic system, going once around the path \mathcal{C}_2 pumps two particles, whereas going around \mathcal{C}_1 pumps no particles.

Theoretically, both bosonic [5,14–18] and fermionic [19–23] topological charge pumps have been studied. Due to

their readily available experimental realization, the interplay of Hubbard interactions and Thouless pumps in a two-component fermionic system is a key area of research. Recent works include theoretical studies of instantaneous topological measures for quantum many-body phases [24], the theoretical [20] and experimental [11] study of the breakdown of topological pumping due to interactions and interaction-induced topological pumping [21,25]. Another direction concerns the study of charge pumps in the presence of disorder [26–32].

Here we address the question whether it is possible to split the degeneracy of the noninteracting Rice-Mele model into two separate ones by adding a repulsive on-site interaction, as sketched in Fig. 1(b). In this case, going along path \mathcal{C}_1 pumps a single charge for a finite interaction strength. With this scheme, it becomes possible to change the amount of charge pumped from zero to one by solely changing the Hubbard interaction strength. Keeping an origin-centered pumping path instead, encircling no singularities at sufficiently large U [$\tilde{\mathcal{C}}_2$ in Fig. 1(b)], leads to a topologically protected pumped charge of zero.

We show that this splitting is possible in three distinct situations that differ by their symmetries: (a) an SU(2) symmetric fermionic model with Hubbard interactions, which can be viewed as an ionic Hubbard model (IHM) with additional alternating hopping amplitudes, (b) a model with an easy-axis spin symmetry, and (c) a model with broken Z_2 symmetry. The three cases vary in the degree of adiabaticity that manifests itself in the nature of the gaps along the zero-dimerization line connecting the two critical points: The SU(2) symmetric model has a vanishing many-body gap on this line, as the Mott phase of the IHM is realized between the critical points

*Corresponding author: fabian.heidrich-meisner@uni-goettingen.de

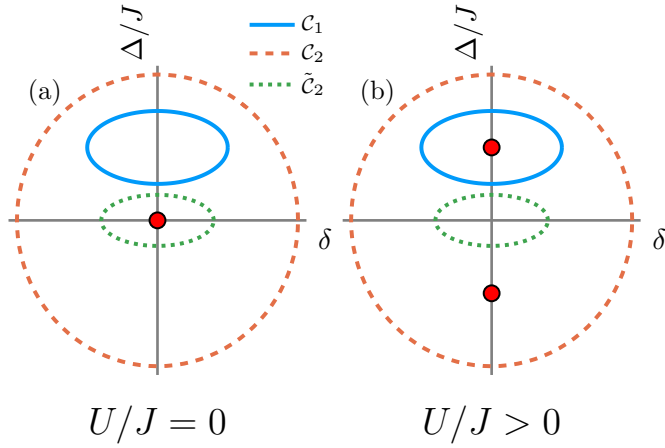


FIG. 1. Sketch of pump cycles in the Rice-Mele-Hubbard model. Δ is the amplitude of the staggered potential. δ is the hopping modulation. Two types of path are considered: \mathcal{C}_1 is centered around a point on the Δ -axis with a nonzero offset, while \mathcal{C}_2 and $\tilde{\mathcal{C}}_2$ are centered around the origin. (a) For $U = 0$, two charges are pumped along \mathcal{C}_2 and $\tilde{\mathcal{C}}_2$ while no charges are pumped along \mathcal{C}_1 . (b) For finite interactions, one charge is pumped along \mathcal{C}_1 instead. Along \mathcal{C}_2 , two charges are pumped still, while along $\tilde{\mathcal{C}}_2$, zero charges are pumped, as no singularity is encircled.

($\delta = 0$ and $-\Delta_s \leq \Delta \leq \Delta_s$, where $\pm\Delta_s$ are the values of Δ at the spin transitions discussed in Sec. IV C) [33,34]. In the easy-axis case, a twofold degenerate ground state is obtained along this line (and in a finite region around $\delta = \Delta = 0$ in the thermodynamic limit) that is well separated from the rest of the spectrum. Finally, the Z_2 -broken case has a nondegenerate ground state separated by a robust gap from the rest of the spectrum everywhere apart from the critical points. We realize these three cases via (a) a Rice-Mele Hubbard model, which we take as a base model, (b) an additional Ising-type term, and (c) via an additional staggered magnetic field added to the Rice-Mele Hubbard model, respectively. This is realized by three Hamiltonians, \hat{H}_{IH} , \hat{H}_{IHZ} , and \hat{H}_{IHB} , respectively.

Conceptually, the Z_2 broken Hamiltonian \hat{H}_{IHB} has the most robust topology at the price of introducing a nonzero quantized spin current. The dimerized ionic Hubbard model \hat{H}_{IH} does not feature a strict topological protection since along pump cycle \mathcal{C}_1 , points exist with a vanishing spin gap. The charge gap remains open in all three cases.

As our main result, we show that we can achieve integer-quantized charge pumping around a single degenerate point. We demonstrate, via finite-time calculations, that \hat{H}_{IHB} and \hat{H}_{IHZ} allow for robust quantized charge pumping of a single charge per pump cycle around a single critical point. For \hat{H}_{IH} , we pump through a many-body gapless phase. Still, for appropriately chosen pump cycles, the pumped charge is practically quantized on the accessible timescales, which is confirmed via time-dependent infinite-system matrix-product-state methods [35,36]. We study the topology of the three models via instantaneous measures such as the energy gaps and the charge (spin) Berry phase calculated via the many-body charge- (spin-) polarization [37–39]. While all models show a well-defined and smooth charge Berry phase, the spin Berry phase of \hat{H}_{IHZ} and \hat{H}_{IH} depicts a jump at a finite hopping modulation.

Our results have consequences for experiments on interacting charge pumps [11]. Especially, the $SU(2)$ -symmetric case is particularly simple to realize in ultracold-atomic gas experiments by adding a time-dependent hopping modulation to an IHM [40]. Even though the pumping happens through a gapless phase in this case, we expect that integer charge pumping can be observed as we do in real-time simulations, due to finite system sizes and the resulting finite-size gaps, at least for a sequence of initial pump cycles. Our results shed additional light on the interpretation of the recent experiment by Walter *et al.* [11], where the authors interpret the behavior along a cycle similar to $\tilde{\mathcal{C}}_2$ as a breakdown of quantized particle pumping as a function of U . We here reinterpret their results in terms of Fig. 1(b) as a consequence of the singularities moving out of the cycle $\tilde{\mathcal{C}}_2$ as U increases.

The paper is structured as follows. In Sec. II, we start by introducing the three models and define the relevant many-body gaps. Section III showcases the instantaneous and time-dependent measures and our numerical methods. In Sec. IV, we present our results by starting with time-dependent simulations for the pumped charge, subsequently discussing energy gaps and concluding with the Berry phases. We conclude in Sec. V with a summary and discuss implications for a recent experimental [11] and a related theoretical [20] study on the breakdown of topological pumping in interacting systems.

II. MODEL

We consider a class of models of correlated fermions with a staggered potential Δ , hopping dimerization δ , a staggered magnetic field of strength b , and an Ising-type term of strength J_z ,

$$\hat{H} = \hat{H}_{\text{IH}}(\delta, \Delta) + \hat{H}_{\text{B}} + \hat{H}_{\text{Z}}, \quad (1)$$

where

$$\begin{aligned} \hat{H}_{\text{IH}}(\delta, \Delta) = & -J \sum_{j=1}^L \sum_{\alpha=\uparrow,\downarrow} (1 + \delta (-1)^j) (\hat{c}_{j,\alpha}^\dagger \hat{c}_{j+1,\alpha} + \text{H.c.}) \\ & + \Delta \sum_{j=1}^L \sum_{\alpha=\uparrow,\downarrow} (-1)^j \hat{c}_{j,\alpha}^\dagger \hat{c}_{j,\alpha} \\ & + U \sum_{j=1}^L \hat{c}_{j,\uparrow}^\dagger \hat{c}_{j,\uparrow} \hat{c}_{j,\downarrow}^\dagger \hat{c}_{j,\downarrow} \end{aligned} \quad (2)$$

is the dimerized IHM,

$$\hat{H}_{\text{B}} = b \sum_{j=1}^L (-1)^j \hat{S}_j^z \quad (3)$$

is a staggered magnetic field, and

$$\hat{H}_{\text{Z}} = J_z \sum_{j=1}^L \hat{S}_j^z \hat{S}_{j+1}^z \quad (4)$$

is an Ising spin coupling. Here, $\hat{c}_{j,\alpha}^\dagger$ creates a fermion of spin $\alpha \in \uparrow, \downarrow$ on site j . The spin operators are given as $\hat{S}_j^z = 1/2(\hat{c}_{j,\uparrow}^\dagger \hat{c}_{j,\uparrow} - \hat{c}_{j,\downarrow}^\dagger \hat{c}_{j,\downarrow})$. L is the number of sites. For $b = J_z = \delta = 0$, the IHM is recovered.

The phase diagram of the IHM has been studied in detail [33,34,41]. The half-filled IHM hosts three phases, depending on the parameters Δ and U : A Mott insulating (MI) phase and a band insulating (BI) phase that are separated by a spontaneously dimerized (SDI) phase.

The IHM has been originally proposed [42] to describe the neutral-ionic transition in mixed-stack donor-acceptor organic crystals [43] and is also relevant for one-dimensional ferroelectric perovskites [44]. Its phase diagram has been determined accurately (minimizing finite-size effects) using the method of topological transitions [39]. For this model, these transitions also coincide with those obtained with the method of crossing of excited energy levels (MCEL) based on conformal field theory [45–47]. There exists considerable theoretical evidence for the existence of a bond-order wave (BOW) phase between the MI and BI phases. This phase occurs naturally when starting in the MI phase for $\delta = 0$ and adding a small δ , because this term breaks the inversion symmetry (see Appendix). However, for $\delta = 0$, this symmetry is broken spontaneously in the thermodynamic limit leading to a spontaneously dimerized insulator (SDI) separating the MI and BI phases. The SDI phase has been found first by bosonization [48]. The IHM has recently been experimentally realized with ultracold atoms in a hexagonal lattice [49,50]. The SDI has not directly been observed in experiments, although its direct measurement with superlattice modulation spectroscopy has recently been proposed [40].

In the following, we consider three families of Hamiltonians to split the charge critical points choosing the following sets of parameters:

- (1) $\hat{H}_{\text{IH}}(\delta, \Delta) : (b, J_z) = (0, 0)$
- (2) $\hat{H}_{\text{IHB}}(\delta, \Delta) : (b, J_z) = (0.5J, 0)$
- (3) $\hat{H}_{\text{IHZ}}(\delta, \Delta) : (b, J_z) = (0, 2J)$.

The exact choice of parameters does not play a role as long as the topologies of pump cycles \mathcal{C}_1 and \mathcal{C}_2 are preserved.

The pumping paths $\mathcal{C}_1, \mathcal{C}_2$ are parameterized via the pump parameter $\theta \in [0, 2\pi)$:

$$\begin{aligned} \mathcal{C}_1(\theta) &= (\Delta(\theta), \delta(\theta)) = (\Delta_c + R_\Delta \sin \theta, R_\delta \cos \theta), \\ \mathcal{C}_2(\theta) &= (\Delta(\theta), \delta(\theta)) = (R_\Delta \sin \theta, R_\delta \cos \theta). \end{aligned} \quad (5)$$

The evolution along path \mathcal{C}_1 for all three models goes through a phase with a nonzero BOW order parameter. In particular, \hat{H}_{IH} passes through the MI phase of the IHM at $\delta = 0$, surrounded by the BOW phase as soon as $\delta \neq 0$. The same has happened in recent theoretical [20] and experimental [11] works for path $\tilde{\mathcal{C}}_2$, for which a breakdown of the quantized charge transport was reported. Using a canonical transformation valid for small J and $|\delta|$ and known results for a Heisenberg chain with alternating exchange, we see that at the MI-BOW transition, the spin gap opens as $|\delta|^{2/3}$ while the change in polarization and the BOW order parameter behave as $\delta^{1/3}$ for small $|\delta|$. The details are in the Appendix.

The three phases in the IHM can be distinguished via the behavior of various many-body gaps. To distinguish the physics of the three models defined above, we introduce the following energy gaps. We define the internal gap

$$\Delta E_{\text{int}} = E_1(N, S_z = 0) - E_0(N, S_z = 0) \quad (6)$$

as the first excitation energy keeping the total number of particles N and the total spin projection $S_z = 0$ constant. We also define the charge gap

$$\begin{aligned} \Delta E_C &= [E_0(N + 2, S_z = 0) + E_0(N - 2, S_z = 0) \\ &\quad - 2E_0(N, S_z = 0)]/2, \end{aligned} \quad (7)$$

the spin gap

$$\Delta E_S = E_0(N, S_z = 1) - E_0(N, S_z = 0), \quad (8)$$

and the second internal gap

$$\Delta E_2 = E_2(N, S_z = 0) - E_0(N, S_z = 0). \quad (9)$$

III. METHODS AND OBSERVABLES

A. Instantaneous measures

For the instantaneous measures, we use the Lanczos method for a finite system with periodic boundary conditions up to $L = 12$. The charge and spin gaps are calculated by searching for the lowest energy in the respective symmetry sectors. For the internal gap calculation, several low-lying eigenstates are computed.

The charge (spin) pumping is related to the charge (spin) Berry phases [34]:

$$\begin{aligned} \gamma_{C,S} = - \lim_{N \rightarrow \infty} \text{Im} \left\{ \ln \left[\prod_{r=0}^{N-2} \langle g(\Phi_r, \pm \Phi_r) | g(\Phi_{r+1}, \pm \Phi_{r+1}) \rangle \right. \right. \\ \left. \left. \times \langle g(\Phi_{N-1}, \pm \Phi_{N-1}) | g(2\pi, \pm 2\pi) \rangle \right] \right\}, \end{aligned} \quad (10)$$

with $|g(2\pi, \pm 2\pi)\rangle = \exp[i2\pi/L \sum_j j(\hat{n}_{j\uparrow} \pm \hat{n}_{j\downarrow})] |g(0, 0)\rangle$, where N is the number of discretization steps for the twisted boundary conditions, $\Phi_r = 2\pi r/N$ and $|g(\Phi, \Phi')\rangle$ is the ground state of the Hamiltonian in which the hopping J for spin up (down) has been changed by a factor $\exp(i\Phi/L)$ [$\exp(i\Phi'/L)$]. Notice that the charge (spin) Berry phase $\gamma_{C,S}$ depends on the pump parameter θ because the ground states $|g(\Phi, \Phi')\rangle$ do. The pumped charge (spin) after one pump cycle in the quasia diabatic limit is given by

$$\Delta Q_{C,S} = \frac{1}{2\pi} \int_0^{2\pi} d\theta \partial_\theta \gamma_{C,S}(\theta). \quad (11)$$

The parameters Δ and δ depend on a geometrical variable θ [see Eq. (5)], which in turn depends on time t . In the quasia diabatic limit under a cyclic evolution in which θ returns to its original value, the charge transport is purely geometrical and does not depend on the explicit time dependence of θ .

In practice, with a number of points $N \sim 10$, one has a very accurate result for $\gamma_{C,S}$. In addition, although with a slower convergence with system size L , the exponential position operator can be used to arrive at the many-body polarization [37,38], which is the one-point approximation of Eq. (10). The position operator defined in Ref. [37] cannot be used for interacting systems with fractional filling but can easily be extended [38]. The extension to γ_S has been introduced in

Ref. [39]. We use the following form of the charge and spin polarization:

$$P_C(\theta) = \frac{1}{2\pi} \text{Im} \ln \langle \Psi(\theta) | \hat{X}_C^e | \Psi(\theta) \rangle, \quad (12)$$

$$P_S(\theta) = \frac{1}{2\pi} \text{Im} \ln \langle \Psi(\theta) | \hat{X}_S^e | \Psi(\theta) \rangle, \quad (13)$$

with $\hat{X}_{C,S}^e = \exp[i(2\pi/L)\Sigma_j j(\hat{n}_{j\uparrow} \pm \hat{n}_{j\downarrow})]$ [39]. $2\pi P_{C,S}$ is equivalent to $\gamma_{C,S}$.

The thermodynamic phases of the IHM are distinguished by their values of the charge and spin Berry phases γ_C and γ_S [34]. More precisely, the Berry phases (γ_C, γ_S) are quantized due to inversion symmetry and have the values $(\pi, \pi)_{\text{MI}}$, $(\pi, 0)_{\text{SDI}}$ and $(0, 0)_{\text{BI}}$. These quantized Berry phases arise in our models for $\delta = 0$. Additionally, due to a spin-rotation symmetry of π around any axis perpendicular to the z axis in spin space for all values of δ and Δ , \hat{H}_{IHZ} and \hat{H}_{IH} can only have spin Berry phases of 0 or π , whereas \hat{H}_{IHB} breaks this symmetry, allowing for arbitrary spin Berry phases.

For all finite-system calculations, we use open-shell boundary conditions (periodic boundary conditions for a number of sites L multiple of four, antiperiodic for even L not a multiple of four) to allow for the resolution of gap closings.

B. Real-time calculations

For the finite-time calculation, we parametrize the pump cycles with the time t as

$$\theta = \frac{2\pi}{T}t, \quad (14)$$

where T is the pump period. The accumulated pumped charge (spin) at time t is calculated via

$$Q_{[S]}(t) = \int_0^t dt' \langle \hat{J}_{[S]}(t') \rangle, \quad (15)$$

where the total particle and spin currents, averaged over two links are

$$\hat{J} = \frac{i}{2} \sum_{j=1,2;\alpha=\uparrow,\downarrow} (J_j \hat{c}_{j,\alpha}^\dagger \hat{c}_{j+1,\alpha} - \text{H.c.}), \quad (16)$$

$$\hat{J}_S = \frac{i}{2} \sum_{j=1,2;\alpha=\uparrow,\downarrow} (\sigma_{\alpha,\alpha}^z J_j \hat{c}_{j,\alpha}^\dagger \hat{c}_{j+1,\alpha} - \text{H.c.}), \quad (17)$$

where $J_j = J(1 + \delta(-1)^j)$. To minimize transient nonadiabatic effects, the pumping is first started slowly via a quadratic ramp-up of the driving [51]. We use a pumping period of $TJ = 50$, which is enough to ensure quasiadiabaticity for the IHB and IHZ models. For the IH model, strong finite-size effects [52] make Lanczos calculations unfeasible. We therefore also use infinite-system density matrix renormalization group (DMRG) methods [53,54] to calculate the pumped charge in time-dependent simulations. The ground state is calculated via the variational uniform matrix-product state method [36]. The time-evolution is carried out via infinite time-evolving block decimation (iTEBD) [55]. For the IH model, we use a period of $TJ = 1000$ and a maximum bond dimension of $\chi = 200$. All DMRG calculations are done using the ITensor library for Julia [56].

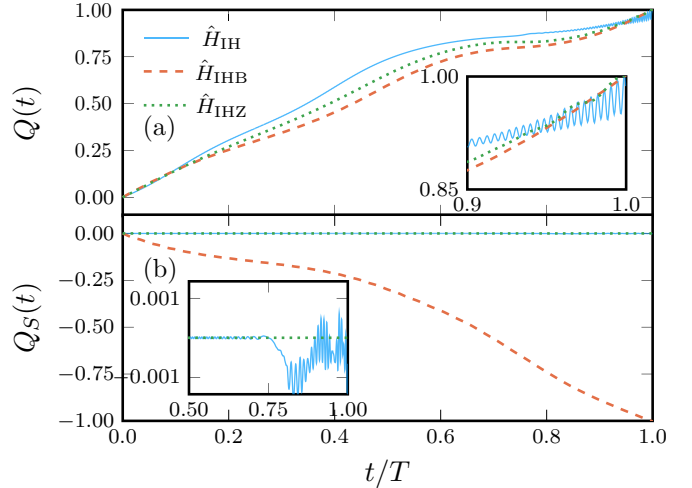


FIG. 2. Real-time calculation of the pumped charge along C_1 . (a) Both models \hat{H}_{IHB} and \hat{H}_{IHZ} show integer-quantized charge pumping. \hat{H}_{IH} shows approximately quantized pumping. (b) \hat{H}_{IHB} additionally shows quantized spin transport, whereas \hat{H}_{IHZ} is a pure charge pump. For IHB and IHZ, we use Lanczos with $L = 12$ and $TJ = 50$. For IH, we use iTEBD with $\chi = 200$ and $TJ = 1000$. Parameters are $U/J = 4$ and IH: $R_\Delta/J = 1$, $R_\delta = 0.2$, $\Delta_c/J = 2.2$. IHB: $R_\Delta/J = 2$, $R_\delta = 0.9$, $\Delta_c/J = 2.24$. IHZ: $R_\Delta/J = 2$, $R_\delta = 0.9$, $\Delta_c/J = 2$.

IV. RESULTS

A. Real-time calculations

First, we consider a finite pumping period and demonstrate the quantized particle pumping in a time-dependent calculation of the integrated current for finite systems. For \hat{H}_{IHB} and \hat{H}_{IHZ} , the results for the pumped charge after one period along pump cycle C_1 from Fig. 1 are shown in Fig. 2(a) for a system size of $L = 12$ and $TJ = 50$. Both models show an integer-quantized pumping of a single charge. We have checked convergence with respect to system size L for both models. In Fig. 2(b), the pumped spin of the same models and pumping path is shown. \hat{H}_{IHZ} pumps no spin and is therefore a pure charge pump. \hat{H}_{IHB} shows an integer-quantized pumping of a single spin along C_1 .

In contrast, for \hat{H}_{IH} along C_1 , finite-system calculations are not sufficient to overcome the large finite-size effects that arise from pumping through a gapless phase [52]. We therefore employ infinite-system size calculations for this model. For a period of $TJ = 1000$ and a maximum bond dimension of $\chi = 200$, the results are presented in Fig. 2 for C_1 . We observe approximate integer charge pumping and no spin pumping. However, local spin oscillations arise when reaching the gapless point between the two critical points for $t/T = 0.75$. This leads to an oscillatory behavior of the pumped charge. Interestingly, the envelope of these oscillations reaches a quantized value of one. The calculations converge with increasing bond dimension until the gapless point. Beyond this, the local spin and charge oscillations show a strong dependence on both the bond dimension χ and the pumping period T . This suggests that in the thermodynamic limit, the quantized pumping may break down. This limit is only recovered for $\chi \rightarrow \infty$ in infinite-system size DMRG. Along C_2 , all models exhibit

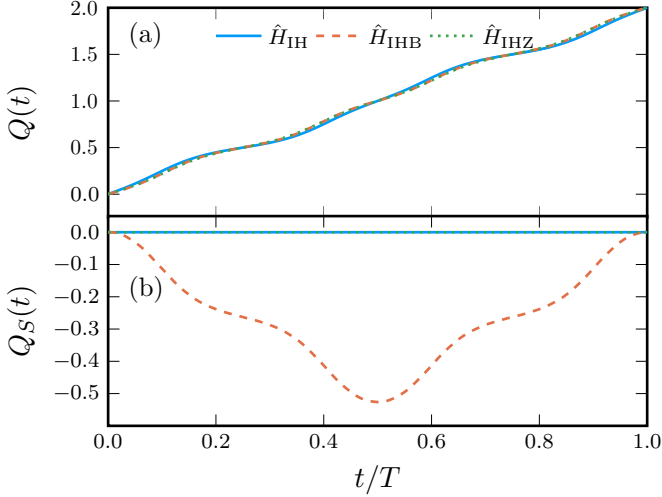


FIG. 3. Lanczos calculation of the pumped charge along \mathcal{C}_2 in a finite system. (a) All models show integer-quantized charge pumping of two particles per cycle. (b) \hat{H}_{IHB} displays a finite spin current but a net-zero pumped spin. Calculated for $L = 12$, $U/J = 4$, $TJ = 50$, $R_\Delta/J = 4$ and $R_\delta = 0.9$.

quantized pumping of two particles and zero spin for $TJ = 50$, which is shown for $L = 10$ in Fig. 3.

We have checked the quantization for the first 20 pump cycles and find a very robust quantization for \mathcal{C}_2 for all models as expected. In the infinite system, calculations for multiple pump cycles around \mathcal{C}_1 indicate a significant deviation from quantization from the second pump cycle onward for \hat{H}_{IH} and \hat{H}_{IHZ} . For a finite system, the pumped charge for both \hat{H}_{IHB} and \hat{H}_{IHZ} is integer quantized for the first 20 pump cycles within experimental accuracies [results not shown here].

B. Energy gaps

To understand the real-time simulations, we consider instantaneous measures for all models. We calculate the lowest 50 eigenenergies for all three models in the symmetry sectors $S_z = 0$ and $S_z = 1$ for $L = 12$ along the path \mathcal{C}_1 . The results are shown in Fig. 4 for $\theta \in [\pi, 2\pi]$, which corresponds to half a pump cycle \mathcal{C}_1 of Fig. 1. At $\theta = 3\pi/2$, the path is in between the two critical points along the $\delta = 0$ line.

The ground state of \hat{H}_{IHB} is nondegenerate for all values of θ and separated from the rest of the spectrum by a robust gap. The ground state of \hat{H}_{IHZ} is twofold degenerate for $L \rightarrow \infty$ in the MI phase, which extends to a region around $\Delta = \delta = 0$. Proceeding as in the Appendix, the ground-state energy becomes

$$E_{MI} = -J_z/4 - 4\tilde{U}J^2(1 + \delta^2)/(\tilde{U}^2 - 4\Delta^2) \quad (18)$$

for both Néel-like states, where $\tilde{U} = U + 3J_z/4$. However, the two crossing levels that make up this ground-state manifold are separated from the rest of the spectrum. The real-time simulations indicate that this is sufficient to ensure quantized particle transport for at least the first few pump cycles. In contrast, \hat{H}_{IH} , which becomes the regular IHM at $\delta = 0$, becomes fully gapless in the thermodynamic limit, since the spin gap vanishes in the MI at $\delta = 0$ [48]. We therefore expect that in the thermodynamic limit, the pumping will ultimately

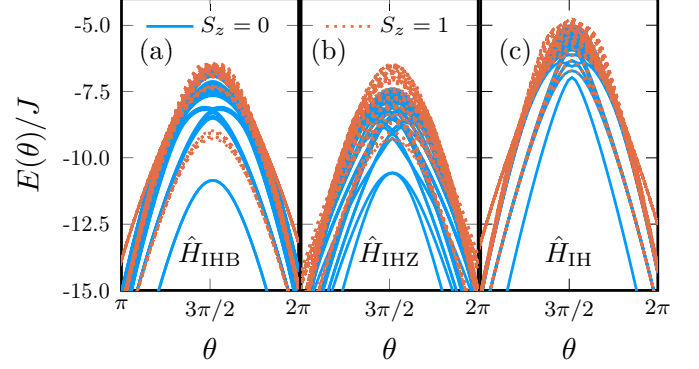


FIG. 4. Energy levels along \mathcal{C}_1 . The lowest 50 energy levels along the path \mathcal{C}_1 are plotted for the $S_z = 0$ and $S_z = 1$ subspaces. \hat{H}_{IHB} has a nondegenerate ground state that is separated from the rest of the spectrum. \hat{H}_{IHZ} has a twofold-degenerate ground state at $\theta = 3\pi/2$ that is separated from the rest of the spectrum. \hat{H}_{IH} becomes fully gapless for $L \rightarrow \infty$. Calculated for $L = 12$, $U/J = 4$, $R_\Delta/J = 2$, $R_\delta = 0.9$, and $\Delta_c/J = 2.24$.

break down in the IH case, consistent with Ref. [20]. In this sense, we believe that for a finite system, which is relevant for ultracold atomic gas experiments, the finite-size gap can be used to protect the pumping of an integer amount of particles for a few pump cycles.

In Fig. 5, the energy gaps defined in Sec. II are shown along the $\delta = 0$ line, where we expect a gapless phase between the two critical points of the IHM. The gaps are calculated

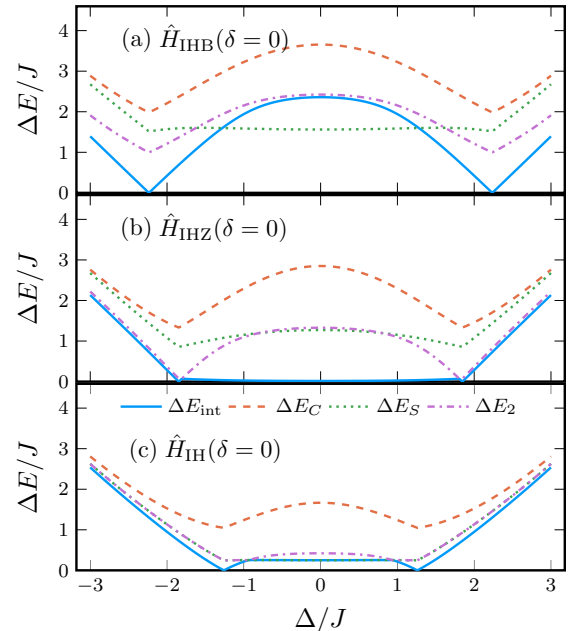


FIG. 5. Energy gaps along the $\delta = 0$ line. (a) In the center between the two critical points, \hat{H}_{IHB} is fully gapped with the smallest gap being the spin gap. (b) For \hat{H}_{IHZ} , the second internal gap approaches the finite spin gap. The internal gap vanishes due to the twofold-degenerate ground state. (c) For \hat{H}_{IH} , the spin gap is equivalent to the internal gap, which becomes zero in the thermodynamic limit. The charge gap is finite for all models. Calculated for $L = 12$ and $U/J = 4$.

for various system sizes and shown for $L = 12$. For all three models, the charge gap is finite for all system sizes, which is a necessary condition for quantized charge transport. For \hat{H}_{IHB} , all gaps are finite except at the critical points. The spin gap becomes the smallest gap between the critical points and is on the order of the staggered magnetic field term, which is independent of the system size. Therefore, the topologically protected charge pumping in this model is robust for all system sizes.

The internal gap of \hat{H}_{IHZ} vanishes between the two critical points, as was already observed in Fig. 4. This is due to a twofold-degenerate ground-state manifold between a Néel-like state ($\uparrow \downarrow \uparrow \downarrow$) and an anti-Néel like one ($\downarrow \uparrow \downarrow \uparrow$) in the thermodynamic limit, which is unaffected by the Ising term. The second internal gap stays finite, which shows that the ground-state manifold is separated by a gap from the rest of the spectrum.

For \hat{H}_{IH} , the internal gap is of the order of a finite-size gap and converges very slowly with system size. The internal gap vanishes at the MI to SDI transition but remains finite in the SDI phase, which has been shown in Ref. [33]. The SDI to MI transition is characterized by a crossing of excited energy levels. The excited even singlet crosses with the excited odd triplet, which has less energy in the MI phase [34]. Specifically, the internal gap becomes the spin gap in the MI phase. This is due to a crossing of energy levels with opposite inversion symmetry. An odd singlet is the ground state in the SDI and MI phases, while in the BI, the ground state is an even singlet [34]. According to conformal field theory, the spin gap scales as $2\pi v_s/L$, where v_s is the spin velocity [45]. Therefore, the IHM becomes gapless in the thermodynamic limit.

C. Berry phase and many-body polarization

We now address the topology of the three models. In particular, we are interested in the charge and spin Berry phases, which give information on the pumped charges and spins in a quasiadiabatically driven system. We use the many-body polarization in Eq. (13) to calculate the Berry phases for a finite system of $L = 10$. The results for the charge (spin) Berry phases are shown in Figs. 6(a), 6(c) and 6(e) [6(b), 6(d), and 6(f)]. For all models, the charge Berry phases are well-defined and smooth everywhere except for the two critical points. Notice that the branch cuts that emerge from the critical points are $\Delta\gamma_{C,S} = \pm 2\pi$ and therefore well-defined. The position of the branch cuts can be changed via a gauge transformation. Physically relevant information is only encoded in the total Berry phase picked up along a closed path.

\hat{H}_{IHB} has a well-defined and smooth spin Berry phase. Notice that around the upper singularity, the sign of the spin-Berry phase is opposite to the charge-Berry phase. This means that encircling one critical point pumps both spin and charge. More specifically, pumping around the upper (lower) critical point pumps only a single spin-down (-up) particle.

The spin Berry phase for \hat{H}_{IHZ} and \hat{H}_{IH} only has the values $\gamma_S \in \{0, \pi\}$. The value of π is realized between the critical points for both models as is expected for the IHM. For $\gamma_S = \pi$, the ground state is in the MI phase. The quantization arises due to the spin-rotation symmetry in these two models which maps $\gamma_S \mapsto -\gamma_S$. For \hat{H}_{IH} , the spin Berry phase is expected to

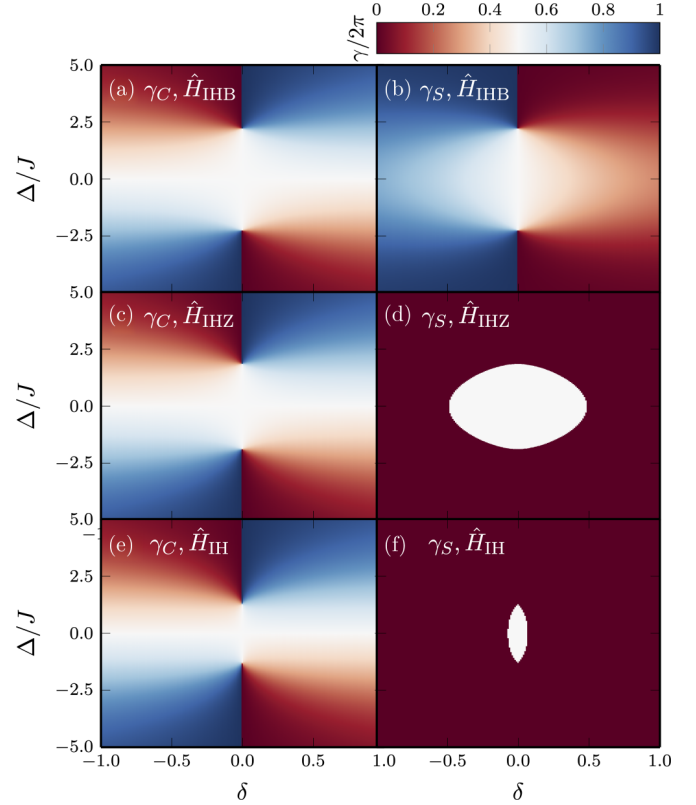


FIG. 6. Charge and spin Berry phases in the $\delta - \Delta$ plane. (a), (c), (e) Charge Berry phase γ_C . (b), (d), (f) Spin Berry phase γ_S . (a), (b) \hat{H}_{IHB} , (c), (d) \hat{H}_{IHZ} , (e), (f) \hat{H}_{IH} . Calculated for $L = 10$ and $U/J = 4$.

be nonzero only for $\delta \neq 0$ in the thermodynamic limit, since a finite δ breaks the inversion symmetry and leads to a finite BOW order parameter (see Appendix). The small lentil shape seen in Fig. 6(f) is therefore likely a finite-size effect. For \hat{H}_{IHZ} , the transition between dimerized phase and Mott phase happens at finite δ . A similar transition has recently been observed in dimerized XXZ Hamiltonians [57]. The value of δ where the transition happens decreases with increasing system size for small systems (not shown here). Perturbation theory along the lines of the Appendix [see Eq. (18)] indicates that this region remains finite, though. In real-time simulations, the jump in γ_S has no effect on the quantization of pumped charge for the IHZ model. We therefore argue that quantized particle pumping without spin pumping is possible around a single critical point in this model. Figure 7 shows the charge (spin) Berry phases γ_C [γ_S] for both paths \mathcal{C}_1 and \mathcal{C}_2 for all three models as the angular variable in a polar plot [26]. This is done because the winding of the Berry phase is equal to the pumped charge. The charge Berry phase shows an integer winding for both \mathcal{C}_1 and \mathcal{C}_2 for all models, which mirrors the results from Fig. 6. The spin Berry phase only shows a well-defined winding of one in the case of \mathcal{C}_1 and zero for \mathcal{C}_2 for \hat{H}_{IHB} . This is consistent with an interacting Rice-Mele pump that pumps one charge per species and no spins. For \mathcal{C}_2 , the IHZ and as IH models show a smooth spin-Berry phase with no winding as well, as long as the lentil shape of $\gamma_S = \pi$ is surrounded completely. The \mathcal{C}_1 paths inevitably go

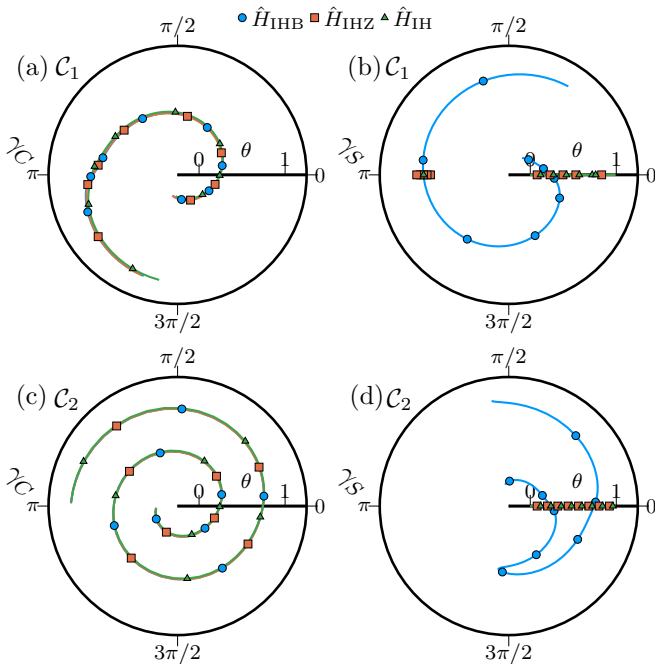


FIG. 7. Charge and spin Berry phases along pump cycles C_1 and C_2 . (a), (c) Charge Berry phase γ_C . (b), (d) Spin Berry phase γ_S . Calculated for $L = 10$ and $U/J = 4$. C_1 : $R_\Delta/J = 2$, $R_\delta = 0.9$, $\Delta_c/J = 2.24$. C_2 : $R_\Delta/J = 4$, $R_\delta = 0.9$.

through the spin transition and therefore show a discontinuity in the spin-Berry phase. This means that the spin-Berry phase no longer has a well-defined winding and no adiabatic spin transport should be possible in an infinite system. However, in practice, we see that in real-time simulations, \hat{H}_{IHZ} effectively behaves as if γ_S has a well-defined zero winding, at least for the first pump cycle. This is true for both finite-size and infinite-system calculations (the latter not shown here). We therefore expect this model to be well-behaved in ultracold atom experiments with finite particle numbers.

V. SUMMARY AND DISCUSSION

We showed that it is possible to split up the degeneracy of a two-component Rice-Mele model via a Hubbard interaction term. We presented three concrete models to achieve this that are based on an interacting two-component Rice-Mele model with a shifted pump cycle: A spin-SU(2) symmetric model, which realizes the IHM during the pump cycle (IH), a model with an additional staggered magnetic field (IHB), and a model with an additional Ising term (IHZ). We confirmed the quantization of the pumped charge via finite and infinite-system real-time calculations and instantaneous measures for periodic boundary conditions.

The quantization is most robust in the IHB case, which is robustly gapped everywhere. As a consequence, both charge and spin Berry phases are well-defined everywhere except at the critical points. However, the staggered field leads to an additional nonzero quantized spin pumping.

For IHZ, quantization holds for the first couple of pump cycles for experimentally relevant timescales in a finite system, despite the twofold-degenerate ground state. While the charge

Berry phase is well-defined as in the IHB case, the spin Berry phase jumps at a finite value of the hopping modulation.

The IHM, which is visited during all of our considered pump cycles in the IH case, features a Mott phase with a vanishing spin gap to a continuum of excitations that we pump through along C_1 , which should lead to an eventual breakdown of quantized particle transport. However, a clear remnant of the underlying topology is preserved and the pumped charge is approximately quantized in the first cycle. This is consistent with the well-defined charge Berry phase in this case. The spin-Berry phase shows a jump similar to the IHZ case, which is only expected at zero hopping modulation in the thermodynamic limit. Unlike the IHB, the spin current is manifestly zero for the IH and IHZ.

In Ref. [20], Nakagawa *et al.* theoretically study the same model and interpret their results in terms of a breakdown of quantized particle pumping due to the repulsive Hubbard interaction. For open boundary conditions, the many-body polarization [37,58–60] shows a quantized jump due to the emergence of edge states in an OBC system [61]. For finite interaction strength, these edge-state contributions are shown to split up along the pump cycle, which eventually leads to a breakdown of quantized pumping. In our context of splitting degenerate points, the breakdown in the interacting two-component Rice-Mele model is seen when the splitting of the single degeneracy at $\Delta = 0$ into two critical points at $\pm\Delta_c$ due to the Hubbard interaction surpasses the Δ radius of the origin-centered pumping path in the $\delta - \Delta$ plane. Therefore, the pumping path \tilde{C}_2 chosen by Nakagawa *et al.* indeed encounters a gapless phase between the two spin-critical points $\pm\Delta_S$ twice but, most importantly, does not encircle an isolated singularity and hence no charge is pumped. We argue that this primarily constitutes a transition from pumping a quantized number of two to zero particles during initial pump cycles, while the breakdown due to the spin-gapless line will manifest itself after sufficiently many pump cycles.

We believe that the same mechanism of this interaction-induced splitting of the degeneracies while keeping the pumping cycle fixed is at the heart of the results reported in the recent experimental work by Walter *et al.* [11] as well. Of course, the SU(2) symmetric model possesses a gapless line, which in principle should prevent quantized pumping altogether. Our numerical results, however, show that this source of a breakdown is very unlikely to manifest itself on initial pump cycles or finite systems even for a uniform system. In a system with an open charge gap but a vanishing spin gap somewhere along the pump cycle, one first expects spin excitations. A heating up of the charge sector may not immediately occur. How exactly the breakdown of quantized pumping due to gapless spin excitations behaves as a function of system size and which timescales are relevant is an open question and demands further research. With regard to the interpretation of the experiment by Walter *et al.*, one should also stress that their system confines particles in a harmonic trap and, as a consequence, arbitrarily slow pumping will not lead to quantized pumping anyway because the metallic edges will hybridize and hence be coupled by a finite tunneling rate [62].

We would further like to emphasize that the realization of a Mott insulator *per se* does not preclude the possibility of

quantized pumping, which is supported by our results for the IHB and IHZ models and the results for pumping in a bosonic MI [14]. Furthermore, it should be noted that based on our results for the IH model, which is most easily realized experimentally, quantized transport around a single critical point may require considerably slower pumping than is currently possible in ultracold atom experiments.

We have chosen several paths in the Δ, δ plane at fixed U but similar effects may be obtained for paths in the U, δ plane at fixed Δ , which we leave for future work. Interesting results are expected when pumping through the SDI phase directly. For example, Nakagawa *et al.* report on the possibility of fractional pumping in this case [20]. In the present paper, we do not see any effect on the pumping when going through the SDI phase. However, we have not further pursued this question due to the problem of pumping close to the degeneracies and consequently large inherent finite-size effects.

The numerical data plotted in the figures are partially available [63].

ACKNOWLEDGMENTS

We are grateful to Jan Albrecht and Michael Fleischhauer for fruitful discussions and we thank Masaya Nakagawa for comments on a previous version of the paper. This research was funded by the Deutsche Forschungsgemeinschaft (DFG, German Research Foundation) via Research Unit FOR 2414 under Project No. 277974659 and by PICT No. 2017-2726 and PICT No. 2018-01546 of the ANPCyT, Argentina. A.A.A. thanks the Alexander von Humboldt Foundation for support.

APPENDIX: SPIN GAP, POLARIZATION AND BOND ORDER PARAMETER OF THE IHM FOR SMALL HOPPING

We write the Hamiltonian in the form

$$\begin{aligned}\hat{H}_{IH} &= \hat{H}_0 + \hat{H}_J, \\ \hat{H}_0 &= \sum_i [\Delta(-1)^i \hat{n}_i + U \hat{n}_{i\uparrow} \hat{n}_{i\downarrow}], \\ \hat{H}_J &= -J \sum_{i\sigma} [1 + (-1)^i \delta] (\hat{c}_{i+1\sigma}^\dagger \hat{c}_{i\sigma} + \text{H.c.}),\end{aligned}\quad (\text{A1})$$

where $\hat{n}_{i\sigma} = \hat{c}_{i\sigma}^\dagger \hat{c}_{i\sigma}$ and $\hat{n}_i = \hat{n}_{i\uparrow} + \hat{n}_{i\downarrow}$. The calculations below correspond to the static situation.

We describe the calculation of the polarization P_C and the order parameter of the BOW phase to lowest nontrivial order in \hat{H}_J for a ring of L sites, starting from either the BI or MI phases. The SDI phase is out of the reach of the validity of the present perturbative treatment.

We perform a canonical transformation similar to the one that transforms the Hubbard model at half filling to a Heisenberg model. To second order in \hat{H}_J , the transformed Hamiltonian is [64]

$$\begin{aligned}\hat{H} &= \hat{P} e^{-\hat{S}} \hat{H} e^{\hat{S}} \hat{P} \\ &= \hat{P} \left\{ \hat{H} + [\hat{H}, \hat{S}] + \frac{1}{2} [[\hat{H}, \hat{S}], \hat{S}] + \dots \right\} \hat{P} \\ &\simeq \hat{P} \{ \hat{H}_0 + [\hat{H}_J, \hat{S}] \} \hat{P},\end{aligned}\quad (\text{A2})$$

where \hat{P} is the projector over the ground state $|g_0\rangle$ of \hat{H}_0 and in the last equality we have used

$$\hat{H}_J + [\hat{H}_0, \hat{S}] = 0 \quad (\text{A3})$$

to eliminate terms linear in \hat{H}_J in \hat{H} . Using this equation, the matrix elements of \hat{S} between eigenstates of \hat{H}_0 are easily determined:

$$\langle n | \hat{S} | m \rangle = \frac{\langle n | \hat{H}_J | m \rangle}{E_n - E_m}. \quad (\text{A4})$$

Note that \hat{S} is anti-Hermitian ($\langle m | \hat{S} | n \rangle^* = -\langle n | \hat{S} | m \rangle$).

Starting from the BI phase, \hat{H} is trivial and reduces to the projector on the nondegenerate ground state $|g_0\rangle$. Instead, starting from the MI phase, $|g_0\rangle$ is degenerate and \hat{H} takes the form of a Heisenberg chain with alternating exchange parameters $J_{1(2)} = 4J(t \pm \delta)^2 U / (U^2 - 4\Delta^2)$. This effective model can be written in the form [20,64]

$$\hat{H}_{\text{Heis}} = \sum_i [J_{\text{Heis}} + (-1)^i x] \hat{\mathbf{S}}_{i+1} \cdot \hat{\mathbf{S}}_i, \quad (\text{A5})$$

with $J_{\text{Heis}} = (J_1 + J_2)/2$ and $x = 4J^2 \delta U / (U^2 - 4\Delta^2)$. Using previous results on this model using bosonization [65], one knows that a gap proportional to $\delta^{2/3}$ opens for small $\delta \neq 0$.

The expectation values of the occupancies can be calculated in the new basis as

$$\langle \hat{n}_i \rangle = \langle g | \hat{n}_i | g \rangle = \langle g | e^{\hat{S}} e^{-\hat{S}} \hat{n}_i e^{\hat{S}} e^{-\hat{S}} | g \rangle = \langle g_0 | \hat{n}_i | g_0 \rangle, \quad (\text{A6})$$

where $|g\rangle = e^{\hat{S}} |g_0\rangle$ and to second order in \hat{H}_J :

$$\hat{n}_i = \hat{P} e^{-\hat{S}} \hat{n}_i e^{\hat{S}} \hat{P} \simeq \hat{P} \left\{ \hat{n}_i + [\hat{n}_i, \hat{S}] + \frac{1}{2} [[\hat{n}_i, \hat{S}], \hat{S}] \right\} \hat{P}. \quad (\text{A7})$$

Since $\langle g_0 | \hat{S} | g_0 \rangle = 0$ and $\hat{n}_i |g_0\rangle = \langle \hat{n}_i^0 |g_0\rangle$, where $\langle \hat{n}_i^0 | = \langle g_0 | \hat{n}_i | g_0 \rangle$, the second term between brackets does not contribute and then

$$\langle \hat{n}_i \rangle = \langle \hat{n}_i^0 \rangle + \langle g_0 | \langle \hat{n}_i^0 | \hat{S}^2 - \hat{S} \hat{n}_i \hat{S} | g_0 \rangle. \quad (\text{A8})$$

Taking matrix elements of the second term, it is clear that only excited states for which $n_i \neq \langle \hat{n}_i^0 \rangle$ contribute to it.

1. Polarization in the band insulating phase

In the BI phase, $\langle \hat{n}_i^0 \rangle = 0$ or 2 and all intermediate states have $n_i = 1$. Then, Eq. (A8) leads to

$$\langle \hat{n}_i \rangle = \langle \hat{n}_i^0 \rangle + (1 - \langle \hat{n}_i^0 \rangle) \sum_k' \frac{|\langle k | \hat{H}_J | g_0 \rangle|^2}{(E_k - E_0)^2}, \quad (\text{A9})$$

where the sum is restricted to the two excited states $|k\rangle$ of \hat{H}_0 obtained after applying \hat{H}_J to $|g_0\rangle$ for which $n_i = 1$. One realizes that for positive Δ there are $L/2$ hops to the right for each spin with matrix element $-J(1 - \delta)$ and $L/2$ hops to the left for each spin with matrix element $-J(1 + \delta)$. For negative Δ , the situation is the opposite. Therefore, the change in polarization with respect to the BI phase for $\hat{H}_J = 0$ is

$$\Delta P_C^{\text{BI}} = -\frac{4J\delta \operatorname{sgn}(\Delta)}{(2\Delta - U)^2}. \quad (\text{A10})$$

To compare with numerical calculations of the charge Berry phase, we have chosen $U = 0$, $\Delta = 10$, $J = 1$, $\delta = 0.1$.

Equation (A10) gives $\Delta P_C^{\text{PBC}} = -10^{-3}$. The numerical calculation for $L = 6, 8$ and 10 gives $\Delta P_{\text{PBC}} = (-9.83 \pm 0.01) \times 10^{-4}$. Both results differ by less than 2%.

2. Polarization near the Mott insulating phase

The calculation of the polarization in this case is more difficult due to the spin structure of $|g_0\rangle$. In particular, there can't be any nearest-neighbor hopping if the spins of the electrons of the sites involved are parallel. Therefore, the result depends on spin correlation functions. From Eq. (A8), one realizes that the contribution of the state in which an electron is displaced from site 1 to 2 is proportional to the probability that the spins of sites 1 and 2 form a singlet, since this hopping is not possible for triplets. The projector on the singlet state is $(1/4 - \hat{\mathbf{S}}_1 \cdot \hat{\mathbf{S}}_2)$ and the matrix element for the singlet has a factor $\sqrt{2}$. Explicitly,

$$\begin{aligned} & -J(1 - \delta) \sum_{\sigma} \hat{c}_{2\sigma}^{\dagger} \hat{c}_{1\sigma} \left[\frac{1}{\sqrt{2}} (\hat{c}_{1\uparrow}^{\dagger} \hat{c}_{2\downarrow}^{\dagger} - \hat{c}_{1\downarrow}^{\dagger} \hat{c}_{2\uparrow}^{\dagger}) |0\rangle \right] \\ & = -\sqrt{2}J(1 - \delta) \hat{c}_{2\uparrow}^{\dagger} \hat{c}_{2\downarrow}^{\dagger} |0\rangle. \end{aligned} \quad (\text{A11})$$

Thus, proceeding as before, the change in polarization with respect to the MI phase with $J = 0$ (with all $\langle n_i \rangle = 1$) is

$$\begin{aligned} \Delta P_C & = \frac{8U\Delta J^2}{(U^2 - 4\Delta^2)^2} \{(1 + \delta)^2 (1/4 - \langle \hat{\mathbf{S}}_3 \cdot \hat{\mathbf{S}}_2 \rangle) \\ & - (1 - \delta)^2 (1/4 - \langle \hat{\mathbf{S}}_1 \cdot \hat{\mathbf{S}}_2 \rangle)\}. \end{aligned} \quad (\text{A12})$$

For $\delta \rightarrow 0$, the correlation functions for all links are the same and $1/4 - \langle \hat{\mathbf{S}}_i \cdot \hat{\mathbf{S}}_{i+1} \rangle = \ln 2$ in the thermodynamic limit [66]. Therefore, in this limit $\delta \rightarrow 0, L \rightarrow \infty$, the above expression can be simplified to

$$\begin{aligned} \Delta P_C & \simeq \frac{8U\Delta J^2}{(U^2 - 4\Delta^2)^2} (4\delta \ln 2 + O_B), \\ O_B & = \langle (\hat{\mathbf{S}}_1 - \hat{\mathbf{S}}_3) \cdot \hat{\mathbf{S}}_2 \rangle. \end{aligned} \quad (\text{A13})$$

O_B is the dimer order parameter of \hat{H}_{Heis} . Using the Hellman-Feynman theorem $\partial E / \partial x = (L/2) O_B$, where $E = \langle \hat{H}_{\text{Heis}} \rangle$. From bosonization [65] and numerical [67] results, one knows that $E \sim x^{4/3}$ and then $O_B \sim \delta^{1/3}$. Therefore, the change in the dimer-order parameter with δ dominates ΔP_C for very small δ .

For a comparison with numerical calculations, we take $J = 1, U/J = 10, \Delta = \delta = 0.1$. This leads to $J_2/J_1 = 0.67$ for which $O_B \simeq 0.517$ according to Fig. 1 of Ref. [68]. Approximating $1/4 - \langle \hat{\mathbf{S}}_{1(3)} \cdot \hat{\mathbf{S}}_2 \rangle = \ln 2 \pm O_B/2$, Eq. (A13) gives $\Delta P_C = 5.24 \times 10^{-4}$. From the numerical calculation of the Berry phases, we obtain $\Delta P_C = z \times 10^{-4}$, with $z = 4.73$,

5.17 and 5.38 for $L = 6, 8$, and 10 , respectively, in reasonable agreement with the above estimation.

3. Bond-order parameter

The parameter of the BOW can be defined as

$$\begin{aligned} O_{\text{BOW}} & = \sum_i \frac{1}{L} (-1)^i \langle \hat{b}_i \rangle, \\ \hat{b}_i & = \hat{c}_{i+1\sigma}^{\dagger} \hat{c}_{i\sigma} + \text{H.c.}, \end{aligned} \quad (\text{A14})$$

where $\langle \hat{b}_i \rangle$ is the expectation value of the hopping between sites i and $i + 1$. For $\delta = 0$, odd and even bonds are equivalent and therefore $O_{\text{BOW}} = 0$ for any finite system with an even number of bonds. In the thermodynamic limit within the SDI phase, there is precisely a spontaneous symmetry breaking and the system chooses one of two possible degenerate states with opposite O_{BOW} [48]. The SDI phase is out of the reach of validity of the present perturbative treatment. For $\delta \neq 0$, $O_{\text{BOW}} \neq 0$ and therefore, the bond-order parameter can be analyzed by perturbation theory in H_I starting from the BI and MI phases. Using Eq. (A7) for $\hat{O} = \hat{b}_i$, it is easy to see that for both phases the first nontrivial contribution is the linear one in \hat{S} (the operator that acts first between \hat{b}_i and \hat{S} leads to some excited state and the other returns to the ground state). Thus,

$$\hat{b}_i \simeq \hat{P} [\hat{b}_i, \hat{S}] \hat{P}. \quad (\text{A15})$$

Doing the calculation for the nondegenerate ground state of the BI phase using Eq. (A4), one obtains

$$\langle \hat{b}_i \rangle_{\text{BI}} = 4J \frac{1 + (-1)^i \delta}{2\Delta - U}. \quad (\text{A16})$$

Inserting this expression into in Eq. (A14), we obtain

$$O_{\text{BOW}}^{\text{BI}} = \frac{4\delta J}{2\Delta - U}. \quad (\text{A17})$$

In the other phases, the calculation is more complicated because of the structure of the ground state in which spin flips are possible. Proceeding in a similar way as in Ref. [64] and above, we obtain

$$\langle \hat{b}_i \rangle = (1 - 4\langle \hat{\mathbf{S}}_i \cdot \hat{\mathbf{S}}_{i+1} \rangle) U J \frac{1 + (-1)^i \delta}{U^2 - 4\Delta^2}. \quad (\text{A18})$$

Inserting this into in Eq. (A14), one obtains

$$O_{\text{BOW}} = \frac{2JU O_B}{U^2 - 4\Delta^2} + \frac{UJ\delta}{U^2 - 4\Delta^2} (1 - 2\langle (\hat{\mathbf{S}}_3 + \hat{\mathbf{S}}_1) \cdot \hat{\mathbf{S}}_2 \rangle), \quad (\text{A19})$$

where O_B was discussed above. For $\delta \rightarrow 0$, $O_B \sim \delta^{1/3}$ and therefore, the first term is the leading one. This means that in this limit the bond-order parameter is proportional to the dimer order parameter of the Heisenberg chain with alternating exchange parameters.

[1] M. P. A. Fisher, P. B. Weichman, G. Grinstein, and D. S. Fisher, *Phys. Rev. B* **40**, 546 (1989).

[2] D. Jaksch, C. Bruder, J. I. Cirac, C. W. Gardiner, and P. Zoller, *Phys. Rev. Lett.* **81**, 3108 (1998).

[3] M. Greiner, O. Mandel, T. Esslinger, T. W. Hänsch, and I. Bloch, *Nature (London)* **415**, 39 (2002).

[4] I. Bloch, J. Dalibard, and W. Zwerger, *Rev. Mod. Phys.* **80**, 885 (2008).

- [5] E. Berg, M. Levin, and E. Altman, *Phys. Rev. Lett.* **106**, 110405 (2011).
- [6] Q. Niu and D. J. Thouless, *J. Phys. A: Math. Gen.* **17**, 2453 (1984).
- [7] D. J. Thouless, *Phys. Rev. B* **27**, 6083 (1983).
- [8] M. Lohse, C. Schweizer, O. Zilberberg, M. Aidelsburger, and I. Bloch, *Nat. Phys.* **12**, 350 (2016).
- [9] S. Nakajima, T. Tomita, S. Taie, T. Ichinose, H. Ozawa, L. Wang, M. Troyer, and Y. Takahashi, *Nat. Phys.* **12**, 296 (2016).
- [10] S. Nakajima, N. Takei, K. Sakuma, Y. Kuno, P. Marra, and Y. Takahashi, *Nat. Phys.* **17**, 844 (2021).
- [11] A.-S. Walter, Z. Zhu, M. Gächter, J. Minguzzi, S. Roschinski, K. Sandholzer, K. Viebahn, and T. Esslinger, [arXiv:2204.06561](https://arxiv.org/abs/2204.06561).
- [12] A. Cerjan, M. Wang, S. Huang, K. P. Chen, and M. C. Rechtsman, *Light: Sci. Appl.* **9**, 178 (2020).
- [13] M. J. Rice and E. J. Mele, *Phys. Rev. Lett.* **49**, 1455 (1982).
- [14] A. Hayward, C. Schweizer, M. Lohse, M. Aidelsburger, and F. Heidrich-Meisner, *Phys. Rev. B* **98**, 245148 (2018).
- [15] Y. Ke, X. Qin, Y. S. Kivshar, and C. Lee, *Phys. Rev. A* **95**, 063630 (2017).
- [16] D. Rossini, M. Gibertini, V. Giovannetti, and R. Fazio, *Phys. Rev. B* **87**, 085131 (2013).
- [17] T.-S. Zeng, W. Zhu, and D. N. Sheng, *Phys. Rev. B* **94**, 235139 (2016).
- [18] S. Greschner, S. Mondal, and T. Mishra, *Phys. Rev. A* **101**, 053630 (2020).
- [19] L. Lin, Y. Ke, and C. Lee, *Phys. Rev. A* **101**, 023620 (2020).
- [20] M. Nakagawa, T. Yoshida, R. Peters, and N. Kawakami, *Phys. Rev. B* **98**, 115147 (2018).
- [21] Y. Kuno, *Eur. Phys. J. B* **92**, 195 (2019).
- [22] B. A. van Voorden and K. Schoutens, *New J. Phys.* **21**, 013026 (2019).
- [23] I. Esin, C. Kuhlenskamp, G. Refael, E. Berg, M. S. Rudner, and N. H. Lindner, [arXiv:2203.01313](https://arxiv.org/abs/2203.01313).
- [24] L. Stenzel, A. L. C. Hayward, C. Hubig, U. Schollwöck, and F. Heidrich-Meisner, *Phys. Rev. A* **99**, 053614 (2019).
- [25] Y. Kuno and Y. Hatsugai, *Phys. Rev. Research* **2**, 042024(R) (2020).
- [26] A. L. C. Hayward, E. Bertok, U. Schneider, and F. Heidrich-Meisner, *Phys. Rev. A* **103**, 043310 (2021).
- [27] S. Hu, Y. Ke, and C. Lee, *Phys. Rev. A* **101**, 052323 (2020).
- [28] M. Ippoliti and R. N. Bhatt, *Phys. Rev. Lett.* **124**, 086602 (2020).
- [29] P. Marra and M. Nitta, *Phys. Rev. Research* **2**, 042035(R) (2020).
- [30] M. M. Wauters, A. Russomanno, R. Citro, G. E. Santoro, and L. Privitera, *Phys. Rev. Lett.* **123**, 266601 (2019).
- [31] R. Wang and Z. Song, *Phys. Rev. B* **100**, 184304 (2019).
- [32] J. Qin and H. Guo, *Phys. Lett. A* **380**, 2317 (2016).
- [33] S. R. Manmana, V. Meden, R. M. Noack, and K. Schönhammer, *Phys. Rev. B* **70**, 155115 (2004).
- [34] M. E. Torio, A. A. Aligia, and H. A. Ceccatto, *Phys. Rev. B* **64**, 121105(R) (2001).
- [35] J. Haegeman, C. Lubich, I. Oseledets, B. Vandereycken, and F. Verstraete, *Phys. Rev. B* **94**, 165116 (2016).
- [36] V. Zauner-Stauber, L. Vanderstraeten, M. T. Fishman, F. Verstraete, and J. Haegeman, *Phys. Rev. B* **97**, 045145 (2018).
- [37] R. Resta, *Phys. Rev. Lett.* **80**, 1800 (1998).
- [38] A. A. Aligia and G. Ortiz, *Phys. Rev. Lett.* **82**, 2560 (1999).
- [39] A. A. Aligia, K. Hallberg, C. D. Batista, and G. Ortiz, *Phys. Rev. B* **61**, 7883 (2000).
- [40] K. Loida, J.-S. Bernier, R. Citro, E. Orignac, and C. Kollath, *Phys. Rev. Lett.* **119**, 230403 (2017).
- [41] M. E. Torio, A. A. Aligia, G. I. Japaridze, and B. Normand, *Phys. Rev. B* **73**, 115109 (2006).
- [42] N. Nagaosa and J.-I. Takimoto, *J. Phys. Soc. Jpn.* **55**, 2735 (1986).
- [43] J. B. Torrance, A. Girlando, J. J. Mayerle, J. I. Crowley, V. Y. Lee, P. Batail, and S. J. LaPlaca, *Phys. Rev. Lett.* **47**, 1747 (1981).
- [44] T. Egami, S. Ishihara, and M. Tachiki, *Science* **261**, 1307 (1993).
- [45] K. Nomura and K. Okamoto, *J. Phys. A: Math. Gen.* **27**, 5773 (1994).
- [46] M. Nakamura, *J. Phys. Soc. Jpn.* **68**, 3123 (1999).
- [47] M. Nakamura, *Phys. Rev. B* **61**, 16377 (2000).
- [48] M. Fabrizio, A. O. Gogolin, and A. A. Nersesyan, *Phys. Rev. Lett.* **83**, 2014 (1999).
- [49] M. Messer, R. Desbuquois, T. Uehlinger, G. Jotzu, S. Huber, D. Greif, and T. Esslinger, *Phys. Rev. Lett.* **115**, 115303 (2015).
- [50] L. Tarruell, D. Greif, T. Uehlinger, G. Jotzu, and T. Esslinger, *Nature (London)* **483**, 302 (2012).
- [51] L. Privitera, A. Russomanno, R. Citro, and G. E. Santoro, *Phys. Rev. Lett.* **120**, 106601 (2018).
- [52] R. Li and M. Fleischhauer, *Phys. Rev. B* **96**, 085444 (2017).
- [53] U. Schollwöck, *Ann. Phys.* **326**, 96 (2011).
- [54] I. P. McCulloch, [arXiv:0804.2509](https://arxiv.org/abs/0804.2509).
- [55] R. Orús and G. Vidal, *Phys. Rev. B* **78**, 155117 (2008).
- [56] Fishman *et al.*, [arXiv:2007.14822](https://arxiv.org/abs/2007.14822).
- [57] Y.-C. Tzeng, L. Dai, M.-C. Chung, L. Amico, and L.-C. Kwek, *Sci. Rep.* **6**, 26453 (2016).
- [58] R. D. King-Smith and D. Vanderbilt, *Phys. Rev. B* **47**, 1651 (1993).
- [59] R. Resta, *Rev. Mod. Phys.* **66**, 899 (1994).
- [60] G. Ortiz, P. Ordejón, R. M. Martin, and G. Chiappe, *Phys. Rev. B* **54**, 13515 (1996).
- [61] Y. Hatsugai and T. Fukui, *Phys. Rev. B* **94**, 041102(R) (2016).
- [62] E. Bertok, Master's thesis, Georg-August Universität Göttingen, 2019.
- [63] E. Bertok, F. Heidrich-Meisner, and A. Aligia, <https://arxiv.org/src/2204.14144v3/anc>.
- [64] A. A. Aligia, *Phys. Rev. B* **69**, 041101(R) (2004).
- [65] M. C. Cross and D. S. Fisher, *Phys. Rev. B* **19**, 402 (1979).
- [66] J. des Cloizeaux and J. J. Pearson, *Phys. Rev.* **128**, 2131 (1962).
- [67] K. Okamoto, H. Nishimori, and Y. Taguchi, *J. Phys. Soc. Jpn.* **55**, 1458 (1986).
- [68] S. Paul, *Condens. Matter Phys.* **20**, 23701 (2017).

Correction: The omission of a data availability statement has been rectified.

7.2 Interaction-induced pumping

In the last section, I presented results for an interacting Rice-Mele model that allowed for the splitting of the critical points around which charge can be pumped adiabatically. In the next section, I will present a paper that is currently in development in collaboration with experimentalists at ETH Zürich, in which we show that such a model can be used to engineer interaction-induced pumping in an ultracold atomic system. For this, we fix the staggering-shifted pump cycle in the Δ - δ plane and increase the Hubbard interaction, which can be done via the Feshbach resonance. At each interaction strength, the pumped charge per cycle can be experimentally measured via in-situ imaging. We pump for multiple cycles and expect near quantized transport during the first cycle, as the previous manuscript shows that without additional gap-opening terms, one expects non-adiabatic effects due to the spin-gapless line at $\delta = 0$ in the Mott phase. We employ a time-evolving block-decimation time-evolution algorithm (see chapter 4) for a closed system with open boundary conditions to calculate the pumped charge and adapt our numerics to the experiment by considering the exact experimentally realized pump cycle, the harmonic trap and an initial state that is not the ground state. The initial state is instead chosen as decoupled dimer-states. This is done due to subtleties in the loading schemes done by the experiment, where one first starts in a band-insulator with double occupancies with strong attractive interaction and subsequently inverts the interactions to be repulsive. As a result, the initial state can be described accurately by disjointed dimer states and an (experimentally unknown) amount of holes for each of the one-dimensional tubes realized in the optical lattice. We also simulate the effect of such holes.

We observe experimentally and verify numerically that there exists a plateau with a finite pumped charge over an extended range of interaction strengths. Outside of this plateau the pump is trivial. We show that the non-adiabatic breakdown that is introduced in the last paper is subtle and hinges on a sequence of excitations in the spin- and charge sector which happen sequentially for each sector, which provides a microscopic picture for the mechanism of the breakdown of quantized charge transport. Specifically, we calculate the nearest neighbor charge- and spin-correlators, for both forward- and backward propagation along the pump cycle. Here, forward and backward propagation merely changes the time at which the gapless line is crossed, which happens late (early) for forward (backward) propagation. The correlators reveal that upon crossing the spin-gapless line in the Mott phase, the spin sector is immediately excited while the charge sector initially remains adiabatic. Once the spin sector is excited, the charge sector is then subsequently excited only upon changing from the Mott regime with strong interaction to the band-insulator regime where the staggering-amplitude dominates. For our chosen initial state, the gapless line is exactly crossed at $3/4$ of the pump cycle for a forward propagation and the correlators show that during the remaining $1/4$ of the pump cycle, the system stays in the Mott regime, where the charge sector cannot be excited, even if the spin sector is. This essentially protects the pumped charge as long as one stays in the Mott regime and explains why we observe quantized charge transport in the first pump cycle despite crossing a gapless line.

7.3 Preprint: Interaction-induced charge pumping in a topological many-body system

Article reprinted with permissions from Konrad Viebahn, Anne-Sophie Walter, Eric Bertok, Zijie Zhu, Marius Gächter, Armando A. Aligia, Fabian Heidrich-Meisner and Tilman Esslinger

Preprint submitted to PRX.

arXiv:2308.03756 (2023)

Author contributions: K.V, A.S.W, Z.Z., M.G. and T.E. planned and carried out the experiment and the analysis of experimental data. K.V wrote the manuscript. K.V, E.B and F.H.M wrote the appendix. E.B. did the numerical calculations and analysis of numerical data. F.H.M. suggested the analysis of spin and charge correlations. All authors contributed to the interpretation of results, discussion of the data and revisions of the manuscript.

Interaction-induced charge pumping in a topological many-body system

Konrad Viebahn,^{1,*} Anne-Sophie Walter,^{1,*} Eric Bertok,^{2,*} Zijie Zhu,¹ Marius Gächter,¹ Armando A. Aligia,³ Fabian Heidrich-Meisner,² and Tilman Esslinger¹

¹*Institute for Quantum Electronics & Quantum Center, ETH Zurich, 8093 Zurich, Switzerland*

²*Institute for Theoretical Physics, Georg-August-Universität Göttingen, 37077 Göttingen, Germany*

³*Instituto de Nanociencia y Nanotecnología CNEA-CONICET, Centro Atómico Bariloche and Instituto Balseiro, 8400 Bariloche, Argentina*

A topological ‘Thouless’ pump represents the quantised motion of particles in response to a slow, cyclic modulation of external control parameters. The Thouless pump, like the quantum Hall effect, is of fundamental interest in physics because it links physically measurable quantities, such as particle currents, to geometric properties of the experimental system, which can be robust against perturbations and thus technologically useful. So far, experiments probing the interplay between topology and inter-particle interactions have remained relatively scarce. Here we observe a Thouless-type charge pump in which the particle current and its directionality inherently rely on the presence of strong interactions. Experimentally, we utilise fermionic atoms in a dynamical superlattice which traces a pump trajectory that remains trivial in the non-interacting limit. Remarkably, the transferred charge in the interacting system is half of its usual value in the non-interacting case, in agreement with matrix-product-state simulations. Our experiments suggest that Thouless charge pumps are promising platforms to gain insights into interaction-driven topological transitions and topological quantum matter.

I. INTRODUCTION

An adiabatic change of an energy landscape represents one of the simplest strategies to induce controlled particle motion. For example, a sliding potential minimum can carry a trapped particle from one point to another, both in classical and quantum mechanics. However, the wave nature of quantum-mechanical states allows for additional physical effects arising from a geometric phase change when the Hamiltonian is time-dependent [1]. A geometric or ‘Berry’ phase is not usually evident from the underlying potential but requires knowledge of eigenstates and their geometric structure. Thouless showed that in a periodic system the geometric phase contributions after one adiabatic cycle sum to integers which correspond to the singularities enclosed by the pump trajectory [2]. Physically, these integers describe the quantisation of transported charge. This phenomenon, known as Thouless charge pumping, is topologically protected against perturbations that are small compared to the energy gap between ground and excited states [1, 3, 4]. Therefore, topological charge pumps may also become technologically relevant as sources of quantised current [5]. An alternative (but equivalent) description of Thouless pumping regards the time-periodic variation as a Floquet drive [6] which gives rise to a synthetic dimension of photon states. In this two-dimensional picture, the topological pump represents a quantised bulk Hall drift.

So far, interactions did not play a major role in pumping experiments [7–17]. Recently, the effects of interactions on pumping have been explored in two experimental

platforms, that is, in the mean-field regime [18, 19] and in a Fermi-Hubbard system [20]. In both cases, interactions which exceeded the protecting energy gap caused a suppression of the quantised pumping motion. In general, theoretical papers have suggested a variety of interaction-related effects in pumping [21–39]. However, the question of whether interactions can cause or even stabilise topological behaviour has largely remained unanswered on the experimental level [40–51].

Here, we report on the experimental observation of interaction-induced charge pumping using interacting fermionic atoms in a dynamically modulated optical lattice. The optical lattice realises a Hubbard model with modulated hopping matrix elements and onsite potentials. For Hubbard interactions larger than a nonzero critical value, the atoms exhibit a pumping motion, while they remain stationary in the non-interacting limit. Our measurements are consistent with a quantised displacement of the atomic cloud in the first pump cycle, in quantitative agreement with time-dependent matrix-product-state (MPS) simulations [52, 53]. Interestingly, the transferred charge per pump cycle is half of its usual value in a non-interacting system, as predicted in Ref. [43], and the pumping mechanism does not have a classical counterpart. At very large interactions and beyond a second critical interaction strength, the pumped charge vanishes again. Crucially, the region with pumping of one charge per cycle cannot be adiabatically connected to the non-interacting limit.

Our work establishes an example of topological phase transitions controlled by the interaction strength. Previously, topological transitions were observed by tuning external parameters in non-interacting models, such as inversion-symmetry in the Haldane model [54–56]. The pump involves the physics of the ionic Hubbard model [57–62], which gives rise to the observed tran-

* These authors contributed equally. Correspondence should be addressed to K.V. (viebahnk@phys.ethz.ch).

sitions. Due to the inherent $SU(2)$ symmetry in the spin sector, this model possesses a Mott-insulating region with gapless spin excitations. Since the pump realised in our experiment traverses through this region, strictly speaking, there cannot be adiabatic pumping and quantised pumping must eventually break down [32]. Notably, though, our numerical simulations for realistic conditions show that the transferred charge in the first pump cycle remains robust and near-quantised. Moreover, an analysis of correlations shows that initial spin excitations are converted into defects in the charge sector with a time delay and therefore do not affect the pumped charge immediately, thus explaining the experimental observation. Therefore, a Thouless pump in a two-component Rice-Mele model with Hubbard interactions allows to systematically study the coupling between the spin and charge sectors on experimentally and numerically accessible time scales.

While many aspects of topological band structures were realised with optical lattices with engineered gauge potentials [54, 55, 63], accessing the interacting regime still poses a significant challenge. The reason is the unavoidable heating in a driven many-body system [64, 65] and the problem of loading the bulk. Therefore, few experiments have explored interacting topological quantum states [66, 67]. Experiments with Thouless pumps circumvent these experimental issues and, as we will demonstrate here, enable the study of interaction effects on the topology of many-body systems.

II. INTERACTION-INDUCED CHARGE PUMP

The specific Hamiltonian studied in this work is the Rice-Mele-Hubbard model

$$\hat{H}(\tau) = - \sum_{j,\sigma} [t + (-1)^j \delta(\tau)] (\hat{c}_{j\sigma}^\dagger \hat{c}_{j+1\sigma} + \text{h.c.}) + \Delta(\tau) \sum_{j,\sigma} (-1)^j \hat{c}_{j\sigma}^\dagger \hat{c}_{j\sigma} + U \sum_j \hat{n}_{j\uparrow} \hat{n}_{j\downarrow}, \quad (1)$$

which is parametrised by the time-dependent bond dimerisation $\delta(\tau)$ and the sublattice site offset $\Delta(\tau)$ [Fig. 1(a)]. The fermionic annihilation and number operators for spin $\sigma \in \{\uparrow, \downarrow\}$ on lattice site j are denoted by $\hat{c}_{j\sigma}$ and $\hat{n}_{j\sigma}$, respectively. Let us first consider the non-interacting limit ($U = 0$) in which the whole parameter space is spanned by δ and Δ [Fig. 1(b)]. The relevant topological invariant for charge pumping is the (charge-) Berry phase of the lowest band which becomes singular at the origin of the δ - Δ plane. At half-filling, that is, two fermions per unit cell, a trajectory enclosing the singularity pumps a total of $\Delta Q = 2$ charges to the neighbouring unit cell per pump cycle (one spin- \uparrow , one spin- \downarrow). For trajectories that do not enclose the singularity [Fig. 1(c)] the pumped charge is zero.

The Rice-Mele model at finite Hubbard U gives rise to a rich many-body phase diagram at half-filling [32, 43,

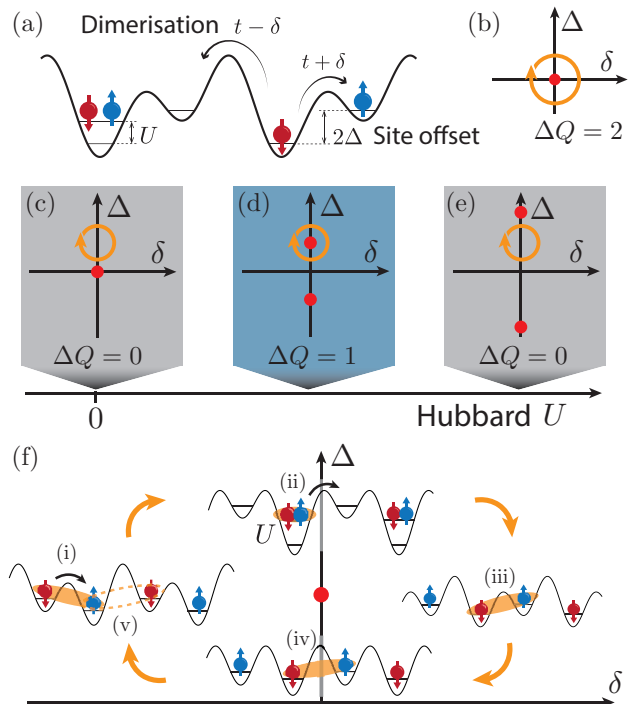


FIG. 1. **Topological pumping induced by Hubbard interactions.** (a) Dynamically modulated Rice-Mele-Hubbard model. The bond dimerisation (δ) and the site offset (Δ) are periodically modulated. (b) Pump trajectory centred at $\Delta = 0$, leading to a pumped charge of $\Delta Q = 2$ for spinful fermions at $U = 0$. (c-e) Pump trajectories centred at $\Delta > 0$. (c) For vanishing interactions ($U = 0$) the pumped charge is zero. (d) A finite Hubbard U causes the splitting of singularities to $\Delta \gtrsim 0$, which leads to interaction-induced topological pumping with $\Delta Q = 1$. (e) Once the Hubbard U is too large, the pump is rendered topologically trivial. (f) Schematic illustration of the interaction-induced pump on the microscopic level. The red dot indicates the position of a single singularity at finite Hubbard U .

57–60, 68, 69]. The phases are governed by the competition and interplay of the parameters U , δ , and Δ . In short, the Su-Schrieffer-Heeger (SSH) lattice with $\Delta = 0$ leads to a dimerised Mott insulator for $U \gg t$ [68], whereas the ionic Hubbard model ($\delta = 0$) exhibits band insulating ($\Delta \gtrsim U/2$ for $U \gg t$) and Mott insulating ($\Delta \lesssim U/2$) phases, with a small dimerised intermediate phase around $\Delta \sim U/2$ [33, 58, 59]. Recent numerical calculations predict a splitting of the non-interacting singularity at the origin [$(\delta, \Delta) = (0, 0)$] into two, for increasing values of Hubbard U [43]. The new singularities each exhibit a 2π winding of the (charge-)Berry phase and should thus be amenable to topological charge pumping in the interacting regime.

The key idea behind interaction-induced pumping is the following: we choose a pump trajectory centred at a finite site offset $\Delta > 0$, which does not enclose the singularity for $U = 0$. This trajectory is topologically trivial in the non-interacting limit and transfers $\Delta Q = 0$ charges

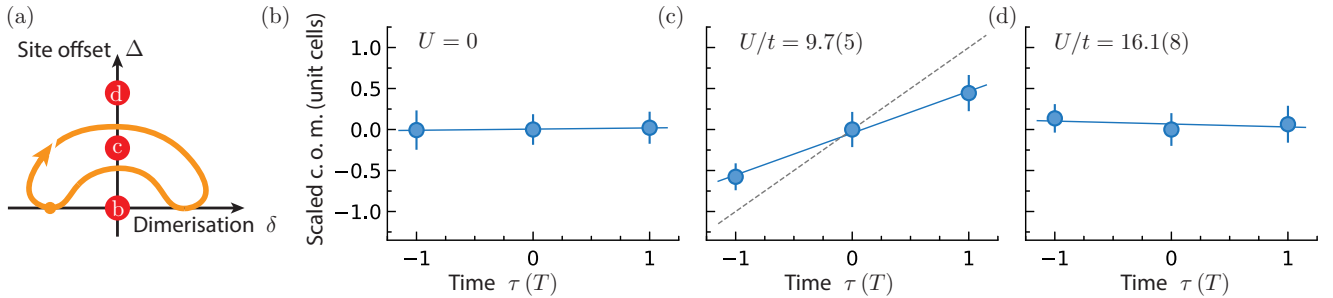


FIG. 2. **Experimental observation of interaction-induced charge pumping.** Panel (a) shows a schematic representation of the experimental pump trajectory (see App. A for details). The singularities are shown as red dots marked (b), (c), and (d), respectively, for increasing values of Hubbard U , corresponding to the following subplots. (b-d) The scaled centre-of-mass position (c. o. m.) is plotted as function of time τ for three different values of Hubbard U (b): $U = 0$, (c): $U/t = 9.7(5)$, and (d): $U/t = 16.1(8)$. The dashed line in (c) represents a pumped charge of $\Delta Q = 2$, typical for the usual Rice-Mele pump [9, 10, 20]. Data points and error bars correspond to mean and standard error of 40 measurements.

per pump cycle as sketched in Fig. 1(c). Now, we successively tune the value of Hubbard U until one of the two singularities (red dots in Fig. 1) moves along the Δ -axis into the pump trajectory which, in turn, becomes topologically non-trivial. Interestingly, the pumped charge in this case is expected to be $\Delta Q = 1$, compared to the usual $\Delta Q = 2$ in the ‘traditional’ trajectory centred at the origin.

We develop an intuition for the interaction-induced pump by adiabatically following the ground states in the interacting Rice-Mele model. Let us start on the left of the (δ, Δ) -plane [Fig. 1(f)] which is characterised by predominant singlet-correlations along the strong bonds. Following a hypothetical singlet-pair (marked as (i) and highlighted in orange) out of the full many-body ground state, the two atoms are converted into a double occupancy for large sublattice offsets (ii, $\Delta > U/2$). Subsequently, the double occupancy is converted back to a singlet ($\delta > 0$), albeit shifted by half a unit cell (iii). In the last section of the pump trajectory, the pair of atoms remains in place, leading to an overall shift of half a unit cell per pump cycle (pumped charge $\Delta Q = 1$ per unit cell) while the local spin and charge correlations adiabatically adjust, ensuring return to the initial state (iv – v). In comparison, a non-interacting atom would only oscillate to and fro during this process (i – v), leading to zero net current. Note that the sketch describes an idealised adiabatic situation in which the system remains in its instantaneous ground state at all times. Specific aspects of the experiment and of the concrete model can affect the adiabaticity, which we will address in Sec. V below.

Crucially, the lattice potential [schematics in Fig. 1(f)] does not exhibit an underlying ‘sliding lattice’, which is used in the usual Rice-Mele pump [9, 10, 24]. Instead, a ‘long’ and a ‘short’ lattice are slowly oscillating with respect to one another. Consequently, this interaction-induced pump does not have a classical, non-interacting counterpart.

III. EXPERIMENTAL REALISATION

We use fermionic ^{40}K atoms in a dynamically controlled optical lattice to realise the Hamiltonian in Eq. (1). Here, atoms take the roles of pumped charges. The value of average tunnelling is $t/h = 371(19)$ Hz, where h is Planck’s constant; the Hubbard U is widely tuneable via a magnetic Feshbach resonance. The lattice laser setup, derived from a single laser source at $\lambda = 1064$ nm, is described in detail in Ref. [20]. In short, a combination of standing waves in x -, y -, and z -directions and a running wave component along the pumping (x -)direction superimpose to form effectively one-dimensional tubes of superlattices (size of one unit cell $\equiv d = \lambda$). The relative phase φ between interfering beams along x and z , as well as the lattice depth V_{Xint} of the interfering x -lattice give independent control over δ and Δ (see App. A). Prior to pumping, we maximise the proportion of doubly occupied unit cells, as described previously [20], and calibrate this value to be $0.415(8)$, independent of the value of Hubbard U , where the number in brackets denotes the standard deviation. Subsequently, pumping is initiated by sinusoidally oscillating φ and V_{Xint} out of phase with respect to one another, causing the ‘long’ lattice (lattice spacing = d) to periodically move back and forth over the ‘short’ lattice (lattice spacing = $d/2$). The trajectory starts at $\Delta = 0$ and $\delta < 0$, then crosses the vertical axis at the maximal Δ above the singularity, passes below the singularity, and finally returns to its initial position, as shown in Fig. 2(a). In order to invert the pumping direction, denoted by negative time τ in Figs. 2-4, we start on the opposite side of the vertical axis at $\delta > 0$ and again move upwards to larger values of Δ . The ‘boomerang’ shape of the experimental pump trajectory is a consequence of having only two modulation parameters (similar to Ref. [10]). In addition to varying δ and Δ , the change in lattice potential leads to a variation in average tunnelling t by as much as 60%, but this variation does not affect any conclusions,

based on our observations.

In a first experiment, we measure the in-situ centre-of-mass (c. o. m.) position of the atomic cloud in units of unit cells (d) as function of time τ . In order to quantify the transferred charge per cycle for doubly-occupied unit cells, the centre-of-mass displacement is divided by the independently calibrated filling fraction $0.415(8)$ described above. The pump period is fixed to $T = 23 \hbar/t = 10$ ms, chosen to be much longer than the maximal inverse single-particle band gap $1/(1.4 \text{ kHz}) = 0.7$ ms. In the non-interacting limit, we find no significant displacement and a linear fit yields a slope of $0.01(1) d/T$. This reflects the topologically trivial nature of the pump trajectory for $U = 0$ [Fig. 2(b)]. The situation changes when performing the same experiment at a Hubbard interaction of $U/t = 9.7(5)$ [Fig. 2(c)]. Here, we measure a slope of $0.51(4) d/T$, consistent with the expected value of $\Delta Q = 1$ pumped charge per cycle and unit cell in a quantised, interaction-induced Thouless pump. Compared to a usual ‘Rice-Mele’ pump with $\Delta Q = 2$ and a measured slope of $1 d/T$, as observed in previous experiments [9, 10, 20] and plotted as a dashed line, the interaction-induced pump transfers only half the amount of charge. A third experiment, this time at $U/t = 16.1(8)$ yields no significant displacement [slope = $-0.03(7) d/T$], since the singularity has moved out of the pump trajectory [Fig. 2(d)]. These findings constitute the main qualitative result of our experiments.

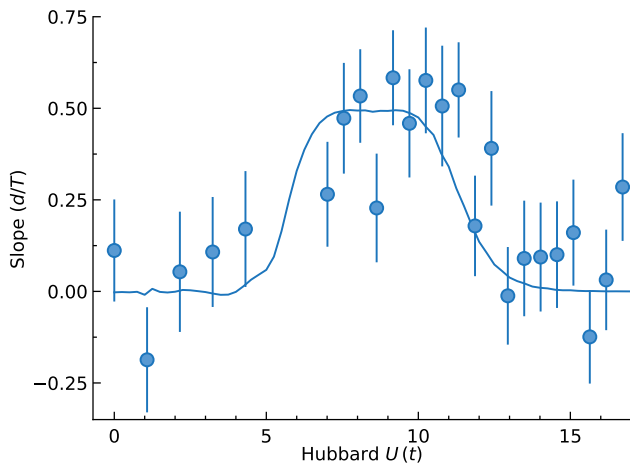


FIG. 3. **Scan of interaction-induced charge pumping as a function of Hubbard U .** Intermediate interactions lead to an extended region of interaction-induced pumping with slopes around $0.5 d/T$. The Thouless pump is rendered trivial for very strong and very weak interactions, in agreement with theory. Data points denote fitted slopes to time traces such as those shown in Figs. 2(b)-(d), error bars correspond to the standard error of the fitted slopes. The ‘gap’ in the data points around $U/t \simeq 6$ is due to the use of different hyperfine mixtures of ^{40}K (App. A). The solid line is a MPS calculation taking into account the experimental trajectory, as well as the trapping potential (App. B).

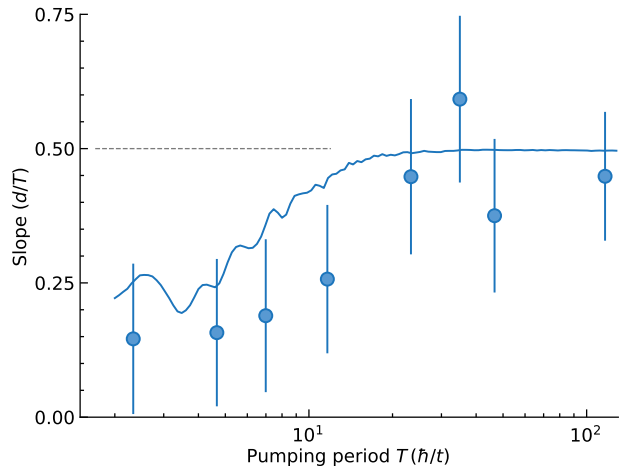


FIG. 4. **Stability of interaction-induced pumping for different pump periods T .** For pump periods longer than 20 tunnelling times, the transferred charge per cycle becomes largely independent of T , supporting the existence of stable interaction-induced pumping. For shorter pump periods, the measured slopes are reduced due to non-adiabatic effects. Data points and error bars are analogous to Fig. 3.

IV. STABILITY OF THE PUMP

A key aspect of our work is the ability to tune interactions and other external parameters in a controlled fashion. In a second set of experiments we map out the parameter regions in which interaction-induced pumping occurs. Here, we vary the Hubbard U from 0 to $17t$, fit lines to the data such as Fig. 2, and plot the resulting slopes in Fig. 3. From this data we can identify three distinct regimes. Firstly, we find vanishing displacements for interaction strengths up to $U/t \lesssim 6$ which matches the topologically trivial ‘pump’ with zero transferred charge. Secondly, we observe displacements of roughly $0.5 d/T$ for intermediate interactions ($6 \lesssim U/t \lesssim 12$), reflecting a large range of Hubbard U for which interaction-induced pumping occurs with $\Delta Q \simeq 1$. Thirdly, a re-entrant phase appears for $U/t \gtrsim 12$ when the interactions dominate and the singularity exits the pump trajectory for strong interactions. This interaction-induced transition to a topologically trivial situation with $\Delta Q = 0$ (or even into a nonadiabatic regime) also occurs for other types of pumps [20], as well as interacting topological insulators [46, 70, 71]. The observed transitions at $U/t \simeq 6$ and $U/t \simeq 12$ roughly coincide with the extremal Δ -values within the pump trajectory, $2\Delta_{\min}/t = 5.4$ and $2\Delta_{\max}/t = 12$. The scatter in the experimental data is due to drifts and shot-to-shot fluctuations of the atomic cloud, as well as our finite imaging resolution. We measure sub- μm movements on an atomic cloud using an imaging system with a resolution of only $5 \mu\text{m}$ while the total cloud diameter is on the order of $25 \mu\text{m}$.

We compare the experimental data with numerical simulations using matrix-product states in Fig. 3. These

theory calculations were performed with the experimental parameters of the time-dependent Hamiltonian [Eq. (1)] including the trapping potential. The starting state was approximated by disjoint singlet states on each dimer with no long-range correlations, in order to take our loading protocol and finite temperature into account (see App. B for details). The results of the U -scan are plotted as a line in Fig. 3 and we find good agreement between theory and experiment, within the error bars of the data points. Smoothing of the topological transitions is present both in theory and experiment, which is a result of nonadiabatic effects. The full-width-half-maximum of interaction-induced pumping plateau is located at $U/t = 5.8(3)$ and $U/t = 11.5(6)$, respectively, which is consistent with the experimental observations.

An important control parameter for adiabatic pumping is the duration of one pump cycle T , which is investigated experimentally in the following. Keeping the interaction strength [$U/t = 8.9(4)$] and all other experimental parameters fixed, we vary the pump period T over two orders of magnitude from 2 to 100 tunnelling times (\hbar/t). The results are plotted in Fig. 4 and the data suggests that for slow-enough pump periods the measured slope converges towards the quantised value of $0.5 d/T$ (dashed line) and becomes largely independent of T . This observation supports the conclusion that stable interaction-induced pumping occurs for a large range of parameters. The experimental data roughly agree with MPS calculations (solid line in Fig. 4). For fast pump periods below 20 tunnelling times, the interaction-induced displacement clearly breaks down due to nonadiabatic effects.

V. DYNAMICS OF SPIN- AND CHARGE-CORRELATIONS DURING PUMPING

So far, both the experimental data and the MPS simulations demonstrate near-quantised pumping in the first pump cycle for a range of finite interactions strengths, neighboured by regions of no pumping at small and large values of U/t , respectively. Since there are spin-gapless excitations in the region of a nonzero pumped charge, in principle, adiabaticity is not guaranteed. We now utilise numerical simulations to explain, on the one hand, why the pumping is initially still robust, consistent with the experimental data, and on the other hand, to develop a microscopic picture of the evolution of correlations in the pumping process.

The presence of a sublattice site offset (Δ) in the model gives rise to a coupling of spin- and charge-degrees of freedom, which can result in complex many-body dynamics. In our case, the ionic Hubbard model ($\delta = 0$) [57–60] is of particular interest due to the presence of two subsequent gap closings in its many-body spectrum. For concreteness, let us fix the value of U/t and vary Δ . A gap related to reordering of the charges vanishes only at the single critical points $\Delta = \pm\Delta_c$ which determine the topology of the charge sector. The spin gap vanishes for

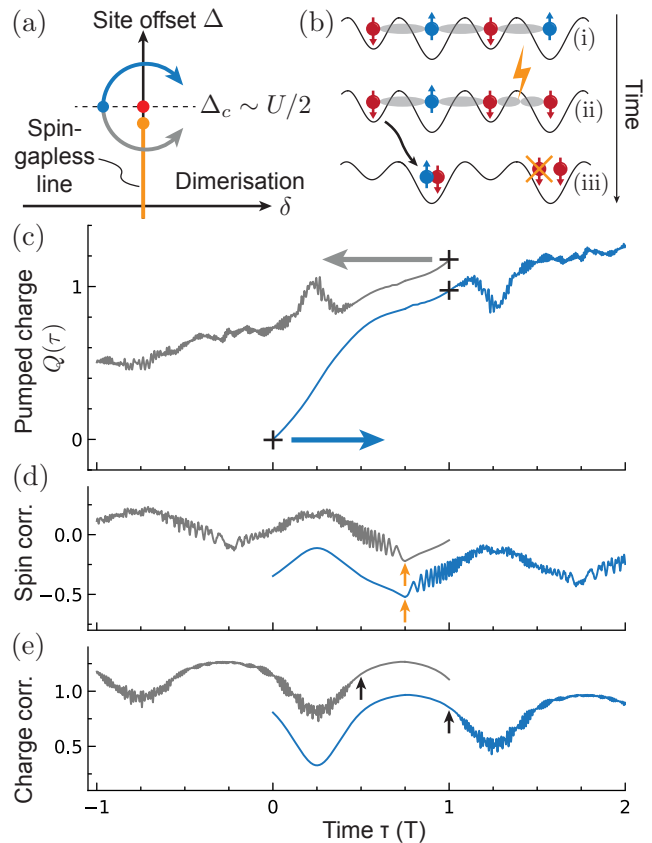


FIG. 5. **Dynamics of pumped charge, charge-, and spin-correlations computed with time-dependent Lanczos.** (a) Schematic of pump trajectory. The charge- and spin-gap closings along the ionic Hubbard axis ($\delta = 0$) are shown in red and orange, respectively. The spin-gapless line extends from $+\Delta_s$ to $-\Delta_s$. (b) Exemplary spin excitation (not the lowest), which can prevent further pumping after one period. (c,d,e) Dynamics of pumped charge, spin correlator, and charge correlator, respectively, calculated with Lanczos for $L = 10$, $T = 100\hbar/t$, $\delta\tau = 0.1\hbar/t$ and antiperiodic boundary conditions (see App. B). The blue line corresponds to counter-clockwise pumping (blue arrow), whereas the grey lines correspond to clockwise pumping (grey arrow, plotted in reverse time $-\tau$ for comparison). The crosses in (c) indicate quantised displacement. The orange arrows in (d) denote the crossing of the spin-gapless line. The black arrows in (e) denote the crossing of the $\Delta = \Delta_c$ line. All three grey curves have been offset on the vertical axis for clarity.

$-\Delta_s \leq \Delta \leq \Delta_s$, where $\Delta_c - \Delta_s \lesssim t$ [57–60], and we will call it ‘spin-gapless line’ in the following, denoted by an orange line in Fig. 5(a). The parameter trajectory for the interaction-induced pump crosses this line and spin excitations can occur, in principle, at zero energy cost.

The schematics in Fig. 5(b) illustrate how spin- and charge-dynamics can become intertwined during the course of a pump cycle. While not the exact ground state, it is instructive to start from an anti-ferromagnetically ordered state in (i) and incur a spin excitation when cross-

ing the spin-gapless line for $\Delta < \Delta_s$ [see (ii)]. The spin excitation can take the form of a spin triplet or more complex patterns; here a spin-flip from \uparrow to \downarrow is shown for simplicity. In the subsequent half-cycle, two neighbouring spins have to form a double occupancy ($\Delta > \Delta_c$) in order to ensure pumping. However, the spin-excited pair precludes the formation of a double occupancy, thereby preventing pumping (iii).

In the following we investigate the mechanism described above using numerical simulations of pumped charge per unit cell $Q(\tau)$, spin-correlations, as well as charge-correlations as functions of time, shown in Figs. 5(c)-(e). Here, we choose an idealised system consisting of ten lattice sites, antiperiodic boundary conditions, and an elliptical pump trajectory in order to draw generic, qualitative conclusions, leaving out some of the specifics of our experimental system (see App. B). We compare two distinct trajectories, both starting on the left of the (δ, Δ) -plane, as shown in Fig. 5(a). The ‘blue’ trajectory crosses the spin-gapless line at $\tau = 3T/4$ while the ‘grey’ one crosses the spin-gapless line at $\tau = T/4$. In Figs. 5(c)-(e), the blue trajectory is always plotted forwards in time (starting from $\tau = 0$) while the grey trajectory is plotted backwards in time (starting from $\tau/T = 1$ and offset on the vertical axis) in order to simplify the comparison. The blue trajectory clearly shows a quantised response (black crosses) for one period, while the pumped charge is visibly reduced during the second period. The grey trajectory follows the blue trajectory for half a period but departs afterwards.

In order to understand the charge dynamics described previously we now consider the dynamics of spin- and charge-correlations in Figs. 5(d) and (e). The spin-correlations visibly start to oscillate when crossing the spin-gapless line after $3/4$ (blue) and $1/4$ (grey) of the pump period (orange arrows). Indeed, the charge dynamics remains smooth up until $\Delta \sim \Delta_c$ which happens after 1 (blue) and $1/2$ (grey) period, respectively (black arrows). We can conclude that the spin excitations are converted to charge excitations with a delay of a quarter period. Interestingly, this effect is largely independent of system size, as shown in Fig. A3. To summarise, crossing the spin-gapless line does not necessarily lead to an immediate breakdown of pumping, but excitations first have to spread to the charge sector in order to influence the pumped charge.

The spin-gapless line plays an important role in determining the long-time behaviour of the interaction-induced charge pump [32]. In the experiment, we observe a reduction of the pumped charge after the first cycle (Fig. A2), which could indicate a breakdown of pumping after one cycle. Indeed, the interplay between spin- and charge-degrees of freedom implies that the dynamics of the second and subsequent pump cycles will become increasingly dependent on the precise system parameters, such as system size and pump trajectory. We investigate these effects using numerical calculations in Fig. A4. The precise values of the excitation gaps matter crucially,

which can be tuned by modifying the pump cycle and the driving protocol. Altering the pump trajectory in the experiment corresponds to including higher harmonics in the driving waveform which we plan to investigate in the future.

Similarly, the addition of an Ising-type interaction term leads to an explicit opening of the spin gap in the Mott-insulating regime of the ionic Hubbard model, which can improve the stability of the pump even further (Fig. A6). Ising-anisotropies have been realised with two-component bosons [72].

A third approach involves the intermediate (third) phase in the ionic Hubbard model, called the spontaneously dimerised insulator (SDI). The three phases of the ionic Hubbard model for repulsive interactions are, in ascending order of Δ , Mott insulator, SDI, and band insulator. The transition from a Mott insulator to the SDI is accompanied by a spin-gap opening. The transition from the SDI to the band insulator is due to a crossing of two ground states with different charge distributions. Thus, adiabatic pumping could potentially be stabilised by enlarging the SDI phase and avoiding the Mott insulator altogether. It has been suggested that including a density-dependent hopping term into the ionic Hubbard model can enlarge the SDI phase [73]. A density-dependent hopping can be engineered by near-resonant Floquet modulation [74–77].

VI. OUTLOOK

In conclusion, we have experimentally demonstrated an interaction-induced charge pump using ultracold fermions in a dynamical superlattice. The observed transport is consistent with quantised pumping within a range of repulsive interactions, while it has no classical counterpart and the pumped charge is zero below a critical Hubbard U . Pumping of one charge per cycle is not possible for $U = 0$, therefore, the pumping protocol is not adiabatically connected to the non-interacting limit. Our numerical simulations unveil the mechanism for the breakdown of adiabatic pumping, in which spin excitations are transferred to the charge sector only later in the pump cycle.

These results open up multiple avenues for future research into topological many-body systems. For example, the presence of trapping potentials in the experiment could lead to interaction-induced edge physics [78], possibly giving rise to novel topological boundary modes [79]. Novel cooling mechanisms in optical lattices may be enabled via density redistribution [80], making use of the inherent backaction between density and pump-induced currents in the interaction-induced charge pump. In addition, the coupling mechanism between spin and charge degrees of freedom could be harnessed to realise singlet pumping, in view to realise measurement-based quantum computation [81]. In general, our work establishes Thouless charge pumping as a promising system to inves-

tigate interaction-driven physics in topological systems and topological quantum matter. Having cross-validated theory and experiment in the limit of one-dimensional dynamics, the experimental platform can be extended to two [82, 83] and even three dimensions, eventually addressing questions beyond the reach of numerical simulations.

ACKNOWLEDGEMENTS

We would like to thank Kaden Hazzard and Philipp Preiss for comments on a previous version of the manuscript. K.V., A.-S.W., Z.Z., M.G., and T.E. ac-

knowledge funding by the Swiss National Science Foundation (Grants No. 182650, 212168, NCCR-QSIT, as well as advanced grant AdiaPump 209376) and European Research Council advanced grant TransQ (Grant No. 742579). E.B. and F.H.-M. acknowledge funding by the Deutsche Forschungsgemeinschaft (DFG, German Research Foundation) – 277974659, 436382789, 493420525 via DFG Research Unit FOR 2414 and large-equipment grants (GOEGrid cluster). A.A.A. acknowledges financial support provided by PICT 2017-2726 and PICT 2018-01546 of the ANPCyT, Argentina. This research was supported in part by the National Science Foundation under Grant No. NSF PHY-1748958.

-
- [1] D. Xiao, M.-C. Chang, and Q. Niu, Berry phase effects on electronic properties, *Rev. Mod. Phys.* **82**, 1959 (2010).
- [2] D. J. Thouless, Quantization of particle transport, *Phys. Rev. B* **27**, 6083 (1983).
- [3] J. K. Asbóth, L. Oroszlány, and A. Pályi, *A short course on topological insulators: band structure and edge states in one and two dimensions*, Lecture notes in physics, Volume 919 (Springer, Cham, 2016).
- [4] N. R. Cooper, J. Dalibard, and I. B. Spielman, Topological bands for ultracold atoms, *Reviews of Modern Physics* **91**, 015005 (2019).
- [5] J. P. Pekola, O.-P. Saira, V. F. Maisi, A. Kemppinen, M. Möttönen, Y. A. Pashkin, and D. V. Averin, Single-electron current sources: Toward a refined definition of the ampere, *Rev. Mod. Phys.* **85**, 1421 (2013).
- [6] T. Oka and S. Kitamura, Floquet Engineering of Quantum Materials, *Annu. Rev. Condens. Matter Phys.* **10**, 387 (2019).
- [7] R. Citro and M. Aidelsburger, Thouless pumping and topology, *Nat. Rev. Phys.* **5**, 87 (2023).
- [8] Y. E. Kraus, Y. Lahini, Z. Ringel, M. Verbin, and O. Zeitlinger, Topological States and Adiabatic Pumping in Quasicrystals, *Phys. Rev. Lett.* **109**, 106402 (2012).
- [9] M. Lohse, C. Schweizer, O. Zeitlinger, M. Aidelsburger, and I. Bloch, A Thouless quantum pump with ultracold bosonic atoms in an optical superlattice, *Nature Physics* **12**, 350 (2016).
- [10] S. Nakajima, T. Tomita, S. Taie, T. Ichinose, H. Ozawa, L. Wang, M. Troyer, and Y. Takahashi, Topological Thouless pumping of ultracold fermions, *Nature Physics* **12**, 296 (2016).
- [11] Y. Ke, X. Qin, F. Mei, H. Zhong, Y. S. Kivshar, and C. Lee, Topological phase transitions and Thouless pumping of light in photonic waveguide arrays, *Laser & Photonics Reviews* **10**, 995 (2016).
- [12] H.-I. Lu, M. Schemmer, L. M. Aycock, D. Genkina, S. Sugawa, and I. B. Spielman, Geometrical Pumping with a Bose-Einstein Condensate, *Physical Review Letters* **116**, 200402 (2016).
- [13] W. Ma, L. Zhou, Q. Zhang, M. Li, C. Cheng, J. Geng, X. Rong, F. Shi, J. Gong, and J. Du, Experimental Observation of a Generalized Thouless Pump with a Single Spin, *Phys. Rev. Lett.* **120**, 120501 (2018).
- [14] A. Cerjan, M. Wang, S. Huang, K. P. Chen, and M. C. Rechtsman, Thouless pumping in disordered photonic systems, *Light: Science & Applications* **9**, 178 (2020).
- [15] S. Nakajima, N. Takei, K. Sakuma, Y. Kuno, P. Marra, and Y. Takahashi, Competition and interplay between topology and quasi-periodic disorder in Thouless pumping of ultracold atoms, *Nat. Phys.* **17**, 844 (2021).
- [16] J. Minguzzi, Z. Zhu, K. Sandholzer, A.-S. Walter, K. Viebahn, and T. Esslinger, Topological Pumping in a Floquet-Bloch Band, *Phys. Rev. Lett.* **129**, 053201 (2022).
- [17] Z.-C. Xiang, K. Huang, Y.-R. Zhang, T. Liu, Y.-H. Shi, C.-L. Deng, T. Liu, H. Li, G.-H. Liang, Z.-Y. Mei, H. Yu, G. Xue, Y. Tian, X. Song, Z.-B. Liu, K. Xu, D. Zheng, F. Nori, and H. Fan, Simulating quantum Hall effects on a superconducting quantum processor (2022), arXiv:2207.11797.
- [18] M. Jürgensen, S. Mukherjee, and M. C. Rechtsman, Quantized nonlinear Thouless pumping, *Nature* **596**, 63 (2021).
- [19] M. Jürgensen, S. Mukherjee, C. Jörg, and M. C. Rechtsman, Quantized fractional Thouless pumping of solitons, *Nat. Phys.* 10.1038/s41567-022-01871-x (2023).
- [20] A.-S. Walter, Z. Zhu, M. Gächter, J. Minguzzi, S. Roschinski, K. Sandholzer, K. Viebahn, and T. Esslinger, Quantization and its breakdown in a Hubbard–Thouless pump, *Nat. Phys.* 10.1038/s41567-023-02145-w (2023).
- [21] Q. Niu and D. J. Thouless, Quantised adiabatic charge transport in the presence of substrate disorder and many-body interaction, *J. Phys. A: Math. Gen.* **17**, 2453 (1984).
- [22] E. Berg, M. Levin, and E. Altman, Quantized Pumping and Topology of the Phase Diagram for a System of Interacting Bosons, *Phys. Rev. Lett.* **106**, 110405 (2011).
- [23] Y. Qian, M. Gong, and C. Zhang, Quantum transport of bosonic cold atoms in double-well optical lattices, *Phys. Rev. A* **84**, 013608 (2011).
- [24] L. Wang, M. Troyer, and X. Dai, Topological Charge Pumping in a One-Dimensional Optical Lattice, *Phys. Rev. Lett.* **111**, 026802 (2013).
- [25] F. Grusdt and M. Hönig, Realization of fractional Chern insulators in the thin-torus limit with ultracold bosons, *Phys. Rev. A* **90**, 053623 (2014).

- [26] T.-S. Zeng, W. Zhu, and D. N. Sheng, Fractional charge pumping of interacting bosons in one-dimensional superlattice, *Phys. Rev. B* **94**, 235139 (2016).
- [27] J. Tangpanitanon, V. M. Bastidas, S. Al-Assam, P. Roushan, D. Jaksch, and D. G. Angelakis, Topological Pumping of Photons in Nonlinear Resonator Arrays, *Phys. Rev. Lett.* **117**, 213603 (2016).
- [28] R. Li and M. Fleischhauer, Finite-size corrections to quantized particle transport in topological charge pumps, *Phys. Rev. B* **96**, 085444 (2017).
- [29] Y. Ke, X. Qin, Y. S. Kivshar, and C. Lee, Multiparticle Wannier states and Thouless pumping of interacting bosons, *Phys. Rev. A* **95**, 063630 (2017).
- [30] L. Taddia, E. Cornfeld, D. Rossini, L. Mazza, E. Sela, and R. Fazio, Topological Fractional Pumping with Alkaline-Earth-Like Atoms in Synthetic Lattices, *Phys. Rev. Lett.* **118**, 230402 (2017).
- [31] A. Hayward, C. Schweizer, M. Lohse, M. Aidelsburger, and F. Heidrich-Meisner, Topological charge pumping in the interacting bosonic Rice-Mele model, *Phys. Rev. B* **98**, 245148 (2018).
- [32] M. Nakagawa, T. Yoshida, R. Peters, and N. Kawakami, Breakdown of topological Thouless pumping in the strongly interacting regime, *Phys. Rev. B* **98**, 115147 (2018).
- [33] L. Stenzel, A. L. C. Hayward, C. Hubig, U. Schollwöck, and F. Heidrich-Meisner, Quantum phases and topological properties of interacting fermions in one-dimensional superlattices, *Phys. Rev. A* **99**, 053614 (2019).
- [34] T. Haug, R. Dumke, L.-C. Kwek, and L. Amico, Topological pumping in Aharonov–Bohm rings, *Commun Phys* **2**, 127 (2019).
- [35] R. Unanyan, M. Kiefer-Emmanouilidis, and M. Fleischhauer, Finite-Temperature Topological Invariant for Interacting Systems, *Phys. Rev. Lett.* **125**, 215701 (2020).
- [36] S. Greschner, S. Mondal, and T. Mishra, Topological charge pumping of bound bosonic pairs, *Phys. Rev. A* **101**, 053630 (2020).
- [37] Y.-L. Chen, G.-Q. Zhang, D.-W. Zhang, and S.-L. Zhu, Simulating bosonic Chern insulators in one-dimensional optical superlattices, *Phys. Rev. A* **101**, 013627 (2020).
- [38] Q. Fu, P. Wang, Y. V. Kartashov, V. V. Konotop, and F. Ye, Nonlinear Thouless Pumping: Solitons and Transport Breakdown, *Phys. Rev. Lett.* **128**, 154101 (2022).
- [39] N. Mostaan, F. Grusdt, and N. Goldman, Quantized topological pumping of solitons in nonlinear photonics and ultracold atomic mixtures, *Nat Commun* **13**, 5997 (2022).
- [40] M. Dzero, J. Xia, V. Galitski, and P. Coleman, Topological Kondo Insulators, *Annu. Rev. Condens. Matter Phys.* **7**, 249 (2016).
- [41] L. Lin, Y. Ke, and C. Lee, Interaction-induced topological bound states and Thouless pumping in a one-dimensional optical lattice, *Phys. Rev. A* **101**, 023620 (2020).
- [42] Y. Kuno and Y. Hatsugai, Interaction-induced topological charge pump, *Phys. Rev. Research* **2**, 042024 (2020).
- [43] E. Bertok, F. Heidrich-Meisner, and A. A. Aligia, Splitting of topological charge pumping in an interacting two-component fermionic Rice-Mele Hubbard model, *Phys. Rev. B* **106**, 045141 (2022).
- [44] P. M. Ostrovsky, I. V. Gornyi, and A. D. Mirlin, Interaction-Induced Criticality in Z_2 Topological Insulators, *Phys. Rev. Lett.* **105**, 036803 (2010).
- [45] L. Wang, X. Dai, and X. C. Xie, Interaction-induced topological phase transition in the Bernevig-Hughes-Zhang model, *EPL* **98**, 57001 (2012).
- [46] J. C. Budich, B. Trauzettel, and G. Sangiovanni, Fluctuation-driven topological Hund insulators, *Phys. Rev. B* **87**, 235104 (2013).
- [47] P. Kumar, T. Mertz, and W. Hofstetter, Interaction-induced topological and magnetic phases in the Hofstadter-Hubbard model, *Phys. Rev. B* **94**, 115161 (2016).
- [48] G. Salerno, G. Palumbo, N. Goldman, and M. Di Liberto, Interaction-induced lattices for bound states: Designing flat bands, quantized pumps, and higher-order topological insulators for doublons, *Phys. Rev. Research* **2**, 013348 (2020).
- [49] J.-H. Zheng, B. Irsigler, L. Jiang, C. Weitenberg, and W. Hofstetter, Measuring an interaction-induced topological phase transition via the single-particle density matrix, *Phys. Rev. A* **101**, 013631 (2020).
- [50] J. Herbrych, M. Środa, G. Alvarez, M. Mierzejewski, and E. Dagotto, Interaction-induced topological phase transition and Majorana edge states in low-dimensional orbital-selective Mott insulators, *Nat Commun* **12**, 2955 (2021).
- [51] S. S. Luntama, P. Törmä, and J. L. Lado, Interaction-induced topological superconductivity in antiferromagnet-superconductor junctions, *Phys. Rev. Research* **3**, L012021 (2021).
- [52] U. Schollwöck, The density-matrix renormalization group, *Rev. Mod. Phys.* **77**, 259 (2005).
- [53] U. Schollwöck, The density-matrix renormalization group in the age of matrix product states, *Annals of Physics* **326**, 96 (2011).
- [54] G. Jotzu, M. Messer, R. Desbuquois, M. Lebrat, T. Uehlinger, D. Greif, and T. Esslinger, Experimental realization of the topological Haldane model with ultracold fermions, *Nature* **515**, 237 (2014).
- [55] M. Tarnowski, F. N. Ünal, N. Fläschner, B. S. Rem, A. Eckardt, K. Sengstock, and C. Weitenberg, Measuring topology from dynamics by obtaining the Chern number from a linking number, *Nat Commun* **10**, 1728 (2019).
- [56] K. Wintersperger, C. Braun, F. N. Ünal, A. Eckardt, M. D. Liberto, N. Goldman, I. Bloch, and M. Aidelsburger, Realization of an anomalous Floquet topological system with ultracold atoms, *Nat. Phys.* **16**, 1058 (2020).
- [57] M. Fabrizio, A. O. Gogolin, and A. A. Nersisyan, From Band Insulator to Mott Insulator in One Dimension, *Phys. Rev. Lett.* **83**, 2014 (1999).
- [58] M. E. Torio, A. A. Aligia, and H. A. Ceccatto, Phase diagram of the Hubbard chain with two atoms per cell, *Phys. Rev. B* **64**, 121105 (2001).
- [59] S. R. Manmana, V. Meden, R. M. Noack, and K. Schönhammer, Quantum critical behavior of the one-dimensional ionic Hubbard model, *Phys. Rev. B* **70**, 155115 (2004).
- [60] M. E. Torio, A. A. Aligia, G. I. Japaridze, and B. Normand, Quantum phase diagram of the generalized ionic Hubbard model for AB_n chains, *Phys. Rev. B* **73**, 115109 (2006).
- [61] D. Pertot, A. Sheikhan, E. Cocchi, L. A. Miller, J. E. Bohn, M. Koschorreck, M. Köhl, and C. Kollath, Relaxation Dynamics of a Fermi Gas in an Optical Superlattice, *Phys. Rev. Lett.* **113**, 170403 (2014).

- [62] M. Messer, R. Desbuquois, T. Uehlinger, G. Jotzu, S. Huber, D. Greif, and T. Esslinger, Exploring Competing Density Order in the Ionic Hubbard Model with Ultracold Fermions, *Phys. Rev. Lett.* **115**, 115303 (2015).
- [63] M. Aidelsburger, M. Lohse, C. Schweizer, M. Atala, J. T. Barreiro, S. Nascimbène, N. R. Cooper, I. Bloch, and N. Goldman, Measuring the Chern number of Hofstadter bands with ultracold bosonic atoms, *Nature Physics* **11**, 162 (2015).
- [64] M. Reitter, J. Näger, K. Wintersperger, C. Sträter, I. Bloch, A. Eckardt, and U. Schneider, Interaction Dependent Heating and Atom Loss in a Periodically Driven Optical Lattice, *Physical Review Letters* **119**, 200402 (2017).
- [65] K. Viebahn, J. Minguzzi, K. Sandholzer, A.-S. Walter, M. Sajani, F. Görg, and T. Esslinger, Suppressing Dissipation in a Floquet-Hubbard System, *Physical Review X* **11**, 011057 (2021).
- [66] T.-W. Zhou, G. Cappellini, D. Tusi, L. Franchi, J. Paravicini, C. Repellin, S. Greschner, M. Inguscio, T. Giamarchi, M. Filippone, J. Catani, and L. Fallani, Observation of universal Hall response in strongly interacting Fermions, *Science* **381**, 427 (2023).
- [67] J. Léonard, S. Kim, J. Kwan, P. Segura, F. Grusdt, C. Repellin, N. Goldman, and M. Greiner, Realization of a fractional quantum Hall state with ultracold atoms, *Nature* 10.1038/s41586-023-06122-4 (2023).
- [68] S. R. Manmana, A. M. Essin, R. M. Noack, and V. Gurarie, Topological invariants and interacting one-dimensional fermionic systems, *Phys. Rev. B* **86**, 205119 (2012).
- [69] A. A. Aligia, Topological invariants based on generalized position operators and application to the interacting Rice-Mele model, *Phys. Rev. B* **107**, 075153 (2023).
- [70] D. Pesin and L. Balents, Mott physics and band topology in materials with strong spin-orbit interaction, *Nature Phys* **6**, 376 (2010).
- [71] T. I. Vanhala, T. Siro, L. Liang, M. Troyer, A. Harju, and P. Törmä, Topological Phase Transitions in the Repulsively Interacting Haldane-Hubbard Model, *Phys. Rev. Lett.* **116**, 225305 (2016).
- [72] P. N. Jepsen, J. Amato-Grill, I. Dimitrova, W. W. Ho, E. Demler, and W. Ketterle, Spin transport in a tunable Heisenberg model realized with ultracold atoms, *Nature* **588**, 403 (2020).
- [73] P. Roura-Bas and A. A. Aligia, Phase diagram of the ionic Hubbard model with density-dependent hopping (2023), arXiv:2304.04563 [cond-mat].
- [74] R. Ma, M. E. Tai, P. M. Preiss, W. S. Bakr, J. Simon, and M. Greiner, Photon-Assisted Tunneling in a Biased Strongly Correlated Bose Gas, *Phys. Rev. Lett.* **107**, 095301 (2011).
- [75] F. Meinert, M. J. Mark, K. Lauber, A. J. Daley, and H.-C. Nägerl, Floquet Engineering of Correlated Tunneling in the Bose-Hubbard Model with Ultracold Atoms, *Phys. Rev. Lett.* **116**, 205301 (2016).
- [76] F. Görg, M. Messer, K. Sandholzer, G. Jotzu, R. Desbuquois, and T. Esslinger, Enhancement and sign change of magnetic correlations in a driven quantum many-body system, *Nature* **553**, 481 (2018).
- [77] M. Messer, K. Sandholzer, F. Görg, J. Minguzzi, R. Desbuquois, and T. Esslinger, Floquet Dynamics in Driven Fermi-Hubbard Systems, *Physical Review Letters* **121**, 233603 (2018).
- [78] Z. Zhu, M. Gächter, A.-S. Walter, K. Viebahn, and T. Esslinger, Reversal of quantised Hall drifts at non-interacting and interacting topological boundaries (2023), arXiv:2301.03583 [cond-mat, physics:physics].
- [79] S. Rachel, Interacting topological insulators: a review, *Rep. Prog. Phys.* **81**, 116501 (2018).
- [80] C. S. Chiu, G. Ji, A. Mazurenko, D. Greif, and M. Greiner, Quantum State Engineering of a Hubbard System with Ultracold Fermions, *Phys. Rev. Lett.* **120**, 243201 (2018).
- [81] K. K. Das, S. Kim, and A. Mizel, Controlled Flow of Spin-Entangled Electrons via Adiabatic Quantum Pumping, *Phys. Rev. Lett.* **97**, 096602 (2006).
- [82] Q. Fu, P. Wang, Y. V. Kartashov, V. V. Konotop, and F. Ye, Two-Dimensional Nonlinear Thouless Pumping of Matter Waves, *Phys. Rev. Lett.* **129**, 183901 (2022).
- [83] A. Padhan, S. Mondal, S. Vishveshwara, and T. Mishra, Interacting bosons on a Su-Schrieffer-Heeger ladder: Topological phases and Thouless pumping (2023), arXiv:2306.09325 [cond-mat].
- [84] G. Vidal, Efficient Simulation of One-Dimensional Quantum Many-Body Systems, *Phys. Rev. Lett.* **93**, 040502 (2004).
- [85] S. R. White and A. E. Feiguin, Real-Time Evolution Using the Density Matrix Renormalization Group, *Phys. Rev. Lett.* **93**, 076401 (2004).
- [86] A. J. Daley, C. Kollath, U. Schollwöck, and G. Vidal, Time-dependent density-matrix renormalization-group using adaptive effective Hilbert spaces, *J. Stat. Mech.: Theor. Exp.* **2004**, P04005 (2004).
- [87] L. Privitera, A. Russomanno, R. Citro, and G. E. Santoro, Nonadiabatic Breaking of Topological Pumping, *Phys. Rev. Lett.* **120**, 106601 (2018).
- [88] S. R. Manmana, Time evolution of one-dimensional Quantum Many Body Systems, in *AIP Conference Proceedings*, Vol. 789 (AIP, Salerno (Italy), 2005) pp. 269–278, iSSN: 0094243X.

Appendix A: Experimental details

The time-dependent optical lattice potential is given by

$$\begin{aligned}
 V(x, y, z, \tau) = & \\
 & - V_X I_{\text{self}} \cos^2(kx + \vartheta/2) \\
 & - V_{X_{\text{int}}}(\tau) I_{\text{self}} \cos^2(kx) \\
 & - V_Y \cos^2(ky) \\
 & - V_Z \cos^2(kz) \\
 & - \sqrt{V_{X_{\text{int}}}(\tau) V_Z} \cos(kz) \cos[kx + \varphi(\tau)] \\
 & - I_{XZ} \sqrt{V_{X_{\text{int}}}(\tau) V_Z} \cos(kz) \cos[kx - \varphi(\tau)] ,
 \end{aligned} \tag{A1}$$

where $k = 2\pi/\lambda$ and $\lambda = 1064$ nm. The constant lattice depths $[V_X, V_Y, V_Z]$ used in this paper are given by $[7.95(7), 20.08(4), 17.0(1)]E_R$, measured in units of recoil energy $E_R = \hbar^2/2m\lambda^2$, where m the mass of the atoms. The values in brackets denote the standard deviations of the lattice depths over 5700 individual measurements. Contrary to our previous work [20], the value of $V_{X_{\text{int}}}(\tau)$ is time-dependent:

$$V_{X_{\text{int}}}(\tau) = V_0[1 + A \times \sin(2\pi\tau/T)]. \tag{A2}$$

The average lattice depth is $V_0 = 0.30(2)E_R$ and the amplitude is $A = 0.67(7)$. Likewise, the superlattice phase is time-dependent:

$$\varphi(\tau) = \pi/2 \times [1 + \cos(2\pi\tau/T)]. \tag{A3}$$

The imbalance factors are $I_{\text{self}} = 0.98(2)$ and $I_{XZ} = 0.81(2)$.

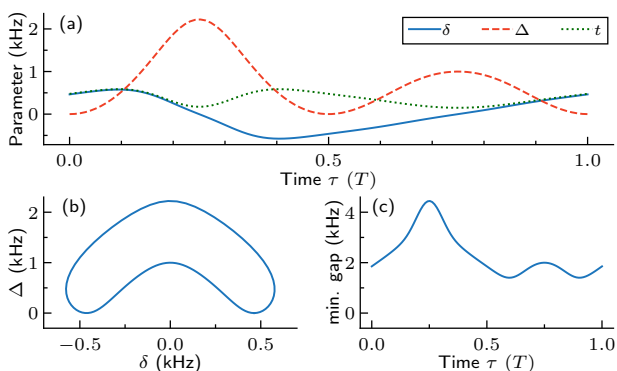


FIG. A1. **Experimental pump trajectory.** (a) Rice-Mele parameters as function of time. (b) The ‘boomerang’ pump trajectory. (c) The single-particle band gap varies during the course of a pump cycle. Its minimum is 1.4 kHz. All energies are given in kHz ($\times \hbar$).

The time-dependent lattice parameters $V_{X_{\text{int}}}(\tau)$ and $\varphi(\tau)$ lead to a periodic variation of the Rice-Mele parameters δ (dimerisation), Δ (sublattice site offset), and t (average tunnelling), as plotted in Fig. A1(a). The resulting

pump trajectory is ‘boomerang’-shaped [Fig. A1(b)]. In addition, we plot the minimal single-particle band gap in Fig. A1(c). The minimum band gap of 1.4 kHz can be used to estimate an adiabatic timescale in the non-interacting limit. The time-dependence of the average hopping matrix element t causes a slight shift of the critical Δ_c at a fixed value of U by an amount which is smaller than t .

A large range of Hubbard U can be accessed by utilising the Feshbach resonances in the hyperfine ground-state manifold $F = 9/2$ of ^{40}K . For small and intermediate values of $U < 6t$, we use the mixture $m_F = \{-9/2, -7/2\}$. For stronger interactions ($U > 7t$), we use the mixture $m_F = \{-9/2, -5/2\}$. In between the two ranges there is a small gap in the measured data points (Fig. 3). The bracketed errors of the values of U/t are dominated by the statistical uncertainty of 5% in the value of t .

As described in the main text, we extract the scaled centre-of-mass position to measure the pumped charges. In Fig. A2 below we plot the measured dynamics beyond one pump cycle. The outlier in Fig. A2(a) can be attributed to slow drifts as well as statistical noise. Similar outliers are responsible for the scatter in Fig. 3 in the main text. Interaction-induced pumping is evident from Fig. A2(b), but the slope does not persist beyond one pump cycle.

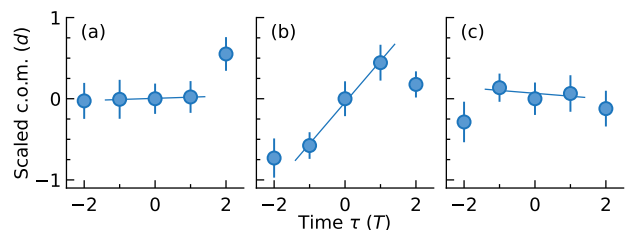


FIG. A2. **Measured centre-of-mass displacements for two pump cycles.** The panels show different values of Hubbard U/t : (a) 0, (b) 9.7, and (c) 16.

Appendix B: Numerical simulations

1. Real-time simulations

For the theory curves in Figs. 2, 3 and 4, we use a variational MPS method for ground-state calculations [52, 53] and time-evolving-block-decimation (TEBD) [84–86] for the time-evolution. The pumping is always started slowly via a quadratic ramp-up of the driving to minimise non-adiabatic effects [87]. In order to make the initial state resemble experimentally realistic conditions, we start with decoupled dimer states. Concretely, we prepare each pair of two sites (a dimer) in their ground state and then form a product of such dimers.

Technically, we start from the ground state for the decoupled Hamiltonian

$$\hat{H}_{\mathcal{D}_N} = \sum_{(i,j) \in \mathcal{D}_N} \hat{H}_{i,j}. \quad (\text{A1})$$

$\mathcal{D}_N = \{\dots, (c-2, c-1), (c, c+1), (c+2, c+3), \dots\}$ is a set of uncoupled dimer sites centred around site c , such that we fill N particles in total. Each initial dimer contains 2 particles (one spin-up and one spin-down fermion). c is chosen to be compatible with the dimerised ground state of the whole system. We use an open system with size $L = 49$, a trap strength of $V/t = 0.034$ and $N = 24$ particles. For the ground-state search, we converge the local density to a tolerance of 10^{-4} . The time-evolution is carried out using TEBD with a time step of $d\tau = 0.01/t$ (where t is the average hopping rate) and an adaptive bond dimension with a cutoff of 10^{-12} . The pump cycle is identical to the experimental one. The pumped charge is computed from the centre-of-mass displacement of the cloud.

For Fig. 5, we study a finite system with open-shell boundary conditions (periodic boundary conditions for a number of sites L multiple of four, antiperiodic for even L not a multiple of four) to allow for the resolving of gap closings. We consider an elliptical pump cycle

$$(\Delta/t, \delta) = [\Delta_c + R_\Delta \sin(\theta), R_\delta \cos(\theta)] , \quad (\text{A2})$$

with $R_\Delta/t = 2.10$ and $R_\delta = 0.88$. The time-evolution is carried out with a time-dependent Lanczos method [88] with a tolerance of 10^{-12} and a time-step of $d\tau = 0.01/t$. The initial state is chosen as the many-body ground state at $\theta = 0$. The pumped charge is computed as the integral over the local particle current over one period:

$$Q(\tau) = \int_0^T d\tau' \langle \hat{J}(\tau') \rangle, \quad (\text{A3})$$

$$\hat{J} = \frac{i}{2} \sum_{j=1,2;\alpha=\uparrow,\downarrow} \left(t_j \hat{c}_{j,\alpha}^\dagger \hat{c}_{j+1,\alpha} - \text{H.c.} \right), \quad (\text{A4})$$

with $t_j(\tau) = t + (-1)^j \delta(\tau)$.

In order to explore the breakdown of quantised charge pumping due to low-lying spin excitations, we calculate the charge and spin nearest-neighbour correlators:

$$C_{\hat{n}}(t) = \frac{1}{L} \langle \Psi(t) | \sum_{j=1}^L \hat{n}_j \hat{n}_{j+1} | \Psi(t) \rangle \quad (\text{A5})$$

$$C_{\hat{S}}(t) = \frac{4}{L} \langle \Psi(t) | \sum_{j=1}^L \hat{S}_j^z \hat{S}_{j+1}^z | \Psi(t) \rangle, \quad (\text{A6})$$

where $\hat{n}_j = \hat{n}_{\uparrow,j} + \hat{n}_{\downarrow,j}$ is the total particle number operator and $\hat{S}_j^z = (\hat{n}_{\uparrow,j} - \hat{n}_{\downarrow,j})/2$ is the total spin projection. $|\Psi(t)\rangle$ are the time-propagated states.

In the calculations for Fig. 5, we simplify the setup and discard the trap, the variation of the hopping matrix element t , and the shape of the pump cycle. As the initial

state, we choose the ground state at the start of the cycle. We verified that this simplification does not affect the main qualitative conclusions from Fig. 5.

We next discuss the individual effect of some of the potential sources for nonadiabatic and nonquantised pumping.

2. Effects of trap, particle number and state preparation

As the experiment works with a harmonic trap, there are limitations concerning the maximum number of cycles that can be carried out. At the latest, when the increase of the onsite potential due to the trap overcomes the required variation of potentials during the pump cycle, quantised and unidirectional pumping will break down. However, this happens much later than the first pump cycle [78].

Another possible source of imperfect pumping could be the inhomogeneous distribution of particle numbers in the various one-dimensional systems probed simultaneously in our experiment. While it is impossible to simulate the dynamics of the full distribution for an interacting system with realistic particle numbers, we studied the behavior when increasing N at fixed trap strength for the initial state used in the experiment. All other parameters are kept fixed and correspond to the situation discussed in the main text in the context of Fig. 3.

Our results are shown in Fig. A3. Clearly, regardless of how many particles are placed into the trap (as long as we do not reach the region of a steep potential increase), during the first three quarters of the pump cycle, the behavior is largely independent thereof and the particle number affects the pumped charge only mildly. After crossing the gapless line, however, the pump efficiency depends on N , with smaller N being detrimental to efficient pumping. Notably, the pumped charge quickly becomes independent of particle number for $N \gtrsim 12$ and the pumped charge converges to a quantised value in the first pump cycle. Since particle numbers are much higher in most of the one-dimensional systems realised in the experiment, we conclude that variations in N can be excluded as a dominant source of imperfect pumping on the time scales investigated.

Another potential source of imperfect pumping could be initial-state-preparation defects, e.g., hole and doublon defects as well as empty unit cells in the string of dimers. Exemplary simulations show that every string of dimers pumps independently on the relevant time scales and hence these defects are not expected to play a crucial role.

3. Role of the pump cycle

For a strictly adiabatic situation, the choice of the pump cycle does not matter. In our situation, where

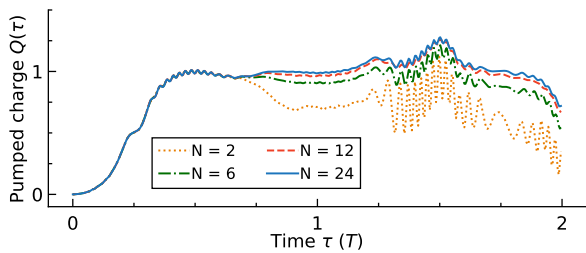


FIG. A3. **Pumping for different particle numbers.** TEBD calculation for a harmonically trapped system with initial strings of dimer states with different particle numbers $N = 2, 6, 12,$ and 24 . The pump charge is calculated via the centre-of-mass displacement. Calculated for the experimental pump cycle with $L = 49$, $U/t = 8$, $T = 23.3\hbar/t$, $d\tau = 0.1\hbar/t$ and $V_0/t = 0.034$.

a spin-gapless region inevitably exists in the thermodynamic limit, a dependence on details of the pump cycle is, in principle, expected. Moreover, the experiment operates at a finite entropy density.

For a finite-size system, there is, strictly speaking, no gapless continuum of spin excitations yet, hence the minimum finite-size gap along the pump cycle should matter. To address this point, we compare the boomerang-shape pump cycle used in the experiment (including the actual variation of the average hopping matrix element) to an elliptical cycle as used for Fig. 5 where we keep the average hopping matrix element constant, both with $N = 10$ particles. These simulations are carried out for a closed system using the time-dependent Lanczos technique for a slow pumping protocol. We remove the trap to single out the effect of the minimum gap.

The results presented in Fig. A4 illustrate that during the first pump cycle, there is no significant difference between the two pump paths. Beyond that, the behavior is strongly path-dependent, but not quantised in either case, yet somewhat larger for the elliptical cycle. This is reflected in the minimum gaps along the two cycles, which are $\Delta E_{\text{exp}} = 0.04t$, $\Delta E_{\text{ellip}} = 0.18t$.

One may further wonder about the effect of total particle number at fixed filling. For the elliptical cycle with $N = L = 6$ and 10 , the respective minimum gaps are $\Delta E_{L=6} = 0.28t$, $\Delta E_{L=10} = 0.18t$, respectively. Consistently, the pump efficiency for $L = 10$ is much worse than for $L = 6$ (results not shown).

4. Effect of dimer initial state instead of ground state.

In the experiment, the loading scheme leads to an initial state that can be approximated by a product of dimers, each with two particles and in their ground state. We compare pumping starting from either this state or the ground state, from the same point in the pump cycle. The results of time-dependent Lanczos calculations are

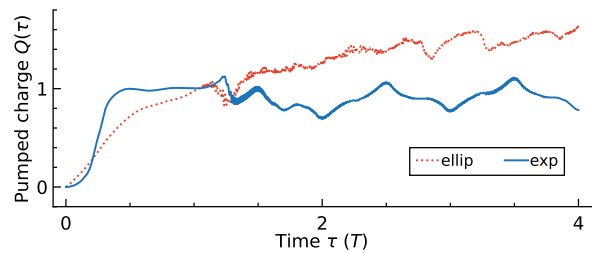


FIG. A4. **Pumping with different trajectories and system sizes.** Time-dependent Lanczos calculation of the pumped charge $Q(\tau)$ in an open-shell antiperiodic system, started from the ground state. Experimentally realised pump-cycle ('exp') and elliptical pump cycle ('ellip') $L = 10$. $U/t = 10$, $d\tau = 0.01\hbar/t$, $T = 100\hbar/t$.

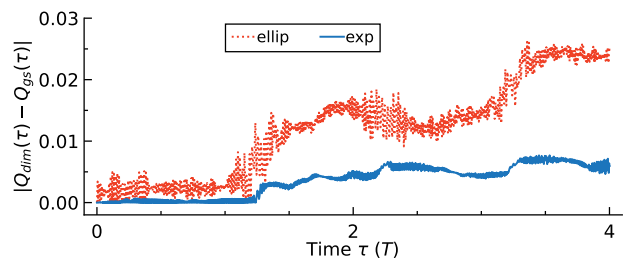


FIG. A5. **Starting from the ground state versus dimer state.** Difference of the pumped charge between a pump starting from the ground state (Q_{gs}) and one starting from the dimer state (Q_{dim}) for the experimental and the elliptical pump cycle, $L = 6$, $U/t = 10$, $d\tau = 0.01\hbar/t$ and $T = 100\hbar/t$.

shown in Fig. A5. The difference in the pumped charge is initially small yet increases significantly once the minimum gap is crossed. The comparison between the two different pump cycles – experimental versus elliptical one – shows that the former leads to smaller differences in the first pump cycle because the starting point has a larger value of δ and therefore a stronger dimerization.

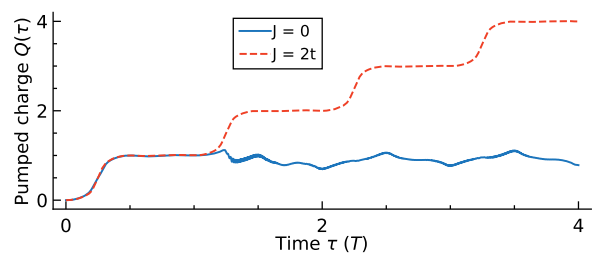


FIG. A6. **Pumping with an additional interaction term.** Time-dependent Lanczos calculation of the pumped charge $Q(\tau)$ from the ground state in an open-shell antiperiodic system for the experimentally realised pump-cycle, $L = 10$, $U/t = 10$, $d\tau = 0.01\hbar/t$, $T = 100\hbar/t$ and two different Ising-coupling strengths ($J = 0$ and $J = 2t$).

5. Improving the robustness of the interaction-induced pump via opening the spin gap

As already discussed in Ref. [43], the $SU(2)$ symmetry of the ionic Hubbard model can be lifted by various perturbations which at the same time gap out the spin sector. This leads to robust quantised pumping over many cycles.

We here demonstrate that this prediction remains valid also for the experimental pump cycle, by adding an Ising interaction to the Hamiltonian (other examples were

studied in Ref. [43]):

$$\hat{H}_Z = J \sum_{j=1}^L \hat{S}_j^z \hat{S}_{j+1}^z. \quad (\text{A7})$$

The comparison between a simulation with and without this Ising term is shown in Fig. A6. The results establish that opening the spin gap significantly stabilises the pump, leading to robust pumping for many pump cycles compared to the bare Rice-Mele-Hubbard model.

8 Finite temperature pumping in the Rice-Mele Hubbard model

In this chapter I will present initial results for work-in-progress project on finite-temperature pumping in the Rice-Mele-Hubbard model. The model is the same as in section 7.1:

$$\hat{H}_{RM} = \sum_{\langle i,j \rangle, \sigma} -J (1 + (-1)^i \delta(t)) \left(\hat{c}_{i,\sigma}^\dagger \hat{c}_{j,\sigma} + \text{h.c.} \right) \quad (8.1)$$

$$+ \Delta(t) \sum_j (-1)^j \hat{n}_j + U \sum_j \hat{n}_{j,\uparrow} \hat{n}_{j,\downarrow}, \quad (8.2)$$

where $\hat{c}_{i,\sigma}^\dagger$ ($\hat{c}_{i,\sigma}$) indicate the fermionic creation (annihilation) operators for a spin $\sigma \in \{\uparrow, \downarrow\}$, Δ denotes the staggering amplitude and δ is the hopping-dimerization parameter. U is a Hubbard interaction as before.

In the last chapter, I have showcased the zero-temperature properties of this model. In particular for repulsive interaction, two critical points are formed that allow for charge pumping when being encircled. Surrounding a single critical point, the pumped charge is quantized until the Mott-BI transition is crossed after crossing the spin-gapless line at $\delta = 0$. Surrounding both points, we recover the Rice-Mele pump with topologically protected quantized charge transport for many cycles. Here, we start considering finite-temperature properties of this system. Ultracold quantum gases have a non-negligible temperature in units of the Fermi energy [228], which makes understanding the finite-temperature effects on the quantized particle transport in charge pumps experimentally relevant.

Finite temperature leads to an occupation of all energy states in a thermal density matrix according to

$$\rho_T = \sum_{\alpha} \exp(-\beta E_{\alpha}) |\alpha\rangle \langle \alpha|, \quad (8.3)$$

with β being the inverse temperature. E_{α} and $|\alpha\rangle$ are the energies and corresponding many-body eigenstates of the system. For a non-interacting Rice-Mele model, the occupations can be calculated analytically [56] according to $n_{\alpha,k}^T = \tanh(-\beta E_{0,k}(0)) n_{\alpha,k} + \frac{e^{\beta E_{0,k}(0)}}{2 \cosh(-\beta E_{0,k}(0))}$. This leads to non-quantized charge pumping for finite temperatures. More concretely, the pumped charge decreases as a function of temperature due to thermal holes [48].

Understanding the finite-temperature properties is very relevant in ultracold-atomic systems, where the temperatures are on the order of 1/10 of the hopping integral, even in

the coldest systems so far realized [228]. The quantum mechanical evolution of the density matrix remains relevant, however, because despite their relatively high temperature, their time-evolution can still be regarded as unitary. Several approaches have been introduced to extend the theory of geometric phases to the finite-temperature setting, such as the Uhlmann phase [138, 145], which is applicable for open quantum systems and the ensemble-geometric phase (EGP) [141, 144]. The EGP can be regarded as an extension of the Berry phase since it reproduces the Berry phase in the zero temperature limit. The EGP is defined via the exponentiated position operator similarly to the many-body polarization [141]:

$$\varphi_E = \text{Im} \ln \langle e^{i \frac{2\pi}{T} \hat{X}} \rangle. \quad (8.4)$$

Crucially, the EGP has been shown to give the same result as the $T = 0$ Berry phase in the thermodynamic limit and below a critical temperature T_c , which has even been extended to interacting systems [144]. It is generally accepted that the EGP has no one-to-one connection to the pumped charge, as the latter is the expectation of a two-point correlator, while the EGP for finite temperature has beyond-two-body terms. Nevertheless, the EGP has been claimed to be experimentally measurable using interferometry experiments [141]. While this means that measurements in usual charge pump experiments are not expected to directly correspond with the EGP, it is however still relevant to understand the effect of finite-temperatures on Thouless pumps, especially in the many-body context.

In fig. 8.1 EGP of model eq. (8.1) is shown for the inverse temperatures $\beta J = 0.1$ (a) and $\beta J = 10$ (b) for $L = 4$ and $U/J = 10$. The critical points along the $\delta = 0$ axis are clearly shifted for larger temperature. Additionally, the transition of the EGP along the horizontal line crossing the critical point becomes sharper. One might therefore expect there to be noticeable differences in the pumped charge. When centering the pump cycle around the origin, one might expect an additional signature in the drop of quantized charge pumping when the critical points have moved out of the pump cycle due to temperature. On the other hand, one might ask if temperature-induced pumping is possible in a similar manner as the interaction-induced pumping of section 7.3.

We fix the pump cycle

$$\delta(t) = \delta_0 \cos(\omega t), \quad (8.5)$$

$$\Delta(t) = \Delta_0 \sin(\omega t) + \Delta_c \quad (8.6)$$

for $L = 6$ and $U/J = 10$, $R_\delta = 0.88$, $R_\Delta = 2.10J$ and consider the Rice-Mele case ($\Delta_c = 0$) and the shifted case ($\Delta_c = 4J$). The pumped charge $\Delta_{Q,\alpha}$ is then calculated for each eigenstate α (with initial eigenenergy E_α) individually and averaged according to the finite-temperature distribution:

$$\langle \delta Q \rangle_T = \frac{1}{Z} \sum_{\alpha} \langle \alpha | e^{-\beta E_\alpha} \Delta_{Q,\alpha} | \alpha \rangle, \quad (8.7)$$

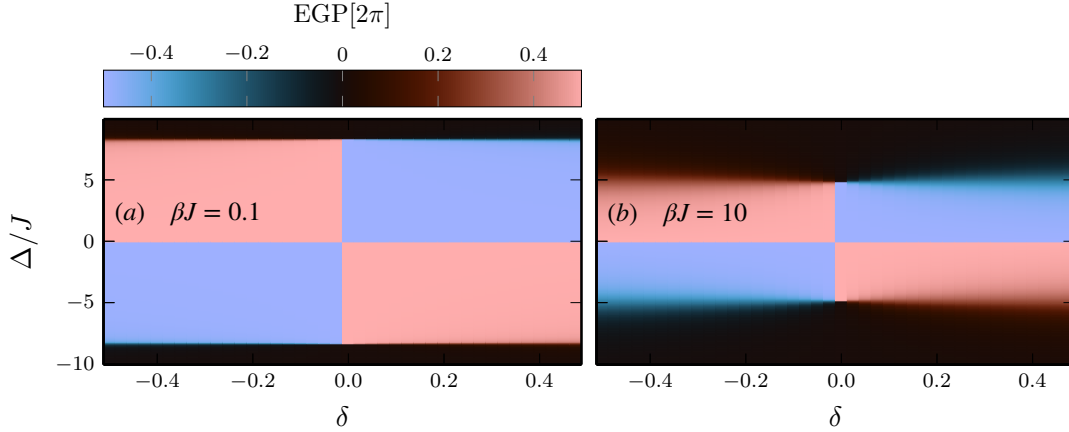


Figure 8.1: Ensemble geometric phase (EGP) for model eq. (8.1) for $L = 4$, $U/J = 10$. The critical points move away from the origin as the temperature is increased from $\beta = 10$ (b) to $\beta = 0.1$ (a).

with $Z = \sum_{\alpha} e^{-\beta E_{\alpha}}$. We also compute the many-body gaps given by

$$\Delta E_I = E_1(N, S_Z = 0) - E_0(N, S_Z = 0) \quad (8.8)$$

$$\Delta E_C = [E_0(N + 2, S_Z = 0) + E_0(N - 2, S_Z = 0) - 2E_0(N, S_Z = 0)] / 2 \quad (8.9)$$

$$\Delta E_S = E_0(N, S_Z = 1) - E_0(N, S_Z = 0), \quad (8.10)$$

where E_{α} denotes the α 'th excitation energy in the symmetry sector given by N and S_Z with $\alpha = 0$ being the ground-state. $N = N_{\uparrow} + N_{\downarrow}$ is the total particle number and S_Z is the total spin projection.

The results for the pumped charge are plotted in fig. 8.2 for the Rice-Mele (a) and shifted (b) cycle. The inverse minimum many-body gaps along the pump cycle are also shown. For small temperature, the results agree with what has been shown in sections 7.1 and 7.3. For temperatures on the order of the tunneling rate J , the pumped charge drops noticeably. The gaps along the Rice-Mele pump cycle line up with the onset of non-quantized charge pumping. In the shifted case, the internal and spin gaps show a similar form of the breakdown of quantization, which is asymmetric and occurs for lower temperatures at larger U . However, the inverse spin and internal gaps do not predict the inverse temperature β of the breakdown of charge pumping in this case, instead it seems to be controlled by the inverse charge gap.

We repeat the computation of the pumped charge along vertical cuts at fixed U (indicated by the black arrows in fig. 8.2) and vary the pump period T . The results are plotted in fig. 8.2 for the Rice-Mele (c) and shifted (d) case. As a function of period T , the temperature dependence is homogeneous and the onset of non-quantized charge pumping occurs at $\beta J \approx 1$ for a range of pumping periods. For the shifted case, this onset is more skewed and occurs for lower temperature when pumping faster. Generally, the shifted pump cycle shows a slower convergence with respect to the pump period,

8 Finite temperature pumping in the Rice-Mele Hubbard model

as is expected due to the gapless nature that was discussed at length in section 7.3. In conclusion, we observe no temperature-induced pumping in the system studied here.

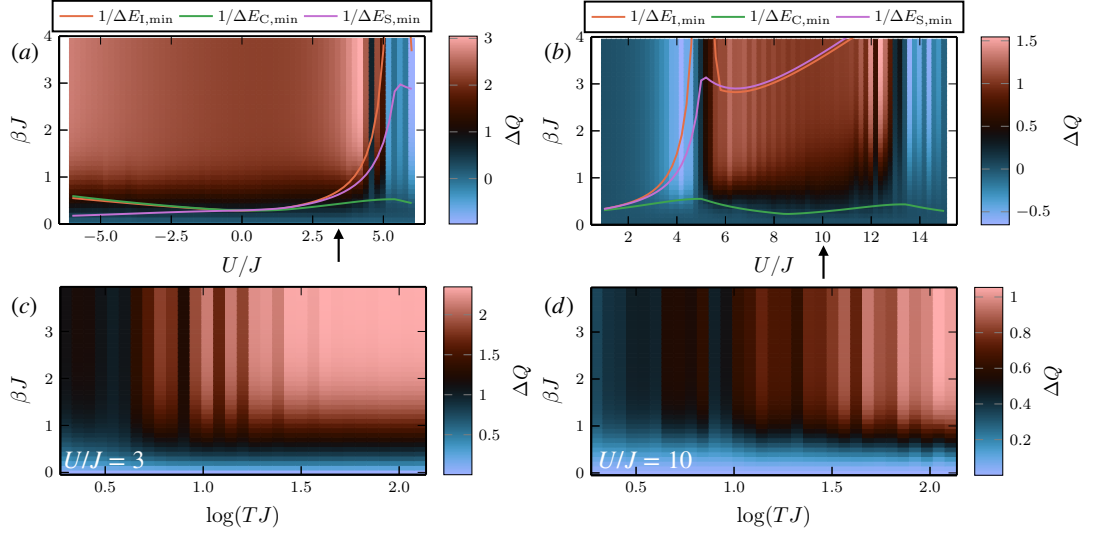


Figure 8.2: Finite-temperature charge pumping. The pumped charge per cycle ΔQ is plotted for the Rice-Mele (a,c) and shifted (b,d) pump cycles as a function of inverse temperature β and interaction strength U (a,b), as well as the pump period T (c,d). Calculated via exact diagonalization for $L = 6$.

9 Conclusion

A topological charge pump, also called Thouless pump [44], is a dynamical, one-dimensional equivalent to the quantum Hall effect [2], in which charges are pumped in integer-quantized numbers across the system upon a time-periodic, slow modulation of system parameters. This charge transport is topologically robust and equal to a topological invariant, the Chern number. Hence, it is not dependent on a fine-tuning of experimental parameters and instead a generic property of a large class of systems, which can be subject to disorder, many-body interactions or an environment coupling.

The aim of this thesis was to gain insight into quantized charge transport in topological Thouless pumps in optical lattices within the platform of ultracold atomic systems [23, 25]. Particular focus was set on experimentally realistic conditions in this setting, such as on-site potential disorder, loss of adiabaticity due to finite pumping speeds, the loss of energy to an environment and finite temperatures. Another goal was researching the possibility of novel topological pumps that are driven by many-body interactions and that have no non-interacting counterpart. The studies have been carried out using numerical techniques.

These objectives have been achieved as evidenced by the four scientific projects that are highlighted in this thesis. The Rice-Mele model [132], a one-dimensional tight-binding chain subject to a time-dependent staggered potential and a dimerized hopping, is used as a basis in all results highlighted here.

In the first publication, we studied a non-interacting Rice-Mele model subject to a static, uncorrelated, bounded, diagonal disorder. We did so by characterizing the topological pumping with a multitude of instantaneous measures, such as the local Chern marker [162], the energy gap, the many-body polarization [301], and the entanglement spectrum [267, 53]. Additionally, we performed a full-time simulation of the pumped charge, taking into account a finite pumping speed. We observe a breakdown of quantized charge pumping beyond a critical disorder strength, in the form of a decreasing, non-quantized pumped charge. The instantaneous measures above all agree with the onset of this breakdown, which happens inside the Anderson localized regime. We find that the disorder-averaged gap is not well-suited to predict the critical disorder strength in finite systems, as found in optical lattice experiments [33, 34, 67, 38]. Instead, the full distributions of the energy gap have to be taken into account: At the transition point, the distributions go from a Gaussian to an exponential distribution, most easily seen by looking at the most likely energy gap becoming zero. Both the many-body polarization and the entanglement spectrum show discontinuities in single disorder realizations. The former is not practical to determine the disorder averaged breakdown point, as these discontinuities appear at random points along the pump cycle. The many-body polarization, albeit having a similar problem, can be analyzed in a disorder

9 Conclusion

average by deploying a circular mean, and this mean becomes discontinuous at the critical disorder strength. The local Chern marker promises to give the most positionally resolved information about the quantized charge transport in a disordered system. A local Chern marker that exceeds unity at a single site signifies an adiabatically pumped charge per cycle across this site that exceeds one. These fluctuations average out in the quantized regime, but non-quantized pumping necessarily requires an asymmetric distribution of local Chern marker deviations. The skewness of the distribution of these deviations from unity have the clearest signature for the onset of non-quantized pumping. However, one shortcoming of this approach is that it is unclear, whether non-local processes, such as those reported in [302] play a role in disordered charge pumps. Future research should consider studying the adiabatic pumping of single, localized particles. As one adiabatically modulates the system parameters, it is expected that a distant site becomes energetically favorable and the particle jumps to this site, which constitutes a non-local process. However, it is unlikely that these non-local jumps are observable in experiments or simulations with finite-pumping speed, as the relevant timescale is likely exponentially large [54]. Experiments along these lines have recently been performed, and no non-local processes have been observed [259, 236].

Another avenue for further investigation is to connect these results to the Floquet picture given in [58]. There, the authors showed a surprising link between a localization-delocalization transition of Floquet states indicating the breakdown of Thouless pumping due to disorder. In general, I recommend further investigations of charge pumps in the Floquet picture, as it is the most natural formulation of the time-periodic modulation in these systems, although the extension of the Floquet picture to many-body interacting systems is non-trivial due to heating. A particularly interesting prospect is the interplay between Thouless pumping in interacting, disordered systems, due to the highly debated many-body localization [269, 270]. In principle all measures used here can be employed for a many-body system. Especially the entanglement spectrum, the many-body polarization and the pumped charge can easily be calculated, while the local Chern marker has also been recently extended to the many-body context [303].

In the second publication of this thesis, we coupled the Rice-Mele model to a phononic bath using a Holstein coupling [177] in a classical approximation. The main motivation was that this is the easiest environment that can be coupled to a charge pump such that the entire system is still closed. The phonons have been treated with a semiclassical multitrajectory Ehrenfest method [178, 179, 180, 243]. As the electronic system is pumped, energy is exchanged with the phonon sector and the number of phonons increases initially. We find an intriguing resonance phenomenon, where the energy of the phonon sector increases until the topological charge transport breaks down. This happens when the phonon frequency is tuned to the pumping frequency and happens at any finite electron-phonon coupling. We employed an effective pumping path constructed out of disorder averaged potential terms arising from the phonon coupling in the Ehrenfest method, the winding of which accurately describes the quantized charge transport, its direction and its eventual breakdown due to the closing of the single-particle electron gap. The same approach was used to show that away from the resonance condition, quantized charge

pumping remains robust below a critical electron-phonon-coupling strength.

An obvious next step is to treat the phonon sector fully quantum mechanically. While the multitrajjectory Ehrenfest method is expected to give accurate results in our regime of slow phonons, it is interesting to see to what degree and with what mechanism the mostly classical resonance phenomena observed in our project carry over to the quantum case. In this context one should also consider many-body interacting Thouless pumps coupled to quantum mechanical phonons. Here, the phonons can be treated effectively using matrix-product-state methods [283, 280, 304]. On the one hand, interacting charge pumps are interesting in their own right and can lead to surprising new phenomena, such as new kinds of topological pumps that are not connected to non-interacting versions, as showcased in the projects of sections 7.1 and 7.3. On the other hand, one might also find connections to many-body localization [270, 269], since the classical phonons effectively realize a time-dependent disorder potential for the electrons. To what degree this carries over to quantum-phonons is an interesting avenue to explore.

The half filled Holstein model (spinless fermions coupled to quantum mechanical phonons locally) is also known to host a charge-density wave with a many-body gap mediated by polarons [305, 306, 307, 280]. It is interesting to see whether the polarons as composite particles of electrons and phonons can inherit the topological character of the electrons, similar to how topological pumping of bound bosonic pairs has recently been reported [62]. Finally, one might also consider phonons with dispersion. Letting phonons carry energy across different sites in this way might make the phonon sector topological. A similar situation has been reported recently in a Su-Schrieffer-Heeger model that interacts with a trivial subsystem [284].

As a last comment, let me stress that phonons are not easily realizable in ultracold atoms. Apart from the purely theoretical considerations, they might become important in real materials. The Rice-Mele model is hard to engineer in real materials, as in a crystal, control over dimerized hoppings and staggered potentials in a time-dependent way is challenging. In semiconductor nanowires, a superlattice can in principle be engineered via folding, and the time-dependent Hamiltonian terms can be achieved through time-dependent Zeeman fields [59]. One might also use alternative models for Thouless pumps that do not need these features. A Thouless pump in the form of a Laughlin pump has recently been experimentally reported in a topological insulator system [308].

The last three projects concern topological charge pumping in a many-body interacting two-component fermionic system. The model is constructed by considering two Rice-Mele models for the two spin flavors and coupling them via an on-site Hubbard interaction. For the non-interacting model, the single-particle gap closing at zero hopping dimerization and potential offset constitutes a critical point, around which the Zak phase winds around. Exactly one particle per spin is pumped through the system per pump cycle around this degeneracy. We have shown that by adding a repulsive Hubbard interaction, the critical point is split into two critical points that move apart on the staggered-potential axis with increasing interaction strength. For an origin-centered pump cycle, the quantized pumping of charge of the Rice-Mele pump needs to encircle both points, and the crossing of the critical points out of the pump cycle predicts the transition from a non-trivial to a

9 Conclusion

trivial pump. This situation has been reported before in [150] and has also been measured experimentally in [38], where it was described as a breakdown of quantized pumping due to many-body interactions. Our work sheds new light on the fact that a topological phase transition from a non-trivial to a trivial pump occurs as the critical points exit the pump cycle, which is confirmed via the many-body polarization. Furthermore, we have calculated the pumped charge for the origin-centered and a shifted pump cycle via time-dependent matrix-product-state methods. We argue that the loss of topological quantization as reported in [150] and measured recently in [38] results from the crossing of a spin-gapless line of the ionic Hubbard model [189, 190, 191, 192, 193, 194, 195, 196], which is hidden during the initial pump cycle and should only manifest in experiments in later cycles. We have shown that gapping out this line via either a staggered magnetic field or an Ising-interaction term, the pumping around a single critical point is quantized and robust, and that such a pumping scheme pumps one out of two particles as opposed to two in the Rice-Mele pump.

Following this paper, we have collaborated with experimentalists from [38] to show the possibility of an interaction-induced pump in this system. Fixing the shifted pump cycle such that initially no critical points are encircled, the Hubbard interaction strength is ramped up. As the critical points move inside the pump cycle, a finite pumped charge is measured for the first pump cycle, which is consistent with the quantized value of one charge per cycle. We have numerically simulated this situation by considering experimental effects such as a confining potential, the loading scheme, finite pump speeds and the shape of the pump cycle. Beyond the first pump cycle, the measured pumped charge drops significantly due to the crossing of the spin-gapless line. We have analyzed this loss of adiabaticity by calculating the charge-charge and spin-spin-correlators. Upon crossing the spin-gapless line, the spin sector immediately excites, while the charge sector remains adiabatic. Only when spin excitations are present can the charge sector be excited upon crossing from the Mott regime to the band-insulating regime. This explains both the measured and numerically reported quantization of pumped charge for the first cycle and the breakdown of charge transport in later cycles.

Theoretically, the spontaneously dimerized phase (SDI), which lies in between the Mott insulator and the band insulator of the ionic Hubbard model, is an interesting focus of future research. The SDI phase is gapped in the spin and charge sector and thus should allow for robust pumping. In [150], fractional pumping through the SDI phase has been reported in an open system. We have tried calculating the pumped charge when pumping through the SDI phase, but finite-size effects, due to the SDI phase being close to the critical points, have made a proper analysis difficult. Recently, it has been proposed [309] to increase the size of the SDI phase via a density-dependent hopping, something that could in principle be done in ultracold atom experiments. Such gap-opening terms make this system robust and a genuine interaction-induced topological pump. Beyond the theoretical interest of interaction-induced pumps, which can connect different symmetry-protected phases [310], this could set the stage for experimental studies of interaction-induced pumping of boundary modes in a harmonic trap [311], topologically protected density distribution [312] and the selective pumping of spin-singlets [313].

Finally, I have presented preliminary data for a further project on finite-temperature effects in the interacting Rice-Mele model. The analysis is based on the ensemble geometric phase (EGP)[141, 146] which is a finite-temperature generalization of the Berry phase. We find that the critical points of the EGP shift as a function of temperature in a similar way to the critical points shifting at zero temperature as a function of interaction strength. It is an open question, whether this might lead to temperature-induced pumping. In general, finite temperature pumping is necessarily dependent on details such as the initial state and the shape of the pump cycle, as excited states which all contribute in a finite-temperature average are never adiabatic. Instead we have focused on numerically calculating the concrete effects that finite temperature has on relevant quantum gas experiments. For both interacting Rice-Mele pumps and the interaction-induced pump, finite temperature leads to a breakdown of quantized pumping. The transition from finite pumping to no pumping seems to be given by the size of the charge gap, which is open for both cases, while the spin-gap seems to control the details of the breakdown.

10 Research data

Chapter 5

The data and the git repository is stored in the archive server of the GWDG Göttingen ("/usr/users/a/bertok/charge-pump-disorder.tar.bz2").

The plot data of the publication can be found at <https://arxiv.org/abs/2010.15249>.

The git repository is also stored at

<https://gitlab.gwdg.de/bertok/charge-pump-disorder>. Eric Bertok and Fabian Heidrich-Meisner have maintainer access.

Chapter 6

The data is stored in the 10-Year-archive of the Institut für Theoretische Physik, Georg-August-Universität Göttingen ("/usr/users/a/mondal1/MTE_pumping_New.zip" and "/usr/users/a/mondal1/MTE_pumping_Old.zip").

The plot data of the publication can be found at <https://arxiv.org/abs/2209.06124>.

The git repository is stored at

https://gitlab.gwdg.de/suman.mondal/rice_mele_holstein_mte. Suman Mondal and Fabian Heidrich-Meisner have maintainer access.

Chapter 7

Sec. 7.1

The data and the git repository is stored in the 10-Year-archive of the Institut für Theoretische Physik, Georg-August-Universität Göttingen ("/net/theorie/rocks/eric.bertok/10-Years-Archive/mps-charge-pump").

The plot data of the publication can be found at <https://arxiv.org/abs/2204.14144>.

The git repository is also stored at

<https://gitlab.gwdg.de/bertok/mps-charge-pump>. Eric Bertok and Fabian Heidrich-Meisner have maintainer access.

Sec. 7.3

The data and the git repository is stored in the 10-Year-archive of the Institut für Theoretische Physik, Georg-August-Universität Göttingen ("/net/theorie/rocks/eric.bertok/10-Years-Archive/mps-charge-pump").

Upon publication, the plot data of the publication will be uploaded to the ETH research collection ("<https://www.research-collection.ethz.ch/>"). The git repository is also stored

10 Research data

at

<https://gitlab.gwdg.de/bertok/mps-charge-pump>. Eric Bertok and Fabian Heidrich-Meisner have maintainer access.

11 Acknowledgements

I would like to take this opportunity to thank everyone who - either directly or indirectly - contributed to this thesis. First, I would like to thank Prof. Fabian Heidrich-Meisner for the opportunity to work in his group from the very beginning here in Göttingen. I would also like to thank my former Masters supervisor Andrew Hayward, from whom I learned much about topology and the mindset you want to have while working as a PhD student. Furthermore, I would like to thank Salvatore Manmana and André Eckardt for reviewing this Thesis, together with Fabian Heidrich-Meisner. I thank the thesis advisory committee, as well as my examination board for their time and interest in my work, as well as Suman Mondal for proofreading a work-in-progress version of this thesis. I also thank everyone in our work group for participating in my practice talk.

I am grateful to all of my scientific collaborators, especially Andrew Hayward, Fabian Heidrich-Meisner, Ulrich Schneider, Armando Aligia, Konrad Viebahn and Anne-Sophie-Walter. I thank the DFG for funding my research as part of the FOR2414.

I would like to thank my parents for their continued support during my studies in Göttingen, especially my mother Gudrun.

Finally, I thank all of my close friends that I have made here in Göttingen. Due to you this has been the best time of my life.

Bibliography

- [1] K. von Klitzing, G. Dorda, and M. Pepper, *Phys. Rev. Lett.* **45**, 494 (1980).
- [2] K. von Klitzing, *Rev. Mod. Phys.* **58**, 519 (1986).
- [3] The Nobel Prize in Physics 1985, <https://www.nobel-prize.org/prizes/physics/1985/summary/>.
- [4] D. J. Thouless, M. Kohmoto, M. P. Nightingale, and M. den Nijs, *Phys. Rev. Lett.* **49**, 405 (1982).
- [5] P. Delplace and A. Venaille, arXiv:2006.08488 (2020), 2006.08488.
- [6] T. Kane and M. Scher, *International Journal of Solids and Structures* **5**, 663 (1969).
- [7] A. Shapere and F. Wilczek, *American Journal of Physics* **57**, 514 (1989).
- [8] J. Carlisle, K. Hammer, R. Hingtgen, and G. Martins, arXiv:2108.06307 (2021), 2108.06307.
- [9] J. M. Kosterlitz and D. J. Thouless, *J. Phys. C: Solid State Phys.* **6**, 1181 (1973).
- [10] A. Altland, M. Fleischhauer, and S. Diehl, *Phys. Rev. X* **11**, 021037 (2021).
- [11] C.-K. Chiu, J. C. Y. Teo, A. P. Schnyder, and S. Ryu, *Rev. Mod. Phys.* **88**, 035005 (2016).
- [12] L. Fidkowski and A. Kitaev, *Phys. Rev. B* **81**, 134509 (2010).
- [13] A. Kitaev, *AIP Conference Proceedings* , 22 (2009), 0901.2686.
- [14] L. Lan-Feng, C. Bo-Lun, and K. Su-Peng, *Communications in Theoretical Physics* **55**, 904 (2011).
- [15] Y.-M. Lu and A. Vishwanath, *Phys. Rev. B* **86**, 125119 (2012).
- [16] A. C. Potter, T. Morimoto, and A. Vishwanath, *Phys. Rev. X* **6**, 041001 (2016).
- [17] S. Rachel, *Rep. Prog. Phys.* **81**, 116501 (2018).
- [18] R. Roy and F. Harper, *Phys. Rev. B* **96**, 155118 (2017).
- [19] C. Wang, A. C. Potter, and T. Senthil, *Science* **343**, 629 (2014).

Bibliography

- [20] I. Buluta and F. Nori, *Science* **326**, 108 (2009).
- [21] F. Schäfer, T. Fukuhara, S. Sugawa, Y. Takasu, and Y. Takahashi, *Nat Rev Phys* **2**, 411 (2020).
- [22] E. Altman *et al.*, *PRX Quantum* **2**, 017003 (2021).
- [23] D. Jaksch, C. Bruder, J. I. Cirac, C. W. Gardiner, and P. Zoller, *Phys. Rev. Lett.* **81**, 3108 (1998).
- [24] I. Bloch, J. Dalibard, and W. Zwerger, *Rev. Mod. Phys.* **80**, 885 (2008).
- [25] N. Goldman, J. Budich, and P. Zoller, *Nature Physics* **12**, 639 (2016).
- [26] M. Aidelsburger *et al.*, *Philosophical Transactions of the Royal Society A: Mathematical, Physical and Engineering Sciences* **380**, 20210064 (2021).
- [27] N. Goldman *et al.*, *Proceedings of the National Academy of Sciences* **110**, 6736 (2013).
- [28] M. Atala *et al.*, *Nature Phys* **9**, 795 (2013), 1212.0572.
- [29] F. Grusdt and M. Hönig, *Phys. Rev. A* **90**, 053623 (2014).
- [30] G. Jotzu *et al.*, *Nature* **515**, 237 (2014).
- [31] M. Aidelsburger *et al.*, *Nature Phys* **11**, 162 (2015).
- [32] L. Duca *et al.*, *Science* **347**, 288 (2015).
- [33] M. Lohse, C. Schweizer, O. Zilberberg, M. Aidelsburger, and I. Bloch, *Nature Physics* **12**, 350 (2016).
- [34] S. Nakajima *et al.*, *Nature Physics* **12**, 296 (2016).
- [35] C. Schweizer, M. Lohse, R. Citro, and I. Bloch, *Phys. Rev. Lett.* **117**, 170405 (2016).
- [36] N. Fläschner *et al.*, *Science* **352**, 1091 (2016).
- [37] L. Asteria *et al.*, *Nat. Phys.* **15**, 449 (2019), 1805.11077.
- [38] A.-S. Walter *et al.*, *arXiv:2204.06561* (2022), 2204.06561.
- [39] B. Mukherjee *et al.*, *Nature* **601**, 58 (2022), 2106.11300.
- [40] R. Yao *et al.*, *arXiv:2304.10468* (2023), 2304.10468.
- [41] M. Aidelsburger *et al.*, *Phys. Rev. Lett.* **107**, 255301 (2011).
- [42] A. Eckardt, *Rev. Mod. Phys.* **89**, 011004 (2017).

- [43] T. Oka and S. Kitamura, *Annual Review of Condensed Matter Physics* **10**, 387 (2019).
- [44] Q. Niu and D. J. Thouless, *Journal of Physics A: Mathematical and General* **17**, 2453 (1984).
- [45] D. J. Thouless, *Phys. Rev. B* **27**, 6083 (1983).
- [46] D. Meidan, T. Micklitz, and P. W. Brouwer, *Phys. Rev. B* **84**, 075325 (2011), 1104.1516.
- [47] D. Rossini, M. Gibertini, V. Giovannetti, and R. Fazio, *Phys. Rev. B* **87**, 085131 (2013).
- [48] L. Wang, M. Troyer, and X. Dai, *Phys. Rev. Lett.* **111** (2013), 1301.7435.
- [49] T.-S. Zeng, C. Wang, and H. Zhai, *Phys. Rev. Lett.* **115**, 095302 (2015).
- [50] J. Qin and H. Guo, *Physics Letters A* **380**, 2317 (2016).
- [51] R. Li and M. Fleischhauer, *Phys. Rev. B* **96**, 085444 (2017).
- [52] P. Marra and R. Citro, *The European Physical Journal Special Topics* **226**, 2781 (2017), 1703.03815.
- [53] A. Hayward, C. Schweizer, M. Lohse, M. Aidelsburger, and F. Heidrich-Meisner, *Phys. Rev. B* **98**, 245148 (2018).
- [54] K.-I. Imura, Y. Yoshimura, T. Fukui, and Y. Hatsugai, *J. Phys.: Conf. Ser.* **969**, 012133 (2018), 1706.04493.
- [55] M. Lohse, C. Schweizer, H. M. Price, O. Zilberberg, and I. Bloch, *Nature* **553**, 55 (2018).
- [56] L. Privitera, A. Russomanno, R. Citro, and G. E. Santoro, *Phys. Rev. Lett* **120**, 106601 (2018).
- [57] B. A. van Voorden and K. Schoutens, *New J. Phys.* **21**, 013026 (2019).
- [58] M. M. Wauters, A. Russomanno, R. Citro, G. E. Santoro, and L. Privitera, *Phys. Rev. Lett.* **123**, 266601 (2019).
- [59] J. Wang, J. F. Liu, and C. S. Ting, *Phys. Rev. B* **100**, 075402 (2019).
- [60] R. Wang and Z. Song, *Phys. Rev. B* **100**, 184304 (2019).
- [61] L. Arceci, L. Kohn, A. Russomanno, and G. E. Santoro, *J. Stat. Mech.* **2020**, 043101 (2020).
- [62] S. Greschner, S. Mondal, and T. Mishra, *Phys. Rev. A* **101**, 053630 (2020).

Bibliography

- [63] B. Höckendorf, A. Alvermann, and H. Fehske, *Phys. Rev. Res.* **2**, 023235 (2020).
- [64] P. Marra and M. Nitta, *Phys. Rev. Research* **2**, 042035 (2020).
- [65] D. Burba, M. Račiūnas, I. B. Spielman, and G. Juzeliūnas, *Phys. Rev. A* **107**, 023309 (2023).
- [66] R. Citro and M. Aidelsburger, *Nature Reviews Physics* **5**, 87 (2023).
- [67] S. Nakajima *et al.*, *Nat. Phys.* **17**, 844 (2021).
- [68] O. Zilberberg *et al.*, *Nature* **553**, 59 (2018).
- [69] A. Cerjan, M. Wang, S. Huang, K. P. Chen, and M. C. Rechtsman, *Light Sci Appl* **9**, 178 (2020).
- [70] M. Fujimoto, H. Koschke, and M. Koshino, *Phys. Rev. B* **101**, 041112 (2020).
- [71] M. Fujimoto and M. Koshino, *Phys. Rev. B* **103**, 155410 (2021).
- [72] Y. Zhang, Y. Gao, and D. Xiao, *Phys. Rev. B* **101**, 041410 (2020).
- [73] D. Dreon *et al.*, *Nature* **608**, 494 (2022).
- [74] S. R. White, *Phys. Rev. Lett.* **69**, 2863 (1992).
- [75] S. R. White, *Phys. Rev. B* **48**, 10345 (1993).
- [76] G. Vidal, *Phys. Rev. Lett.* **93**, 040502 (2004).
- [77] A. J. Daley, C. Kollath, U. Schollwöck, and G. Vidal, *J. Stat. Mech.* **2004**, P04005 (2004).
- [78] S. R. White and A. E. Feiguin, *Phys. Rev. Lett.* **93**, 076401 (2004).
- [79] J. Haegeman *et al.*, *Phys. Rev. Lett.* **107**, 070601 (2011).
- [80] J. Haegeman, C. Lubich, I. Oseledets, B. Vandereycken, and F. Verstraete, *Phys. Rev. B* **94**, 165116 (2016).
- [81] S. Paeckel *et al.*, *Annals of Physics* **411**, 167998 (2019).
- [82] L. Vanderstraeten, J. Haegeman, and F. Verstraete, *SciPost Phys. Lect. Notes* , 7 (2019).
- [83] T. Tokieda, *Topology & Geometry - LECTURE 02 Part 01/03* - by Dr Tadashi Tokieda, <https://youtu.be/8YDw4YxT-FM>, 2014.
- [84] D. Tong, *arXiv:1606.06687* (2016), 1606.06687.
- [85] F. D. M. Haldane, *Phys. Rev. Lett.* **50**, 1153 (1983).

- [86] W. J. L. Buyers *et al.*, Phys. Rev. Lett. **56**, 371 (1986).
- [87] M. Kenzelmann *et al.*, Phys. Rev. Lett. **90**, 087202 (2003).
- [88] F. D. M. Haldane, Phys. Rev. Lett. **61**, 2015 (1988).
- [89] H.-S. Kim and H.-Y. Kee, npj Quant Mater **2**, 1 (2017).
- [90] W. Zhao *et al.*, arXiv:2207.02312 (2022), 2207.02312.
- [91] C. L. Kane and E. J. Mele, Phys. Rev. Lett. **95**, 146802 (2005).
- [92] B. A. Bernevig and S.-C. Zhang, Phys. Rev. Lett. **96**, 106802 (2006).
- [93] M. König *et al.*, Science **318**, 766 (2007).
- [94] B. Béri and N. R. Cooper, Phys. Rev. Lett. **107**, 145301 (2011).
- [95] F. Mei, S.-L. Zhu, Z.-M. Zhang, C. H. Oh, and N. Goldman, Phys. Rev. A **85**, 013638 (2012).
- [96] K.-H. Jin and S.-H. Jhi, Sci Rep **5**, 8426 (2015).
- [97] C.-X. Liu, S.-C. Zhang, and X.-L. Qi, Annual Review of Condensed Matter Physics **7**, 301 (2016).
- [98] W. Liu *et al.*, Nano Lett. **20**, 1329 (2020).
- [99] S. Grover *et al.*, Nat. Phys. (2022).
- [100] A. Kitaev, Phys.-Usp. **44**, 131 (2001).
- [101] X.-L. Qi and S.-C. Zhang, Rev. Mod. Phys. **83**, 1057 (2011).
- [102] J. Alicea, Rep. Prog. Phys. **75**, 076501 (2012).
- [103] S. D. Sarma, M. Freedman, and C. Nayak, npj Quantum Inf **1**, 1 (2015).
- [104] J.-B. Fu *et al.*, Sci. China Phys. Mech. Astron. **64**, 107001 (2021).
- [105] L. Fu and C. L. Kane, Phys. Rev. Lett. **100**, 096407 (2008).
- [106] R. M. Lutchyn, J. D. Sau, and S. Das Sarma, Phys. Rev. Lett. **105**, 077001 (2010).
- [107] Y. Oreg, G. Refael, and F. von Oppen, Phys. Rev. Lett. **105**, 177002 (2010).
- [108] J. C. Budich and E. Ardonne, Phys. Rev. B **88**, 075419 (2013), 1306.4459.
- [109] A. Rajak and A. Dutta, Phys. Rev. E **89**, 042125 (2014), 1312.7109.
- [110] J. K. Asbóth, L. Oroszlány, and A. Pályi, arXiv:1509.02295 (2016), 1509.02295.

Bibliography

- [111] E. Prodan and H. Schulz-Baldes, arXiv:1510.08744 (2016), 1510.08744.
- [112] J.-W. Rhim, J. H. Bardarson, and R.-J. Slager, Phys. Rev. B **97**, 115143 (2018).
- [113] Y.-T. Lin *et al.*, Phys. Rev. B **102**, 085122 (2020).
- [114] M. Pletyukhov, D. M. Kennes, J. Klinovaja, D. Loss, and H. Schoeller, Phys. Rev. B **101**, 165304 (2020).
- [115] M. Pletyukhov, D. M. Kennes, J. Klinovaja, D. Loss, and H. Schoeller, Phys. Rev. B **101**, 161106 (2020).
- [116] Y. Kuno and Y. Hatsugai, Phys. Rev. B **104**, 125146 (2021).
- [117] J. F. Wienand, F. Horn, M. Aidelsburger, J. Bibo, and F. Grusdt, Phys. Rev. Lett. **128**, 246602 (2022).
- [118] J. Zak, Phys. Rev. Lett. **62**, 2747 (1989).
- [119] K. Wintersperger *et al.*, Nat. Phys. **16**, 1058 (2020).
- [120] C. Chin, R. Grimm, P. Julienne, and E. Tiesinga, Rev. Mod. Phys. **82**, 1225 (2010).
- [121] H. Lignier *et al.*, Phys. Rev. Lett. **99**, 220403 (2007).
- [122] M. A. Khamehchi, C. Qu, M. E. Mossman, C. Zhang, and P. Engels, Nat Commun **7**, 10867 (2016).
- [123] J. Struck *et al.*, Phys. Rev. Lett. **108**, 225304 (2012).
- [124] J. Struck *et al.*, Nature Phys **9**, 738 (2013).
- [125] C. J. Kennedy, W. C. Burton, W. C. Chung, and W. Ketterle, Nature Phys **11**, 859 (2015).
- [126] Y.-J. Lin, K. Jiménez-García, and I. B. Spielman, Nature **471**, 83 (2011).
- [127] W. S. Bakr, J. I. Gillen, A. Peng, S. Fölling, and M. Greiner, Nature **462**, 74 (2009).
- [128] L. W. Cheuk *et al.*, Phys. Rev. Lett. **114**, 193001 (2015).
- [129] J. Yang, L. Liu, J. Mongkolkiattichai, and P. Schauss, PRX Quantum **2**, 020344 (2021).
- [130] C. Gross and W. S. Bakr, Nat. Phys. **17**, 1316 (2021).
- [131] Archimedische Schraube, https://de.wikipedia.org/w/index.php?title=Archimedische_Schraube&oldid=233816882, 2023.
- [132] M. J. Rice and E. J. Mele, Phys. Rev. Lett. **49**, 1455 (1982).

- [133] M. Z. Hasan and C. L. Kane, *Rev. Mod. Phys.* **82**, 3045 (2010).
- [134] F. Grusdt, *Phys. Rev. B* **95**, 075106 (2017).
- [135] P. P. Aseev, P. Marra, P. Stano, J. Klinovaja, and D. Loss, *Phys. Rev. B* **99**, 205435 (2019).
- [136] C.-E. Bardyn *et al.*, *New J. Phys.* **15**, 085001 (2013).
- [137] Y. He and C.-C. Chien, *Phys. Rev. B* **106**, 024310 (2022).
- [138] Z. Huang and D. P. Arovas, *Phys. Rev. Lett.* **113**, 076407 (2014).
- [139] C. Knapp, T. Karzig, R. M. Lutchyn, and C. Nayak, *Phys. Rev. B* **97**, 125404 (2018).
- [140] D. Linzner, L. Wawer, F. Grusdt, and M. Fleischhauer, *Phys. Rev. B* **94**, 201105 (2016).
- [141] C.-E. Bardyn, L. Wawer, A. Altland, M. Fleischhauer, and S. Diehl, *Phys. Rev. X* **8**, 011035 (2018).
- [142] M. Buser, F. Heidrich-Meisner, and U. Schollwöck, *Phys. Rev. A* **99**, 053601 (2019).
- [143] P. Mognini and N. R. Cooper, *Phys. Rev. Res.* **5**, 023004 (2023).
- [144] R. Unanyan, M. Kiefer-Emmanouilidis, and M. Fleischhauer, *Phys. Rev. Lett.* **125**, 215701 (2020).
- [145] O. Viyuela, A. Rivas, and M. A. Martin-Delgado, *Phys. Rev. Lett.* **112**, 130401 (2014).
- [146] R. Unanyan, M. Kiefer-Emmanouilidis, and M. Fleischhauer, *Phys. Rev. Lett.* **125**, 215701 (2020).
- [147] E. Berg, M. Levin, and E. Altman, *Phys. Rev. Lett.* **106**, 110405 (2011).
- [148] Y. Ke, X. Qin, Y. S. Kivshar, and C. Lee, *Phys. Rev. A* **95**, 063630 (2017).
- [149] F. Mei, G. Chen, N. Goldman, L. Xiao, and S. Jia, *New J. Phys.* **21**, 095002 (2019).
- [150] M. Nakagawa, T. Yoshida, R. Peters, and N. Kawakami, *Phys. Rev. B* **98**, 115147 (2018).
- [151] T. Qin *et al.*, *Phys. Rev. A* **98**, 033601 (2018).
- [152] L. Stenzel, A. L. C. Hayward, C. Hubig, U. Schollwöck, and F. Heidrich-Meisner, *Phys. Rev. A* **99**, 053614 (2019).
- [153] R. Gawatz, A. C. Balram, E. Berg, N. H. Lindner, and M. S. Rudner, *Phys. Rev. B* **105**, 195118 (2022).

Bibliography

- [154] J. Tangpanitanon *et al.*, Phys. Rev. Lett. **117**, 213603 (2016).
- [155] M. Jürgensen, S. Mukherjee, and M. C. Rechtsman, Nature **596**, 63 (2021).
- [156] Y. Kuno, K. Shimizu, and I. Ichinose, New Journal of Physics **19**, 123025 (2017).
- [157] T.-S. Zeng, W. Zhu, and D. N. Sheng, Phys. Rev. B **94**, 235139 (2016).
- [158] L. Taddia *et al.*, Phys. Rev. Lett. **118**, 230402 (2017).
- [159] Y. Kuno and Y. Hatsugai, Phys. Rev. Research **2**, 042024 (2020).
- [160] L. Lin, Y. Ke, and C. Lee, Phys. Rev. A **101**, 023620 (2020).
- [161] G. Salerno, G. Palumbo, N. Goldman, and M. Di Liberto, Phys. Rev. Res. **2**, 013348 (2020).
- [162] R. Bianco and R. Resta, Phys. Rev. B **84** (2011).
- [163] P. W. Anderson, Phys. Rev. **109**, 1492 (1958).
- [164] S. Nakajima *et al.*, Nat. Phys. **17**, 844 (2021).
- [165] M. D. Caio, G. Möller, N. R. Cooper, and M. J. Bhaseen, Nat. Phys. **15**, 257 (2019).
- [166] B. Irsigler, J.-H. Zheng, and W. Hofstetter, Phys. Rev. A **100**, 023610 (2019).
- [167] A. Markov and A. Rubtsov, Phys. Rev. B **104**, L081105 (2021), 2009.01801.
- [168] J. Sykes and R. Barnett, Phys. Rev. B **103**, 155134 (2021).
- [169] W. Chen, Phys. Rev. B **107**, 045111 (2023).
- [170] Z.-Z. Li, J. Atalaya, and K. B. Whaley, Phys. Rev. A **105**, 052418 (2022).
- [171] R. Lin, T. Tai, L. Li, and C. H. Lee, Front. Phys. **18**, 53605 (2023).
- [172] H. Liu *et al.*, Nanophotonics **12**, 2273 (2023).
- [173] H. Nasari, G. G. Pyrialakos, D. N. Christodoulides, and M. Khajavikhan, Opt. Mater. Express, OME **13**, 870 (2023).
- [174] Q. Yan *et al.*, Nanophotonics **12**, 2247 (2023).
- [175] K. J. Vahala, Nature **424**, 839 (2003).
- [176] F. Mivehvar, F. Piazza, T. Donner, and H. Ritsch, Advances in Physics **70**, 1 (2021).
- [177] T. Holstein, Annals of Physics **8**, 325 (1959).

- [178] P. Ehrenfest, *Z. Physik* **45**, 455 (1927).
- [179] G. Li, B. Movaghar, A. Nitzan, and M. A. Ratner, *The Journal of Chemical Physics* **138**, 044112 (2013).
- [180] J. C. Tully, *Faraday Discuss.* **110**, 407 (1998).
- [181] C. N. Varney, K. Sun, M. Rigol, and V. Galitski, *Phys. Rev. B* **84**, 241105 (2011).
- [182] L. Wang, X. Dai, and X. C. Xie, *EPL* **98**, 57001 (2012).
- [183] T. Yoshida, R. Peters, S. Fujimoto, and N. Kawakami, *Phys. Rev. Lett.* **112**, 196404 (2014).
- [184] T. I. Vanhala *et al.*, *Phys. Rev. Lett.* **116**, 225305 (2016).
- [185] J.-H. Zheng, B. Irsigler, L. Jiang, C. Weitenberg, and W. Hofstetter, *Phys. Rev. A* **101**, 013631 (2020).
- [186] D. C. Tsui, H. L. Stormer, and A. C. Gossard, *Phys. Rev. Lett.* **48**, 1559 (1982).
- [187] H. L. Stormer, D. C. Tsui, and A. C. Gossard, *Rev. Mod. Phys.* **71**, S298 (1999).
- [188] Y.-C. He, F. Grusdt, A. Kaufman, M. Greiner, and A. Vishwanath, *Phys. Rev. B* **96**, 201103 (2017).
- [189] N. Nagaosa and J.-I. Takimoto, *J. Phys. Soc. Jpn.* **55**, 2735 (1986).
- [190] M. E. Torio, A. A. Aligia, and H. A. Ceccatto, *Phys. Rev. B* **64**, 121105 (2001).
- [191] A. A. Aligia, *Phys. Rev. B* **69**, 041101 (2004).
- [192] S. R. Manmana, V. Meden, R. M. Noack, and K. Schönhammer, *Phys. Rev. B* **70**, 155115 (2004).
- [193] M. Hafez-Torbati, Master Thesis TU Dortmund (2014).
- [194] M. Messer *et al.*, *Phys. Rev. Lett.* **115**, 115303 (2015).
- [195] M. E. Torio, A. A. Aligia, G. I. Japaridze, and B. Normand, *Phys. Rev. B* **73**, 115109 (2006).
- [196] K. Loida, J.-S. Bernier, R. Citro, E. Orignac, and C. Kollath, *Phys. Rev. Lett.* **119**, 230403 (2017).
- [197] M. Berry, *Proc. R. Soc. Lond. A* **392**, 45 (1984).
- [198] M. Nakahara, *Geometry, Topology and Physics, Second Edition* (Taylor & Francis, 2003).
- [199] G. Rigolin, G. Ortiz, and V. H. Ponce, *Phys. Rev. A* **78**, 052508 (2008).

Bibliography

- [200] G. Rigolin and G. Ortiz, Phys. Rev. Lett. **104**, 170406 (2010).
- [201] S. Teufel, *Adiabatic Perturbation Theory in Quantum Dynamics*, Lecture Notes in Mathematics Vol. 1821 (Springer, Berlin, Heidelberg, 2003).
- [202] R. Resta, Ferroelectrics **136**, 51 (1992).
- [203] D. Vanderbilt, *Berry Phases in Electronic Structure Theory: Electric Polarization, Orbital Magnetization and Topological Insulators* (Cambridge University Press, Cambridge, 2018).
- [204] W. P. Su, J. R. Schrieffer, and A. J. Heeger, Phys. Rev. Lett. **42**, 1698 (1979).
- [205] T. Kato, J. Phys. Soc. Jpn. **5**, 435 (1950).
- [206] J. C. Budich and B. Trauzettel, physica status solidi (RRL) – Rapid Research Letters **7**, 109 (2013), 1210.6672.
- [207] G. Rigolin and G. Ortiz, Phys. Rev. A **85** (2012), 1111.5333.
- [208] R. Resta, Phys. Rev. Lett. **80**, 1800 (1998).
- [209] A. P. Schnyder, S. Ryu, A. Furusaki, and A. W. W. Ludwig, Phys. Rev. B **78** (2008).
- [210] S. Stützer *et al.*, Experimental realization of a topological Anderson insulator, in *CLEO: 2015*, p. FTh3D.2, San Jose, California, 2015, OSA.
- [211] N. Parappurath, F. Alpeggiani, L. Kuipers, and E. Verhagen, Science Advances **6**, eaaw4137 (2020).
- [212] P. Titum, E. Berg, M. S. Rudner, G. Refael, and N. H. Lindner, Phys. Rev. X **6**, 021013 (2016), 1506.00650.
- [213] Y. Kuno, Eur. Phys. J. B **92**, 195 (2019).
- [214] R. D. King-Smith and D. Vanderbilt, Phys. Rev. B **47**, 1651 (1993).
- [215] N. Marzari, A. A. Mostofi, J. R. Yates, I. Souza, and D. Vanderbilt, Rev. Mod. Phys. **84**, 1419 (2012).
- [216] D. M. Ceperley and B. J. Alder, Phys. Rev. Lett. **45**, 566 (1980).
- [217] S. Zhang, J. Carlson, and J. E. Gubernatis, Phys. Rev. B **55**, 7464 (1997).
- [218] P. H. Acioli, Journal of Molecular Structure: THEOCHEM **394**, 75 (1997).
- [219] G. H. Booth, A. J. W. Thom, and A. Alavi, J. Chem. Phys. **131**, 054106 (2009).
- [220] H. Weisbrich, R. Klees, G. Rastelli, and W. Belzig, PRX Quantum **2**, 010310 (2021).

- [221] H. Pothier *et al.*, *Physica B: Condensed Matter* **169**, 573 (1991).
- [222] M. W. Keller, J. M. Martinis, N. M. Zimmerman, and A. H. Steinbach, *Appl. Phys. Lett.* **69**, 1804 (1996).
- [223] M. Möttönen, J. J. Vartiainen, and J. P. Pekola, *Phys. Rev. Lett.* **100**, 177201 (2008).
- [224] S. H. Autler and C. H. Townes, *Phys. Rev.* **100**, 703 (1955).
- [225] T. Ozawa *et al.*, *Rev. Mod. Phys.* **91**, 015006 (2019).
- [226] W. D. Phillips, *Rev. Mod. Phys.* **70** (1998).
- [227] W. Ketterle and N. J. V. Druten, *Advances In Atomic, Molecular, and Optical Physics* **37** (1996).
- [228] S. Taie *et al.*, *Nat. Phys.* **18**, 1356 (2022).
- [229] T. Ozawa and H. M. Price, *Nat Rev Phys* **1**, 349 (2019).
- [230] T. Xiao *et al.*, *Science Bulletin* **66**, 2175 (2021).
- [231] V. Ahufinger, L. Sanchez-Palencia, A. Kantian, A. Sanpera, and M. Lewenstein, *Phys. Rev. A* **72**, 063616 (2005).
- [232] D. Dudley, W. M. Duncan, and J. Slaughter, *MOEMS Display and Imaging Systems* **4985**, 14 (2003).
- [233] S. Lee, J. K. Kim, Y. Won, and K. Oh, *Proceedings of SPIE - The International Society for Optical Engineering* (2006).
- [234] X. Qiu, J. Zou, X. Qi, and X. Li, *npj Quantum Inf* **6**, 1 (2020).
- [235] A. Szameit and S. Nolte, *J. Phys. B: At. Mol. Opt. Phys.* **43**, 163001 (2010).
- [236] S. Hu, Y. Ke, and C. Lee, *Phys. Rev. A* **101**, 052323 (2020).
- [237] R. Li *et al.*, *Commun Phys* **5**, 1 (2022).
- [238] J. Bezanson, A. Edelman, S. Karpinski, and V. B. Shah, *SIAM Review* **59**, 65 (2017).
- [239] M. Fishman, S. White, and E. Stoudenmire, *SciPost Physics Codebases* , 004 (2022).
- [240] L. N. Trefethen and D. B. III, *Numerical Linear Algebra* (SIAM, 1997).
- [241] J. Crank and P. Nicolson, *Adv Comput Math* **6**, 207 (1996).

Bibliography

- [242] S. R. Manmana, A. Muramatsu, and R. M. Noack, *AIP Conference Proceedings* **789**, 269 (2005).
- [243] M. Ten Brink *et al.*, *J Chem Phys* **156**, 234109 (2022).
- [244] C. Lanczos, *J. RES. NATL. BUR. STAN.* **45**, 255 (1950).
- [245] A. W. Sandvik, A. Avella, and F. Mancini, *Computational Studies of Quantum Spin Systems*, in *LECTURES ON THE PHYSICS OF STRONGLY CORRELATED SYSTEMS XIV: Fourteenth Training Course in the Physics of Strongly Correlated Systems*, pp. 135–338, Vietri sul Mare, (Italy), 2010.
- [246] A. W. Sandvik and J. Kurkijärvi, *Phys. Rev. B* **43**, 5950 (1991).
- [247] A. N. Rubtsov, V. V. Savkin, and A. I. Lichtenstein, *Phys. Rev. B* **72**, 035122 (2005).
- [248] A. Georges, G. Kotliar, W. Krauth, and M. J. Rozenberg, *Rev. Mod. Phys.* **68**, 13 (1996).
- [249] I. P. McCulloch, *arXiv:0804.2509* (2008), 0804.2509.
- [250] U. Schollwoeck, *Annals of Physics* **326**, 96 (2011), 1008.3477.
- [251] R. Orús, *Annals of Physics* **349**, 117 (2014).
- [252] M. B. Hastings, *J. Stat. Mech.* **2007**, P08024 (2007).
- [253] J. Eisert, M. Cramer, and M. B. Plenio, *Rev. Mod. Phys.* **82**, 277 (2010).
- [254] ITensorInfiniteMPS (<https://github.com/ITensor/ITensorInfiniteMPS.jl>), 2023.
- [255] G. Roati *et al.*, *Nature* **453**, 895 (2008).
- [256] J. Billy *et al.*, *Nature* **453**, 891 (2008).
- [257] M. Ippoliti and R. N. Bhatt, *Phys. Rev. Lett.* **124**, 086602 (2020).
- [258] C. Hamaguchi *et al.*, *Jpn. J. Appl. Phys.* **34**, 4519 (1995).
- [259] Y. Ke *et al.*, *Phys. Rev. Research* **2**, 033143 (2020).
- [260] S. Hu, Y. Ke, and C. Lee, *Phys. Rev. A* **101**, 052323 (2020).
- [261] P. Marra and M. Nitta, *Phys. Rev. Research* **2**, 042035 (2020).
- [262] J. Li, R.-L. Chu, J. K. Jain, and S.-Q. Shen, *Phys. Rev. Lett.* **102**, 136806 (2009).
- [263] D. A. Huse, R. Nandkishore, V. Oganesyan, A. Pal, and S. L. Sondhi, *Phys. Rev. B* **88**, 014206 (2013).

- [264] L. Guidoni, C. Triché, P. Verkerk, and G. Grynberg, *Phys. Rev. Lett.* **79**, 3363 (1997).
- [265] A. Szabó and U. Schneider, *Phys. Rev. B* **101**, 014205 (2020).
- [266] R. Bianco, PhD thesis, Università degli studi di Trieste (2014).
- [267] H. Li and F. D. M. Haldane, *Phys. Rev. Lett.* **101**, 010504 (2008).
- [268] E. Prodan, T. L. Hughes, and B. A. Bernevig, *Phys. Rev. Lett.* **105**, 115501 (2010).
- [269] R. Nandkishore and D. A. Huse, *Annual Review of Condensed Matter Physics* **6**, 15 (2015).
- [270] D. A. Abanin, E. Altman, I. Bloch, and M. Serbyn, *Rev. Mod. Phys.* **91**, 021001 (2019).
- [271] A. A. Markov and A. N. Rubtsov, *Phys. Rev. B* **104**, L081105 (2021).
- [272] J. E. Avron, M. Fraas, G. M. Graf, and O. Kenneth, *New J. Phys.* **13**, 053042 (2011).
- [273] E. P. L. van Nieuwenburg and S. D. Huber, *Phys. Rev. B* **90**, 075141 (2014).
- [274] O. Viyuela, A. Rivas, and M. A. Martin-Delgado, *Phys. Rev. B* **86**, 155140 (2012).
- [275] A. Rivas, O. Viyuela, and M. A. Martin-Delgado, *Phys. Rev. B* **88**, 155141 (2013).
- [276] Y. He and C.-C. Chien, *Phys. Rev. B* **106**, 024310 (2022).
- [277] H. Fröhlich, *Advances in Physics* **3**, 325 (1954).
- [278] H. Matsueda, S. Sota, T. Tohyama, and S. Maekawa, *J. Phys. Soc. Jpn.* **81**, 013701 (2012).
- [279] F. Dorfner, L. Vidmar, C. Brockt, E. Jeckelmann, and F. Heidrich-Meisner, *Phys. Rev. B* **91**, 104302 (2015).
- [280] J. Stolpp, J. Herbrych, F. Dorfner, E. Dagotto, and F. Heidrich-Meisner, *Phys. Rev. B* **101**, 035134 (2020).
- [281] D. Jansen, C. Jooss, and F. Heidrich-Meisner, *Phys. Rev. B* **104**, 195116 (2021).
- [282] J. Kogoj, L. Vidmar, M. Mierzejewski, S. A. Trugman, and J. Bonča, *Phys. Rev. B* **94**, 014304 (2016).
- [283] C. Brockt, F. Dorfner, L. Vidmar, F. Heidrich-Meisner, and E. Jeckelmann, *Phys. Rev. B* **92**, 241106 (2015).
- [284] S. Mondal, S. Greschner, L. Santos, and T. Mishra, *Phys. Rev. A* **104**, 013315 (2021).

Bibliography

- [285] N. F. Mott, Proc. Phys. Soc. A **62**, 416 (1949).
- [286] M. Imada, A. Fujimori, and Y. Tokura, Rev. Mod. Phys. **70**, 1039 (1998).
- [287] S. Raghu, X.-L. Qi, C. Honerkamp, and S.-C. Zhang, Phys. Rev. Lett. **100**, 156401 (2008), 0710.0030.
- [288] D. P. Arovas, E. Berg, S. A. Kivelson, and S. Raghu, Annual Review of Condensed Matter Physics **13**, 239 (2022).
- [289] P. W. Anderson, Materials Research Bulletin **8**, 153 (1973).
- [290] L. Savary and L. Balents, Rep. Prog. Phys. **80**, 016502 (2016).
- [291] G. Grüner, Rev. Mod. Phys. **60**, 1129 (1988).
- [292] H. Polshyn *et al.*, Nat. Phys. **18**, 42 (2022).
- [293] S. Vijay, J. Haah, and L. Fu, Phys. Rev. B **92**, 235136 (2015).
- [294] Y.-Y. He, H.-Q. Wu, Z. Y. Meng, and Z.-Y. Lu, Phys. Rev. B **93**, 195164 (2016).
- [295] Z. Tao *et al.*, arXiv:2303.04582 (2023), 2303.04582.
- [296] C. Nayak, S. H. Simon, A. Stern, M. Freedman, and S. Das Sarma, Rev. Mod. Phys. **80**, 1083 (2008).
- [297] M. Banerjee *et al.*, Nature **559**, 205 (2018).
- [298] S. A. Parameswaran, R. Roy, and S. L. Sondhi, Comptes Rendus Physique **14**, 816 (2013).
- [299] L. Taddia *et al.*, Phys. Rev. Lett. **118**, 230402 (2017).
- [300] M. Jürgensen, S. Mukherjee, C. Jörg, and M. C. Rechtsman, Nat. Phys. **19**, 420 (2023).
- [301] R. Resta, Phys. Rev. Lett. **80**, 1800 (1998).
- [302] V. Khemani, R. Nandkishore, and S. L. Sondhi, Nature Physics **11**, 560 (2015).
- [303] A. A. Markov and A. N. Rubtsov, Phys. Rev. B **104**, L081105 (2021).
- [304] T. Köhler, J. Stolpp, and S. Paeckel, SciPost Physics **10**, 058 (2021).
- [305] J. E. Hirsch and E. Fradkin, Phys. Rev. B **27**, 4302 (1983).
- [306] R. H. McKenzie, C. J. Hamer, and D. W. Murray, Phys. Rev. B **53**, 9676 (1996).
- [307] R. J. Bursill, R. H. McKenzie, and C. J. Hamer, Phys. Rev. Lett. **80**, 5607 (1998).
- [308] M. Kawamura *et al.*, Nat. Phys. **19**, 333 (2023).

- [309] P. R. Bas and A. A. Aligia, arXiv:2304.04563 (2023), 2304.04563.
- [310] Y. Hatsugai and Y. Kuno, Phys. Rev. B **107**, 235106 (2023).
- [311] B. Zhu, L.-J. Lang, Q. Wang, Q. J. Wang, and Y. D. Chong, Phys. Rev. Res. **5**, 023044 (2023).
- [312] C. S. Chiu, G. Ji, A. Mazurenko, D. Greif, and M. Greiner, Phys. Rev. Lett. **120**, 243201 (2018).
- [313] K. K. Das, S. Kim, and A. Mizel, Phys. Rev. Lett. **97**, 096602 (2006).